Investigation on the Influence of Porous Carrier Materials on the Loading and Dissolution Behavior of R/S-Ibuprofen

Untersuchung zum Einfluss von porösen Trägern auf die Beladung und Freisetzung von R/S-Ibuprofen

zur Erlangung des akademischen Grades eines
DOKTORS DER INGENIEURWISSENSCHAFTEN (Dr.-Ing.)

der Fakultät für Chemieingenieurwesen und Verfahrenstechnik des Karlsruher Instituts für Technologie (KIT)

genehmigte
DISSERTATION

von
Dipl.-Ing. Sarah Reiser
geboren in Wolfach

Referent:	Prof. Dr.-Ing. Michael Türk
Korreferent:	Prof. Dr. Jürgen Hubbuch
Tag der mündlichen Prüfung:	20.04.2018

Acknowledgement

Diese Arbeit ist im Rahmen meiner wissenschaftlichen Tätigkeit am Institut für Technische Thermodynamik (ITTK) des Karlsruher Instituts für Technologie entstanden. Zu ihrem Gelingen haben einige Menschen beigetragen, denen ich an dieser Stelle danken möchte.

Zunächst gilt ein ganz besonderer Dank meinem Doktorvater Prof. Dr.-Ing. Michael Türk für seine hervorragende fachliche Betreuung, die inspirierenden Diskussionen, das mir entgegengebrachte Vertrauen und die kreativen Freiräume bei der Bearbeitung meines Themas. Prof. Dr. Jürgen Hubbuch danke ich für die freundliche Übernahme des Korreferats und die Möglichkeit der Labor- und HPLC-Nutzung.

Für die finanzielle Unterstützung des Projekts bedanke ich mich herzlich bei der Deutschen Forschungsgemeinschaft. Des Weiteren danke ich Prof. Dr. Claus Feldmann für die Möglichkeit der Benutzung des STADI-MP Diffraktometers, der Firma Rubotherm für die freundliche Bereitstellung der Magnetschwebewaage sowie der Firma Quantachrome Instruments für die freundliche Bereitstellung des Analysegerätes Nova 2000e. Ein weiterer Dank gilt auch Prof. Dr. rer. nat. Alfred Weber, PD Dr. habil. Monika Johannsen, Dr. Masoom Shaban und Miaotian Sun für die gute Zusammenarbeit, die Expertise sowie die Herstellung der Trägermaterialien. Zusätzlich möchte ich mich noch bei Prof. Dr.-Ing. habil. Reiner Staudt und Dr. Jens Möllmer für ihre fachliche Unterstützung im Bereich der Adsorption bedanken. Vielen Dank auch an Anne und Philipp die durch ihr Engagement während ihrer Masterarbeit zum Gelingen dieser Arbeit beigetragen haben.

Ein besonderer Dank geht auch an...

...Marlene - für deine helfende Hand, immer offenen Ohren, aufmunternden Worte, kritischen Korrekturen und die harte Schule der Wortwahl.

...Simone - für die gute Büronachbarschaft, offene Gespräche und die Versorgung mit Nervennahrung.

...Antje und Gertraud - für eure Hilfe bei der Bezwingung administrativer Hürden.

...Andreas, Claudio, Goran, Jörg und Manfred - für eure technische Unterstützung.

...die ITTK-Arbeitskollegen - für Rat und Hilfe bei Fragen, den ein oder anderen netten Abend, legendäre Sommerfeste und weitere ITT-Aktionen.

...die Kollegen des MABs - dass ihr mich im Labor ertragen habt und mir bei Fragen mit Rat und Tat zur Seite standet. Nicht zu vergessen der Spiel und Spaß beim Beachhandball. Hierbei gilt Josi noch ein besonderer Dank für die äußerst kritische Korrektur meiner Arbeit.

...die Adsorbatoren-Clique (Frede, Christian, Frederik, Roman, Sebastian, Hannes und viele mehr) - für inspirierende und spaßige Workshops, eure Expertise, Rat und Hilfe.

...Karsten - durch deine Hilfe habe ich auch endlich die Herausforderungen der HPLC in Griff bekommen.

...Stephan - für dein Verständnis, Ablenkung und die Aufmunterungen im Endspurt.

Und last but not least geht ein besonderer Dank an meine Familie für euren Rückhalt, viel Verständnis, aufmunternden Worte und eure Unterstützung.

Content

Abstract

One of the big challenges in pharmaceutical research is to improve the bioavailability of orally administered active ingredients to ensure a fast and efficient relief of patients' suffering. The bioavailability of active ingredients depend on their dissolution and resorption in the gastrointestinal tract (GIT). With regard to substances which are highly permeable but poorly soluble in aqueous solutions (class II of the Biopharmaceutical Classification System (BCS) [1]) their bioavailability is particularly limited by their dissolution in the GIT. To still ensure a sufficient concentration of such active ingredients at the site of action, the orally applied dosage can be increased. Nevertheless, this can cause dangerous side effects to the human body [2]. For this reason, it is aimed to administer the lowest possible dose. In order to still provide a sufficient concentration of active substances at the site of action, the production of formulations with improved dissolution behavior is essential, especially for active ingredients which belong to class II of the BCS.

The field of process engineering offers several possibilities to improve the solubility, such as the use of surfactants, co-solvents, solid dispersions or nano-suspensions [3, 4]. Furthermore, particle size reduction or the deposition on carrier materials can improve the dissolution velocity significantly [3]. Conventional particle size reduction processes such as milling, grinding or spray drying cause several disadvantages (e.g. broad particle size distribution, thermal or chemical degradation of the product or organic residues in the final product). To prevent these disadvantages, supercritical fluid (SCF) processes can be used [5].

ABSTRACT

SCFs are characterized by their numerous positive properties such as gas-like transport properties and liquid-like densities [6], low toxicity and the fact that they are chemically inert [7]. CO_2 is commonly used as a SCF ($scCO_2$) due to its low critical data (T_c = 304 K, p_c = 7.4 MPa). Therefore, mild process conditions can be realized which is of special interest for processing thermolabile active ingredients. SCFs are used e.g. in the Controlled Particle Deposition (CPD) process [8]. In this process, a particle size reduction as well as a subsequently formulation of the active ingredient can be accomplished in one processing step. During the impregnation step of the CPD process the active ingredient is dissolved in the SCF at constant process conditions ($T > T_c$ and $p > p_c$), due to the liquid-like density of the SCF. Furthermore, the diffusion of the molecularly dissolved active ingredient inside a porous carrier material (which is insoluble in the SCF) is possible due to the gas-like transport properties of the SCF. In the final depressurization step (~20 s) the solubility of the active ingredient in the SCF is decreased. Due to this and the resulting supersaturation, the active substance is deposited inside the pores of the carrier material. Depending on the carrier material CPD products for a controlled release of the active ingredient can be obtained [8 - 10].

In general, the dissolution behavior of active ingredients needs to be investigated e.g. in vitro according to the recommendations of the Food and Drug Administration (FDA) [11]. As it was mentioned before, an enhanced or retarded dissolution is dependent on the active ingredient-carrier system. Hence, time and cost intensive in vitro studies need to be carried out for each CPD active ingredient-carrier system. In order to ensure a fast decision of a suitable system for a targeting application, an efficient and cost-effective selection method is demanded, to prevent expensive experimental studies. The idea is to base this method on the prediction of the CPD loading and the dissolution performance of new active ingredient-carrier systems. This prediction should be possible solely by the knowledge of the chemical nature of the active ingredient as well as the knowledge of the chemical nature and structural specific properties (e.g. specific surface area, pore volume, pore size and surface functionalization) of the carrier material.

Previous CPD studies were focused on the identification of suitable chemical carrier properties for a controlled release of active ingredients [8 - 10, 12 - 15]. The impact of specific carrier properties such as specific surface area, pore volume, pore size or surface functionalization has not been investigated, yet.

Therefore, the first part of this work aims to identify the impact of specific carrier material properties mentioned above on CPD loading and its impact on the

dissolution behavior of active ingredients in aqueous media. For the design and modeling of the CPD process the knowledge of the adsorption behavior of $scCO_2$ and the active ingredient on the carrier material is essential. Hence, the second part of this work is attributed to the determination of this knowledge. In addition to this the question arises, if there is a competitive adsorption between the $scCO_2$ and the active ingredient on the carrier material. The clarification of this question is also focused in the second part.

Racemic R/S-ibuprofen (ibuprofen) which is a typical representative of class II of the BCS and used as an analgesic and anti-inflammatory drug is systematically investigated in this work. Silica materials are considered to be suitable carriers for a controlled dissolution of active ingredients in aqueous solutions [9, 10]. Thus, different silica materials were used to investigate the impact of specific carrier material properties mentioned above on CPD loading and their dissolution behavior. Besides commercially available mesoporous carrier materials (MCM-41 and SBA-15) ibuprofen was deposited on silica carriers which were synthesized by different project partners. Carrier materials with variations in specific surface area, pore volume and pore size were prepared by Salt Assissted Spray Pyrolysis at the Institute of Particle Technology, Technical University of Clausthal (group of A. Weber) [16]. Commercially available Kromasil® was functionalized with S-(+)-ibuprofen by the Covalent Bonding Reaction at the Institute for Thermal Separation Processes (V8), Technical University Hamburg-Harburg (group of M. Johannsen) to investigate the influence of a surface functionalization [17]. The experimental conditions for the deposition of ibuprofen were set to $T = 313$ K and $p = 15$ MPa respectively, while $scCO_2$ was used as SCF.

The dissolution experiments were carried out due to the recommendations of the FDA. In this context, a suitable method to analyze the dissolution samples by High Pressure Liquid Chromatography was developed.

To evaluate the dissolution behavior of the obtained CPD products their dissolution was compared to the dissolution of an ibuprofen-ß-cyclodextrin inclusion complex. This complex was considered to be the benchmark for the evaluation because it shows a high dissolution rate of ibuprofen [8] due to the high water solubility of ß-cyclodextrin (18.5 mg/ml at $T = 298$ K [18]). The inclusion complex was also produced by the CPD process.

Within this work, a master thesis [19] was supervised. As an important pre-work it aimed to design and build a dissolution apparatus at the department, according to the recommendations of the FDA. Due to low drug loadings on certain carrier

materials (e.g. ß-cyclodextrin) and limited sample amounts the dissolution volume of the apparatus was scaled down on basis of the dimensions proposed by Klein und Shah [20]. These dimensions were validated by a fluid dynamic simulation in ANSYS Fluent [19]. It was shown that the fluid dynamic profile was particularly influenced by the position of the paddle stirrer. Thus, the position of the paddle stirrer as well as its rotation speed in the down-scaled apparatus was validated to obtain the same fluid dynamic profile compared to the profile of an FDA apparatus.

The exact sample injection method is not specified by the FDA. Therefore, different sample injection methods were investigated in a reproducibility study [19]. The best reproducibility was obtained by sieving the sample onto the dissolution media. The exact dimensions as well as some selected results of the fluid dynamic simulation and the reproducibility study can be found in the appendix.

In the first part of this work it was possible to identify the impact of specific carrier material properties (e.g. specific surface area, pore volume, pore size and surface functionalization) [16, 17, 21]. The highest loading (~50 wt%) was achieved by the carrier materials (MCM-41 and SBA-15) with the highest specific surface area. Initially, a linear dependency has been assumed. An increasing specific surface area led to higher CPD loadings. The influence of pore size and pore volume was also noticed. Wider mesopores ($D_P \geq 25$ nm) are beneficial for higher CPD loadings, because of the fact, that there is enough space for a multilayer deposition of ibuprofen. This was also evident from the value of the calculated "number of monolayer" [22] ($D_P = 25$ nm: $NML = 4.09$, $D_P = 30$ nm: $NML = 9.07$). Nevertheless, increasing pore size was decisive for the increasing "degree of crystallinity" [22] of the deposited ibuprofen, which was detected by X-ray diffraction (XRD) and differential scanning calorimetry (DSC). Compared to this, the formation of amorphous ibuprofen structures was observed in small mesopores ($D_P \leq 4$ nm). The functionalization of the carrier materials with S-(+)-ibuprofen led to lower loading results than it would have been assumed by the assumption of the linear dependency mentioned above. On the functionalized carriers the formation of amorphous fractions of the deposited ibuprofen was favored.

The dissolution performance of the CPD processed carrier materials was investigated at pH = 2.0 and 5.5. It was obvious that nearly all CPD processed carrier materials showed an improved dissolution performance compared to the unprocessed ibuprofen. Due to the pH dependent solubility of ibuprofen in aqueous solutions [19, 23] the dissolution behavior of all investigated systems was increased with increasing pH.

In general, the dissolution rate of ibuprofen out of wider mesopores ($D_P \geq 25$ nm) was faster compared to small ($D_P \leq 4$ nm) and channel-like mesopores. Still, the increasing "degree of crystallinity" with increasing pore size led to a diminished dissolution behavior especially at pH = 2.0. At pH = 5.5 it was found that the "degree of crystallinity" played a minor role. At this pH the dissolution performance is primarily influenced by the particle size of the ibuprofen. Therefore, the knowledge of the "degree of crystallinity" is a crucial factor for the prediction of the dissolution behavior of the obtained CPD products.

Regarding the carrier materials which were functionalized with S-(+)-ibuprofen, it was revealed that the location and the amount of the functionalization influences the dissolution behavior. The carrier material with a high amount of functionalization on its outer surface tended to agglomeration. Furthermore, this carrier was poorly wettable by the aqueous media due to the hydrophobic character of S-(+)-ibuprofen. As a result of this, the dissolution rate of the deposited ibuprofen was diminished.

In comparison to the ß-cyclodextrin inclusion complex, which was considered to be the benchmark as mentioned above, all investigated silica carrier materials showed a lower dissolution at pH = 2.0. At pH = 5.5 only the carrier materials with the widest mesopores ($D_P \geq 25$ nm) showed a similar dissolution performance to the inclusion complex.

The dissolution profiles were fitted with different models to ensure an easier comparison of the experimental results. In this context, the smallest deviation was achieved by the model of 1st-order from Gibaldi und Feldman [24] including the modification from Costa [25].

N_2-sorption experiments at $T = 77$ K are widely used for a fast and easy characterization of carrier materials. These measurements were carried out for unprocessed and CPD processed carrier materials. The unprocessed carrier materials with small mesopores ($D_P \leq 4$ nm) showed a typical capillary condensation step at $p/p_0 = 0.3 - 0.4$. This step was less distinctive and shifted towards lower relative pressures for the same CPD processed carrier materials. It was possible to definitely assign the shift of the capillary condensation to the ibuprofen which was deposited inside the pores of the carrier material. On basis of this shift it is possible to verify the deposition of ibuprofen inside the porous carrier materials in comparison to previously used XRD or DSC analysis.

In the second part of this work, the adsorption of CO_2 on two important carrier materials (MCM-41 and SBA-15) was investigated by a magnetic suspension balance

(MSB) [26] experimentally and theoretically to gain information of the adsorption behavior during the CPD process [27, 28].

The accurate function of the MSB was validated by measuring the adsorption of N_2 and CO_2 on AC Norit R1 Extra, which is considered to be a reference adsorbent [27]. Next, the adsorption of CO_2 on MCM-41 and SBA-15 was measured in a wide range of temperature ($T = 298 - 353$ K), pressure ($p = 0 - 25$ MPa) and density ($\varrho_{CO2,bulk} = 0 - 900$ kg/m^3) [28]. Due to the buoyancy effect of the MSB, excess isotherms were measured. Therefore, the absolute amount adsorbed (which does not correspond to the excess values) needs to be calculated by a suitable model [29 - 31].

In the low density range ($\varrho_{CO2,bulk} \leq 200$ kg/m^3) all CO_2 excess isotherms increased, generally. With increasing density, they reached a maximum and decreased afterwards. At higher temperatures the excess values were lower, whereas the maximum of the excess isotherms was shifted towards higher densities.

Based on the excess values the absolute amount adsorbed of CO_2 was calculated by the model of Menon [29] in a next step. The saturation amount adsorbed on both carrier materials (MCM-41: $n_{abs,sat} = \sim$13.0 mmol/g; SBA-15: $n_{abs,sat} = \sim$13.5 mmol/g) was reached at high CO_2 densities ($\varrho_{CO2,bulk} \geq 600$ kg/m^3).

The values of the calculated "isosteric heat of adsorption" (MCM-41: $\Delta H_{iso} =$ -21.7 kJ/mol, SBA-15: $\Delta H_{iso} =$ -18.6 kJ/mol) implied an exothermic physisorption of CO_2 on the carrier materials [32]. An energetically heterogeneous surface of MCM-41 and SBA-15 was assumed due to the non-constant curve of the "heat of adsorption" as a function of CO_2 loading [33].

With the obtained results of the absolute amount adsorbed of CO_2 on the carrier materials, conclusions on the binary adsorption behavior during the deposition step of the CPD process at $T_{CPD} = 313$ K and $p_{CPD} = 15$ MPa were drawn. An initial estimation of the ternary adsorption behavior (scCO_2 and ibuprofen on the carrier material) during the CPD process was possible by comparing the CO_2 adsorption results with the CPD ibuprofen loading results. On this basis, it was found that approximately six times more CO_2 than ibuprofen molecules adsorbed on MCM-41 and SBA-15.

Summing up, it was achieved in this work to identify decisive impacts of specific carrier material properties on CPD loading and their dissolution performance. With the obtained results this work contributes valuable information for the development of an active ingredient-carrier selection method to predict CPD loading and the dissolution behavior of new CPD formulations. The deposition of the ibuprofen on the inner surface of CPD processed carrier materials ($D_P \leq 4$ nm) was reliably proved

by the shift of the capillary condensation step with an easy to handle and cost-effective method (N_2-sorption experiments). The transferability of the obtained results to other active ingredient-carrier systems needs to be investigated in further studies.

Additionally, this work provides experimental results for the description of the adsorption behavior ($scCO_2$-carrier material and ibuprofen-carrier material) during the deposition step of the CPD process. These results offer a first solid database for a subsequently modelling of the ternary interactions and phase equilibria. In a first approach it was found that approximately six times more CO_2 than ibuprofen molecules adsorbed on the carrier material (MCM-41 and SBA-15) during the CPD process. The complete clarification of the question if there is a competitive adsorption between CO_2 and ibuprofen on the carrier material could be achieved by investigating the adsorption behavior of the ternary system by an MSB.

German Abstract - Zusammenfassung

Eine der großen Herausforderungen im Bereich der pharmazeutischen Forschung ist die Verbesserung der Bioverfügbarkeit um einen schnellen und effektiven Effekt, oral verabreichter Wirkstoffe, zu gewährleisten. Die Bioverfügbarkeit ist maßgeblich durch die Freisetzung der Wirkstoffe (Dissolution) und deren Aufnahme (Resorption) im Magen-Darm-Trakt bestimmt. Viele Wirkstoffe können zwar gut über die Schleimhäute ins Blut gelangen, sind jedoch in wässrigen Medien sehr schlecht löslich. Vertreter dieser Stoffe werden der Klasse II des Biopharmazeutischen Klassifizierungssystems (BCS) [1] zugeordnet. Ihre Bioverfügbarkeit ist besonders durch ihre Dissolution im Magen-Darm-Trakt limitiert. Um trotzdem eine ausreichende Menge dieser Stoffe am Wirkort gewährleisten zu können, wird beispielsweise die oral verabreichte Dosis erhöht, was wiederum zu starken gesundheitlichen Beeinträchtigungen führen kann [2]. Aus diesen Gründen wird die Verabreichung einer möglichst niedrigen Wirkstoffdosis angestrebt. Gerade bei Wirkstoffen der Klasse II des BCS ist die Herstellung von Formulierungen mit verbesserten Dissolutionseigenschaften essentiell um trotz einer geringeren Dosis eine ausreichende Wirkstoffkonzentration am Wirkort gewährleisten zu können.

Zur Verbesserung der Löslichkeit bietet die Verfahrenstechnik einige Lösungsansätze wie z.B. die Verwendung von Tensiden, Co-Lösungsmitteln, Feststoffdispersionen oder Nano-Suspensionen [3, 4]. Aber auch durch die Reduktion der Partikelgröße oder auch die Abscheidung auf Trägermaterialien lässt sich eine deutliche Steigerung der Dissolutionsgeschwindigkeit erreichen [3]. Konventionelle Verfahren wie z.B.

Mahlen, Sprüh- oder Gefriertrocknung weisen jedoch erhebliche Nachteile (wie eine breite Partikelgrößenverteilung, thermische oder chemische Veränderung des Produkts, der Verbleib von organischen Rückständen im Produkt etc.) auf. Um diese Nachteile zu umgehen, können Verfahren mit überkritischen Fluiden (SCFs) eingesetzt werden [5]. SCFs zeichnen sich maßgeblich durch ihre zahlreichen positiven Eigenschaften wie z.B. ihre gasähnlichen Transporteigenschaften und ihre flüssigkeitsähnlichen Dichten [6], ihre geringe Toxizität sowie, dass sie chemisch inert sind aus [7]. CO_2 wird in vielen Fällen als überkritisches Fluid ($scCO_2$) verwendet, da sich durch seine niedrigen kritischen Daten (T_c = 304 K, p_c = 7,4 MPa) moderate Prozessbedingungen realisieren lassen. Diese sind vor allem für die Verarbeitung thermolabiler Stoffe von besonderer Bedeutung. Überkritische Fluide werden unter anderem im Controlled Particle Deposition (CPD) Prozesses [8] verwendet. Mit diesem kann, durch die Abscheidung von Wirkstoffen auf entsprechenden Trägermaterialien, sogar eine Verkleinerung der Partikelgröße und ihre spätere Formulierung in einem Prozessschritt realisiert werden. Während des Beladungsschrittes wird der Wirkstoff zunächst bei konstanten Prozessbedingungen ($T > T_c$ und $p > p_c$) in einem überkritischem Fluid (z.B. $scCO_2$), aufgrund dessen flüssigkeitsähnlicher Dichte, gelöst. Anschließend kann der molekular gelöste Wirkstoff durch die gasähnlichen Transporteigenschaften des SCFs in ein poröses Trägermaterial, welches sich nicht im SCF löst, hinein diffundieren. Durch einen schnellen Druckablass auf Umgebungsbedingungen, am Ende des Prozesses, vermindert sich die Löslichkeit des Wirkstoffes im SCF. Aufgrund der entstehenden Übersättigung wird der Wirkstoff in den Poren des Trägermaterials abgeschieden, da diesem nicht genügend Zeit verbleibt um aus dem Träger wieder hinaus zu diffundieren. Je nach Trägermaterial können mit dem CPD-Prozess Produkte hergestellt werden, mit denen eine kontrollierte Freisetzung des Wirkstoffes (zeitverzögert oder beschleunigt) möglich ist [8 - 10].

Zur Untersuchungen des Dissolutionsverhalten pharmazeutischer Wirkstoffe müssen entsprechend den Vorgaben der FDA in vitro Studien durchgeführt werden [11]. Um geeignete Kombinationen für eine gezielte Wirkstofffreisetzung zu identifizieren müssen diese Untersuchungen für jedes neue CPD Wirkstoff-Trägersystem durchgeführt werden. Zur Umgehung dieser sehr zeit- und kostenintensiven in vitro-Studien besteht großes Interesse an der Entwicklung einer einfachen, schnellen und kosteneffizienten Wirkstoff-Träger-Auswahl-Methode. Die Idee ist, die CPD-Beladung neuer Wirkstoff-Trägersysteme sowie deren Dissolutionsverhalten mit möglichst wenigen Versuchen vorhersagen zu können. Alleine durch die Kenntnis der chemischen Eigenschaften des Wirkstoffes sowie der chemischen und strukturellen

(z.B. spezifischen Oberfläche, Porengröße, Porenvolumen und Oberflächenfunktionalisierung) Trägereigenschaften soll eine Auswahl möglich sein. Der Fokus bisheriger CPD-Untersuchungen lag vor allem auf der Identifizierung geeigneter chemischer Trägereigenschaften zur kontrollierten Freisetzung des Wirkstoffes [8 - 10, 12 - 15]. Der Einfluss der oben genannten spezifischen strukturellen Trägereigenschaften wurde bisher nicht untersucht.

Der erste Teil dieser Arbeit widmet sich deshalb dem Ziel, den Einfluss der oben genannten spezifischen Trägereigenschaften auf die CPD-Beladung sowie deren Einfluss auf das Dissolutionsverhalten in wässrigen Medien zu identifizieren.

Zur Beschreibung und Modellierung des CPD Beladungsvorgangs ist die Kenntnis der zwischenmolekularen Zweier- bzw. Dreier-Wechselwirkungen im ternären System zwischen $scCO_2$, Wirkstoff und Trägermaterial essentiell. Diese Wechselwirkungen können vereinfachend durch Adsorptions- und Löslichkeitsgleichgewichte beschrieben werden. Deshalb liegt der Fokus des zweiten Teils dieser Arbeit auf der Untersuchung des Adsorptionsverhaltens des ternären Systems sowie auf der Klärung der Frage, ob eine Konkurrenzadsorption von $scCO_2$ und Wirkstoff am Trägermaterial beim Beladungsvorgang besteht.

Im Rahmen der Untersuchungen wurde die Modellsubstanz R/S-Ibuprofen verwendet. Der Wirkstoff R/S-Ibuprofen, welcher im Folgenden nur noch als Ibuprofen bezeichnet wird, ist ein typischer Vertreter der Klasse II des BCS und findet vor allem als schmerzstillendes und fiebersenkendes Mittel seine Anwendung. Um den Einfluss einiger spezifischer Trägereigenschaften zu untersuchen wurden verschiedene Silika-materialien als Träger verwendet. Diese haben sich in bisherigen Studien als geeignet für eine Beladung mit Wirkstoffen und deren kontrollierte Freisetzung in wässrigen Medien erwiesen [9, 10].

Mit dem CPD-Prozess wurden neben kommerziell verfügbaren porösen Silikaten (MCM-41 und SBA-15) auch Silikate, die von verschiedenen Projektpartnern synthetisiert wurden, mit Ibuprofen beladen. Zur Variation der spezifischen Oberfläche, Porengröße und des Porenvolumens wurden am Institut für Mechanische Verfahrenstechnik (AG Weber) der TU Clausthal die Silika-Träger mit Hilfe der Salt Assissted Spray Pyrolyse hergestellt [16]. Zur Überprüfung, welchen Einfluss eine Funktionalisierung der Trägeroberfläche mit S-(+)-Ibuprofen auf die Beladung und das Dissolutionsverhalten hat, wurden weitere Silika-Träger mit dem Verfahren der „Kovalenten Bindungsreaktion“ in der AG Johannsen (Institut für Thermische

Verfahrenstechnik der TU Hamburg Harburg) hergestellt [17]. Die Beladung der Träger mit Ibuprofen wurde mit $scCO_2$ bei $T = 313\ K$ und $p = 15\ MPa$ durchgeführt.

Das Dissolutionsverhalten von Ibuprofen aus diesen Trägermaterialien in wässrigen Lösungen wurde auch in dieser Arbeit nach den Vorgaben der Food and Drug Administration (FDA) untersucht. Im Zuge dessen wurde auch eine geeignete Methode zur Probenanalyse mittels High Pressure Liquid Chromatography entwickelt.

Zur Bewertung des Dissolutionsverhaltens der hergestellten CPD Produkte, wurde dieses mit dem Dissolutionsverhalten eines, mit dem CPD Prozess selbst hergestellten, Ibuprofen-ß-Cyclodextrin-Inklusionskomplexes verglichen. Dieser weißt aufgrund der guten Wasserlöslichkeit des ß-Cyclodextrins (18,5 mg/ml bei $T = 298\ K$ [18]) eine sehr schnelle Dissolutionsgeschwindigkeit auf und wurde deshalb als Bewertungsmaßstab gewählt.

Als wichtige Vorarbeit wurde deshalb im Rahmen dieser Arbeit einer Masterarbeit betreut, welche das Ziel hatte eine Dissolutionsanlage nach Vorgaben der FDA zu konzipieren und am Institut aufzubauen [19]. Aufgrund der begrenzten Menge an Wirkstoff wurde die Anlage nach den Empfehlungen von Klein und Shah [20], mit einem geringeren Volumen als es die FDA vorgibt, konzipiert. Die von Klein empfohlenen Abmessungen wurden mit Hilfe einer Strömungssimulation in ANSYS Fluent validiert [19]. Hierbei war ersichtlich, dass vor allem die Position des Paddelrührers einen erheblichen Einfluss auf die Fluidbewegung hat. Mit Hilfe der durchgeführten Simulation konnte die exakte Position und die Umdrehungsgeschwindigkeit des Paddelrührers in der verkleinerten Anlage validiert werden um das gleiche Strömungsprofil, wie in einer von der FDA vorgegebenen Dissolutionsanlage, zu erzeugen.

Die Art der Probenaufgabe wird von der FDA nicht genau spezifiziert, weshalb unterschiedliche Möglichkeiten der Probenaufgabe in einer Reproduzierbarkeitsstudie [19] untersucht wurden. Die beste Reproduzierbarkeit der Versuche konnte gewährleistet werden, wenn das Probenmaterial in gesiebter Form frei auf das Dissolutionsmedium aufgegeben wurde.

Zur Identifizierung des Einflusses der spezifischen Trägereigenschaften (spezifische Oberfläche, Porengröße, Porenvolumen und Oberflächenfunktionalisierung) auf die Beladung konnte im ersten Teil dieser Arbeit [16, 17, 21] gezeigt werden, dass die höchste Beladung von ~50 wt% auf den Trägern mit der größten Oberfläche erzielt

werden konnte. Ein linearer Zusammenhang, mit dem eine größere spezifische Oberfläche zu einer höheren Beladung führte, wurde zunächst vermutet. Zusätzlich dazu konnte der Einfluss der Porengröße und des Porenvolumens auf die Beladung identifiziert werden. Große Mesoporen ($D_P \geq 25$ nm) waren für eine erhöhte Beladung der Träger von Vorteil, da in ihnen das Ibuprofen in Multilayern abgeschieden wurde. Dies spiegelte sich auch im Wert der „Number of Monolayer“ [22] ($D_P = 25$ nm: $NML = 4.09$, $D_P = 30$ nm: $NML = 9.07$) wider. Mit Hilfe der Röntgendiffraktionsanalyse (XRD) und der Dynamischen Differenzkalorimetrie (DSC) konnte nachgewiesen werden, dass sich Ibuprofen mit steigender Porengröße ($D_P \geq 25$ nm) zunehmend in kristalliner Form auf dem Träger abschied. Im Gegensatz dazu bildeten sich in kleinen Mesoporen ($D_P \leq 4$ nm) hauptsächlich amorphe Ibuprofenstrukturen aus. Eine Funktionalisierung der Trägeroberfläche mit S-(+)-Ibuprofen trug zu einer niedrigeren Trägerbeladung bei, als es auf Grundlage des oben genannten linearen Zusammenhangs zu vermuten war. Ibuprofen schied sich außerdem auf diesen Trägern hauptsächlich in amorpher Form ab.

Das Dissolutionsverhalten von Ibuprofen aus den beladenen Trägermaterialien in wässrigen Medien wurde bei einem pH-Wert von 2,0 und 5,5 untersucht. Im Hinblick auf die Dissolutionsergebnisse konnte festgestellt werden, dass fast alle CPD-Produkte im Vergleich zum unbehandelten Wirkstoff ein verbessertes Dissolutionsverhalten von Ibuprofen aufwiesen. Aufgrund der pH-Wert abhängigen Löslichkeit von Ibuprofen [19, 23] zeigten alle beladenen Trägermaterialien bei einem pH-Wert von 5,5 ein deutlich besseres Dissolutionsverhalten als bei pH = 2,0.

Obwohl die Dissolutionsgeschwindigkeit der Wirkstoffe aus großen Mesoporen ($D_P \geq 25$ nm) höher war als bei engen, kanalartigen Mesoporen ($D_P \leq 4$ nm), trug kristallin abgeschiedenes Ibuprofen gerade bei einem niedrigen pH-Wert von 2,0 zu einer deutlich verlangsamten Dissolutionsgeschwindigkeit bei. Bei einem pH-Wert von 5,5 spielte die Kristallinität („degree of crystalinity“ [22]) des abgeschiedenen Ibuprofens eine eher untergeordnete Rolle, hier war vor allem die Partikelgröße für das Dissolutionsverhalten ausschlaggebend. Die Kenntnis der Kristallinität des abgeschiedenen Ibuprofens ist somit für eine Vorhersage des Dissolutionsverhaltens von zentraler Bedeutung.

Bei den mit S-(+)-Ibuprofen vorfunktionalisierten Trägern war ersichtlich, dass sowohl die Menge als auch der Ort der Funktionalisierung für das Dissolutionsverhalten entscheidend war. Befand sich ein großer Teil der untersuchten Funktionalisierung an der äußeren Trägeroberfläche neigte dieser Träger zu Agglomeration. Zusätzlich ließ sich dieser auf Grund der Hydrophobizität des S-(+)-

Ibuprofens nur schlecht vom Dissolutionsmedium benetzen, was sich in einer langsamen Dissolutionsgeschwindigkeit widerspiegelte.

Im Vergleich zum ß-Cyclodextrin-Inklusionskomplex zeigten alle Silika-Träger bei einem pH-Wert von 2,0 ein schlechteres Dissolutionsverhalten. Bei einem pH-Wert von 5,5 wiesen nur die Silika-Träger mit den größten Mesoporen ($D_P \geq 25$ nm) eine zum Inklusionskomplex vergleichbare Dissolutionsgeschwindigkeit auf.

Zur mathematischen Beschreibung des zeitlichen Verlaufs des Dissolutionsverhaltens lieferte das Modell der „ersten Ordnung“ von Gibaldi und Feldman [24] mit der Erweiterung von Costa [25] die beste Anpassung der experimentellen Daten.

Mit Hilfe von N_2-Sorptions-Experimenten bei $T = 77$ K lässt sich die Charakterisierung von Trägermaterialien einfach und schnell realisieren. Diese Experimente wurden für nicht beladene und beladene Trägermaterialien durchgeführt [16]. Die nicht beladenen Trägermaterialien mit sehr kleinen Mesoporen ($D_P \leq 4$ nm) wiesen einen deutlichen Kapillarkondensationssprung bei $p/p_0 = 0{,}3 - 0{,}4$ auf. Dieser Sprung war bei den entsprechenden beladenen Trägermaterialien jedoch deutlich kleiner ausgeprägt und zu niedrigeren Relativdrücken verschoben. Diese Verschiebung des Kapillarkondensationssprungs konnte zweifelsfrei auf das beladene Ibuprofen zurückgeführt werden, welches sich auf der inneren Oberfläche des Trägermaterials abgeschieden hatte. Somit konnte im Gegensatz zu bisher durchgeführten XRD oder DSC Analysen die Abscheidung des Ibuprofens innerhalb der Poren zweifelsfrei nachgewiesen werden.

Im zweiten Teil dieser Arbeit wurde das Adsorptionsverhalten von CO_2 an zwei der wichtigsten Trägermaterialien (MCM-41 und SBA-15) mit Hilfe einer Magnetschwebewaage (MSB) [26] experimentell und theoretisch untersucht [27, 28], um Informationen über die intermolekularen Wechselwirkungen während des CPD-Prozesses zu erhalten.

Durch die Messungen der Adsorption von N_2 und CO_2 an Aktivkohle (AC Norit R1 Extra, welches in Fachkreisen als Referenzadsorbens dient) konnte zunächst die korrekte Funktionsweise der verwendeten MSB nachgewiesen werden [27]. Darauf aufbauend wurde die Adsorption von CO_2 an MCM-41 und SBA-15 im Bereich von $T = 298 - 353$ K, $p = 0 - 25$ MPa und $\varrho_{CO2,bulk} = 0 - 900$ kg/m^3 gemessen [28]. Mittels der MSB wurden so genannte Exzessisothermen gemessen, welche aufgrund des Auftriebseffektes der MSB nicht der absolut adsorbierten Masse entsprechen.

Diese muss auf Basis der Exzessergebnisse mit Hilfe mathematischer Modelle [29 - 31] berechnet werden.

Bei niedrigen Dichten ($\varrho_{CO2,bulk} \leq 200$ kg/m^3) war generell ein Anstieg der adsorbierten CO_2-Exzessmenge zu beobachten, welcher jedoch bei weiterer Erhöhung der Dichte wieder abnahm. Bei steigender Temperatur nahmen die Exzesswerte ab und das Maximum der Adsorptionsisothermen verschob sich hin zu höheren Dichten.

In einem weiteren Schritt wurde die an den Trägern absolut adsorbierte CO_2-Menge mit Hilfe des Modells von Menon [29] berechnet. Bei sehr hohen Adsorptivdichten ($\varrho_{CO2,bulk} \leq 600$ kg/m^3) wurde bei allen Isothermen die vom Trägermaterial abhängige Sättigungsabsolutbeladung (MCM-41: $n_{abs,sat}$ = ~13,0 mmol/g; SBA-15: $n_{abs,sat}$ = ~13,5 mmol/g) erreicht. Die auf Basis der absolut adsorbierten CO_2-Menge berechnete „isosteric heat of adsorption“ (MCM-41: ΔH_{iso} = -21,7 kJ/mol, SBA-15: ΔH_{iso} = -18,6 kJ/mol) ließ bei beiden untersuchten Trägermaterialien auf eine exotherme Physisorption des Gases schließen [32]. Aufgrund des nicht konstanten Verlaufs der „heat of adsorption“ in Abhängigkeit der Beladung konnte auf eine energetisch heterogene Oberfläche der untersuchten Silika-Träger geschlossen werden [33].

Zur Klärung der Frage, ob eine Konkurrenz-Adsorption zwischen CO_2 und Ibuprofen am Trägermaterial stattfindet, wurde in einer ersten Abschätzung die absolut adsorbierte CO_2-Menge bei den entsprechenden CPD-Prozessbedingungen (T_{CPD} = 313 K, p_{CPD} = 15 MPa) mit der Ibuprofenbeladung der Träger verglichen. Auf dieser Grundlage ließ sich feststellen, dass ca. sechs Mal mehr CO_2- als Ibuprofen-Moleküle an MCM-41 und SBA-15 adsorbierten.

Zusammenfassend konnten in dieser Arbeit Einflüsse verschiedener spezifischer Trägereigenschaften auf deren Beladung und deren Dissolutionsverhalten identifiziert werden. Diese Informationen liefern einen wertvollen Beitrag zur Entwicklung eines schnellen und kosteneffizienten Wirkstoff-Träger-Auswahl-Methode zur Vorhersage der Beladung und des Dissolutionsverhaltens neuer CPD-Formulierungen. Durch Verschiebung des Kapillarkondensationssprungs bei beladenen Trägern ($D_P \leq 4$ nm) konnte die Abscheidung des Ibuprofens auf der inneren Oberfläche der Träger zweifelsfrei mit einer einfachen und kostengünstigen Methode nachgewiesen werden. Die Übertragbarkeit der erhaltenen Ergebnisse auf andere Wirkstoff-Trägersysteme sollte Gegenstand zukünftiger Arbeiten sein. Des Weiteren liefert diese Arbeit experimentelle Ergebnisse zur Beschreibung des Adsorptionsverhaltens (scCO_2-Trägermaterial) während des CPD-Prozesses. Diese bieten eine erste solide

Datengrundlage zur späteren gezielten Modellierung der entsprechenden Phasengleichgewichte. In einem ersten Ansatz wurde festgestellt, dass während des CPD-Beladungsvorgangs sechs Mal mehr CO_2- als Ibuprofenmoleküle mit dem Träger wechselwirken. Die vollständige Klärung der Frage, ob eine Konkurrenzadsorption zwischen CO_2 und Ibuprofen am Träger stattfindet, könnte gelingen, wenn weitere Untersuchungen des ternären Systems mit Hilfe einer MSB durchgeführt werden.

1. Introduction

1.1 Dissolution of active ingredients

Pharmaceutical drugs can be applied either in liquid, solid or semisolid dosage forms. Possible types are e.g. oral, ophthalmic, inhalational, parenteral, and topical or suppository application. The effect of the drug depends on the bioavailability of its active ingredients. With regard to orally applied drugs, which are in focus of this work, their bioavailability is significantly limited by the solubility, dissolution and resorption of the active ingredients in the gastrointestinal tract.

This chapter is arranged as followed: First of all the Biopharmaceutical Classification System, which provides a relation between the bioavailability of active ingredients and their solubility and resorption, is introduced. In a next step the conditions in the gastrointestinal tract are clarified before the recommendations of the Food and Drug Administration how to investigate the dissolution of active ingredients are introduced. Furthermore, a short overview of mathematical approaches to describe experimental dissolution results are given in the last part.

1.1.1 Biopharmaceutical Classification System

For the evaluation of active ingredients, the bioavailability is one of the most important parameters. Investigations of bioavailability require a large number of time-consuming and cost-intensive in vivo studies. To circumvent these, Amidon et

al. [1] developed in 1995 the Biopharmaceutical Classification System (BCS). In this system, a correlation between bioavailability of active ingredients and its solubility and/or its permeability was established for the first time. With this relation it can be clarified whether bioavailability is more dependent on the physical properties of the active ingredient (solubility) or the physiological conditions in the human body (permeability). A high solubility is considered if 85 % of the active ingredient dissolves within 15 min in a 0.1 N HCl solution [1]. In addition to this, the permeability is classified as high, if more than 90 % of an active ingredient is resorbed in the human body in comparison to an intravenous reference dose [11].

Tab. 1 Biopharmaceutical Classification System established by Amidon et al. [1] including some examples of typical active ingredients of each group. Furthermore the market shares of class I – class IV active ingredients and new molecular entities (NMEs) of these classes are presented [34].

Class	Solubility	Permeability	Marketed active ingredients [34]	NMEs [34]	Typical active ingredients [35 - 38]
I	High	High	40%	18%	Amlodipine, paracetamol, diazepam
II	Low	High	33%	54%	Ibuprofen, ketoprofen, naproxen, fenofibrate, griseofulvin
III	High	Low	21%	22%	Fexofenadine, ranitidine, metformin
IV	Low	Low	6%	6%	Amphotericin B, furosemide, acetazolamide, ritonavir, paclitaxel

The classification of different active ingredients depending on their solubility and permeability is listed in Tab. 1. Active ingredients which belong to class I are characterized by a high solubility and high permeability. Due to this fact, their bioavailability is only limited by the gastric emptying.

Active ingredients which are poorly soluble but highly permeable belong to class II. Their bioavailability is limited in particular on their solubility in the gastrointestinal tract. Because of their low solubility, these active ingredients migrate through the gastrointestinal tract while they are exposed to different pH-values from the stomach to the end of the large intestine (pH = 1.4 – 8.0 [39]). For this reason, investigations on bioavailability should be carried out at different pH-values. An improvement of their bioavailability can be achieved by enhancing their solubility and dissolution.

In contrast to their high solubility in the gastro intestinal tract, active ingredients of class III are poorly permeable. Therefore, their bioavailability is determined by their resorption in the human body.

The active ingredients of class IV show a low solubility and permeability. Thus, they are not suitable for oral applications.

1.1.2 Class II active ingredients research interest and improved bioavailability

Tab. 1 shows that active ingredients of class II are ranked in second position after those of class I in terms of their market shares. Especially with regard to new molecular entities (NMEs), class II of the BCS is a very important group of active ingredients. As described previously, the bioavailability of orally applied active ingredients strongly depends on their solubility and permeability in the gastrointestinal tract. Due to the poor solubility of class II active ingredients, their bioavailability is considerably limited by their solubility and dissolution. As a result, their solubility and dissolution behavior has to be improved in order to guarantee a fast effect of the active ingredient at its side of action. The growing research interest for enhancing the solubility and the dissolution behavior of class II active ingredients is also reflected in the increased number of publications published in recent years (see Fig. 1)

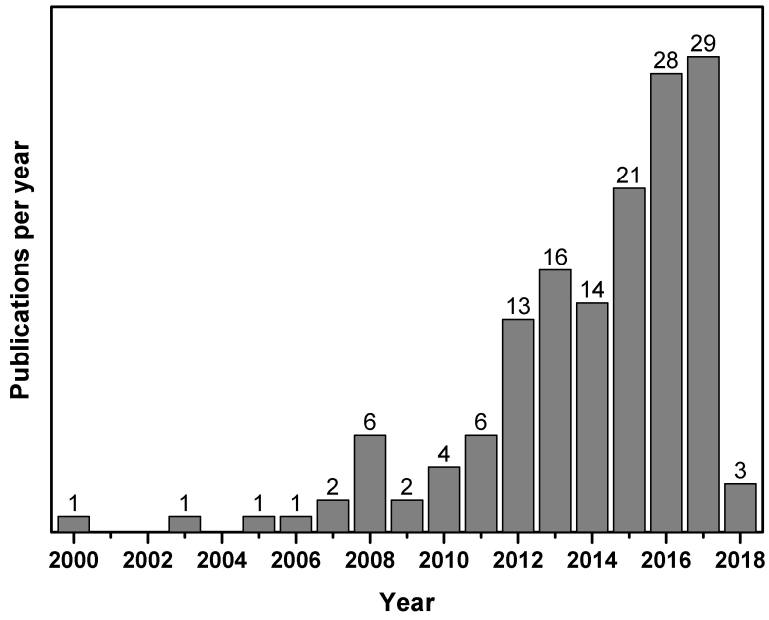

Fig. 1 Number of matches when keywords "BCS II, improved solubility" are entered in "Web of Science", date of research March 2018.

An enhanced solubility and dissolution behavior of active ingredients can be achieved e.g. by solid dispersions, nanosuspensions, cryogenic and inclusion complex formation techniques or the deposition on carrier materials [3, 4]. Besides this, another very important factor can be the reduction of the particle size. In Fig. 2, the influence of particle size is illustrated exemplary for the solubility of ibuprofen in water at $T = 298$ K. It is evident that the solubility increases significantly due to micronization of the ibuprofen particles to the nanometer scale.

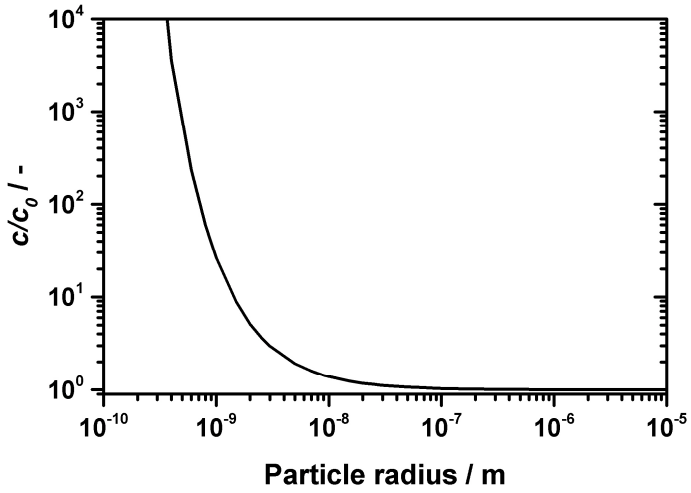

Fig. 2 Calculated solubility (c/c_0) of the active ingredient ibuprofen as a function of the particle radius at $T = 298$ K by Eq.(1) *).

*) The solubility of a solid substance in aqueous solutions can be calculated by the Ostwald-Freundlich equation (see Eq.(1)) [4].

$$\ln \frac{c}{c_0} = \frac{2 \cdot \sigma \cdot v^s}{R \cdot T \cdot r} \tag{1}$$

In this equation c is the saturated solubility, c_0 is the solubility of the solid consisting of large particles, σ corresponds to the interfacial tension between the solid and the liquid, v^s is the specific molar volume of the solid, r is the radius of the solid, R is the universal gas constant and T is the temperature.
In case of ibuprofen the following values were used to calculate the water solubility as a function of particle size at $T = 298$ K: $\sigma = 21.6$ mN/m^3 [40], $v^s = 1.875 \cdot 10^{-4}$ m^3/mol [8].

1.1.3 Ibuprofen – an active ingredient of the BCS-class II

Typical representatives of the BCS-class II are profens, which are non-steroidal anti-inflammatory drugs. In particular, they are used as pain killers and therefore a fast-acting effect is expected. The most popular active ingredient of this group is ibuprofen which is used in this work. The chemical structure of ibuprofen is shown in Fig. 3. It

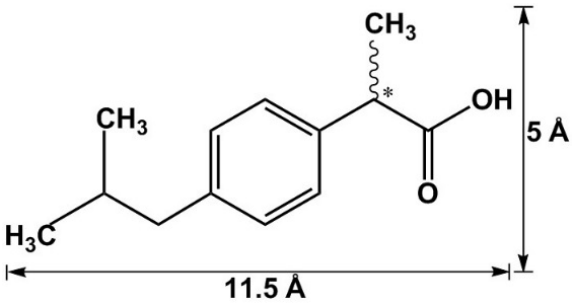

Fig. 3 Molecular structure and dimensions of ibuprofen according to [46].

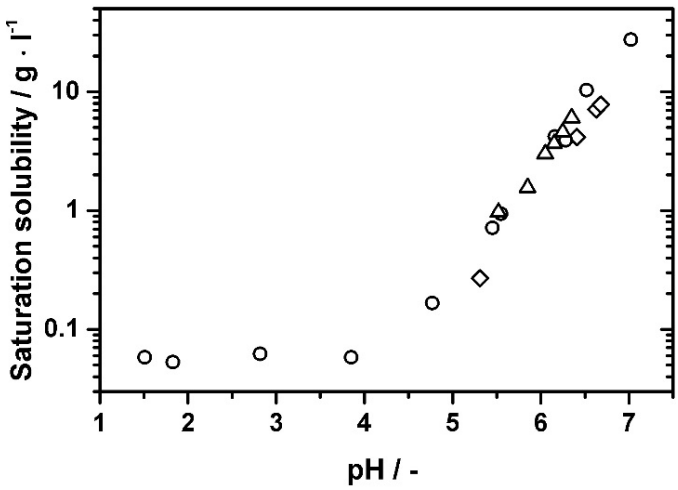

Fig. 4 Solubility of ibuprofen. Experimental results of Friebel [19] (diamonds), Levis et al. [23] (triangles) and Shaw et al. [44] (circles).

consists of a phenyl ring and an acetyl group which is in para position to the propyl group. Furthermore it possesses a chiral center (* in Fig. 3) in the acetyl group. The two stereoisomers are called R-(-)- and S-(+)-ibuprofen. It was shown in several studies that S-(+)-ibuprofen shows a significantly higher potency [41, 42]. In the subsequent sections the term ibuprofen is used as a simplified description of the racemic mixture R/S-ibuprofen.

In different studies it has been shown that ibuprofen is a weak acid ($pK_a = 4.4$ [43]) and that its solubility in aqueous solutions is pH dependent [19, 23, 44] (Fig. 4). Below its pK_a value nearly all molecules exist in their undissociated form [45]. In the stomach, ibuprofen shows a very low solubility due to the predominant low pH of 2 but its solubility is increased with increasing pH in the small and large intestine (pH = 5.5 – 8.0 [39]). Nevertheless, the permeability of ibuprofen through the mucosa is high at low pH-values due to its undissociated form [3].

1.1.4 Conditions in the gastrointestinal tract

Orally administered active ingredients are usually absorbed in the gastrointestinal tract (see Fig. 5), where its dissolution rate is determined by the prevailing conditions. After ingestion, the active ingredient enters the stomach where the conditions can vary considerably due to the food intake. In the fasted state, the stomach has a pH of 1.4 – 2.1 while postprandial the pH is in the range of 6.0 – 7.0 [39]. The linger-time of an active ingredient in the stomach is determined by its emptying. If the active ingredient is not completely resorbed in the stomach, it enters

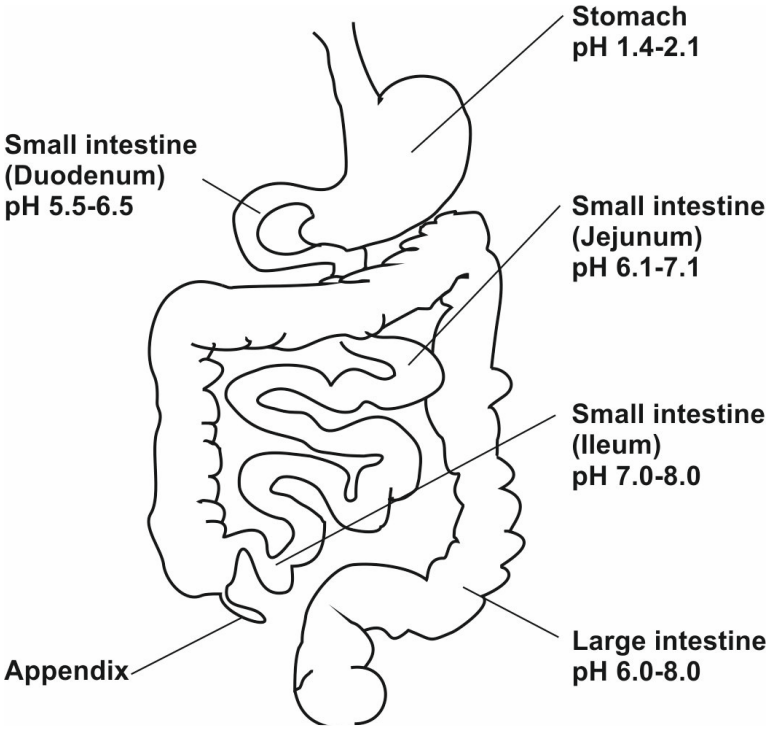

Fig. 5 Terms and conditions [39] of the gastrointestinal tract.

the small intestine. The pH-value varies from pH = 5.5 in duodenum to pH = 8 in the ileum. After 3 – 4 h retention time in the small intestines the active ingredient reaches the large intestine [39].

For a rapid effect of the active ingredient a fast dissolution and high resorption in the stomach is important. With regard to active ingredients which belong to class II of the BCS, formulations to increase their solubility and dissolution are required. To investigate the dissolution performance of such formulations, so called "dissolution experiments" are carried out. In order to ensure the comparability of these tests, the Food and Drug Administration (FDA) of the United States provides recommendations which are introduced in the next section.

1.1.5 Dissolution experiments – recommendations by the Food and Drug Administration

For the approval of drugs the FDA proposes certain procedures to carry out in vitro experiments to prevent time and cost intensive in vivo studies on animals and human test persons. To carry out such experiments various test apparatuses (see Fig. 6) which are based on specifications from the United States Pharmacopeia (USP) are suggested. These apparatuses differ e.g. in the type of mixing (e.g. stirrer model, speed of rotation or flow rates) and the type of sample placement [11, 47]. In addition

to this, the volume of the dissolution media is recommended to be 500 – 1000 ml [11]. To simulate the conditions in the gastro intestinal tract, the FDA suggests to carry out tests in a pH-range between 1.0 and 6.8 [48]. HCl/NaOH mixtures are proposed for tests in the low pH-range, whereas phosphate buffers are suitable for pH-ranges between 4.5 and 7.2 [49, 50]. However, in all test apparatuses the dissolution media is tempered to $T = 310$ K and the amount of active ingredient is defined by the "sink conditions" [51]. Sink conditions are specified by the FDA as the amount which corresponds to $1/3^{\text{rd}} - 1/5^{\text{th}}$ of the saturation concentration of the active ingredient at corresponding pH and temperature multiplied by the volume of the dissolution media. With regard to dissolution tests of expensive active ingredients or formulations with a low active ingredient content a smaller dissolution volume might be advisable to ensure the required sink conditions. Klein and Shah [20] designed an apparatus with down-scaled dimensions ($V = 250$ ml) which was validated in experimental studies.

Besides the recommendations of the FDA and the USP there are many methods used in literature to simulate the real conditions of the human body. For example, it is widely spread to use simulated gastric or intestine fluids as dissolution media. Furthermore, it is possible to use different types of lipids and surfactants (e.g. Tween® 80) to enhance the dissolution of active ingredients. Nevertheless, it has to be considered that the solubility and therefore the dissolution of an active ingredient is influenced by different factors. Besides the pH-value, also ionic strength [45], buffer capacity [52], viscosity [52] and surface tension [53] of the media are important parameters. Therefore, it is difficult to compare dissolution data presented in literature.

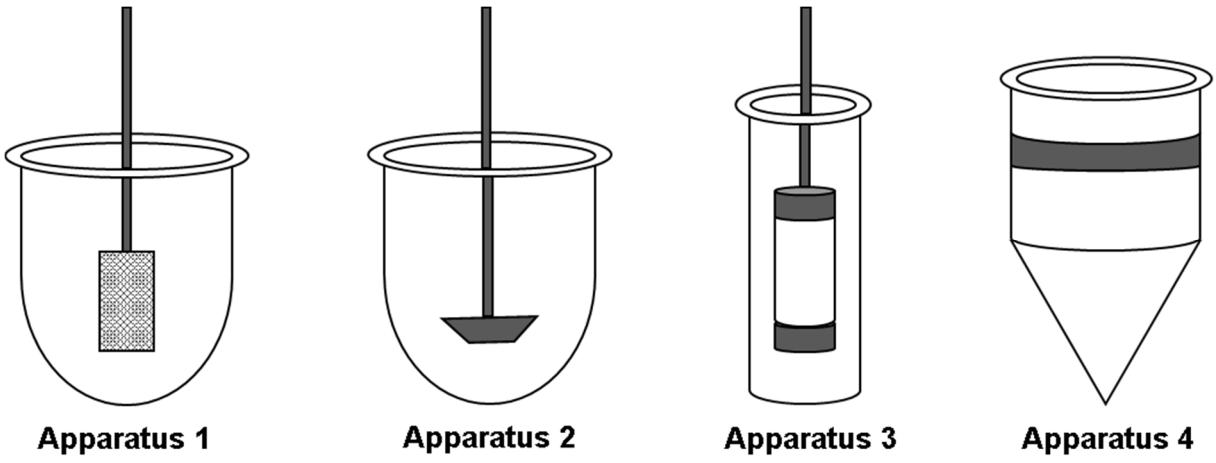

Fig. 6 Different dissolution apparatuses defined by USP<1088> [47]. Design by [19].

1.1.6 Dissolution rate and its mathematical description

In the previous section, recommendations to perform dissolution experiments were introduced. To present the results of these experiments it is established to depict the dissolution as a function of time *D(t)*. Whereby *D(t)* is defined as the relation of the dissolved amount of the active ingredient at a certain time $c_{dis}(t)$ and its initial concentration c_0 (Eq.(2)).

$$D(t) = \frac{c_{dis}(t)}{c_0} \tag{2}$$

For the mathematical description of $c_{dis}(t)$ different kinetic approaches can be found in literature. The model of 1st-order provides a linear approach which is easy and suitable to describe many dissolution kinetics. Nevertheless, multiple modifications are published to enhance the quality of modelling experimental data. Besides the kinetic approach of 1st-order the most popular models (Noyes-Whitney, Hixson-Crowell and Weibull) are described in detail below. An overview of further approaches can be found in [25]. The mathematical description of dissolution results is a suitable and easy way to compare different experimental data sets.

Kinetic of 1st-order

The kinetic of 1st-order is considered to be the most basic model. This linear approach was applied on the dissolution of drugs for the first time by Gibaldi and Feldman [24]. It describes the reaction velocity v_{dis} as a function of the concentration of the dissolving active ingredient c and the constant k (Eq.(3)).

$$v_{dis} = \frac{dc}{dt} = -k \cdot c \tag{3}$$

Based on this equation the concentration of the active ingredient in the dissolution media as a function of time *c(t)* is described in Eq.(4). In this equation, c_0 corresponds to the initial sample of the dissolving active ingredient in the dissolution media. The dissolved concentration of the active ingredient at a certain time $c_{dis}(t)$ can be referred to Eq.(5).

$$c(t) = c_0 \cdot e^{-k \cdot t} \tag{4}$$

$$c_{dis}(t) = c_0 \cdot (1 - e^{-k \cdot t}) \tag{5}$$

The dissolution *D(t)* is described in Eq.(6) while Eq.(5) was applied to Eq.(2).

$$D(t) = 1 - e^{-k \cdot t} \tag{6}$$

Curves which reach a complete dissolution, which is equal to 100%, can be described by Eq.(6). Nevertheless, a complete dissolution is not always the case. Therefore, the fitting constant D_{100} (Eq.(7)) was inserted to describe curves with end values below 100% [25].

$$D(t) = D_{100} \cdot (1 - e^{-k \cdot t}) \tag{7}$$

Noyes-Whitney-Equation

The model of Noyes-Whitney [54], which is based on the first Fick's law is also considered to be a 1st-order approach. In this model it is assumed that a solid active ingredient is surrounded by an indefinitely thin film of saturated solution. The diffusion out of this film is expected to be proportional to the difference between the concentration of its saturated solution c_{sat} and the concentration of the active ingredient in the dissolution media *c(t)* multiplied by a constant C_{NW} (Eq.(8)).

$$c_{dis}(t) = C_{NW} \cdot (c_{sat} - c(t)) \tag{8}$$

$$c_{dis}(t) = \frac{D \cdot A}{V \cdot h} \cdot (c_{sat} - c(t)) \tag{9}$$

The fact that the surface area of the active ingredient is decreasing during the dissolution process is not taken into account in the Noyes-Whitney-Equation. Therefore a term which incorporates the value of the solid area which is accessible to the dissolution media was implemented in Eq.(9) [25]. In this equation D corresponds to the diffusion coefficient of the solid in the liquid, A to its surface area, V to the volume of the dissolution media and h to the width of the diffusion layer.

Hixson–Crowell model

Hixson and Crowell [55] recognized that the particle regular area is proportional to the cubic root of its volume. Therefore, Eq.(10) can be derived to describe the undissolved amount of the active ingredient at a certain time *m(t)*.

$$m(t)^{\frac{1}{3}} = m_0^{\frac{1}{3}} - C_{HC} \cdot t \tag{10}$$

In this equation $m(t)$ is a function of the initial amount of the active ingredient m_0 and a parameter C_{HC} which incorporates the surface-volume relation. If Eq.(10) is divided by the volume of the dissolution media V, the concentration of the dissolved amount of the active ingredient $c_{dis}(t)$ can be written as in Eq.(11).

$$c_{dis}(t) = \frac{m_0}{V} \cdot (1 - (1 - C_{HC} \cdot t)^3) \tag{11}$$

Appling Eq.(11) to Eq.(2) and assuming that m_0 is equal to $c_0 \cdot V$ leads to Eq.(12) for the description of the dissolution. In this equation the constant D_{HC} is included to describe dissolution curves with end values below 100 %.

$$D(t) = D_{HC} \cdot (1 - (1 - C_{HC} \cdot t)^3) \tag{12}$$

Weibull model

In comparison to the models described before the model of Weibull [56] is empirical and has no kinetic fundament. Nevertheless, it can be successfully applied to almost all kinds of dissolution curves. The Weibull model describes the accumulated fraction of the active ingredient $m(t)$ in the dissolution media at a certain time t (Eq.(13)).

$$m(t) = 1 - \exp\left[\frac{-(t - T_i)^b}{a}\right] \tag{13}$$

In this equation, the parameter a corresponds to the time scale of the process whereas T_i defines the lag time before the onset of the dissolution. In most cases $T_i = 0$. With the shape parameter b, exponential ($b = 1$), sigmoidal ($b > 1$) and parabolic dissolution curves ($b < 1$) can be described. With the correlation of $a = (T_d)^b$, a can be replaced by T_d. In this case T_d represents the time interval which is necessary to dissolve or release 63.2 % of the active ingredient.

The Weibull constant C_W which is the inverse of T_d is a widely used parameter in literature to compare experimental dissolution results.

1.2 Formulation of active ingredients with enhanced dissolution behavior by supercritical fluids

The urgency of enhancing the dissolution of active ingredients which belong to class II of the BCS was described in the previous section. Nowadays, formulations with improved dissolution behavior can be produced e.g. by particle size reduction processes, solid dispersions, nanosuspensions, cryogenic and inclusion complex formation techniques [3, 4].

Nevertheless, in these processes the active ingredients are exposed to extreme mechanical forces, physical stress, high or cryogenic temperatures and organic solvents which cause a high risk of product degradation. To prevent damages of the final product processes with supercritical fluids (SCF) are under investigation.

With regard to conventional particle size reduction processes like milling, spray-drying or crystallization the utilization of SCFs offers many advantages. The low critical data of many fluids allow e.g. the realization of mild process conditions while mass transport limitations can be reduced due to the high diffusivity of molecules in SCFs. Furthermore SCF processes are considered as environmentally friendly methods due to the fact that organic solvents are not required. In a depressurization step an easy removal of the SCF can be realized which results in the formation of dry and solvent free final products [7, 57].

A short overview of SCF applications in industry as well as the fundamentals of supercritical fluids (pure components and mixtures with low volatile substances) are given in the first part of the section. Next, the Controlled Particle Deposition (CPD) process, which is a suitable SCF process for the formation of active ingredients with improved dissolution behavior is described. Furthermore, a detailed description of the interactions of the ternary system used in this work (CO_2, ibuprofen and carrier material) during the CPD process is given.

1.2.1 Applications of supercritical fluids in industry

In the early 1970, the focus of the industry shifted more and more from classical methods such as distillation or liquid extraction towards alternative separation techniques. Due to the fact, that organic solvents are used in classical methods the development of new environmentally friendly strategies is urgently needed. In this context, the utilization of SCFs are considered to be an attractive environmentally friendly and energy-saving alternative to organic solvents [57, 58]. One of the major

milestones in industrial scale is the decaffeination of coffee with SCFs [59]. Furthermore SCFs play an important role in processing sensitive active ingredients or in their extraction from plant materials [60] because of the fact that they show a good solubility in SCFs. For the production of e.g. submicron particles SCF processes like the Rapid Expansion of Supercritical Solutions (RESS) [61 - 67], Gas Anti Solvent (GAS) [68 - 70], Particle Generation from Gas Saturated Solutions (PGSS) [71, 72] and their numerous modifications [73] are established. Nevertheless, further processing of submicron particles produced by RESS in solid dosage forms is difficult due to agglomeration of the obtained products. To prevent this the Controlled Particle Deposition process was invented in 2007 [8]. In this process substances which are soluble in SCFs can be deposited on carrier materials. Therefore, particle size reduction and formulation can be realized in one processing step.

A large number of substances can be used as SCF e.g. CO_2, ethane, fluoroform, sulfur hexafluoride or water [73]. Especially CO_2 has become established because of its low critical pressure and temperature ($p_c = 7.4$ MPa, $T_c = 304$ K) [74]. Because of this, moderate process conditions are realizable, which are important for processing temperature sensitive substances like active ingredients in particular. More advantages of CO_2 are its low toxicity and its abundance in nature. Furthermore, it is non-flammable and cost-effective.

1.2.2 Fundamentals of supercritical fluids – pure components

As an example the phase behavior of CO_2 [74 - 76] is shown in Fig. 7. Three characteristic phase boundaries can be found. At low temperatures and pressures the sublimation boundary characterizes the equilibrium between the solid and gaseous state of CO_2. The solid and the liquid state are divided by the solid-liquid equilibrium curve. The third boundary characterizes the liquid-gas equilibrium which ends in the critical point (CP). All boundaries converge in the triple point (TP) where all three phases co-exist. Above the critical temperature (T_c) and its corresponding critical pressure (p_c), the pure substance exists in a one-phase homogenous state which is called supercritical fluid. In general SCFs combine liquid-like densities and transport properties which magnitudes are comparable to those of gases (Tab. 2) [6].

In Fig. 8 the density of CO_2 is plotted as a function of pressure for three isotherms. A density jump of the sub-critical isotherm ($T = 298$ K) is obvious in the region of its phase transition from the gas to the liquid state. An enormous density change with small variations in pressure in the region close to the critical point can be seen

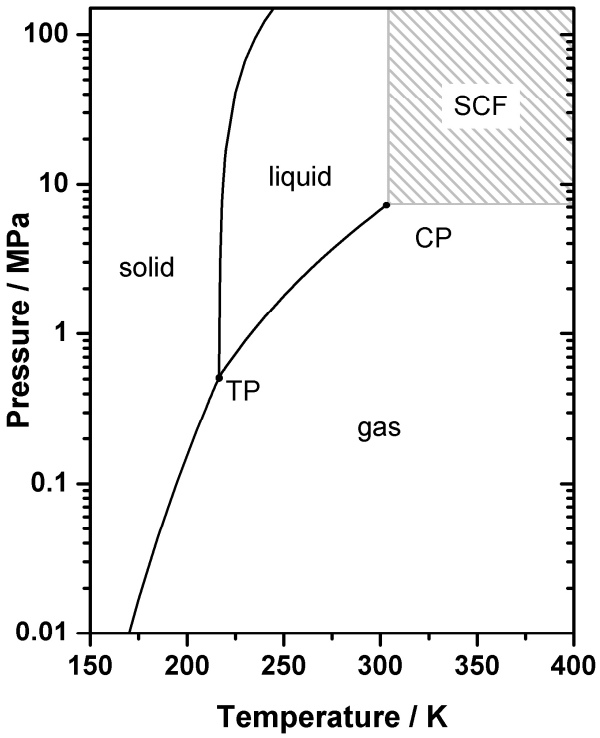

Fig. 7 Phase diagram of pure CO_2. Data obtained from REFPROP [74].

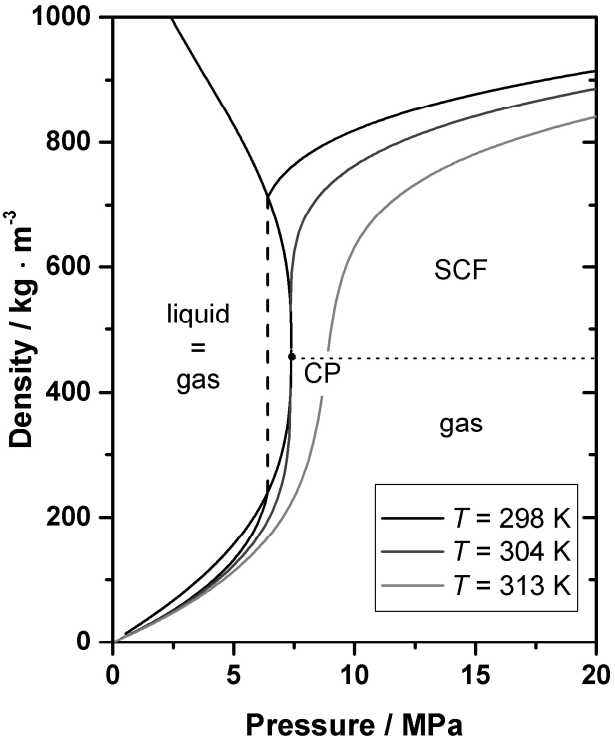

Fig. 8 Density of CO_2 as a function of pressure. Data obtained from REFPROP [74].

Tab. 2 Order of magnitude of different physical and transport properties of gases, SCFs and liquids [6].

		Gas	**SCF**	**Liquid**
Density	g/cm^3	$10^{-3*)}$	0.3	1
Diffusivity	cm^2/s	$10^{-1*)}$	$10^{-3} - 10^{-4}$	$<10^{-5}$
Viscosity	g/cm·s	10^{-4}	$10^{-4} - 10^{-3}$	10^{-2}

*) at $p = 0.1$MPa

for the critical isotherm ($T = 304$ K) whereas this effect is less pronounced with increasing temperature ($T = 313$ K). Due to the liquid-like densities SCFs show good solubility capacities for low volatile substances (e.g. ibuprofen). Their solubility in the SCF can be systematically influenced due to the significant density changes with small pressure variations, which is exploited in many SCF processes. Interesting temperature and pressure ranges for those kind of processes are $1 < T/T_c < 1.1$ and $1 < p/p_c < 3$ [73].

Another characteristic is that supercritical fluids have zero interfacial tension which allows excellent wetting of different substances [77]. In addition to this, the high diffusivity and its low viscosity allows good penetration of small pores and a fast adjustment of equilibria [78] which is utilized e.g. in the CPD process [8].

1.2.3 Fundamentals of supercritical fluids – Mixtures of supercritical fluids and low volatile substances

Mixtures of supercritical fluids (comp. 1) (e.g. CO_2) and low volatile substances (comp. 2) (e.g. ibuprofen) are known as "asymmetric mixtures", because both components show large differences in mass, size, polarity, shape, interaction strength and their critical data [73]. Therefore, these systems possess a miscibility limit and as a result of this an interrupted critical line of the mixture. A schematic phase diagram of an asymmetric mixture is shown in Fig. 9 (left side). The diagram shows different phase boundaries depending on p and T. The black solid line at low temperatures and pressures represents the vapor pressure curve of pure comp. 1 which ends in the critical point (CP_1; $p_{c,CO2} = 7.4$ MPa, $T_{c,CO2} = 304$ K [8]). The critical temperature of comp. 1 ($T_{c,1}$) is much lower than the temperature of the triple point of comp. 2 ($T_{TP,2}$). Due to the fact that the solid comp. 2 is soluble in liquid comp. 1 the vapor pressure of the mixture is decreased whereas the boiling temperature is increased (colligative effect). The critical line of this mixture ends in the LCEP (lower critical endpoint) due to the fact that the solubility of comp. 2 in comp. 1 is limited.

At higher temperatures, the three solid lines represent the sublimation-, melting- and vapor pressure curve of pure comp. 2 including its triple point (TP_2) and its critical point (CP_2; $p_{c,ibuprofen} = 2.3$ MPa, $T_{c,ibuprofen} = 750$ K, calculated by the group

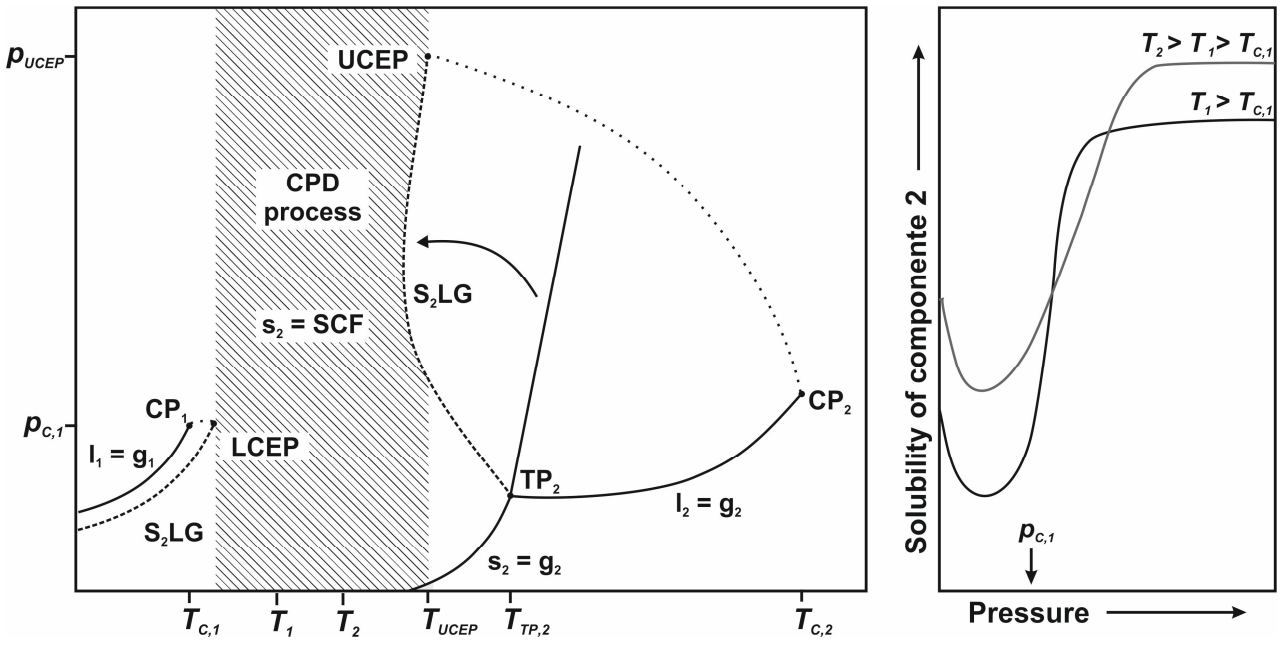

Fig. 9 Phase diagram of a SCF (comp. 1) and a low volatile substance (comp. 2) (left side). Solubility of a low volatile substance (comp. 2) as a function of pressure (right side).

contribution method of Lyderson [8]). Due to the fact that the SCF (comp. 1) is soluble in liquid comp. 2, the melting temperature of the mixture is decreased which results in the course of the S_2LG (solid-liquid-gas) line. The S_2LG line and the critical line of the mixture converge in the upper critical end point (UCEP). On the right side of the S_2LG line a two-phase-equilibrium between the SCF (comp. 1) and liquid comp. 2 exists, whereas a one-phase-equilibrium can be found on the left side. In this area solid comp. 2 is molecularly dissolved in the SCF (comp. 1). Therefore, the temperature and pressure range between the LCEP and UCEP (dashed region) is the most interesting part of the phase equilibria for the CPD process. In this part the solubility of comp. 2 in SCF (comp. 1) can be systematically controlled by pressure and temperature.

In Fig. 9 (right side) the schematic curve of the solubility of comp. 2 in comp. 1 is plotted as a function of fluid pressure of comp.1. The solubility curve can be divided in three parts with increasing pressure. It is obvious, that it is decreased in the low pressure range due to the fact that comp. 1 is still in a gaseous state. With increasing pressure the solubility is drastically increased while it becomes nearly constant at high pressures. The slope of this curve is proportional to the density increase of comp. 1 with increasing pressure at $p > 0.5\ p_c$ (see also Fig. 8). In general, a higher solubility is obtained at higher temperature. Nevertheless, in the "retrograde region" a higher temperature leads to a lower solubility.

1.2.4 The Controlled Particle Deposition process

The Controlled Particle Deposition (CPD) process [8], allows to deposit substances which are soluble in SCFs on carrier materials. A big advantage of this process is the fact that particle size reduction and formulation can be realized in one processing step. A schematic diagram of the process is depicted in Fig. 10. The substance (e.g. ibuprofen) and the carrier material which is in general porous and insoluble in the SCF (e.g. CO_2) are placed in two different sample containers in the reactor. In a next step, the reactor is filled with CO_2 until the operating process conditions (in this work: $T = 313$ K and $p = 15$ MPa) are reached. The experiment is kept at these conditions for a certain time to guarantee the deposition. The deposition time depends on the equilibrium of the ternary system. In this work a deposition time of 72 h was chosen. To ensure a good mixing of the $scCO_2$ a stirrer is placed in the middle of the reactor. Because of the liquid-like density of SCFs ibuprofen dissolves in the $scCO_2$ during the deposition time. The molecular dissolved ibuprofen diffuses into the porous carrier material due to the gas-like transport properties of $scCO_2$. As

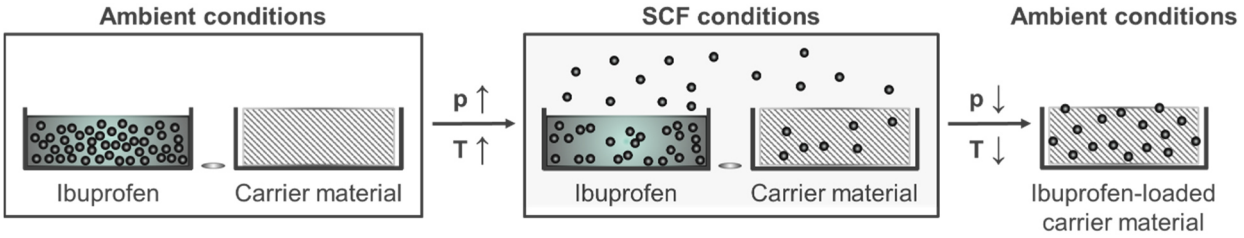

Fig. 10 Schematic diagram of the CPD process.

a final step, the reactor is depressurized. During this step, the solubility of ibuprofen is drastically decreased and therefore ibuprofen particles are formed inside the carrier material.

The different interactions and phase equilibria of the three components $scCO_2$, ibuprofen and the carrier material inside the reactor during the deposition time are depicted in Fig. 11. For the exact design and modeling of the CPD process the solubility and dissolution of ibuprofen in $scCO_2$, the adsorption of ibuprofen on the carrier material and the adsorption of $scCO_2$ on the carrier material needs to be considered. Therefore, a detailed knowledge of the phase behavior in the ternary system is necessary.

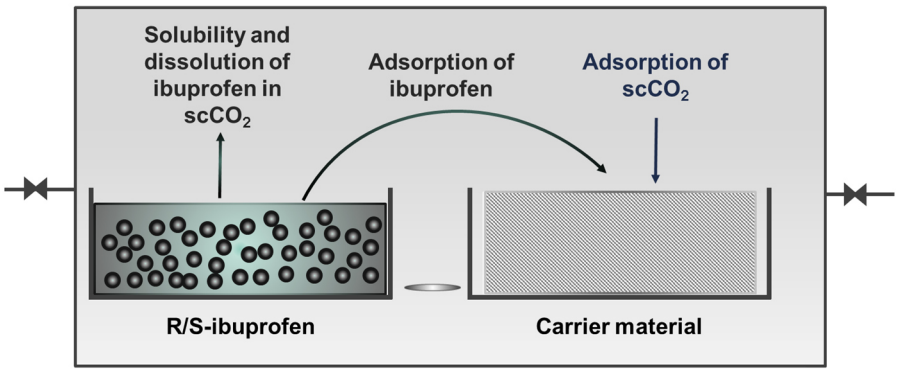

Fig. 11 Interactions and phase equilibria of the ternary system $scCO_2$, ibuprofen and carrier material in the CPD process.

1.2.5 Solubility of ibuprofen in $scCO_2$ - approach of Mendez-Santiago and Teja

In section 1.2.3 the schematic course of the solubility of a low volatile substance in an SCF was discussed. With regard to the CPD process it is important to gain information of the solubility of the active ingredient ibuprofen in $scCO_2$ at the operating process conditions. The solubility of ibuprofen in $scCO_2$ was investigated

at different temperatures and pressures a.i. by Charoechaitrakool et al. [63] and Ardjmand et al. [79]. In order to test the consistency of existing literature data and to apply these to operating process conditions, the approach of Mendez-Santiago and Teja (MST) [80] (Eq.(14)) can be used.

$$T \ln(E) = A + B \cdot \rho \quad \text{with} \quad E = \frac{y_2 \cdot p}{p_{2,sub}} \tag{14}$$

In this approach the solubility of ibuprofen y_2 is expressed as a function of its sublimation pressure $p_{2,sub}$, the density of the supercritical fluid ϱ, temperature T and two adjustable parameters A and B. The experimental determination of $p_{2,sub}$ is difficult for many substances. Therefore, MST developed a further refinement which is shown in Eq.(15). In this equation the solubility of ibuprofen y_2 is independent from its sublimation pressure three adjustable parameters A', B' and C' are implemented.

$$T \ln(y_2 \cdot p) = A' + B' \cdot \rho + C' \cdot T \tag{15}$$

With the approach of MST, consistent solubility data is aligned to one line (two-dimensional approach) or to a plane (three dimensional-approach). The available literature data of [63, 79] was fitted by Eq.(15) in MATLAB®. The obtained values for the parameter A, B, C and the average relative deviation (ARD) are listed in Tab. 3 while the resulting plane is shown in Fig. 12.

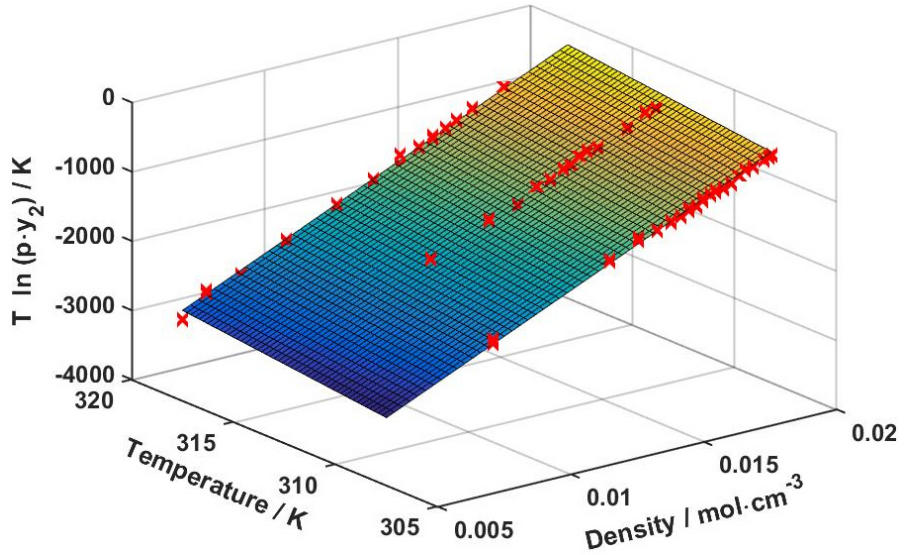

Fig. 12 Experimental data of [63, 79] depicted in a Mendez-Santiago and Teja plot.

Tab. 3 Derived parameters (*A*-*C*) and the average relative deviation (ARD) for the approach of Mendez-Santiago and Teja obtained from solubility data of [63, 79].

		value
A	K	$-1.41 \cdot 10^4$
B	$K \cdot cm^3/mol$	$1.71 \cdot 10^5$
C	-	32.56
$\mathbf{ARD_{y2}}$ *)	%	10.43

*) $ARD_{y_2} = \frac{1}{N} \sum_{i}^{N} \frac{\left| y_{2,calc.} - y_{2,exp.} \right|}{y_{2,exp.}} \cdot 100$

1.2.6 Different carrier materials and their interactions in the ternary system during the CPD process

Cyclodextrins

Cyclodextrins are well known for their excellent water solubility (see Tab. 4) and their ability to form inclusion complexes with hydrophobic molecules. Therefore, they are used in particular in the pharmaceutical industry to improve the bioavailability of poorly water-soluble active ingredients [81]. Cyclodextrins consist of α-D-glucopyranoses linked by (α-1,4)-glycosidic bonds which results in a conical spatial structure (Fig. 13). A hydrophobic cavity is formed due to the fact, that carbon atoms form the skeleton of the cone. The hydroxyl groups of the glucopyranoses form a hydrophilic surface which can interact with surrounding water molecules via hydrogen bonds (H-bonds). This leads to the formation of a hydrate-layer which enables the good solubility of cyclodextrin in aqueous solutions [82]. There are more than 1500 derivatives described in literature [83]. The three natural cyclodextrins α-, β-, γ-cyclodextrin differ e.g. in the number of glucopyranoses and thus in their spatial dimensions (see Tab. 4).

Tab. 4 Dimensions and solubility of different cyclodextrins.

		α-CD	**β-CD**	**γ-CD**
Amount of glucopyranoses [81]		6	7	8
Size of Cavity [81] :				
• **Height**	nm	0.78	0.78	0.78
• **Inner diameter**	nm	1.37	1.53	1.69
• **Outer diameter**	nm	0.57	0.78	0.95
Aqueous solubility*) [83]	g/l	145	18.5	232

*) at $T = 298$ K

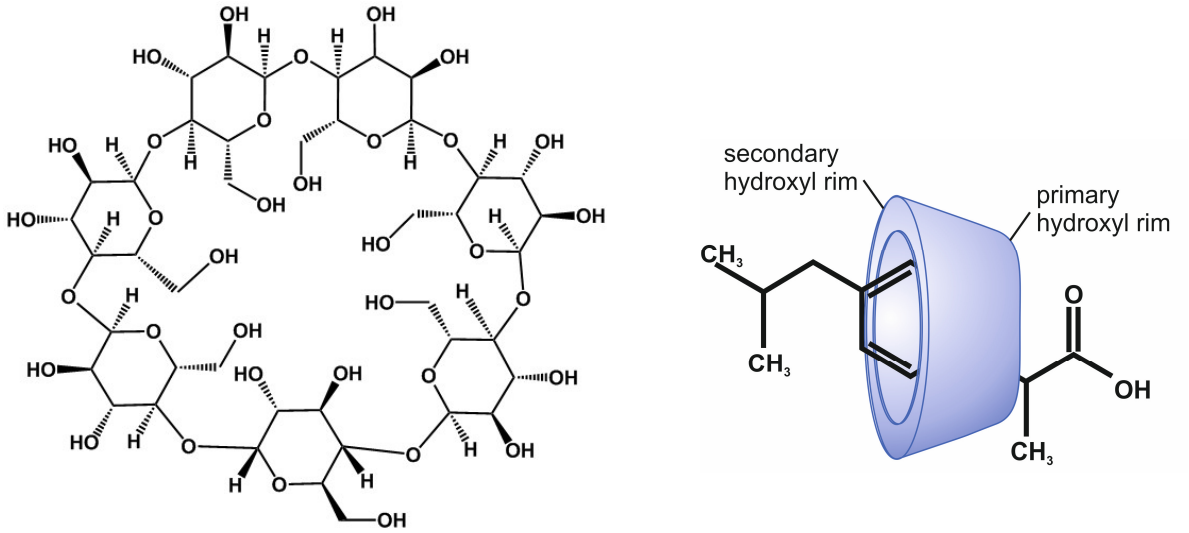

Fig. 13 Chemical structure of ß-cyclodextrin (left side, design from [92]) and ibuprofen-ß-cyclodextrin inclusion complex according to [87] (right side).

In aqueous solutions as well as in crystalline form cyclodextrins can form physiochemical, non-covalent dynamic inclusion complexes with hydrophobic guest molecules, while hydrophobic interactions, non-bonded van der Waals interactions and hydrogen bonds play an essential role [84 - 87]. The hydrophobic part of the guest molecule is entrapped inside the cavity, while its hydrophilic part is aligned towards the bulk phase [88]. The binding strength between the guest and host molecule is highly dependent on the hydrophobicity of the active pharmaceutical ingredient. It is widely reported that there is only one guest molecule inside the cavity of the cyclodextrin [85, 89], however, some exceptions with more guest molecules inside the cavity are also reported [90, 91].

The formation of inclusion complexes can be achieved e.g. by kneading [93], co-precipitation [94, 95], spray-drying [96], freeze-drying [95, 97] or with supercritical fluids [8, 95].

During the deposition step of the CPD process ibuprofen interacts with ß-cyclodextrin by non-bonded van der Waals intermolecular interactions, H-bonds and hydrophobic interactions which leads to the formation of inclusion complexes [87]. The preferred orientation of ibuprofen inside the cavity was found to be the mode where the non-polar group of ibuprofen faces the secondary hydroxyl rim of the ß-cyclodextrin (see Fig. 13) [87]. Besides the interactions mentioned above the formation of H-bonds between $scCO_2$ and ß-cyclodextrin is possible.

Silica carriers

Since it has been shown that silica particles are not capable of passing the mucosa of the gastrointestinal tract [98], they are widely used as carrier materials to improve the dissolution of active ingredients. For their preparation various synthesis methods are described in literature [54, 99 - 101]. With those methods it is possible to determine porous carriers with defined specific surface area, pore size and pore volume. Furthermore, the synthesis of defined pore structures (like in MCM-41 [99], MCM-48 [102] or SBA-15 [100]), as well as surface functionalization [17, 103 - 106] can be easily realized. Two of the most popular silica carriers (e.g. MCM-41 and SBA-15) are used in this work. Their schematic pore structure is depicted in Fig. 14. Both adsorbents consist of hexagonally ordered mesoporous and cylindrical pores. Furthermore, both adsorbents have a high specific surface area. In comparison to MCM-41, SBA-15 possesses additional cross linking channels.

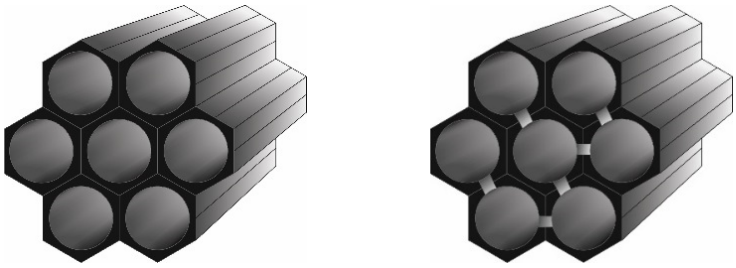

Fig. 14 Schematic pore structure of MCM-41 (left side) and SBA-15 (right side) according to [107].

During the CPD process different interactions between the carrier material, CO_2 and ibuprofen are possible. It was observed by Loganathan et al. [108] that different molecular groups on silica surfaces cause different interactions (see Fig. 15). Ibuprofen can form H-bond interactions with siloxane bridges and isolated silanol groups. Further H-bonds are formed between CO_2 and the isolated silanol groups [108]. The formation of dispersive forces in the form of dipol-quadrupole interactions between CO_2 and siloxane bridges and the formation of ion-quadrupole interactions between CO_2 and the silica cation (Si^+) were also described by Loganathan et al. [108].

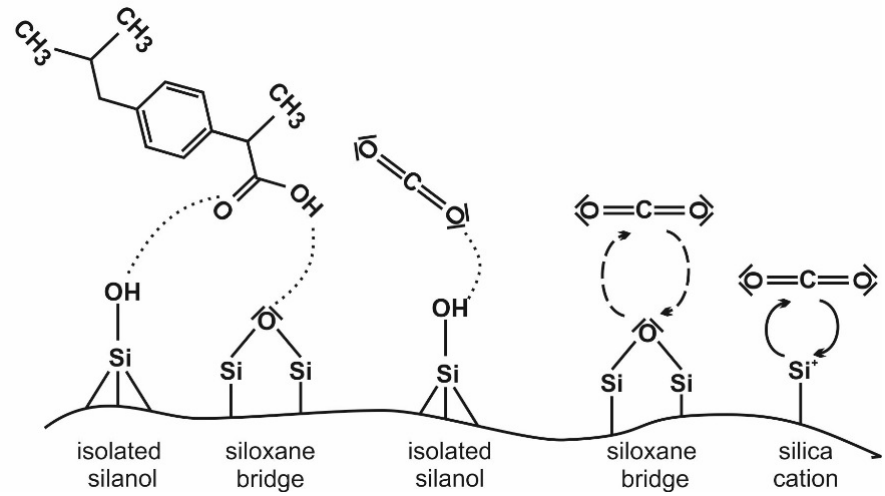

Fig. 15 Different interactions between the surface groups of silica carriers and ibuprofen or carbon dioxide. H-bonds are symbolized by dotted lines, while the dashed arrows correspond to dipol-quadrupole interactions. Between the silica cation and CO_2 ion-quadrupole interactions are obvious.

1.3 Adsorption

Information about the adsorption equilibria between the carrier surface and $scCO_2$ as well as ibuprofen during the deposition step are necessary for the design and modeling of the CPD process.

This section will give a short introduction to the fundamentals of adsorption while the technical terms are clarified first before the measurement technique used in this work is explained in detail. Furthermore, some basic approaches which can be used for the mathematical descriptions of adsorption isotherms and to determine thermodynamic parameters from experimental results are introduced.

1.3.1 Fundamentals of adsorption

In 1972 the technical terms and symbols of gas adsorption were defined by the International Union of Pure and Applied Chemistry (IUPAC) for the first time [109, 110].

The term adsorption describes the exothermic accumulation of molecules, atoms or ions of a fluid phase (adsorptive) in the vicinity of a solid interface (adsorbent) (Fig. 16). Molecules which are already adsorbed on the surface are called adsorbate. The release of adsorbed molecules from the surface is denoted as desorption.

Adsorption processes on porous materials are dependent on the internal specific surface area, pore volume, -structure, -size distribution and -diameter. For the characterization of porous materials a distinction is made between micro-, meso- and macropores depending on the pore size of the adsorbents (Tab. 5) [111].

Tab. 5 Classification of pores according to their size [111].

	Pore diameter nm
Micropores	< 2
Mesopores	2 - 50
Macropores	> 50

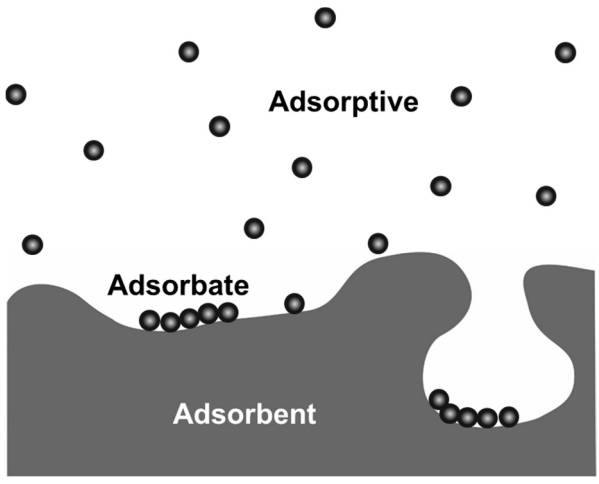

Fig. 16 Specific terms of adsorption.

Adsorption is either physical (physisorption) or chemical (chemisorption) depending on the type of interactions between adsorbent and adsorbate. Attractive dispersion forces, short range repulsive forces and specific molecular interactions are formed between the adsorptive and adsorbate if the adsorption is based on physisorption. Chemisorption occurs if the adsorbate molecules form chemical bonds with the surface of the adsorbent, which results in the formation of monolayers [110].

1.3.2 Adsorption isotherms

Adsorption isotherms describe the amount of molecules adsorbed on surfaces at a constant temperature with increasing pressure. It is widely considered to represent experimental results of the amount adsorbed n [$\mathrm{mol_{adsorbate}/g_{outgassed\ adsorbent}}$] as a function of relative pressure (p/p_0 while p_0 corresponds to the saturation pressure of the adsorptive) or total pressure (p). The amount adsorbed of physisorption processes depends on the interactions between the adsorptive and adsorbent as well as on its structural properties. Therefore, physisorption isotherms can be classified in different types (Fig. 17) [111, 112].

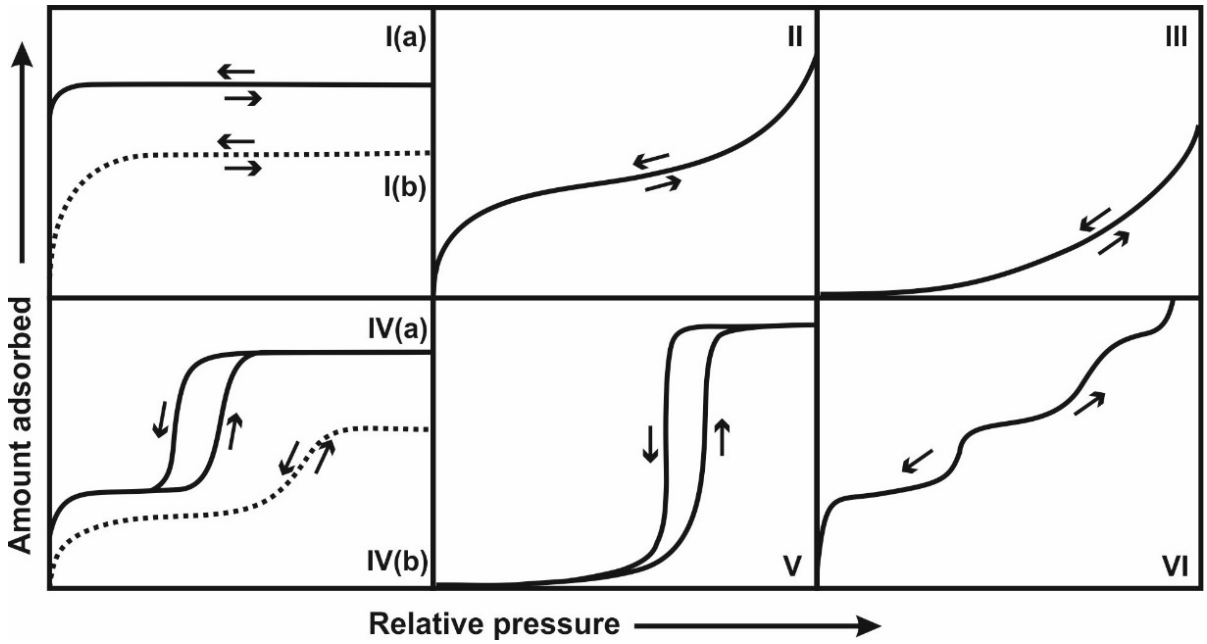

Fig. 17 Classification of different physisorption isotherms according to IUPAC [112].

Adsorption isotherms of type I are characteristic for microporous solids with a small external surface. The reversible isotherms show a steep increase at low relative pressures and reach a plateau afterwards. Another differentiation can be done depending on the magnitude of the amount adsorbed at low relative pressures. A very steep increase of the amount adsorbed (type I(a)) is characteristic for

microporous materials with a narrow pore size distribution (pore width < ~1 nm). A curve according to type I(b) is more specific for materials with a wider pore size distribution and/or mesopores (pore width < ~2.5 nm).

The shape of type II isotherms is particularly observed for nonporous and macroporous adsorbents. Monolayer adsorption in the low pressure range is followed by multilayer adsorption at higher relative pressures. At a relative pressure of 1, a finite value is not reached. Nevertheless, these isotherms are completely reversible.

Due to the weak adsorbent-adsorbate interactions, clusters are formed in preferred places on the surface of nonporous or macroporous adsorbents (type III). In contrast to type II, the amount adsorbed of these isotherms remains finite at a relative pressure of 1.

The type IV isotherms represent the typical curve of gas adsorption on mesoporous adsorbents. Initial monolayer and multilayer adsorption is followed by pore condensation. During pore condensation the density of the adsorbate is liquid-like while the pressure in the bulk phase (outside the pores) is still below the saturation vapour pressure. A hysteresis effect can be detected in type IV(a) isotherms while type IV(b) isotherms are completely reversible. The phenomenon of hysteresis depends on pore size. If the pores are larger than the critical pore size (which is dependent on the system and temperature), hysteresis occurs. In smaller pore diameters as well as conical or cylindrical mesopores, type IV(b) are primarily observed.

The nonreversible course of type V isotherms is similar to type III at low relative pressures, which can be attributed to the weak adsorbate-adsorbate interactions. With increasing relative pressure cluster formation is followed by pore filling at high relative pressures.

Type VI isotherms represent a “layer per layer” adsorption on uniform non-porous surfaces. The magnitude of the steps characterizes the adsorption capacity of the layers.

1.3.3 Characterization of adsorbents by N_2-sorption

For the interpretation of CPD loading results and the dissolution experiments it is important to gain knowledge of structural properties of mesoporous carrier materials. These information can be obtained e.g. from physisorption measurements with nitrogen at $T = 77$ K. These experiments are carried out in special devices provided e.g. by Quantachrome or Micromeritics which are equipped with their own evaluation

software to derive the structural properties from adsorption isotherms. Many mistakes can be done if some theoretical basics are ignored, because a large number of parameters and calculation models can be chosen. Therefore, the models used in this work to determine the specific surface area A_{BET}, pore volume V_P, pore size D_P and pore size distribution are introduced in the following.

Experimental method

Before the N_2-physisorption can be measured the IUPAC recommends to outgas the samples under vacuum ($p < 1$ Pa) at high temperatures for at least 16 h to purify the sample surface from e.g. crystal water [112]. In a next step the outgassed sample is impinged with e.g. N_2 in small pressure steps from $10^{-4} < p/p_0 < 1$ at $T = 77$ K while the amount adsorbed is measured. Examples of obtained isotherms are depicted in Fig. 17. A detailed description of the experimental method can be derived from [113].

Determination of the specific surface area A_{BET} by the BET-method

Nowadays, the Brunauer, Emmett and Teller (BET) [114] approach is one of the most important method for the characterization of porous adsorbents. The specific surface area A_{BET} can be determined with Eq.(16). In this equation n_m corresponds to the monolayer capacity of the adsorbed N_2-molecules on the adsorbent surface, N_A to the Avogadro number, σ to the cross-sectional area of the adsorptive and $m_{adsorbent}$ to the mass of the outgassed adsorbent.

$$A_{BET} = \frac{n_m \cdot N_a \cdot \sigma}{m_{adsorbent}} \tag{16}$$

The monolayer capacity n_m can be either determined by a single point or multipoint analysis from the experimental results. For the single point analysis a certain p/p_0-value ($0.05 < p/p_0 < 0.3$) is chosen to calculate the monolayer capacity by the mathematic model developed by BET Eq.(30). For the multipoint analysis the experimental results $1/(n(p/p_0 - 1))$ are plotted as a function of p/p_0 in the pressure range of $0.05 < p/p_0 < 0.3$ before pore condensation occurs. The monolayer capacity n_m can be derived by the resulting slope and intercept of a linear regression. However, in some adsorbate adsorptive systems pore condensation occurs in lower p/p_0-ranges, therefore the linear BET range is shifted towards lower pressures.

Determination of the pore volume V_P by the Gurvich rule

If the resulted adsorption isotherm shows the shape of type I or type IV the pore volume V_P can be determined from the volume adsorbed V_{ads} at relative pressures close to unity ($p/p_0 \rightarrow 1$). In the Gurvich rule it is assumed that at this pressure the pore is completely filled with adsorbate in the bulk liquid state [115, 116]. Therefore, Eq.(17) can be used to calculate V_P.

$$V_P = \frac{V_{ads} \cdot M \cdot p}{\rho \cdot R \cdot T} \tag{17}$$

In this equation M corresponds to the molecular weight of the adsorptive, ϱ to the liquid density of the adsorptive, R to the universal gas constant, T and p to temperature and pressure at standard conditions.

Pore size analysis

In well-defined pores the mean hydraulic radius r_h of a group of mesopores is defined as the ratio of the pore volume V_P to the specific surface area of the adsorbent A (Eq.(18)). In case of non-intersecting cylindrical capillaries the mean pore diameter D_P is defined in Eq.(19).

$$r_h = \frac{V_P}{A} \tag{18}$$

$$D_P = 4 \cdot r_h \tag{19}$$

The pore size distribution is the distribution of pore volume with respect to pore size [111]. Pore size analysis methods like e.g. the Barrett-Joyner-Halenda (BJH) [117] method are based on the Kelvin equation. The Kelvin equation describes the shift of the vapor saturation pressure above a curved liquid–vapor interface and for a cylindrical pore it can be written in the form of Eq.(20) [115, 116].

$$\ln \frac{p}{p_0} = -\frac{2 \cdot \gamma \cdot V_m}{R \cdot T \cdot (r_p - t_c)} \tag{20}$$

In this equation γ corresponds to the surface tension of the bulk fluid, V_m to the molar liquid volume, R to the universal gas constant, r_P to the pore radius and t_c to the thickness of the adsorbed multilayer film which is formed before the adsorptive condenses inside the pore (see also Fig. 18). Using this approach it is necessary to assume a model for the pore shape and that the curvature of the meniscus is directly

related to the pore width [111]. However, the pore size for narrow mesopores (D_P < ~10 nm) are significantly underestimated by these methods due to the fact that the curvature and enhanced surface forces are not properly taken into account [112]. To prevent these limitations molecular simulation techniques or the application of the density functional theory (DFT) were established [112, 116]. If a hysteresis effect occurs it has to be considered, that pore size distribution is dependent on the branch (adsorption or desorption branch) used for its calculation [111].

1.3.4 Capillary condensation

Capillary condensation is a typical phenomenon of mesoporous adsorbents which belong to Type IV of the IUPAC-System [112]. At temperatures below the critical temperature of the adsorptive the adsorbate phase exists in a liquid-like state [118]. Due to multilayer adsorption with increasing relative pressure a concave meniscus of the liquid-like adsorbed phase is formed inside the mesopores. Above this meniscus the saturation vapor pressure of the adsorptive inside the pore is decreased in comparison to the saturation vapor pressure above a flat surface (see Fig. 18). Therefore, the transition from a gas-like state to a liquid like state of the pore fluid occurs at a pressure less than the saturation vapor pressure of the bulk fluid if the critical adsorbate thickness is reached [116]. Capillary condensation, which is considered to be a fist order phase transition, occurs essentially in the core of the pore [116]. As a result of this, the adsorbed amount increases significantly due to small pressure variations close to the saturation pressure [118]. This is indicated by the steep increase of the adsorption isotherm (see Fig. 17, type IV). The relative

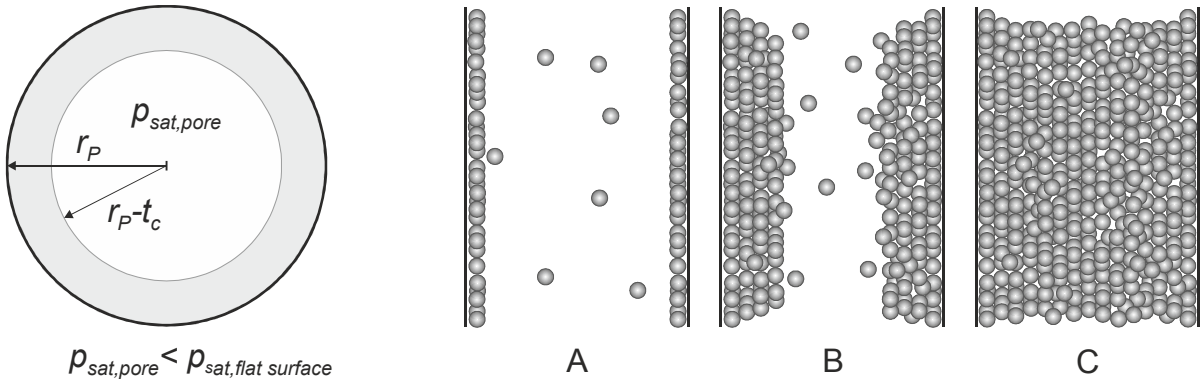

Fig. 18 Formation of a meniscus inside mesopores (left side). The phenomenon of capillary condensation (right side). Monolayer adsorption (A) is followed by multilayer adsorption (B) until the critical adsorbate thickness is reached. Transformation of the pore fluid from a gas-like phase into a liquid-like phase (C).

pressure at which capillary condensation occurs is dependent on the pore radius. A relation of this is given by the Kelvin equation (Eq.(20)) for pores of uniform shape and width.

1.3.5 Adsorption measurement techniques - magnetic suspension balance

Adsorption isotherms can be measured either statically by gravimetric [110] and volumetric [119] methods or dynamically by breakthrough curves [120]. In the following section the measurement principle of a magnetic suspension balance (MSB), a typical gravimetric method, is introduced. The major advantage of an MSB in comparison to conventional measuring systems is the contactless weighing method. This means that the weighing instrument is decoupled from the measuring chamber. Due to this, the measurement is unaffected by any influences of the test substances and test conditions, while damages of the balance can also be avoided. In addition to this, the sample can be set down by the sample coupling and therefore tarring and calibration of the balance can be realized during the measurement.

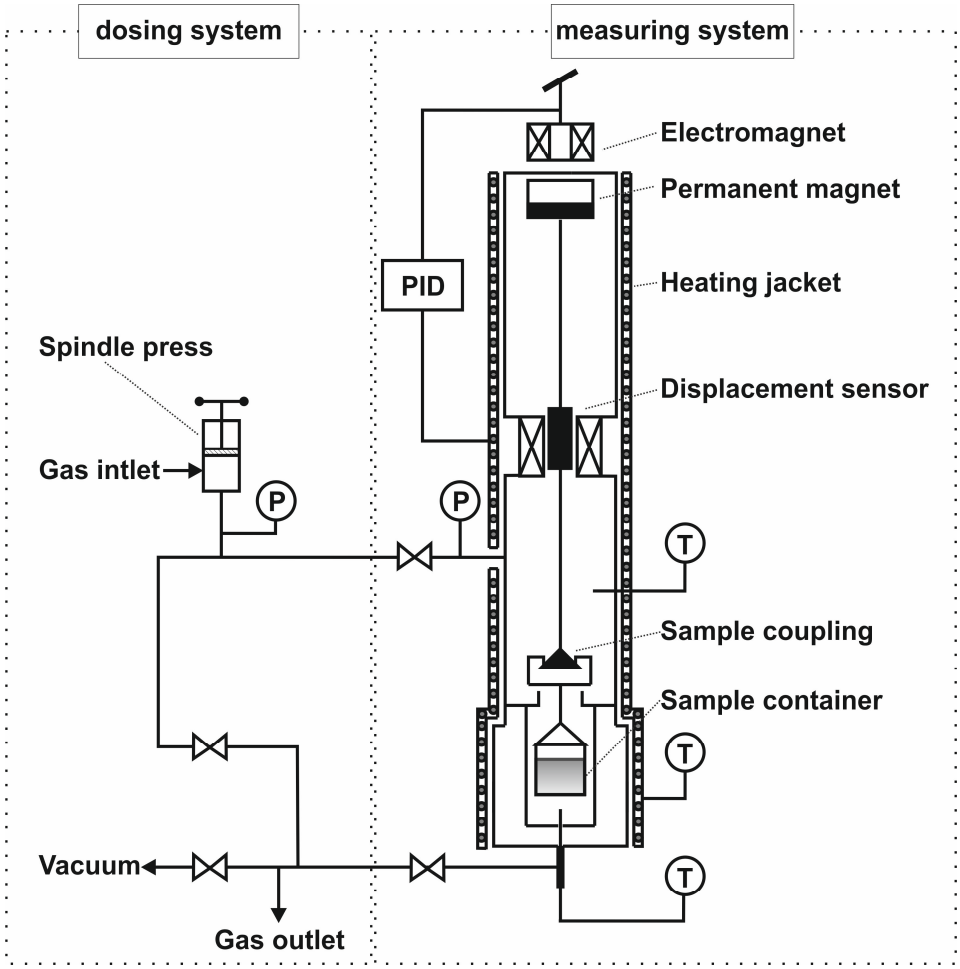

Fig. 19 Schematic setup of a magnetic suspension balance.

A schematic sketch of an MSB setup is depicted in Fig. 19. The dosing system (including gas inlet/outlet and spindle press) is located on the left side whereas the measuring system is shown on the right side. Via the dosing system the test gases are able to stream into the measuring cell. In case of CO_2, pressures above 9 MPa are achieved by a spindle press.

Inside the measuring cell the sample container is connected to a rod by the sample coupling. The permanent magnet at the upper end of the rod is coupled to an electromagnet which is placed outside the measuring cell. The electromagnet is connected to a displacement sensor and a PID controller. This unit controls the electromagnet in such a way, that the sample is permanently floating during the measurement.

There are two factors effecting the measurement. The first factor is the weight increase due to adsorption and the second is an apparent weight loss. This weight loss is caused by the fact that the sample and the internal parts of the balance receive a buoyancy by the density of the gas. Thus, a direct determination of the adsorbed mass is not possible.The mass which can be monitored on the display m is composed of different proportions (Eq.(21)).

$$m = m_{ads} + m_s + m_{ip} - \rho_{bulk} \cdot (V_{ads} + V_s + V_{ip}) \tag{21}$$

In this equation m_s and V_s are the mass and volume of the sample, m_{ip} and V_{ip} are the mass and the volume of the internal parts of the MSB, m_{ads} and V_{ads} is equivalent to the mass and volume of the adsorbate and ϱ_{bulk} corresponds to the bulk density.

The values of m_{ip} and V_{ip} can be determined by an empty measurement using e.g. helium or nitrogen as test gas. Therefore, measuring points at different pressures are taken. In a mass versus density diagram the buoyancy results in a linear dependency. V_{ip} can be determined from the slope and m_{ip} from the intercept. The same procedure including the sample is used to determine m_s and V_s with helium as adsorptive. It is assumed that the helium adsorption on the sample is negligibly small under the corresponding test conditions.

If Eq.(21) is rearranged the reduced mass Ω (Eq.(22)), which was introduced by Staudt et al. [121] in 1993 is obtained. In this equation V_{ads} and V_s are combined into one term V^{as}. Thus, the adsorbed mass m_{ads} can be calculated using Eq.(23).

$$\Omega = m_{ads} - \rho_{bulk} \cdot V_{ads} = m - m_s - m_{ip} + \rho_{bulk} \cdot V_{ip} \tag{22}$$

$$m_{ads} = \Omega + \rho_{bulk} \cdot V_{ads} \tag{23}$$

Because of the fact that V_{ads} (and therefore V^{as}) cannot be determined experimentally the calculation of the Gibbs surface excess m^{GE} (Eq.(24)) gives a first approach of the amount adsorbed.

$$m^{GE} = \Omega + \rho_{bulk} \cdot V_s^{He} \tag{24}$$

In this approach the volume of the adsorbate can be neglected because it is assumed that the adsorbate behaves like a 2-dimentional gas [110]. Therefore, V^{as} is equivalent to the volume of the sample which can be determined by a helium measurement (V_s^{He}).

In this work, the specific excess amount adsorbed n^{ex} (Eq.(25)) is calculated from the experimental results. In this equation the Gibbs surface excess m^{GE} is divided by the mass of the outgassed sample m_s and the molecular weight of the adsorptive M.

$$n^{ex} = \frac{m^{GE}}{m_s \cdot M} \tag{25}$$

1.3.6 Determination of the absolute amount adsorbed

It has been mentioned in the previous section that the absolute amount adsorbed (m_{abs}) cannot be measured directly. For its determination different methods are proposed in literature. The absolute amount adsorbed can be derived either by assuming the volume V_{ads} (Eq.(26)) or the density ϱ_{ads} (Eq.(27)) of the adsorbed phase.

$$m_{abs} = m^{GE} + \rho_{bulk} \cdot V_{ads} \tag{26}$$

$$m_{abs} = \frac{m^{GE}}{(1 - \frac{\rho_{bulk}}{\rho_{ads}})} \tag{27}$$

Menon [29] suggested to estimate V_{ads} from a linear regression of the high pressure range of experimental excess data. It is assumed that the gas behaves like a condensed phase with a density ϱ_{ads} and a volume V_{ads}. A linear relation can be determined between m^{GE} and the bulk density ϱ_{bulk}, if the adsorbed phase is saturated at high pressures. From the slope of this linear dependency V_{ads} can be determined.

Dubinin [30] established another method to estimate V_{ads} depending on the adsorption conditions. If $T > T_c$, V_{ads} corresponds to the Van der Waals co-volume

b which can be calculated from the critical data of the fluid (T_c and p_c) and the universal gas constant R ($b = R{\cdot}T_c/(8{\cdot}p_c) = 42.7$ cm^3/mol for CO_2). This method seemed to be particularly suitable for the "early part" of the high-pressure adsorption isotherm, where the gas behaves like a mobile 2-dimensional gas. At temperatures which are higher than the boiling temperature of the gas (T_{boil}), Dubinin used tabulated values for the density of the adsorbate to calculate its volume. If $T_{boil} < T < T_c$, specific calculation methods are developed to determine ϱ_{ads}. In addition to this adsorption on two different pore structure types are distinguished. In contrast to structure type II, type I consists of micropores. In these pores overlapping force fields of opposite pore walls increase the adsorption capacity [30].

If it can be considered that all adsorptive molecules inside the pore are adsorbed on the surface, V_{ads} can be equalized to the pore volume V_{pore}. This approach is especially suitable for microporous adsorbents where opposite force fields are overlapping, which results in an enhanced adsorption ability [122].

A method to estimate ϱ_{ads} is suggested by Tsai et al. [31]. In this model two cases are taken into account. Either ϱ_{ads} can be equal to the density of the liquefied gas at its boiling point or to the density of the solidified gas. The first assumption might be suitable for adsorption conditions below the critical point of the fluid [123].

1.3.7 Mathematical description of adsorption data

To determine important thermodynamic parameters (e.g. the isosteric heat of adsorption) or to compare different experimental results, mathematical descriptions of the experimental data are desirable. Depending on the interactions between the adsorptive and adsorbent several methods for the description of adsorption phenomena of pure components and mixtures on solid surfaces are published in literature.

Polanyi [124] published in 1914 the first considerations for the mathematical description of adsorption isotherms based on the dynamic behavior of adsorptive molecules in the potential field above the adsorbent surface. These ideas were the basis for numerous future developments [33]. Based on the kinetic energy of gases, Langmuir developed an approach in 1918 [125] to describe the dynamic equilibrium between adsorption and desorption on homogeneous surfaces. This concept is mainly used to describe adsorption in microporous materials [126]. While Langmuir used the kinetic energy of gases, isotherms based on Gibbs deliver a thermodynamic approach. In this model the adsorbed phase is treated as a two dimensional surface to which

the classical thermodynamic equations of the bulk phase are applied [127, 128]. The physical approaches mentioned above and numerous developments provide an exact picture of the equilibrium between the adsorbent and the adsorbate phase. Nevertheless, theoretical laws or parameters are not applicable to all adsorption phenomena. Especially in complex pore structures and on energetically heterogeneous surfaces existing physical approaches fail. Therefore, semi-empirical developments were established e.g. by Freundlich [129] in 1932. To describe multilayer adsorption the method suggested by Brunauer Emmett and Teller (BET) [114] in 1938 can be used.

The models mentioned above provide good descriptions for the adsorption at low pressures but fail to describe excess isotherms at high pressures because they possess a maximum of the amount adsorbed [33]. Therefore, empirical approaches are mainly used to describe such isotherms.

Subsequently, the models of Langmuir, Freundlich, BET and the empirical Padé equation are described in detail. A precise description of many physical, semi-empirical and empirical approaches can be found in [33, 128].

Langmuir

The adsorption of molecules on flat surfaces can be described by the approach of Langmuir (Eq.(28)) [125]. It is based on the kinetic theory of gases and proposes that a fraction of gas molecules is condensed and is held by the surface force until the adsorbed molecules evaporate again. In this model, the surface is described as homogenous where all adsorption sites are energetically equal. The adsorption is considered to be localized and takes place at definite adsorption sites and only one molecule interacts per adsorption site which results in the formation of monolayers on the surface.

$$\theta = \frac{b \cdot p}{1 + b \cdot p} \tag{28}$$

In Eq.(28) the fractional loading Θ is expressed as a function of the Langmuir constant b (which is a measure how strong adsorbents are attracted onto surfaces) and the equilibrium pressure p. If $b \cdot p << 1$ the fractional loading increases linearly. At high equilibrium pressures ($p \rightarrow \infty$) Θ reaches its saturation capacity when all adsorption sites are occupied with adsorbate molecules.

Freundlich

Another possibility to describe monolayer adsorption is the semi-empirical approach of Freundlich [129] which is described in Eq.(29). In contrast to Langmuir, the surface is regarded as heterogeneous. It includes a patch wise distributed adsorption energy where all adsorption sites inside a patch possess the same energy. Interactions between the patches are not considered. To describe the adsorption equilibrium of each patch the Langmuir equation can be applied.

$$C_{\mu} = K \cdot p^{\frac{1}{n}} \tag{29}$$

In this equation the concentration of the adsorbed species C_{μ} is a function of the equilibrium pressure p and the shape parameters K and n which are temperature dependent. With increasing n the isotherm becomes less linear. Furthermore, there is no finite limit of the isotherm at high pressures. To prevent this, extensions proclaimed by Sips [130] can be applied.

Brunauer, Emmett and Teller

During the adsorption process monolayers are formed at low pressures whereas multilayers are developed with increasing pressure. Brunauer, Emmett and Teller [114] were the first authors who provided a mathematical description of multilayer adsorption (Eq.(30)) in 1938. In this model, the same assumptions as those used in the Langmuir model were made. The only difference is that adsorption takes place on a flat surface with no limitations in layer formation. For the application of this approach on experimental results the physisorption data needs to be transferred into a so called "BET-plot" in which the specific amount adsorbed n is depicted as a function of the relative pressure (p/p_0). In Eq.(30) n_m corresponds to the specific monolayer capacity and C is an adjustable parameter which is exponentially related to the monolayer adsorption energy.

$$n = \frac{n_m \cdot C \cdot (p / p_0)}{(1-(p / p_0)) \cdot (1-(p / p_0) + C \cdot (p / p_0))} \tag{30}$$

Padé equation

Because of the fact that high pressure excess isotherms possess a maximum, many classical methods for their description fail. Therefore, empirical approaches are implemented to describe such isotherms properly. It was shown that the Padé

equation, which is a development of the virial equation, is a suitable model to fit high pressure excess isotherms of numerous adsorbent - adsorbate systems [123, 131, 132]. In Eq.(31) the form suggested in [123] is presented. In this equation the amount adsorbed n is a function of the adjustable parameters a - e which are temperature dependent.

$$n = \frac{a \cdot p + b \cdot p^2 + c \cdot p^3}{1 + d \cdot p + e \cdot p^2} \tag{31}$$

1.3.8 Isosteric heat of adsorption

The isosteric heat of adsorption is a key thermodynamic variable for the design and modelling of adsorption processes. It is a measure of the temperature change during adsorption [133]. It can be determined either by thermal and thermogravimetric analysis data [134] or out of adsorption measurements [33].

On the basis of the Clausius-Clapeyron equation and the assumption that the chemical potentials between the adsorbed phase and the gas phase are equal at constant amount adsorbed, it can be calculated by Eq.(32).

$$\left(\frac{\partial \ln p}{\partial T}\right)_n = -\frac{\Delta H}{RT^2} \tag{32}$$

In this equation R corresponds to the universal gas constant. The change in enthalpy ΔH is considered to be temperature independent. Therefore, the plot of $ln\ p$ as a function of $1/T$ is linear at constant amount adsorbed n. From its slope the isosteric heat of adsorption at corresponding n can be determined.

At zero loadings ($n = 0$) it is suitable to calculate the isosteric heat of adsorption from the Henry constants K which is temperature dependent [33] (see Eq.(33)).

$$\frac{\partial \ln K(T)}{\partial T} = -\frac{\Delta H_0}{RT^2} \tag{33}$$

The Henry constant K can be determined directly out of the experimental data at different temperatures if they are plotted in a $ln(p/n^{ex})$ versus n^{ex} diagram. At low n^{ex} ($n^{ex} \rightarrow 0$) a linear dependency is obvious. In this case, K corresponds to the intercept of the linear regression of the experimental data in this region. The Henry constant is a measure for the strength of interactions between the adsorbate molecules and the adsorbent surface [110].

Furthermore, from the value of the isosteric heat of adsorption it can be distinguished if the adsorption is based on physisorption ($\Delta H < 40$ kJ/mol) or chemisorption ($\Delta H > 40$ kJ/mol). An adsorption energy of 40 kJ/mol is considered to be a rough borderline [32].

The curve of the isosteric heat of adsorption at constant loadings ($n_{abs} > 0$) indicates if the surface is energetically uniform or heterogeneous [33] (see Fig. 20). It can be can be calculated indirectly by the Clausius-Clapeyron equation [128, 135]. From the slope of a *ln(p)* versus *ln(T)* plot the heat of adsorption can be determined at constant loadings. An energetically uniform surface is represented by a constant curve, while a heterogeneous surface shows a deviant behavior.

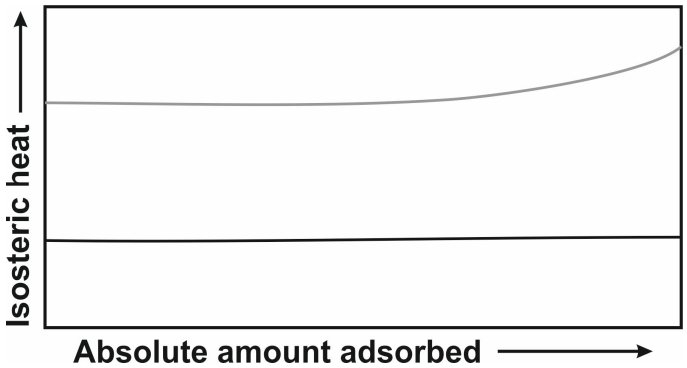

Fig. 20 Schematic curves of the isosteric heat of adsorption of heterogeneous (light grey) and homogeneous surfaces (black).

2. Research proposal

Patients' expectations on administered active ingredients are a fast and efficient relief of their suffering. The effect is influenced by the bioavailability of the active ingredient. If they are applied orally their bioavailability is dependent on the dissolution and resorption in the gastro intestinal tract (GIT). Especially with regard to active ingredients which are poorly water soluble but highly permeable through the mucosa of the GIT (class II of the Biopharmaceutical Classification System [1]) their bioavailability is limited by their dissolution. To ensure the sufficient concentration of the active ingredient at its side of action, it is not advisable to increase the applied dose. Because a higher dose can cause dangerous side effects to the human body [2]. As a consequence, one of the key challenges in pharmaceutical research is the design of formulations with improved dissolution performance to guarantee a fast and efficient effect with the lowest possible dose. An enhanced dissolution performance can be realized e.g. by methods such as particle size reduction or by deposition on suitable carrier materials [3]. Conventional particle size reduction methods like milling, grinding or spray drying cause several disadvantages (e.g. thermal or chemical degradation of the product, broad particle size distribution and/or organic residues in the final product). To prevent these disadvantages, processes with supercritical fluids (SCFs) can be used [5]. One example of such a process is the Controlled Particle Deposition (CPD) process [8], which is considered to be a suitable environmental and product friendly method to obtain products with enhanced dissolution behavior. In this process the active ingredient is dissolved in

the SCF and deposited onto carrier materials which are insoluble in the SCF. Due to the deposition of the active ingredient onto carrier materials its particle size reduction and a subsequently formulation can be combined in one processing step. It has been shown in various studies, that the CPD process is able to produce active ingredient-carrier systems for a controlled release of the active ingredient [8 - 10].

In order to examine the CPD process and to evaluate the dissolution behavior of its products, this work is divided in two main parts. The first part is focused on the evaluation of the obtained products while the second part is addressed to describe the adsorption behavior of the SCF and the active ingredient on the carrier material during the CPD process.

To investigate the dissolution behavior of active ingredients in vitro studies need to be carried out according to the recommendations of the FDA. These studies are time and cost intensive. As mentioned before it has been shown that products obtained by the CPD process are suitable for a controlled release of active ingredients. Because of this, a fast and efficient method is demanded to predict the loading and the dissolution performance of new CPD products for a targeting application. This prediction should be possible just by the knowledge of the chemical nature of the active ingredient and the knowledge of the chemical and structural properties of the carrier material. In this work active ingredient-carrier systems obtained by the CPD process will be investigated. Previous CPD studies were focused on identifying the impact of the chemical nature of carrier materials on the CPD loading and the dissolution behavior of active ingredients [8 - 10, 12 - 15]. In this context carrier materials for a controlled release of the active ingredient have been identified. Furthermore, it has been shown that mesoporous, silica based carrier materials are suitable to deposit active ingredients and to enhance their dissolution performance [9, 10]. Nevertheless, the impact of specific carrier material properties (e.g. specific surface area, pore size, pore volume and surface functionalization) on the loading of active ingredients by the CPD process and their dissolution behavior from the obtained products was not studied systematically, yet. Consequently, the first part of this work is attributed to investigate the impact of specific properties mentioned above of silica based carrier materials. With the obtained results it will be possible to contribute to the development of a fast, cost-effective and easy to handle active ingredient-carrier selection method. The identification of suitable active ingredient-carrier systems for a targeting application will prevent time and cost intensive in vitro studies.

In order to evaluate the dissolution performance of the obtained silica based CPD products, investigated in this work, ß-cyclodextrin is used. It has been shown in literature that active ingredient-ß-cyclodextrin inclusion complexes show fast dissolution rates due to the high water-solubility of ß-cyclodextrin [8, 86, 89]. Thus, the active ingredient-ß-cyclodextrin-inclusion complex is considered to be the benchmark for the evaluation.

The FDA provides instructions of e.g. the experimental setup or the investigated sample amount [11, 51]. The sample amount is defined by the sink conditions and depends on the volume of the dissolution media. Due to low drug loadings on certain carrier materials (e.g. ß-cyclodextrin) and small amounts of the obtained CPD products the design of an apparatus with smaller dimensions is necessary. With the down-scaled dissolution volume it is possible to ensure the required sample amount. Klein and Shah [20] investigated the dissolution behavior of active ingredients in a down-scaled apparatus experimentally. Their dissolution results were similar to those obtained in a setup with the dimensions recommended by the FDA. A fluid dynamic simulation needs to be carried out to validate the dimensions of the down-scaled apparatus and to identify further parameters which influence the fluid dynamic profile. In addition to this, the FDA does not give exact recommendations for the type of sample injection. To generate reproducible results different types of sample injection, need to be systematically examined.

The second part of this work is addressed to gain knowledge of the adsorption behavior of the SCF and active ingredient on the carrier material. This knowledge is a mandatory requirement for the design and modelling of the CPD process in a subsequently step. Furthermore, the question arises, if there is a competitive adsorption between the SCF and the active ingredient at the carrier material during the deposition step of the CPD process. The clarification of this question is also aimed to be answered in this part.

To describe the interactions during the CPD process it is necessary to gain a deeper understanding of the adsorption behavior of the SCF on the carrier material at the operating process conditions, first. The amount adsorbed of the SCF on the carrier material, which is also a measure of the binary interactions, is specific for each SCF-carrier system and depends on pressure and temperature. Due to the fact that there is a lack of literature data at the operating CPD process conditions, the determination of high pressure adsorption data is a central part of this work.

High-pressure adsorption isotherms are widely measured by magnetic suspension balances (MSB) [26]. The most important benefit of this device is the fact that the

weighing instrument is decoupled from the measuring chamber. This prevents influences of the test substances and test conditions to the weighing results. AC Norit R1 Extra is considered to be a reference adsorbent to validate the experimental set up of the MSB [26, 136]. According to this, the adsorption of N_2 and CO_2 on AC Norit R1 Extra is examined and compared to reliable literature data.

Values of the absolute amount adsorbed are necessary to describe the adsorption behavior of the SCF on the carrier material and to determine thermodynamic parameters. Nevertheless, besides the many advantages of an MSB its big disadvantage is the fact that due to the buoyancy effect only excess values can be determined. These excess values do not correspond to the absolute amount adsorbed. Therefore, the calculation of the absolute amount adsorbed is another important part of this work. For its calculation a suitable model for high-pressure data described in literature [29 - 31] needs to be chosen.

The chemical or thermodynamic nature of the SCF adsorption on the carrier materials can be characterized by the isosteric heat of adsorption [33]. The value of the isosteric heat of adsorption provides the information if the adsorption process is due to physisorption (physical interactions: e.g. H-bonds, electrostatic interactions) or chemisorption (chemical interactions: e.g. covalent bonds) [32]. Furthermore, it indicates whether the adsorption process is endothermic or exothermic [133]. It has been shown in literature that the values differ inter alia with pore size and with different silica surface groups [137, 138]. Hence, the determination of the isosteric heat of adsorption is required to provide a precise description of the SCF-carrier adsorption. The adsorption of the SCF on the carrier material can be described by different models. For the decision of a suitable model the information about the energy distribution on the investigated carrier materials is necessary. This information can be obtained by the curve of the heat of adsorption [33]. Considering the aspects mentioned above this work aims to provide the crucial values of the isosteric heat of adsorption as well as the curve of the heat of adsorption for the investigated CPD carrier materials.

To clarify the question, if there is a competitive adsorption between the SCF and the active ingredient on the carrier material, the CPD loading results can be compared to the adsorption results (SCF-carrier material) in a first approach.

In summary, this work provides information to the development of a fast, cost-effective and easy to handle method to predict the dissolution performance of obtained CPD products. It will be possible to carry out the prediction solely by the knowledge of chemical and structural properties of the active ingredient and the

carrier material. Furthermore, this work provides knowledge about the adsorption behavior of the ternary system (SCF-active ingredient-carrier material) and therefore a solid data base for a subsequently design and modeling of the CPD process.

3. Publications & Manuscripts

3.1 Influence of chemical nature of carrier materials on the dissolution behavior of racemic ibuprofen 49

Sarah Reiser[1)], Miaotian Sun[2)], Monika Johannsen[2)], Michael Türk[1)]*

[1)] Institute for Technical Thermodynamics and Refrigeration, Karlsruhe Institute of Technology (KIT), Engler-Bunte-Ring 21, D - 76131 Karlsruhe

[2)] Institute for Thermal Separation Processes (V8), Technical University Hamburg-Harburg, Eissendorfer Str. 38, D - 21073 Hamburg

*Corresponding author, Email: tuerk@kit.edu, phone: +49 721 608 42330

Journal of Supercritical Fluids 132 (2018) 91–98

In this paper different carrier materials were loaded with R/S-ibuprofen by the Controlled Particle Deposition (CPD) process to investigate the impact of specific carrier properties (specific surface area and surface functionalization) on the loading and dissolution of obtained CPD products. Therefore, two different silica carrier materials were functionalized with S-(+)-ibuprofen by the Covalent Bonding Reaction. Their loading and dissolution was compared to commercially available MCM-41 and SBA-15. High ibuprofen loadings up to 50 wt% were found on MCM-41 and SBA-15. It was assumed that ibuprofen loadings increase nearly linearly with increasing specific surface area of the carrier material. Furthermore, ß-cyclodextrin

was investigated as another carrier material. The ibuprofen-ß-cyclodextrin inclusion complex was considered to be the benchmark for evaluating the dissolution behavior of the obtained CPD products. The dissolution of untreated ibuprofen and the CPD products was investigated at $T = 310$ K and pH = 2.0 and pH = 5.5. It was found that the dissolution rate of all materials investigated increased with increasing pH-value and that the highest dissolution rate was obtained with β-cyclodextrin. Furthermore, it was found, that the dissolution rate was also dependent on the amount and the location of the surface functionalization. The silica carrier with a high amount of functionalization on its outer surface was poorly wettable by the dissolution media and tended to agglomeration which led to a diminished dissolution rate.

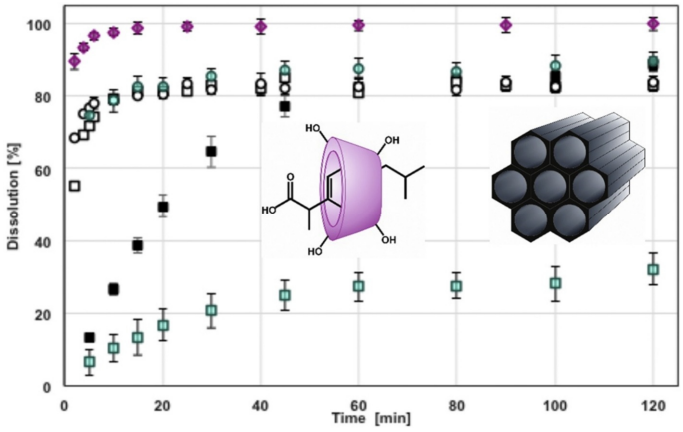

3.2 CO_2 assisted deposition of R/S-ibuprofen on different porous carrier materials: influence of carrier properties on loading and dissolution behavior 71

Sarah Reiser[1)], Masoom Shaban[2)], Alfred Weber[2)], Michael Türk[1)]*

[1)] Institute for Technical Thermodynamics and Refrigeration, Karlsruhe Institute of Technology (KIT), Engler-Bunte-Ring 21, D - 76131 Karlsruhe

[2)] Institute of Particle Technology, Technical University of Clausthal, Leibnizstraße 19, D - 38678 Clausthal-Zellerfeld

*Corresponding author, Email: tuerk@kit.edu, phone: +49 721 608 42330

Journal of CO_2 Utilization 25 (2018) 216–225

This paper deals with investigating the influence of specific surface area, pore size and pore volume of carrier materials on CPD loading and their dissolution behavior.

Therefore, carrier materials with defined properties were produced by Salt Assisted Spray Pyrolysis (SASP) and loaded with R/S-ibuprofen by the Controlled Particle Deposition (CPD) process. The obtained loading and dissolution results were compared to CPD processed MCM-41 and SBA-15. It was found that the loading results of the SASP prepared carrier materials were smaller compared to MCM-41 and SBA-15 due to their lower specific surface area. In the wider mesopores of the SASP prepared carrier materials multilayer formation was possible and the formation of crystalline ibuprofen fractions in these pores was detected by X-ray diffraction analysis. The dissolution rate of the SASP prepared carriers was enhanced compared to MCM-41 and SBA-15. Nevertheless, it was found that the crystal state of the deposited ibuprofen influences the dissolution behavior especially at pH = 2.0.

The CPD processed and unprocessed carrier materials were characterized by N_2-adsorption/desorption experiments at $T = 77$ K. It was observed that the typical capillary condensation step of unprocessed MCM-41 and SBA-15 was shifted towards lower relative pressures of the CPD processed carriers. This led to the assumption, that the small mesopores of MCM-41 or SBA-15 were occupied by the deposited ibuprofen.

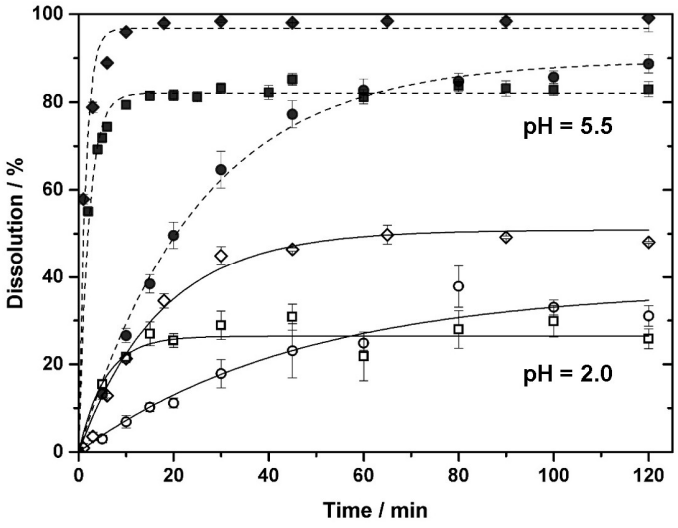

3.3 Adsorption of N_2 and CO_2 on Activated Carbon, AlO(OH) Nanoparticles, and AlO(OH) Hollow Spheres

Sarah Reiser[1)], Dennis Bolten[1)], Reiner Staudt[2)], Michael Türk[1)]*

[1)] Institute for Technical Thermodynamics and Refrigeration, Karlsruhe Institute of Technology (KIT), Engler-Bunte-Ring 21, D - 76131 Karlsruhe

[2] Department of Mechanical Engineering and Process Engineering, Offenburg University of Applied Sciences, Badstraße 24, D - 77652 Offenburg

*Corresponding author, Email: tuerk@kit.edu, phone: +49 721 608 42330

Chemical Engineering & Technology 38(12) (2015) 2261–2269

In this paper the adsorption of N_2 and CO_2 on AC Norit R1 Extra was investigated by a magnetic suspension balance (MSB) to validate the correct function of the experimental setup. Furthermore, the adsorption of CO_2 on AlO(OH) nanoparticles and hollow spheres was measured under different temperature (T = 298 K, 313 K, 328 K) and pressure (p = 0 – 23.5 MPa) conditions. All measured excess isotherms ($T \geq$ 313 K) increase with increasing pressure, reach a maximum and decrease afterwards. It was also shown in this paper, that the conversion of the liquid into a supercritical adsorbate phase does not take place suddenly. Some selected experimental data were correlated with different model approaches. The obtained results are in good agreement to reliable literature data.

3.4 Influence of temperature and high pressure on the adsorption behavior of scCO$_2$ on MCM-41 and SBA-15 113

Sarah Reiser, Michael Türk*

Institute for Technical Thermodynamics and Refrigeration, Karlsruhe Institute of Technology (KIT), Engler-Bunte-Ring 21, D - 76131 Karlsruhe

*Corresponding author, Email: tuerk@kit.edu, phone: +49 721 608 42330

In preparation

In this paper the adoption of CO_2 on MCM-41 and SBA-15 was investigated by an MSB. Therefore, six isotherms in a wide range of pressures (p = 0 – 25 MPa) and temperatures (T = 298 K – 353 K) were measured. The absolute amount adsorbed was calculated on the basis of the measured excess isotherms by the model of Menon. Furthermore, the iososteric heat of adsorption, which is an important thermodynamic parameter, was calculated for MCM-41 and SBA-15. It has been assumed that the adsorption of CO_2 on the investigated carrier materials is exothermic and caused by physisorption. In addition to this, it was found that the surface energy is distributed heterogeneously on both carrier materials. The investigated silica adsorbents are

suitable carrier materials for the deposition of active ingredients by the CPD process. With the obtained experimental data this paper gives an initial indication of the ternary adsorption behavior (SCF–active ingredient–carrier material) during the deposition step of the CPD process. It was concluded that six times more CO_2 adsorbed on the silica surface compared to ibuprofen molecules.

J. of Supercritical Fluids 132 (2018) 91–98

Contents lists available at ScienceDirect

The Journal of Supercritical Fluids

journal homepage: www.elsevier.com/locate/supflu

Influence of chemical nature of carrier materials on the dissolution behavior of racemic ibuprofen

Sarah Reiser[a], Miaotian Sun[b], Monika Johannsen[b], Michael Türk[a,*]

[a] Institute for Technical Thermodynamics and Refrigeration, Karlsruhe Institute of Technology (KIT), Engler-Bunte-Ring 21, D-76131 Karlsruhe, Germany
[b] Institute for Thermal Separation Processes (V8), Technical University Hamburg-Harburg, Eissendorfer Str. 38, D-21073 Hamburg, Germany

ARTICLE INFO

Article history:
Received 20 January 2017
Received in revised form 16 February 2017
Accepted 16 February 2017
Available online 22 February 2017

Keywords:
Racemic ibuprofen
$scCO_2$
Silica carrier
β-Cyclodextrin
Dissolution behavior
Bioavailability

ABSTRACT

The poor aqueous solubility of ibuprofen due to its hydrophobicity limits the bioavailability of the drug in the aqueous environment of the human body. Therefore particle deposition experiments were performed with ibuprofen and different carrier materials. Furthermore, the dissolution behavior of the untreated ibuprofen and the ibuprofen loaded carriers has been investigated at 310 K and pH = 2.0 and pH = 5.5.

The results of this investigation demonstrate that drug loadings up to 50 wt% drug onto silica materials could be achieved and that the drug loading increases nearly linear with increasing surface area of the silica materials. Furthermore, the study reveals that the highest dissolution rate was obtained with β-cyclodextrin and that the dissolution rate of all materials investigated increases with increasing pHvalue.

Note: The paper is formatted in the style of this work. Mistakes which were not recognized during the review process were corrected. Citations and References are according to journal style.

1. Introduction

One of the biggest challenges in pharmaceutical research is to improve the bioavailability of orally applied drugs since the bioavailability of these mainly poorly water soluble compounds depends strongly on the size, particle size distribution and morphology of the particles. It is well known that especially in case of anti-inflammatory drugs such as ibuprofen or naproxen, which are highly permeable but poorly water soluble (class II of the Biopharmaceutical Classification System [1]), the bio-absorption processes are strongly limited by the dissolution behavior in aqueous media. Due to this, there is an enormous need for the development of efficient technologies, which increase the dissolution behavior. Until today, several ways are known to improve the drug solubility and dissolution behavior, for example the use of surfactants or co-solvents, solid dispersions or lipid-based formulations [2]. Other

suitable ways to increase the solubility are complex formation with cyclodextrins or the reduction of the particle size [2, 3]. Conventional particle size reduction methods like milling, spray-/freeze drying or grinding show different disadvantages (broad particle size distribution, thermal or chemical degradation of the product etc.). To prevent these drawbacks new methods like processing with supercritical fluids (SCF) [4, 5] are under examination because they are characterized by liquid-like densities whereas mass transfer properties (diffusion and viscosity coefficients) resemble more those of gases [6]. CO_2 is considered as a suitable solvent since it is non-toxic, non-flammable, inexpensive, and allows the production of a solvent-free and dry product [4]. Despite this, the low critical data (T_c = 304 K, p_c = 7.4 MPa) allow moderate process conditions.

Reliable and well-known methods to form submicron or nano-sized particles are the rapid expansion of supercritical solutions (RESS) or various modifications such as CORESS (coprecipitation during rapid expansion of supercritical solutions), RESOLVE and RESSAS (rapid expansion of supercritical solutions into liquid or aqueous solutions) [5, 7 - 15]. Numerous investigations have shown that the particles formed by these processes enhance the dissolution rate of poorly soluble active ingredients in aqueous media at pH-values ranging from 2 to 7.4 [5, 8, 15].

However, submicron particles are difficult to handle and to include into solid dosage forms. Therefore, measures to incorporate poorly water-soluble drugs into appropriate solid dosages forms receive increased attention. In general, different techniques, such as kneading, grinding, co-precipitation, and freeze-drying, can be used to incorporate poorly water-soluble substances into a fast dissolving hydrophilic carrier. The drawbacks of these methods are high processing temperatures or the need to require the use of organic solvents that can be found as residual in the product. To overcome this, Türk et al. developed the controlled particle deposition process (CPD) [8, 16]. The key idea behind CPD is to dissolve the drug in a supercritical fluid, followed by permeation of the supercritical mixture into the pores of a carrier and subsequent precipitation of the drug inside the pores caused by a fast pressure drop in the system. Thus, the attractive feature of CPD is the possibility to produce solvent-free, drug loaded carrier particles in a single processing step. Among others, a suitable group of carrier material are cyclodextrins [16 - 21]. Besides the formation of inclusion complexes between drugs and cyclodextrins the supercritical impregnation of aerogels [22, 23], porous silicas [24, 25], polymers [26, 27], microcrystalline cellulose pellets and hydroxyethylcellulose [28], sugar cubes [28] etc. with drugs are used. Furthermore, coated tablets with optimized drug release profiles

can be produced. Thereto it must be pointed out that the choice of the carrier material and its interaction with the drug molecule determines whether accelerated or retarded dissolution behavior is achieved.

2. State of the art

The following two chapters give a short overview (that cannot pretend to be complete) of published knowledge classified according to two different concepts that are, among others, currently considered as a viable option to obtain an improved dissolution behavior of poorly soluble drugs in aqueous media.

2.1 Cyclodextrins (CDs)

CDs have indeed been explored extensively as additives in the pharmaceutical industry due to their unique ability to host and solubilize hydrophobic guest molecules including poorly water-soluble drugs. The most common cyclodextrins are α-, β- and γ-CD. These natural CDs consist of six, seven or eight glucopyranose units, and are characterized by a hydrophilic surface and a hydrophobic cavity. Due to their high water solubility and the ability to form inclusion complexes with hydrophobic molecules [3, 29] CDs are often used in different pharmaceutical applications.

Already in 1999 van Hees et al. started investigations about the preparation of a piroxicam/ β-CD complex [30]. By treating a physical mixture of both components with $scCO_2$ for 3 h ($T = 423$ K and $p = 45$ MPa) a complete inclusion of 94 % was achieved.

Numerous investigations on the formation of ibuprofen/CD inclusion complexes and their dissolution behavior have been performed in the past [8]. Charoenchaitrakool et al. have investigated the complex formation of methyl-β-CD and ibuprofen [19]. At $T = 308$ K and $p = 22$ MPa high ibuprofen loadings of 10.8 wt% that are close to a 1:1 complex (13.6 wt%) were reached. In comparison to a physical mixture the dissolution behavior of the $scCO_2$ treated mixture was significantly enhanced at pH = 5.5 during the initial period. This behavior can be explained by the amorphous nature of the product and its improved wettability.

The $scCO_2$ based impregnation of β-CD with ibuprofen was investigated by Türk et al. applying the CPD process at $T = 313$ K and $p = 25.7$ MPa [16]. High loadings up to 88 mol% were obtained. Furthermore, the dissolution behavior of an unprocessed physical mixture was compared to the CPD products and untreated

ibuprofen at pH 2.0 and 5.5. All inclusion complexes showed an improved dissolution behavior in comparison to untreated ibuprofen, whereas the CPD products offered the best dissolution behavior. Furthermore, CPD experiments performed by Hussein et al. showed an improved dissolution behavior of CPD impregnated β-CD [17]. Under process conditions of $T = 313$ K and $p = 24.4$ MPa ibuprofen loadings of 2.8 wt% on β-CD powder [17] and 17.4 wt% on β-CD granules [31] were obtained.

Tozuka et al. investigated the effect of different CDs, in particular β-CD, dimethyl-β-CD and trimethyl-β-CD, on the inclusion complex formation with racemic ibuprofen [18]. Within the process conditions investigated a complex formation occurred only with trimethyl-β-CD while no inclusion formation between ibuprofen and β-CD was observed after processing with $scCO_2$.

Banchero and Manna investigated the influence of lysine on the formation of ketoprofen/CD complexes [32]. In this study lysine was selected as co-solvent and yields up to 92 % on β-CD and 83 % on 2-hydroxypropyl-β-CD were achieved at $T = 343$ K and $p = 30$ MPa. Furthermore, the authors reported that increased drug loadings could be achieved if water was used as an additive during the impregnation step [32, 33].

2.2 Mesoporous silica carriers

The possibility to fine-tune the pore size, surface area and the surface chemistry in ordered mesoporous materials such as MCM-41 (i.e. Mobil Composition of Matter or Mobil Crystalline Materials) and SBA-15 (i.e. Santa Barbara Amorphous type material) enables the improvement of the dissolution behavior of poorly soluble drugs since these ordered materials easily liberate adsorbed hydrophobic compounds into aqueous media. However, until now, only a small number of studies investigated the SCF based deposition of drugs onto these mesoporous silica materials.

Ni et al. investigated the deposition of ibuprofen on SBA-15 at $T = 310$ K and $p = 17$ MPa [25]. Depending on the ibuprofen concentration in the $scCO_2$ high loadings up to 42 wt% were obtained. However, adding a small amount of ethanol (5 ml) to the system the drug loadings were decreased from 37 wt% to 8 wt%. Nevertheless, all samples showed a fast drug release in a simulated body fluid (SBF). Hillerström et al. used liquid CO_2 to impregnate MCM-41 with ibuprofen and this method led to a high drug content of 0.3 g ibuprofen/g SiO_2 [34]. If additives such as acetone, cyclohexane or methanol were used, the drug loadings were significantly decreased due to a competition between the H-bonds on the surface Si-OH-groups, the additive and the ibuprofen molecules. All samples showed an improved

dissolution performance in aqueous media compared to the untreated crystalline ibuprofen [35].

Li-Hong et al. impregnated MCM-41 with ibuprofen at $T = 313$ K and pressures ranging from $p = 20 - 30$ MPa [24]. Thereby the impregnation time was fixed to 2 h and drug loadings up to 38.6 wt% were achieved. Additional dissolution experiments were performed at $T = 310$ K and the results showed that after 15 min a drug release of 50 % and of 90 % after 60 min was reached. In comparison thereto samples, which were prepared by the organic solvent immersion method (OSIM) reached lower loadings (15.1 wt%) but showed an improved dissolution behavior. The authors explained this result by the differences in the drug location inside the pores. Thereby they assumed that the molecules that were deposited by SCF impregnation are deposited deeper inside the pores than those molecules deposited by OSIM. The latter case facilitates a faster transfer of the molecules from the silica matrix to the aqueous solution that leads to a fast drug release.

Charnay et al. studied the influence of different solvents (dimethyl sulfoxide, methyl methacrylate, dimethylformamide, ethanol, and hexane) and loading procedures on the deposition of ibuprofen in mesoporous MCM-41 [36]. The experiments showed that a decrease of the solvent polarity results in an increase of drug loading, that ibuprofen could be loaded with a high efficiency into MCM-41 (up to 0.59 g/g) and that the loading extent is influenced by the loading procedure. Additional dissolution experiments performed in a simulated gastric (pH = 1.2) and intestinal fluid (pH = 7.4) showed a rapid and nearly 90 % release of the ibuprofen molecules after 60 min.

Vallet-Regi et al. investigated the effect of pore sizes on drug loading and dissolution behavior [37]. In these investigations MCM-41 materials were synthesized by using two different surfactants (C16TAB and C12TAB), which led to two different pore sizes. Independent from the surfactants a maximum ibuprofen loading of 30 wt% was achieved while a slow ibuprofen dissolution rate, i.e. around 80 % release after 3 days in a simulating body fluid (SBF) solution, was observed.

Functionalizing the MCM-41 pores with different silane derivates led to ibuprofen loadings up to 20 wt% as reported by Muñoz et al. [38]. The results of dissolution experiments showed that the modification of MCM-41 led to a delayed dissolution behavior compared with untreated ibuprofen. Szegedi et al. functionalized SBA-15 and MCM-41 with amino groups prior drug loading [39]. In case of MCM-41 the functionalization led to higher ibuprofen loadings (31 wt% compared to 15 wt%) and faster dissolution rates in a SBF solution compared to the not functionalized material.

However, the opposite behavior was observed for SBA-15 (18 wt% compared to 35 wt%). Hwang et al. investigated the effects of SBA-15 surface functionalization with amine, diamine and sulfonic acid on ibuprofen delivery [40]. The experimental results showed that the fastest ibuprofen release was obtained with carriers that are modified with the sulfonic acid groups. Horcajada et al. investigated the influence of different pore sizes of MCM-41 matrices on ibuprofen release [41]. The obtained results showed that the amount of ibuprofen adsorbed from a hexane solution is directly related with the pore size of MCM-41. Furthermore, the release of ibuprofen in a SBF solution increased with increasing pore diameter. A similar result was obtained using SBA-15 as carrier material as reported by Yin and Liang [42].

Gao et al. compared the influence of pore channel structure of ordinary MCM-41 and SBA-15 material with that of bimodal mesoporous silica (BMM) on carrier loading and drug release [43]. An ethanol solution was used to impregnate these carrier materials with ibuprofen. In case of BMM the highest drug loadings up to 25 wt% and, compared with ordinary MCM-41, improved dissolution behavior was reached. This result might be caused by the short channel length and large pore diameter of the BMM material. Nevertheless, the best ibuprofen release was observed for SBA-15, which might be the result of relatively large pore diameter in combination with the branched open pore structure.

Azaïs et al. reported that solid-state NMR analyses of ibuprofen encapsulated in MCM-41 revealed an original physical state of ibuprofen that does not behave at ambient temperature as a true solid, but exhibits an extreme mobility inside the pores [44]. The authors concluded from these results that incipient wetness impregnation leads to a weak interaction between ibuprofen and the silica surface that favors a fast drug release from MCM-41 in aqueous media.

Investigations performed by Shen et al. showed that co-spray drying ibuprofen with mesoporous SBA-15 particles enabled the formation of stable amorphous ibuprofen with a significant enhancement in the dissolution rate as compared with original crystalline ibuprofen [45]. DSC analysis showed that up to an ibuprofen loading of 50 wt% no endothermic peak around $T = 350$ K, caused by the melting of crystalline ibuprofen, was observed. This result confirms in agreement with the results of XRD measurements the amorphous state of spray-dried ibuprofen. Mellaerts et al. investigated the influence of different loading methods i.e. adsorption from solution, incipient wetness impregnation, and heating of a mixture of drug and SBA-15 powder [46]. The results of their investigations showed, that itraconazole was successfully introduced into the pores of SBA-15 using incipient wetness impregnation and

adsorption from dichloromethane. In opposite thereto, ibuprofen was successfully loaded onto SBA-15 using the melt method. Furthermore, both drugs showed a fast release from SBA-15 when exposed to simulated gastric fluid (SGF).

Thus, from the large number of experimental results published in literature one could conclude that besides the SCF based method, i.e. the CPD process, different "low-pressure" processes such as co-precipitation [17, 47, 48], freeze-drying [17, 48, 49], spray-drying [48, 50], solution immersion [31, 51], kneading [51, 52] or wet granulation [53, 54] are used to form drug delivery systems with improved dissolution behavior. Quite often each of these methods lead to higher drug loadings compared to the SCF based methods. Furthermore, compared to the unprocessed drug and the untreated drug/carrier physical mixture, improved dissolution behavior can be attained. Nevertheless, the highest dissolution rate can be achieved by using the SCF based formation of inclusion complexes.

The objectives of this study are to impregnate different powdery carriers with ibuprofen by using the CPD process and to investigate the influence of substrate properties e.g. specific surface area on the ibuprofen loading and the dissolution behavior of the loaded carrier.

3. Experimental

3.1 Materials

CO_2 (Linde AG) was chosen as supercritical solvent to load different carrier materials by CPD. In the present investigation racemic ibuprofen (Knoll Pharmaceuticals) was used as an example of a drug whose dissolution rate and therewith bioavailability is limited by its poor water-solubility. Ibuprofen is most often prescribed to treat arthritis, menstrual symptoms, fever and pains. The side effects and required application rate of ibuprofen can be reduced by improving its effectiveness i.e. increasing the dissolution rate in aqueous media. Racemic ibuprofen contains S-(+)-ibuprofen and R-(-)-ibuprofen molecules, generally in equal amounts. Furthermore, it is worthy to notice that the solubility of crystalline ibuprofen in aqueous media depends strongly on the pH-value of the dissolution media. In the range from pH = 1.5 – 4.0 the ibuprofen solubility is nearly constant at 0.06 g/dm^3, thereafter a rapid increase up to 27 g/dm^3 at pH = 7.0 is observed [55]. Two commercially available silica carriers (SBA-15 (ACS Materials) and MCM-41 (Sigma

Aldrich)) and two self-synthesized, with S-(+)-ibuprofen functionalized Kromasil® carriers (Kromasil-100 and Kromasil-300) were loaded with ibuprofen.

Self-synthesized silica carriers based on surface modification of chromatographic silica gel by adding ligands through covalent bonding were tested for an enantiomeric separation. Two commercial chromatographic silica gels Kromasil 100-5-SIL and 300-5-SIL with a particle diameter of 5 µm and pore diameters of 100 and 300 Å, respectively, were chosen as a basis for the surface modification. In order to immobilize S-(+)-ibuprofen onto the surface of the silica gel through covalent bonding, a two-step method was applied [56]. In the first step, a spacer, 3-glycidoxypropyltrimetoxy-silane (GLYMO) was added onto the surface of silica by a salinization reaction. In the second step, S-(+)-ibuprofen was added onto the silica through the spacer by a reaction between epoxy ring and carboxylic group. In order to evaluate the immobilization of S-(+)-ibuprofen on commercial silica gel by this method, the functionalization by S-(+)-ibuprofen on the product was calculated from the experimentally determined carbon content.

Some important information about the carrier materials is listed in Tab. 1. Thus, from the values given in Tab. 1 it follows that the amount of S-(+)-ibuprofen on the surface of Kromasil-300 (3.3 µmol/m^2) is approximately 4 times higher compared to Kromasil-100 (0.8 µmol/m^2).Furthermore, β-CD (Cavamax W7 Pharma, Wacker Chemie AG) was chosen as another suitable carrier due to its efficiency of drug complexation and relatively low cost.

To simulate the gastric fluid (pH = 2.0) hydrochloric acid (0.2 M) and potassium chloride (both Carl Roth) were used. Sørensen buffers which were used in HPLC analysis and in the dissolution experiments at pH = 5.5 were made with distilled water (0.055 µS), potassium dihydrogen phosphate (Sigma Aldrich) and sodium hydrogen phosphate (Carl Roth). Furthermore, acetonitrile (ACN, Sigma Aldrich) was used to perform the HPLC analysis. All materials and solvents were of the purest grade available and used as received without further purification.

Tab. 1 Selected properties of the carrier materials.

	Specific surface area A_{BET} m^2/g	**Pore volume** V_P cm^3/g	**Pore diameter** D_P nm	**Functionalization** mol S-(+)-ibu/kg
MCM-41	1030	1.09	3 - 6	-
SBA-15	920	0.84	3.5 – 4.5	-
Kromasil-100	281	0.74	10	0.23
Kromasil-300	63	0.72	30	0.21

3.2 Experimental set up

3.2.1 Controlled particle deposition process

As described in detail elsewhere, all CPD experiments were carried out using a static technique [5, 8, 16, 17, 31]. Thereby the drug and the carrier material were placed in two separate sample containers in a high-pressure cell (see Fig. 1). Then the system was evacuated for 2 h in order to remove atmospheric moisture and air. Thereafter the required amount of CO_2 was filled into the high-pressure cell and heated to the desired temperature of $T = 313$ K resulting in a pressure of $p = 15$ MPa. To ensure a good mixing of the supercritical phase a magnetic stirrer (300 rpm) was placed between the containers. The impregnation time was set to 72 h to guarantee enough time for equilibration. To prevent crystallization of surplus ibuprofen which is still dissolved in the supercritical phase the high pressure cell was flushed with N_2 at $p = 16$ MPa for 20 s at the end of the experiment and was then quickly depressurized.

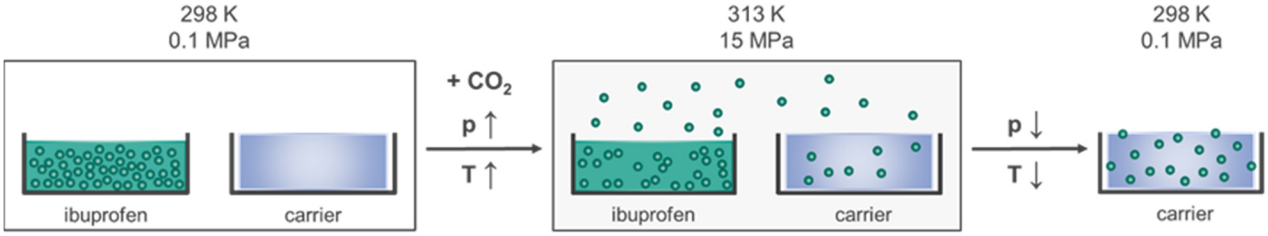

Fig. 1 Schematic diagram of the CPD impregnation mechanism.

3.2.2 Dissolution experiments

The experiments were performed according to the food and drug administration (FDA) IV standards [57]. Therein it is recommended to test the dissolution of drugs in aqueous buffers in a pH range of 1.0 – 7.4 at $T = 310$ K. It is recommended by the FDA to perform the dissolution experiments considering so-called sink conditions that are equivalent to $1/3^{rd}$ to $1/5^{th}$ of the saturated solubility at corresponding pH-value [55]. In the context of this work $1/3^{rd}$ of the saturated solubility was used as sink conditions. Thus, at pH = 2.0 a sample quantity of around 5 mg ibuprofen is needed. In order to enable analyzing small sample quantities the dissolution experiments were performed in a "down-scaled" USP apparatus 2 (see Fig. 2) according to the recommendations by Klein and Shah [58] that were verified by an AnsysFluent-Simulation of the flow and velocity profile in the glass vessel at a stirring speed of the paddle of 100 rpm [59].

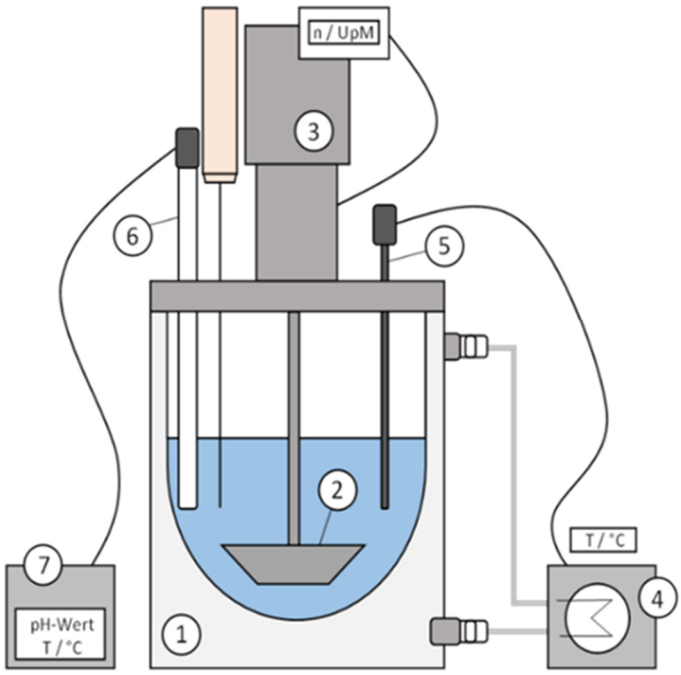

Fig. 2 Schematic diagram of the USP apparatus 2 according to Klein and Shah [58].

In brief, the experimental set up consists of the self-made jacketed glass vessel (1), paddle mixer (2) and motor (3). A thermostat (4) including a Pt-100 temperature sensor (5) was used for tempering the dissolution media. For the continuous determination of the pH-value of the dissolution media a pH electrode (6) (Mettler-Toledo) in combination with a Sevenmulti^{TM} (7) was used.

The dissolved amount of ibuprofen at a certain time can be expressed by the following equation:

$$D(t)/[\%] = \frac{c_t}{c_0} \cdot 100 \tag{1}$$

In Eq.(1) c_0 is defined as the initial concentration defined by the sink conditions and c_t corresponds to the ibuprofen concentration in the dissolution media at a well-defined time t. All dissolution experiments were performed threefold.

3.3 Characterization methods

Differential scanning calorimetry (DSC, SETARAM MicroDSC VII) was used for physical characterization (i.e. melting point) of the unprocessed and the processed materials. The sample (~5 mg/run) was heated in a standard pan under a nitrogen gas flow. A heating rate of 2 K/min was used in the temperature range from $T = 293$ K to 393 K.

Powder X-ray diffraction (XRD) pattern of the unprocessed substances and the loaded carrier materials were determined by using a STADI-MP diffractometer (Stoe & Cie. GmbH) with Ge-monochromatized Cu-$K_{\alpha 1}$ radiation ($\lambda = 1.54060$ Å) in a 2Θ range of 2 – 91.985° using a step size of 0.015° (1200 s).

In order to determine the quantity of ibuprofen deposited on the carrier material a certain amount was dissolved in acetonitrile (ACN) and stored in an overhead shaker for 25 h. The samples were centrifuged afterwards and the ibuprofen concentration of the permeate was analyzed by high-pressure liquid chromatography (HPLC) using an Agilent HP 1100 Series (Agilent Technologies). Samples were injected into a LiChrosphere 100-5 RP18 (125 × 4 mm) column (Agilent Technologies) with a flow rate of 1 ml/min of a 70: 30 Sørensen-buffer (pH = 7.1):ACN liquid phase. Two different diode array detection (DAD) signals (210.4 nm; reference: 360/100 nm and 230.4 nm; reference: 360/100 nm) were evaluated and the analysis of the ibuprofen quantity was repeated twice. The same analyzing method was used for determination of the ibuprofen concentration in the dissolution media.

4. Experimental results

Discussing the influence of CPD processing conditions on the substances investigated, it is advisable to distinguish the following nomenclature. In case of the raw material prior to any treatment the term “untreated” and of the CPD product the term “CPD” will be used in the subsequent paragraphs, tables and figures.

4.1 Loading

The results of the ibuprofen loadings on the different substrates caused by CPD impregnation are listed in Tab. 2 and depicted in Fig. 3.

Apparently similar loadings were achieved for the commercial available carriers MCM-41 and SBA-15. This result can be explained due to the similar specific surface area and pore size (MCM-41: $A_{BET} = 1030$ m^2/g, $D_P = 3 - 6$ nm, SBA-15: $A_{BET} = 920$ m^2/g, $D_P = 3.5 - 4.5$ nm). Caused by the high specific surface area of these carrier materials ibuprofen loadings of approximately 50 wt% were obtained.

Tab. 2 Ibuprofen loadings on different carrier materials obtained by HPLC.

		MCM-41	**SBA-15**	**Kromasil-100**	**Kromasil-300**	**ß-CD**
Loading	wt%	49.1 ± 0.5	50.0 ± 0.5	20.6 ± 1.2	10.2 ± 1.4	2.25 ± 0.04

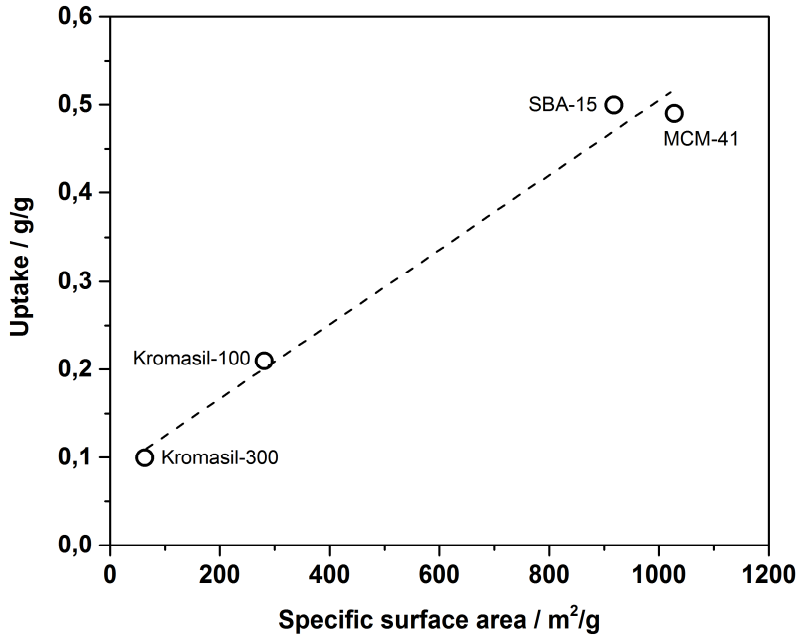

Fig. 3 Uptake of ibuprofen vs. specific surface area of the different carrier materials.

Similar loadings of 42 wt% were attained by Ni et al. [25] who investigated the deposition of ibuprofen into ordered mesoporous silica SBA-15 at $p = 17$ MPa and $T = 310$ K. Furthermore, it was found out by Ni et al. and by Charoenchaitrakool et al. that the increase of drug concentration in CO_2 leads to higher drug loadings [19, 25]. In case of the self-synthesized carrier materials Kromasil-100 ($A_{BET} = 281$ m^2/g) and Kromasil-300 ($A_{BET} = 63$ m^2/g) lower ibuprofen loadings of 20.6 wt% and 10 wt% were achieved. It is illustrated in Fig. 3 that increasing the specific surface area resulted in an increased drug loading of the carrier material. Thus, the results depicted in Fig. 3 suggest a linear relationship between specific surface area and obtained drug loading within the range of the operating conditions studied.

In contrast to the silica based substrates the ibuprofen loading of 2.25 wt% on β-CD is low but it is still in good agreement to other results published in literature [17]. However, in comparison to a conventional organic solution immersion method the obtained loadings are low. One reason is that β-CD is insoluble in $scCO_2$ and therefore the only way for ibuprofen molecules to form inclusion complexes is to penetrate into the cavity of the β-CD. Thereby it should be considered that it is difficult for ibuprofen molecules (height: 5 Å, width: 7.6 Å; length: 11.5 Å) [44] to form inclusion complexes since the average size of the β-CD cavity is around 6 – 7.9 Å [60]. In opposite thereto, if β-CD is dissolved in its molecular form in a liquid solution,

the formation of inclusion complexes is easier to realize and therefore higher loadings can be obtained with the organic solution immersion technique.

4.2 DSC and XRD analyses

DSC analyses were carried out for untreated ibuprofen, the raw carrier materials and the loaded carrier materials. As shown in Fig. 4, pure crystalline ibuprofen exhibits a sharp endothermic melting peak around $T = 350$ K. In contrast thereto, the DSC curves of the different CPD products show no endothermic peak at $T = 350$ K, indicating a more or less complete encapsulation of the drug inside of the carrier materials [16]. Nevertheless, it is important to notice that the absence of the endothermic peak at $T = 350$ K might be the result of the transformation of the crystalline ibuprofen into the amorphous state. In Fig. 5 the XRD pattern of untreated ibuprofen and carrier materials as well as of the drug loaded carrier materials are depicted. In agreement with the DSC results the XRD pattern of the untreated ibuprofen confirms its crystalline structure. Similarly, it is obvious that the XRD pattern of the CPD complex shows peaks similar to those of untreated β-CD. Again, the absence of the ibuprofen XRD patterns indicates the formation of an inclusion complex in which ibuprofen is entrapped in the CD cavity. Furthermore, it can be seen that the XRD patterns of the untreated and drug loaded two Kromasil,

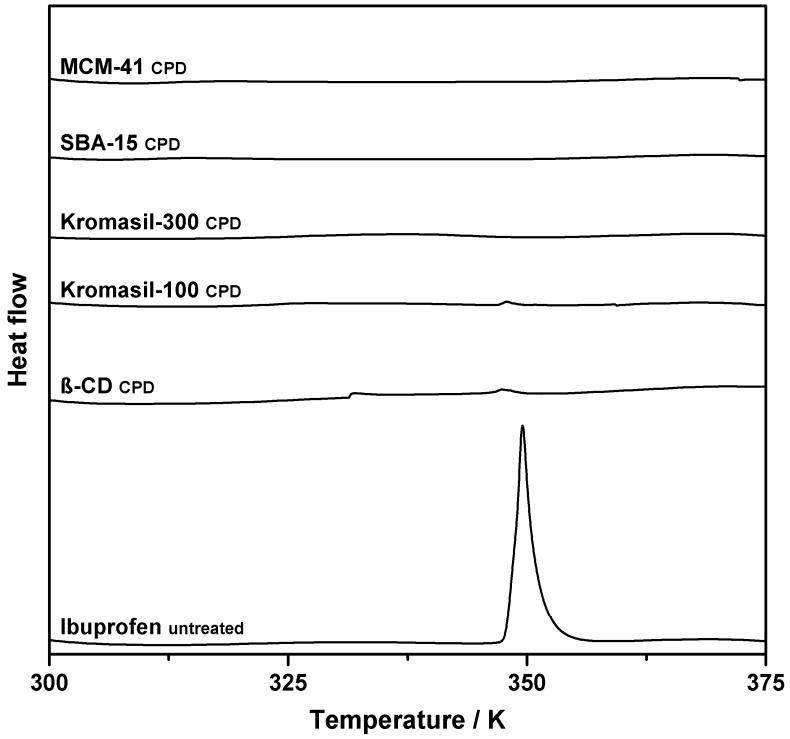

Fig. 4 DSC results of the loaded carrier materials and for comparison of untreated ibuprofen.

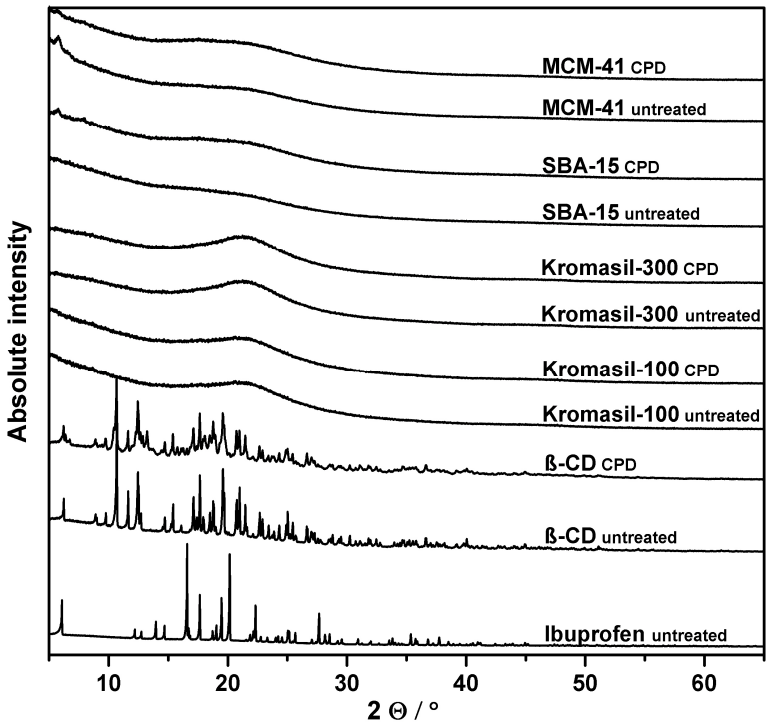

Fig. 5 XRD pattern of the loaded carrier materials and the original raw materials and for comparison of untreated ibuprofen.

MCM-41 and SBA-15 samples do not show any characteristic peak of ibuprofen. Thus, these results indicate that the vast majority of the drugs were loaded inside the pores of the porous carriers and that they are amorphous. These findings are in accordance with the results of previous studies published in literature (e.g. [16, 17, 19, 22, 30, 31, 61]).

4.3 Dissolution behavior

The dissolution experiments were performed in an apparatus according to FDA standards. In Figs. 6 and 7 the drug release profiles of the loaded carrier materials as well as the dissolution of untreated ibuprofen at pH = 2.0 and 5.5 are depicted. Different kinetic models were used to fit the experimental dissolution curves and the so-called "1st-order model" [62] enables the best description of the experimental results. In this model the dissolution behavior *D(t)* is described by the following equation:

$$D(t) = D_{100} \cdot (1 - e^{-k \cdot t}) \tag{2}$$

In Eq.(2) k is defined as the dissolution constant and D_{100} is an adjustable parameter to describe an incomplete dissolution behavior i.e. lower than 100 %. The fitted parameters for the different ibuprofen loaded carrier materials and the untreated

Tab. 3 Correlation results for the dissolution behavior of untreated ibuprofen and ibuprofen loaded carrier materials using the 1st-order model according Eq.(2).

	pH = 2.0			**pH = 5.5**		
	k 1/s	***D*$_{100}$** %	**St.dev** %	***k*** 1/s	***D*$_{100}$** %	**St.dev** %
Ibuprofen	0.0213	37.5	0.7	0.0398	89.5	0.4
MCM-41	0.1810	26.4	0.7	0.4858	82.0	0.6
SBA-15	0.2326	29.3	0.4	0.8311	81.5	0.7
Kromasil-100	0.4776	28.0	2.6	0.3779	85.9	0.7
Kromasil-300	0.0316	20.8	0.3	0.0401	29.9	0.1
ß-CD	3.4189	87.1	0.1	1.1582	98.4	0.3

ibuprofen at pH = 2.0 and 5.5 are summarized in Tab. 3. More details about the different concepts and methods used for modeling and comparison of dissolution profiles can be found in literature, e.g. see [62].

In general, the comparison of the results depicted in Fig. 6 and 7 show that the dissolution rate of all materials investigated increases with increasing pH-value. This can be explained by the fact that the ibuprofen solubility is strongly pH-dependent and it displays a very low aqueous solubility at pH-values below and close pH = 4 [55]. Hence the increase of the pH-value from pH = 2.0 to pH = 5.5 leads to a higher equilibrium solubility of ibuprofen in aqueous media and therewith in an improved dissolution behavior. The effect of this can be observed in the dissolution profiles of the untreated ibuprofen and of the drug loaded MCM-41, SBA-15 and Kromasil-100 materials. In opposite thereto, the dissolution of ibuprofen from Kromasil-300 seems to be less pH-value dependent. After 120 min, the dissolved amount of untreated ibuprofen increases from 37.5 % at pH = 2.0 to 89.5 % at pH = 5.5. A similar dissolution behavior with dissolved amounts in the range from 26 % to 29 % at the lower and from 82 % to 86 % at the higher pH-value were obtained for ibuprofen loaded Kromasil-100, MCM-41 and SBA-15, while in case of Kromasil-300 a significantly lower dissolution behavior with dissolved amounts of 21 % at pH = 2.0 and 30 % at pH = 5.5 was observed.

In this context it is worthy to notice that, in accordance with results reported in literature, for both untreated ibuprofen and Kromasil-300, aggregation and therewith a low wettability of the powder during the dissolution tests was observed. Such a behavior might be caused by the hydrophobic nature of ibuprofen [11, 19].

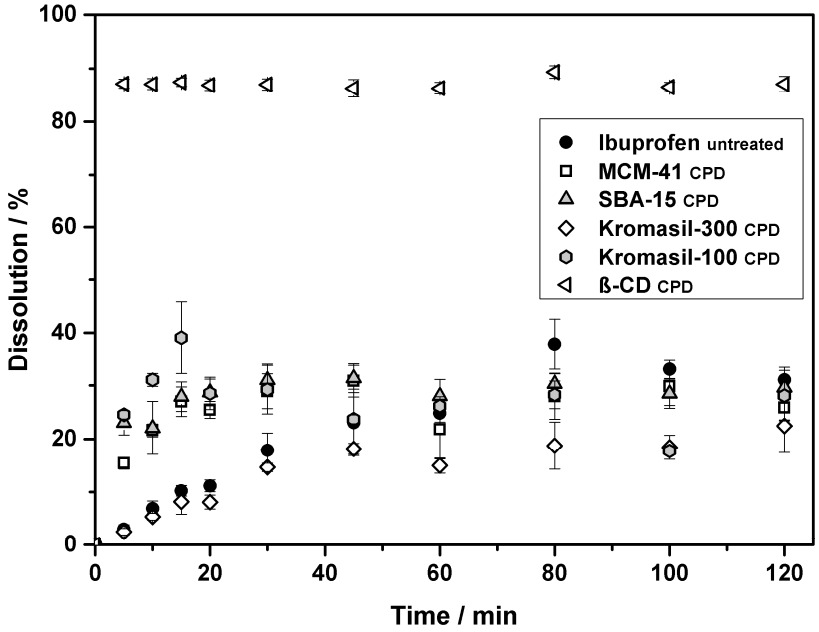

Fig. 6 Dissolution profiles of ibuprofen and different ibuprofen/carrier formulations at pH = 2.0.

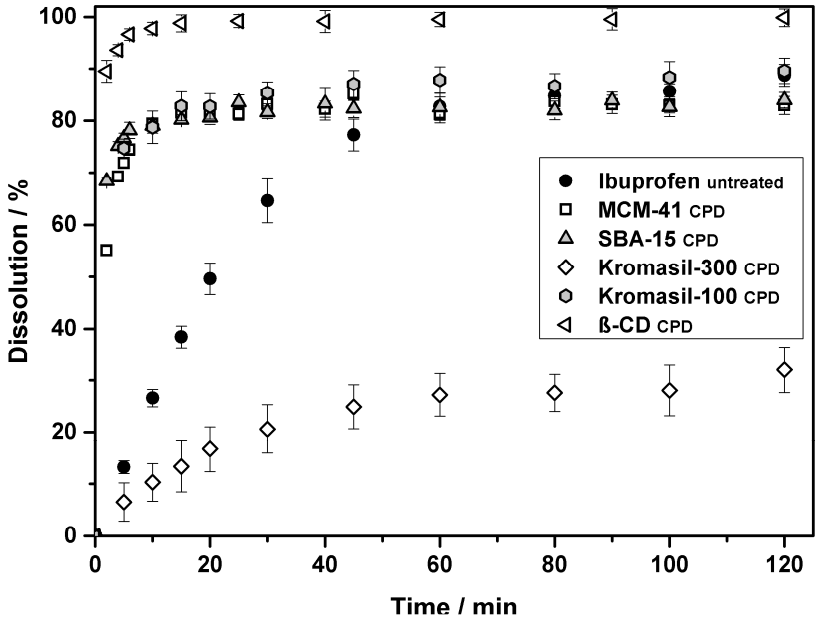

Fig. 7 Dissolution profiles of ibuprofen and different ibuprofen/carrier formulations at pH = 5.5.

A significantly faster and higher drug release was observed for the ibuprofen loaded β-CD samples. At both pH-values the maximum value of 87 % and of 98 % was reached within the first 10 min. This significant enhancement in the dissolution rate of the ibuprofen/β-CD complex could be attributed to the amorphous character of the complex, the hydrophilic surface of β-CD that leads to a high solubility in water

(18.5 g/dm^3 at $T = 298$ K) [60] and therewith the improved wettability of the hydrophobic drug [5, 8, 11, 16].

5. Conclusion

The poor aqueous solubility of ibuprofen due to its hydrophobicity limits the bioavailability of the drug in the aqueous environment of the human body. Therefore, CPD experiments were performed with ibuprofen and different carrier materials. Furthermore, the dissolution behavior of the untreated ibuprofen and the ibuprofen loaded carriers has been investigated at $T = 310$ K and pH = 2.0 and pH = 5.5.

The results of this investigation demonstrate that the CPD process is an efficient method for the formation of inclusion complexes and the deposition of drugs inside the pores of the different porous carriers without using any additional substances. Furthermore, it has been shown that drug loadings up to 50 wt% drug onto silica materials could be achieved and that the drug loading increases nearly linear with increasing surface area of the silica materials.

The obtained CPD products showed different dissolution behavior. The highest dissolution rate has been achieved for the ibuprofen/β-CD complex while MCM-41, SBA-15 and Kromasil-100 showed an improved dissolution behavior due to the probably amorphous state of the drug compared to untreated crystalline ibuprofen. In opposite thereto Kromasil-300 tended to aggregation during testing and showed a minor dissolution behavior that might be the result of inefficient wetting. Nevertheless, materials such as Kromasil-300 can be used as carrier materials when a delayed drug application such as controlled release is required.

Thus, CPD enables the formation of a ready to use solid dosage form with predictable, uniform drug content and improved dissolution behavior and process improvement because it contains only a single deposition step that combines several steps of conventional processes.

In summary, the CPD process is a suitable and innovative method for the preparation of dissolution enhancing solid dosage forms without using any additional auxiliary materials.

Acknowledgements

This work was supported by the grants TU 93/18-1 and JO 339/8-1 of the DFG (Deutsche Forschungsgesellschaft), which is gratefully acknowledged. Furthermore, the authors thank Dr. Jens Möllmer, Institut für Nichtklassische Chemie e.V. (INC) Leipzig, for the determination of the specific surface area, pore volume and diameter of MCM-41, SBA-15 and β-CD as well as Mr. Philipp Even for conducting parts of the dissolution measurements.

References

[1] G.L. Amidon, H. Lennernäs, V.P. Shah, J.R. Crison, A theoretical basis for a biopharmaceutic drug classification: the correlation of in vitro drug product dissolution and in vivo bioavailability, Pharm. Res. 12(3) (1995) 413–420.

[2] H.D. Williams, N.L. Trevaskis, S.A. Charman, R.M. Shanker, W.N. Charman, C.W. Pouton, C.J. Porter, Strategies to address low drug solubility in discovery and development, Pharmacol. Rev. 65(1) (2013) 315–499.

[3] M.M. Nitalikar, D.M. Sakarkar, P.V. Jain, The cyclodextrins: a review, J. Curr. Pharm. Res. 10(2) (2012) 1–6.

[4] J. Jung, M. Perrut, Particle design using supercritical fluids: literature and patent survey, J. Supercrit. Fluids 20 (2001) 179–219.

[5] M. Türk, Particle Formation with Supercritical Fluids – Challenges and Limitations, first ed., Elsevier, 2014.

[6] G.M. Schneider, Physicochemical aspects of fluid extraction, Fluid Phase Equilibr. 10(2) (1983) 141–157.

[7] H.J. Martin, Charakterisierung von schwerlöslichen Arzneistoff-Nanopartikeln hergestellt durch das RESS-Verfahren zur Verbesserung der Bioverfügbarkeit (PhD thesis), Eberhard-Karls-Universität Tübingen, 2003.

[8] M. Türk, Manufacture of submicron drug particles with enhanced dissolution behavior by rapid expansion processes, J. Supercrit. Fluids 47 (2009) 537–545.

[9] M. Türk, D. Bolten, Formation of submicron poorly water-soluble drugs by rapid expansion of supercritical solution (RESS): results for naproxen, J. Supercrit. Fluids 55 (2010) 778–785.

[10] M. Türk, Erzeugung von organischen Nanopartikeln mit überkritischen Fluiden (Professorial Dissertation), Universität Karlsruhe (TH), 2001.

[11] M. Charoenchaitrakool, F. Dehghani, N.R. Foster, H.K. Chan, Micronization by rapid expansion of supercritical solutions to enhance the dissolution rates of poorly water-soluble pharmaceuticals, Ind. Eng. Chem. Res. 39(12) (2000) 4794–4802.

[12] N.R. Foster, F. Dehghani, M. Charoenchaitrakool, B. Warwick, Application of dense gas techniques for the production of fine particles, AAPS PharmSciTech 5 (2003) 105–111.

[13] M. Türk, B. Helfgen, P. Hils, R. Lietzow, K. Schaber, Micronization of pharmaceutical substances by rapid expansion of supercritical solutions (RESS): experiments and modelling, Part. Part. Syst. Charact. 19(5) (2002) 327–335.

[14] M. Türk, R. Lietzow, Formation and stabilization of submicron particles via rapid expansion processes, J. Supercrit. Fluids 45 (2008) 346–355.

[15] M. Perrut, J. Jung, F. Leboeuf, Enhancement of dissolution rate of poorly-soluble active ingredients by supercritical fluid processes Part I: micronization of neat particles, Int. J. Pharm. 288 (2005) 3–10.

[16] M. Türk, G. Upper, M. Steurenthaler, Kh. Hussein, M.A. Wahl, Complex formation of Ibuprofen and β-Cyclodextrin by controlled particle deposition (CPD) using SC-CO_2, J. Supercrit. Fluids 39 (2007) 435–443.

[17] K. Hussein, M. Türk, M.A. Wahl, Comparative evaluation of ibuprofen/β-cyclodextrin complexes obtained by supercritical carbon dioxide and other conventional methods, Pharm. Res. 24(3) (2007) 585–592.

[18] Y. Tozuka, T. Fujito, K. Moribe, K. Yamamoto, Ibuprofen-Cyclodextrin inclusion complex formation using supercritical carbon dioxide, J. Incl. Phenom. Macrocycl. Chem. 56 (2006) 33–37.

[19] M. Charoenchaitrakool, F. Dehghani, N.R. Foster, Utilization of supercritical carbon dioxide for complex formation of ibuprofen and methyl-ß-cyclodextrin, Int. J. Pharm. 239 (2002) 103–112.

[20] M. Banchero, S. Ronchetti, L. Manna, Characterization of ketoprofen/methyl-β-cyclodextrin complexes prepared using supercritical carbon dioxide, J. Chem. 2013 (2013) 1–8.

[21] J. He, W. Li, Preparation of borneol-methyl-ß-cyclodextrin inclusion complex by supercritical carbon dioxide processing, J. Incl. Phenom. Macrocycl. Chem. 65 (2009) 249–256.

[22] C.A. García-González, I. Smirnova, Use of supercritical fluid technology for the production of tailor-made aerogel particles for delivery systems, J. Supercrit. Fluids 79 (2013) 152–158.

[23] M. Betz, C.A. García-González, R.P. Subrahmanyam, I. Smirnova, U. Kulozik, Preparation of novel whey protein-based aerogels as drug carriers for life science applications, J. Supercrit. Fluids 72 (2012) 111–119.

[24] W. Li-Hong, C. Xin, X. Hui, Z. Li-Li, H. Jing, Z. Mei-Juan, L. Jie, L. Yi, L. Jin-Wen, Z. Wei, C. Gang, A novel strategy to design sustained-release poorly water-soluble drug mesoporous silica microparticles based on supercritical fluid technique, Int. J. Pharm. 454 (2013) 135–142.

[25] M. Ni, Q.-Q. Xu, J.-Z. Yin, Preparation of controlled release nanodrug ibuprofen supported on mesoporous silica using supercritical carbon dioxide, J. Mater. Res. 27(22) (2012) 2902–2910.

[26] Y.A. Hussain, C.S. Grant, Ibuprofen impregnation into submicron polymeric films in supercritical carbon dioxide, J. Supercrit. Fluids 71 (2012) 127–135.

[27] S.G. Kazarian, G.G. Martirosyan, Spectroscopy of polymer/drug formulations processed with supercritical fluids: in situ ATR-IR and Raman study of impregnation of ibuprofen into PVP, Int. J. Pharm. 232 (2002) 81–90.

[28] R.S. Wischumerski, M. Türk, M.A. Wahl, Direct drug loading into preformed porous solid dosage units by the controlled particle deposition (CPD), a new concept for improved dissolution using SCF-technology, J. Pharm. Sci. 97(10) (2008) 4416–4424.

[29] T. Loftsson, D. Duchêne, Cyclodextrins and their pharmaceutical applications, Int. J. Pharm. 329 (2007) 1–11.

[30] T. Van Hees, G. Piel, B. Evrard, X. Otte, L. Thunus, L. Delattre, Application of supercritical carbon dioxide for the preparation of a piroxicam-β-cyclodextrin inclusion compound, Pharm. Res. 16(12) (1999) 1864–1870.

[31] K. Hussein, M. Türk, M.A. Wahl, Drug loading into β-cyclodextrin granules using a supercritical fluid process for improved drug dissolution, Eur. J. Pharm. Sci. 33(3) (2008) 306–312.

[32] M. Banchero, L. Manna, The use of lysine to enhance the supercritical complexation of ketoprofen and cyclodextrins, J. Supercrit. Fluids 67 (2012) 76–83.

[33] A. Bounaceur, E. Rodier, J. Fages, Maturation of a ketoprofen/β-cyclodextrin mixture with supercritical carbon dioxide, J. Supercrit. Fluids 41 (2007) 429–439.

[34] A. Hillerström, J. van Stam, M. Andersson, Ibuprofen loading into mesostructured silica using liquid carbon dioxide as a solvent, Green Chem. 11 (2009) 662–667.

[35] A. Hillerström, M. Andersson, J. Samuelsson, J. van Stam, Solvent strategies for loading and release in mesoporous silica, Colloid Interface Sci. Commun. 3 (2014) 5–8.

[36] C. Charnay, S. Bégu, C. Tourné-Péteilh, L. Nicole, D.A. Lerner, J.M. Devoisselle, Inclusion of ibuprofen in mesoporous templated silica: drug loading and release property, Eur. J. Pharm. Biopharm. 57(3) (2004) 533–540.

[37] M. Vallet-Regí, A. Rámila, R.P. del Real, J. Pérez-Pariente, A new property of MCM-41: drug delivery system, Chem. Mater. 13 (2001) 308–311.

[38] B. Muñoz, A. Rámila, J. Pérez-Pariente, I. Díaz, M. Vallet-Regí, MCM-41 organic modification as drug delivery rate regulator, Chem. Mater. 15 (2003) 500–503.

[39] A. Szegedi, M. Popova, I. Goshev, J. Mihály, Effect of amine functionalization of spherical MCM-41 and SBA-15 on controlled drug release, J. Solid State Chem. 184 (2011) 1201–1207.

[40] D.H. Hwang, D. Lee, H. Lee, D. Choe, S.H. Lee, K. Lee, Surface functionalization of SBA-15 particles for ibuprofen delivery, Korean J. Chem. Eng. 27(4) (2010) 1087–1092.

[41] P. Horcajada, A. Rámila, J. Pérez-Pariente, M. Vallet-Regí, Influence of pore size of MCM-41 matrices on drug delivery rate, Microporous Mesoporous Mater. 68 (2004) 105–109.

[42] Z. Jin, H. Liang, Effects of morphology and structural characteristics of ordered SBA-15 mesoporous silica on release of ibuprofen, J. Dispers. Sci. Technol. 31 (2010) 654–659.

[43] L. Gao, J. Sun, L. Zhang, J. Wang, B. Ren, Influence of different structured channels of mesoporous silicate on the controlled ibuprofen delivery, Mater. Chem. Phys. 135 (2012) 786–797.

[44] T. Azaïs, C. Tourné-Péteilh, F. Aussenac, N. Baccile, C. Coelho, J.-M. Devoisselle, F. Babonneau, Solid-state NMR study of ibuprofen confined in MCM-41 material, Chem. Mater. 18(26) (2006) 6382–6390.

[45] S.-C. Shen, W.K. Ng, L. Chia, Y.-C. Dong, R.B. Tan, Stabilized amorphous state of ibuprofen by co-spray drying with mesoporous SBA-15 to enhance dissolution properties, J. Pharm. Sci. 99(4) (2010) 1997–2007.

[46] R. Mellaerts, J.A. Jammaer, M. Van Speybroeck, H. Chen, J. Van Humbeeck, P. Augustijns, G. Van den Mooter, J.A. Martens, Physical state of poorly water soluble therapeutic molecules loaded into SBA-15 ordered mesoporous silica carriers: a case study with itraconazole and ibuprofen, Langmuir 24 (2008) 8651–8659.

[47] D.D. Chow, A.H. Karara, Characterization, dissolution and bioavailability in rats of ibuprofen-β-cyclodextrin complex system, Int. J. Pharm. 28 (1986) 95–101.

[48] G.M. Khan, F. Wazir, J. Zhu, Ibuprofen-cyclodextrin inclusion complexes: evaluation of different complexation methods, J. Med. Sci. 1(4) (2001) 193–199.

[49] P. Mura, G.P. Bettinetti, A. Manderioli, M.T. Faucci, G. Bramanti, M. Sorrenti, Interactions of ketoprofen and ibuprofen with β-cyclodextrins in solution and in the solid state, Int. J. Pharm. 166(2) (1998) 189–203.

[50] C.M. Vozone, H.M. Cabral Marques, Complexation of budesonide in cyclodextrins and particle aerodynamic characterization of the complex solid form for dry powder inhalation, J. Incl. Phenom. Macrocycl. Chem. 44 (2002) 111–115.

[51] P.J. Salústio, G. Feio, J.L. Figueirinhas, J.F. Pinto, H.M. Cabral Marques, The influence of the preparation methods on the inclusion of model drugs in a β-cyclodextrin cavity, Eur. J. Pharm. Biopharm. 71 (2009) 377–386.

[52] M. Cirri, C. Rangoni, F. Maestrelli, G. Corti, P. Mura, Development of fast-dissolving tablets of flurbiprofen-cyclodextrin complexes, Drug. Dev. Ind. Pharm. 31(7) (2005) 697–707.

[53] M.K. Ghorab, M.C. Adeyeye, Enhancement of ibuprofen dissolution via wet granulation with β-cyclodextrin, Pharm. Dev. Technol. 6(3) (2001) 305–314.

[54] M.K. Ghorab, M.C. Adeyeye, Enhanced bioavailability of process-induced fast-dissolving ibuprofen cogranulated with β-Cyclodextrin, J. Pharm. Sci. 92(8) (2003) 1690–1697.

[55] L.R. Shaw, W.J. Irwin, T.J. Grattan, B.R. Conway, The effect of selected water-soluble excipients on the dissolution of paracetamol and ibuprofen, Drug Dev. Ind. Pharm. 31(6) (2005) 515–525.

[56] C. Tourné-Péteilh, D. Brunel, S. Bégu, B. Chiche, F. Fajula, D.A. Lerner, J.-M. Devoisselle, Synthesis and characterisation of ibuprofen-anchored MCM-41 silica and silica gel, New J. Chem. 27 (2003) 1415–1418.

[57] Food and Drug Administration (FDA): http://www.fda.gov. FDA IV, Guidance for Industry: waiver of in vivo bioavailability and bioequivalence studies for immediate-release solid oral dosage forms based on a biopharmaceutics classification system, (10.2014).

[58] S. Klein, V.P. Shah, A standardized mini paddle apparatus as an alternative to the standard paddle, AAPS PharmSciTech 9(4) (2008) 1179–1184.

[59] A. Friebel, Aufbau und Inbetriebnahme einer Anlage zur Untersuchung der Auflösungsgeschwindigkeit von pharmazeutischen Wirkstoffen (master's thesis), Karlsruher Institut für Technologie (KIT), 2015.

[60] M.E. Brewster, T. Loftsson, Cyclodextrins as pharmaceutical solubilizers, Adv. Drug Deliv. Rev. 59 (2007) 645–666.

[61] M. Sliwinska-Bartkowiak, G. Dudziak, R. Gras, R. Sikorski, R. Radhakrishnan, K.E. Gubbins, Freezing behavior in porous glasses and MCM-41, Colloids Surf. A 187–188 (2001) 523–529.

[62] P. Costa, J.M. Sousa Lobo, Modeling and comparison of dissolution profiles, Eur. J. Pharm. Sci. 13 (2001) 123–133.

Journal of CO_2 Utilization 25 (2018) 216–225

Contents lists available at ScienceDirect

Journal of CO_2 Utilization

journal homepage: www.elsevier.com/locate/jcou

CO_2 assisted deposition of R/S-ibuprofen on different porous carrier materials: Influence of carrier properties on loading and dissolution behavior

Sarah Reiser[a], Masoom Shaban[b], Alfred Weber[b], Michael Türk[a,*]

[a] Institute for Technical Thermodynamics and Refrigeration, Karlsruhe Institute of Technology (KIT), Engler-Bunte-Ring 21, D - 76131 Karlsruhe, Germany
[b] Institute of Particle Technology, Technical University of Clausthal, Leibnizstraße 19, D-38678 Clausthal-Zellerfeld, Germany

ARTICLE INFO

Keywords:
CO_2
Ibuprofen
Carrier materials
Controlled particle deposition
Dissolution

ABSTRACT

With regard to bioavailability of poorly water-soluble drugs a big goal in research is to improve their dissolution behavior in the gastrointestinal tract. One suitable way to enhance the bioavailability is the use of drug loaded carrier materials. However, the effect of carrier properties such as specific surface area, pore size and pore volume on the dissolution of drugs is not well known yet. To investigate this, carrier materials with defined properties were produced by Salt Assisted Spray Pyrolysis (SASP) and loaded with racemic ibuprofen by the Controlled Particle Deposition (CPD) process. Their loadings and dissolution rates were compared to those of MCM-41 and SBA-15. It was found that the ibuprofen loading on the SASP carrier materials is lower due to their smaller specific surface areas, whereas their dissolution rates were higher in comparison to CPD processed MCM-41 and SBA-15. Furthermore, it was observed that pore size and pore volume influence the loading capacity of carrier materials. Wider mesopores lead to multilayer formation where crystalline ibuprofen structures were detected by XRD analysis. N_2-adsorption/desorption experiments at $T = 77$ K on the CPD processed carriers lead to the assumption that the small mesopores of MCM-41 or SBA-15 were occupied by ibuprofen due to the shift of the typical capillary condensation step at $p/p_0 = 0.3$–0.4 (untreated material) towards lower relative pressures of the CPD processed carriers.

Note: The paper is formatted in the style of this work. Mistakes which were not recognized during the review process were corrected. Citations and References are according to journal style.

1. Introduction

Nanoparticles are widely spread in industrial and scientific applications. Their increasing production and utilization in advanced materials, catalysts, semiconductors, food, optical components and many more requires intensive research. Another important application can be found in the pharmaceutical field. The efficiency of drugs, which are applied orally, is often limited by their dissolution and permeability in the gastrointestinal tract. Solubility enhancement of hydrophobic drugs can be realized with different methods like surfactants, co-solvents, solid dispersions, nano-suspensions or inclusion complexes [1 - 3]. Nevertheless, the dissolution rate of poorly water-soluble drugs (e.g. class II of the Biopharmaceutical

Classification System (BCS) [4]) can be increased enormously by the reduction of their particle size [5 - 7]. Therefore, many processes to form pharmaceutical nanoparticles have been investigated in recent years. Conventional methods to reduce the particle size like milling, grinding or spray drying cause several disadvantages. The obtained products often show a broad particle size distribution while further disadvantages are thermal / chemical degradation or their contamination with organic residues. To prevent these drawbacks different processes with supercritical fluids (SCFs) are under investigation [8, 9]. SCFs are characterized by their liquid like density and transport properties, which are comparable to those of gases [10]. Supercritical CO_2 ($scCO_2$) is considered to be a suitable solvent since it is non-toxic, non-flammable and inexpensive [11]. Additionally, the low critical data ($T_c = 304$ K, $p_c = 7.4$ MPa) allow moderate process conditions. Typical SCF based processes to form submicron particles are the Rapid Expansion of Supercritical Solutions (RESS) [6, 7, 12 - 16], Gas Anti Solvent (GAS) and its numerous modifications such as Supercritical Anti-Solvent (SAS) [17 - 19] or Particle generation from Gas Saturated Solutions (PGSS) [20, 21]. The most important among many advantages in that kind of processes is the manufacturing of solvent free products. It was shown that drugs, which were processed by RESS showed improved dissolution behavior compared to their unprocessed forms [6, 7, 8, 9, 12, 14, 15, 16, 22]. Nevertheless, formulation and further processing of these nanoparticles is difficult [9]. Therefore, the Controlled Particle Deposition process (CPD) was proposed to deposit submicron drug particles into porous carrier materials [2]. The fact that nonpolar and weak polar active ingredients show high solubility in SCFs [12, 23, 24] is exploited in this process. The key idea behind CPD is to dissolve the solute of interest in $scCO_2$, followed by permeation of the supercritical solution into the pores of the carrier and precipitation of the drug inside the pores, caused by a fast pressure drop. Since CO_2 is a dilute gas after the final depressurization step, the CPD process offers a highly pure final "ready to use" product [7, 9]. Thus, the product is achieved in a single step process using $scCO_2$ without the use of any organic or toxic solvents, which would be required in the conventional methods. Moreover, it has been shown that drugs, which are produced by the CPD process, show improved dissolution performances compared to their unprocessed counterparts [2, 7, 9, 25]. In addition, already about 10 years ago, it is proved in various publications of our group, that the CPD product shows a significantly improved dissolution behavior compared to materials obtained by conventional methods such as co-precipitation, solution immersing or freeze-drying [2, 7, 9, 26].

With regard to a controlled release of active ingredients their dissolution behavior depends strongly on the carrier material used, since the interaction with the guest molecule determines whether an improved or retarded dissolution is achieved.

An intensively investigated group of carrier materials are cyclodextrins, which form inclusion complexes with their guest molecules [2, 27 - 30]. Especially the dissolution in aqueous media of hydrophobic drugs is improved due to their hydrophilic surface. Furthermore, the supercritical impregnation of drugs on aerogels [31 - 33], various polymers [34, 35], microcrystalline cellulose pellets and hydroxyethylcellulose [36], sugar cubes [36] etc. have been reported.

Among them, mesoporous silica materials have attracted great attention as drug supports due to their low cost, good biocompatibility, non-toxic nature, suitable and adjustable pore diameter, high specific surface area and the ability to be easily functionalized. This is suitable for loading and releasing a large variety of drug molecules [37, 38]. However, the mesoporous silica materials obtained by conventional liquid phase methods are generally polydisperse in size and an accurate control of the porous structure is difficult. Moreover, such methods contain complicated sequences of multiple time-consuming steps and usually mesoporous materials with irregular bulk morphology are produced which is not suitable for drug delivery system. Therefore, to overcome these disadvantages, one strategy is to synthesize mesoporous silica microspheres by spray drying methods. In contrast to the traditional solution methods, this gas phase synthesis involves a very limited number of preparation steps and particles with a high purity can be simply produced using an economical, continuous and rapid process [39 - 43]. In particular, the pore size and structure can be easily adjusted at the desired nanoscale by tuning the chemical composition of the starting solution [44]. Furthermore, this gas phase process produces particles with a spherical shape, which are agglomeration-free [45]. From a clinical point of view, microspheres are widely accepted as useful drug delivery systems [46]. As a result, spray drying synthesized mesoporous silica materials in the form of microspheres represent a significant advance in the field of drug delivery.

Racemic ibuprofen is a typical representative of the class II according to the BCS. It is widely used as an analgesic and anti-inflammatory drug and possesses one carboxylic acid group, which can form strong bonds with other functional groups via acid–base reactions. Furthermore, it has been shown that its solubility in aqueous media is strongly pH dependent [47]. Especially at low pH the solubility of ibuprofen is weak but its permeability through the gastric mucosa is high due to its un-

dissociated form at this pH [1]. Thus, a significant improvement of the dissolution rate in low pH-values is necessary.

Until now it is not known exactly how specific surface area, pore volume and pore size influence the impregnation step and the dissolution behavior of drugs. Therefore, in this paper the loading and dissolution behavior of ibuprofen on novel carrier materials, which were synthesized by Salt Assisted Spray Pyrolysis (SASP), has been investigated. The obtained results are compared to those of CPD processed MCM-41 and SBA-15 which has been published earlier [25]. Thus, the objectives of this study are to investigate the influence of the specific surface area, pore size and pore volume on the impregnation and dissolution behavior of different silica based carrier materials with defined properties.

2. Experimental and characterization

2.1 Material section

CO_2 (Linde AG) was chosen as supercritical solvent since it is a non-flammable, inexpensive, and non-toxic solvent. Due to the low critical temperature (304.1 K), $scCO_2$ allows processing at moderate temperatures. Racemic ibuprofen (Knoll Pharmaceuticals) is a non-stereoidal anti-inflammatory drug and contains S-(+)-ibuprofen and R-(-)-ibuprofen molecules in equal amounts. Please note that in all experiments racemic ibuprofen was used. The commercially available silica carriers (SBA-15 (ACS Materials) and MCM-41 (Sigma Aldrich)) as well as two by Salt Assisted Spray Pyrolysis (SASP) synthesized carrier materials (SMS-1.0 and SMS-0.8) were loaded with ibuprofen. All materials and solvents were of the purest grade available and used as received without further purification.

2.2 Preparation of SASP carrier materials

The large-pore spherical mesoporous silica (SMS) particles were prepared using simple inorganic salts ($NaNO_3$+$LiNO_3$) as a pore template and colloidal SiO_2 suspension (Köstrosol 2040AS, 40 wt%) as building blocks according to literature [48, 49]. In this method, colloidal SiO_2 was added to an aqueous salt ($NaNO_3$+$LiNO_3$) solution to give a desired salt-to-SiO_2 ratio and total solution concentration. The solutions were sonicated for 15 min to ensure a full dispersion and aerosol particles were generated by a pneumatic atomizer (Palas GmbH AGK-2000) through the tube furnace with $T = 773$ K. The powder was collected in two bubblers containing

deionized water. The products were washed with water afterwards and centrifuged at 4000 rpms. In a next step the supernatant was removed to extract the salt template. This washing procedure was done twice. Finally, the product was dried in an oven at $T = 353$ K for 2 h. Further details about the Salt Assisted Spray Pyrolysis process can be found in literature e.g. [48 - 51].

2.3 Controlled particle deposition process (CPD)

In the CPD experiments the drug and the carrier material (in each case approx. 0.5 g) were filled in two separate sample containers (half shell, $V \leq 0.2$ cm^3) that are placed in a tubular reactor (see Fig. 1). The reactor ($V = 49$ cm^3) was evacuated for 2 h ($p \leq 10^{-2}$ mbar) and afterwards flushed with CO_2. Thereafter, the required amount of CO_2 (approx. 40 g) was condensed into the high-pressure cell and heated to the desired temperature. A magnetic stirrer (300 rpm) was placed between the containers to ensure an intensive mixing of the supercritical phase. It is worthy to notice that the supercritical mixture is non-saturated since the equilibrium solubility of ibuprofen at the given process conditions is around $2 \cdot 10^{-2}$ g/g [12]. The impregnation time was set to 72 h to guarantee equilibrium conditions. To prevent crystallization of surplus ibuprofen (which was not adsorbed on the carrier material

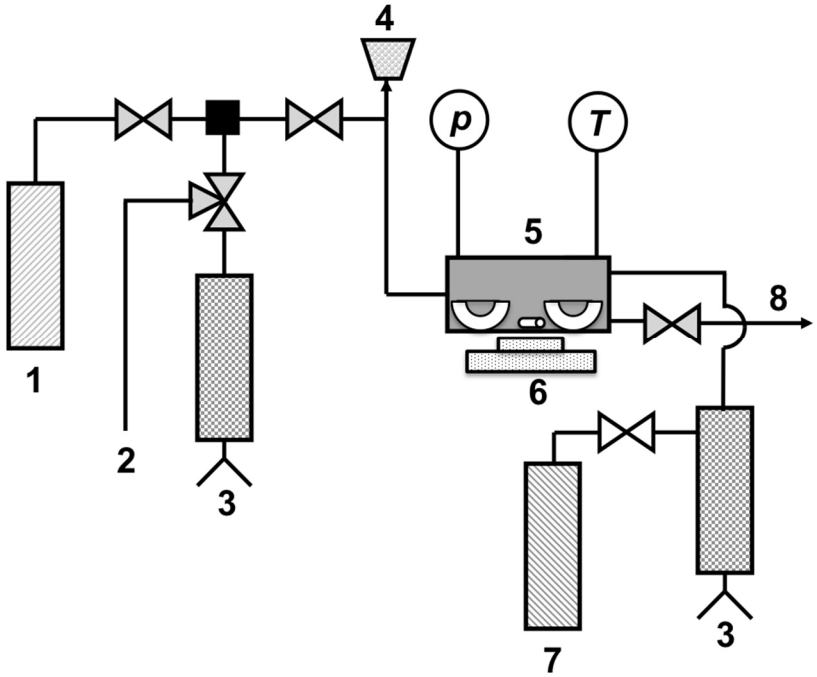

Fig. 1 Schematic graph of the experimental set up: 1, CO_2 reservoir; 2, connection to vacuum pump; 3, manual piston pump; 4, pressure-relief valve; 5, reactor; 6, magnetic stirrer; 7, N_2 reservoir; 8, outlet; p, pressure indicator; T, temperature indicator.

and is still dissolved in the supercritical phase) the reactor was flushed with N_2 at $p = 16$ MPa for approx. 20 sec and was then depressurized within 30 sec [25]. The ibuprofen loading on the carrier materials was analyzed by high-pressure liquid chromatography (HPLC) as described below. A more detailed description of the CPD process can be found in literature e.g. [2, 9, 25].

2.4 Dissolution experiments

The experiments were performed according to the Food and Drug Administration (FDA) IV standards [52]. It is recommended to test the dissolution of drugs in aqueous buffers in a pH range of 1.0 - 7.4 at $T = 310$ K. To investigate the dissolution of ibuprofen at pH = 2.0, hydrochloric acid (0.2 M) and potassium chloride (Carl Roth) were used to simulate the gastric fluid. Sørensen buffers, which were used to investigate the dissolution at pH = 5.5, were prepared from distilled water (0.055 µS), potassium dihydrogen phosphate (Sigma Aldrich) and sodium hydrogen phosphate (Carl Roth). As recommended by the FDA [52], all dissolution experiments were performed at the so-called "sink conditions". These are defined as the drug concentration, which is equivalent to $1/3^{rd}$ to $1/5^{th}$ of the equilibrium solubility at the current pH-value [52]. In the context of this work $1/3^{rd}$ of the equilibrium solubility was used as sink conditions (equilibrium solubility of ibuprofen at pH = 2.0: 0.06 g/l [47]; pH = 5.5: 0.27 g/l [53]). Concerning investigations of carriers with low drug loadings a "down-scaled" USP apparatus 2 according to the recommendations by Klein and Shah [54] with a volume of 250 ml was built (Fig. 2). In this minimized setup the paddle stirrer speed was set to 100 rpm [53].

The experimental set up consists of the self-made glass vessel (1), paddle mixer (2) and motor (3). A thermostat (4) with a Pt-100-temperature sensor (5) was used for tempering the dissolution media. The pH-value of the dissolution media was determined with a Sevenmulti™ including an InLab® Routine Pro pH electrode (6, 7) (Mettler-Toledo). Samples (8) of 0.5 mL were taken out of the vessel in predetermined time intervals and replaced with an equal amount of pure dissolution fluid.

The dissolution behavior of ibuprofen is described by the following equation:

$$D(t)/[\%] = \frac{c_t}{c_0} \cdot 100 \qquad (1)$$

In this equation $D(t)$ [%] is the dissolved amount at a certain time, c_0 is defined as the initial ibuprofen concentration, which is equivalent to the concentration at sink

conditions mentioned above, and *c(t)* corresponds to the ibuprofen concentration in the dissolution media at different time steps. All dissolution experiments were performed in triplet.

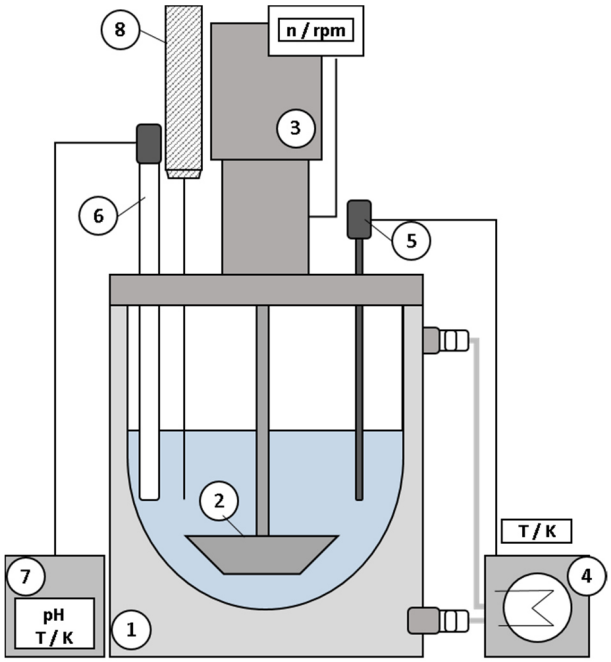

Fig. 2 USP apparatus 2 according to the recommendations of Klein and Shah [54].

2.5 Characterization methods

For the characterization of the SASP carriers, MCM-41 and SBA-15 N_2-sorption (i.e. adsorption and desorption) isotherms at $T = 77$ K were measured using a Nova 2000e setup (Quantachrome). The samples were outgassed at $T = 573$ K to a residual pressure lower than 10^{-4} Torr for 16 h before the measurements.

The pore size distribution was calculated using the NovaWin Software (Version 11.03). The pore size distributions of the SASP carriers were calculated by the Barrett-Joyner-Halenda (BJH) method including Halsey t-method for calculating the statistical thickness of the adsorption layer. Due to the fact that the BJH method underestimates the size of narrow mesopores ($D_P \leq 10$ nm) significantly [55] the Density Functional Theory (DFT) method was used to calculate the pore size distribution of MCM-41 and SBA-15. Therefore, the calculation model "N_2 at 77 K on silica (cylindrical pore, Non Linear Density Functional Theory equilibrium model)" was chosen. Furthermore, the CPD processed carrier materials were also characterized by N_2-sorption measurements. To prevent evaporation of the deposited ibuprofen ($T_{melt} = 349$ K, at ambient pressure), these samples were outgassed at

$T = 393$ K to a residual pressure lower than 10^{-4} Torr for 16 h before the measurements.

The morphology of the SASP carrier materials was investigated by transmission electron microscopy (TEM) and scanning electron microscopy (SEM). TEM was performed with a JEOL JEM2100 (160kV) while SEM images were taken with a Zeiss DSM Gemini 982 operated at 10kV.

The amount of ibuprofen deposited onto the carrier materials were analyzed by HPLC. Therefore 5 - 10 mg of the CPD processed samples were dissolved in acetonitrile (ACN) and stored in an overhead shaker for 25 h. In a next step, the samples were centrifuged and the ibuprofen concentration in the permeate was analyzed using an Agilent HP 1100 Series (Agilent Technologies). Samples were injected into a LiChrosphere 100-5 RP18 (125 x 4 mm) column (Agilent Technologies) with a flow rate of 1.8 ml/min of a 50 : 50 Sørensen-buffer (pH = 3.0) : ACN liquid phase. Sørensen buffers were made with distilled water (0.055 µS), potassium dihydrogen phosphate (Sigma Aldrich) and sodium hydrogen phosphate (Carl Roth). Two different diode array detector (DAD) signals (wavelength: 210.4 nm, reference: 360/100 nm and wavelength: 230.4 nm, reference: 360/100 nm) were evaluated. To determine the ibuprofen concentration in the dissolution media the same HPLC method was used.

Powder X-ray diffraction (XRD) pattern of the unprocessed carriers and the CPD processed samples were determined by using a STADI-MP diffractometer (Stoe & Cie. GmbH) with Ge-monochromatized Cu-$K_{\alpha 1}$ radiation ($\lambda = 1.54060$ Å) in a 2Θ range of 2-91.985° with a step size of 0.015° (1200 sec).

Thermogravimetric analysis (TGA) was carried out in the temperature range from ambient to 1273 K in air atmospheres at a heating rate of 10 K/min using a TG 209 F1 thermogravimetric analyzer (TG209 F1, Netzsch).

3. Experimental results

3.1 Preparation of SASP carriers, influence of salt-to-SiO_2 ratio on carrier properties

In order to achieve first results of the influence of the salt-to-SiO_2 ratio on particle morphology and carrier characteristics of mesoporous silica prepared by SASP, two different experiments were carried out using the same inorganic salt in different salt-to-SiO_2 molar ratios (SMS-1.0: 1:1, SMS-0.8: 1:0.8). Under the same synthesis

conditions particles with different properties were obtained. TEM (Fig. 3) and SEM (Fig. 4) analysis were used to investigate the morphology of these particles. With the SASP preparation method spherical particles in the submicron range were formed. As illustrated by the example of SMS-1.0 in TEM images (Fig. 3), the porous structure was formed after the samples have been washed with water. Therefore, it can be concluded that salt is responsible to induce porosity in the structure. Furthermore, TEM images of the washed samples showed the formation of pores also in the interior of the particles (Fig. 3).

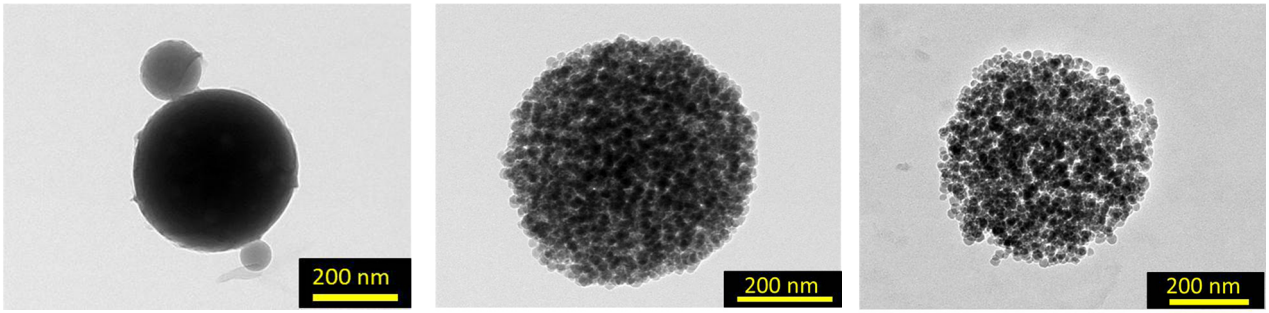

(a) (b) (c)

Fig. 3 TEM images of unwashed SMS-1.0 (a), washed SMS-1.0 (b) and washed SMS-0.8 (c).

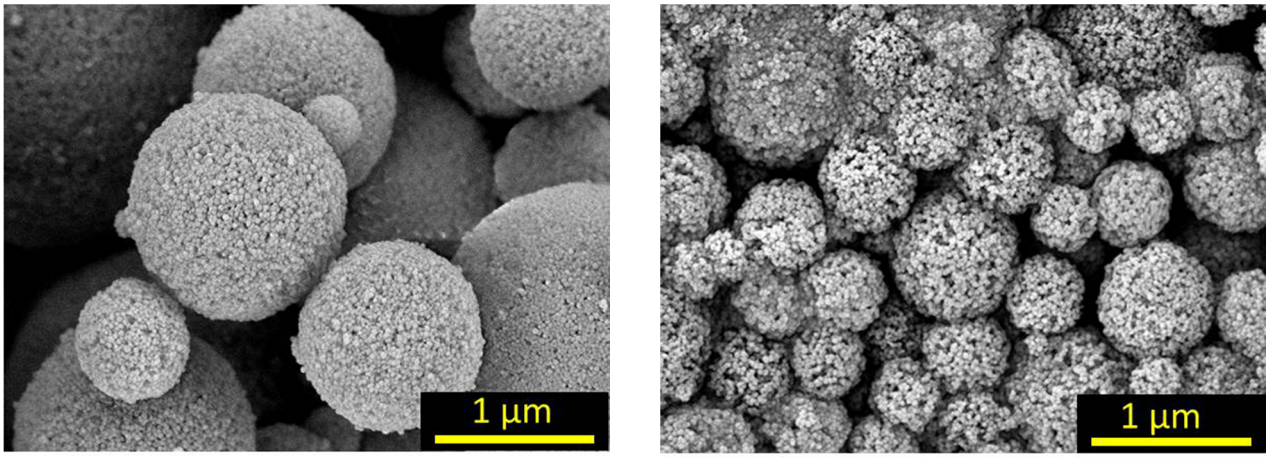

(a) (b)

Fig. 4 SEM images of SMS-1.0 (a) and SMS-0.8 (b).

Smaller pores were observed for SMS-1.0 which was synthesized with the lower salt-to-SiO_2 molar ratio (Fig. 4). These results are in good agreement with observations found in literature e.g. on the formation of Al_2O_3 nanoparticles. Kim et al. reported that the specific surface area and the total pore volume were decreased with higher NaCl mass fraction whereas pore diameters were increased [56]. It was concluded in literature that bigger pores are obtained due to the formation of larger salt precipitates. This might also be the fact in the systems investigated in this study.

3.2 Characterization of the untreated carrier materials

N_2-sorption isotherms, which were obtained at $T = 77$ K for the different untreated carrier materials are depicted in Fig. 5. MCM-41 and SBA-15 showed typical type IV isotherms, which are characteristic for mesoporous materials [57]. Pore condensation occurred in the range of $p/p_0 = 0.3 - 0.4$ while a narrow hysteresis in this region was also obvious. At higher p/p_0-values MCM-41 showed a second significant increase in the range of $p/p_0 = 0.9 - 1.0$ which indicates N_2 condensation in larger pores. This increase was less pronounced for SBA-15 compared to MCM-41. With respect to the Gurvich rule the total pore volume of MCM-41 was calculated at $p/p_0 = 0.986$ while the total pore volume of SBA-15 was calculated at $p/p_0 = 0.991$.

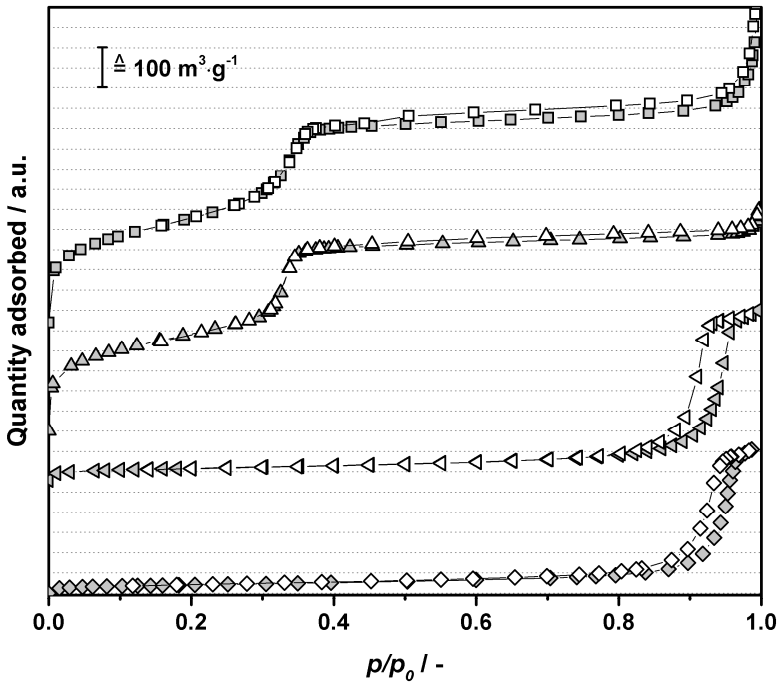

Fig. 5 N_2-sorption isotherm for untreated MCM-41 (square), SBA-15 (triangle) SMS-1.0 (triangle, left sided) and SMS-0.8 (diamond). The adsorption branch is represented by filled symbols while white symbols indicate the desorption branch.

A steep increase in the range of $p/p_0 = 0.8 - 0.97$ was obvious in the N_2-sorption isotherms of the SASP carriers. The narrow hysteresis in this range indicates large but uniform mesopores [57]. Their pore volume was calculated by the Gurvich rule at $p/p_0 = 0.987$ (SMS-1.0) and $p/p_0 = 0.987$ (SMS-0.8). Pore condensation at high p/p_0-values is an indication of large mesopores in the SASP carrier materials. Due to this fact the pore size distribution was calculated by the BJH method. The pore size of narrow mesopores (pore width < 10 nm) is significantly underestimated by this

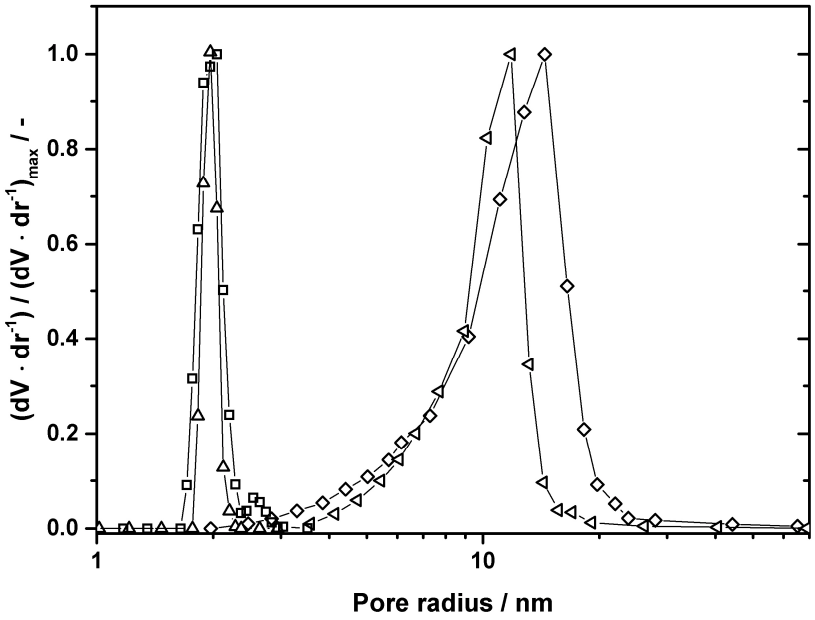

Fig. 6 Pore size distribution of untreated MCM-41 (square), SBA-15 (triangle) SMS-1.0 (triangle, turned left) and SMS-0.8 (diamond).

Tab. 1 Characteristic properties of untreated carrier materials.

	Specific surface area	**Total pore volume**	**Av. pore diameter**
	A_{BET}	V_P	D_P
	m^2/g	cm^3/g	nm
MCM-41	1030	1.09	4.0
SBA-15	920	0.84	3.6
SMS-1.0	102	0.63	25
SMS-0.8	73	0.55	30

method [55]. Therefore, the DFT method was used to calculate the pore size distribution of MCM-41 and SBA-15. In all cases the desorption branch was used for the calculation of the pore size distribution. The obtained results are depicted in Fig. 6 while a brief overview of all carrier properties can be found in Tab. 1.

The specific surface area of the carrier materials was calculated by the Brunauer-Emmitt-Teller (BET) method. It was obvious that the SASP carrier materials showed smaller specific surface areas with a smaller total pore volume and a broad pore size distribution in comparison to the conventional carrier materials. SBA-15 and MCM-41 showed similar narrow pore size distributions whereas a second small peak was detected in a pore radius range of 2.25 – 3 nm for MCM-41. Furthermore, it was observed that the SASP carrier material which was synthesized with the lower salt-to-SiO_2 molar ratio (SMS-1.0) showed the higher specific surface area (SMS-1.0: $A_{BET} = 102$ m^2/g; SMS-0.8: $A_{BET} = 73$ m^2/g) and the higher total pore volume

(SMS-1.0: $V_P = 0.63$ cm^3/g; $V_P =$ SMS-0.8: 0.55 cm^3/g) whereas the pore size was smaller (SMS-1.0: $D_P = 25$ nm; SMS-0.8: $D_P = 30$ nm) in comparison to SMS-0.8. These observations are in good agreement with the TEM and SEM results discussed in 3.1 and [56].

3.3 Drug loading

It has been reported that porous particles, which were impregnated by a SCF based process, show higher loadings compared to those, which were impregnated by other techniques (e.g. solution immersion) [37]. Furthermore, it was observed that loading results were also dependent on the ibuprofen concentration in the $scCO_2$ [36, 38]. In the following section loading is defined as ($m_{ibuprofen}$ / $m_{carrier} \cdot 100$) [wt %] according to [58].

The results of the ibuprofen loading caused by CPD on the different carriers are listed in Tab. 2. It was obvious that MCM-41 and SBA-15, which were investigated recently by Reiser et al. [25] showed higher loadings compared to the SASP carriers. Similar loadings of MCM-41 (49 wt%) and SBA-15 (50 wt%) might be an effect of their similar high surface area (MCM-41: $A_{BET} = 1030$ m^2/g, SBA-15: $A_{BET} = 920$ m^2/g) [25]. In comparison to this SMS-0.8 (25 wt%) and SMS-1.0 (16 wt%) showed much lower loadings due to the smaller specific surface area (SMS-0.8: $A_{BET} = 73$ m^2/g, SMS-1.0: $A_{BET} = 102$ m^2/g). As a first result it was obvious that the ibuprofen loading depends on the value of the specific surface area. Nevertheless, other factors might have an influence since SMS-0.8 showed high loadings despite its comparatively small specific surface area. Other impacts could be the pore size and / or the pore structure. With regard to SMS-1.0 ($D_P = 25$ nm) and SMS-0.8 ($D_P = 30$ nm) it was evident that higher loadings were obtained with increasing pore size. A possible explanation might be that in larger pores more ibuprofen molecules are able to diffuse into the pore system during the impregnation step. The diffusion of ibuprofen out of these pores during the depressurization step seems to be much slower than its particle formation kinetics and therefore the ibuprofen molecules might be entrapped inside the pores. Due to this multilayer

Tab. 2 Ibuprofen loadings on MCM-41 [25], SBA-15 [25] and SASP silica carriers and number of monolayers, which were loaded by the CPD process.

	MCM-41	**SBA-15**	**SMS-1.0**	**SMS-0.8**
Loading [wt%]	49.1 ± 0.5	49.9 ± 0.5	16.3 ± 0.6	25.4 ± 1.4
Number of monolayers	1.2	1.4	4.1	9.1

adsorption and the formation of crystals could be possible in larger pores. In small mesopores like those of MCM-41 or SBA-15 only monolayer adsorption seems to be possible due to the limited space. Furthermore, the slightly higher loading of SBA-15 in comparison to MCM-41 can be explained by their differences in pore structure. The cross-linking channels of SBA-15 seem to have a beneficial effect on maintaining a high loading of ibuprofen.

To distinguish if the loading of drugs on carrier materials is based on physical adsorption or due to precipitation and nucleation Gurikov and Smirnova [58] proclaimed to calculate the number of monolayers (*NML*) (Eq.(2)).

$$NML = \frac{Y \cdot N_a \cdot a_{drug}}{M_{drug} \cdot A_{BET}} \tag{2}$$

In this equation Y is equivalent to the loading [$g_{drug}/g_{carrier}$], N_A is the Avogadro number [mol^{-1}], a_{drug} describes the projection area of the drug molecule [m^2], M_{drug} is the molar mass of the drug [g/mol] and A_{BET} the specific surface area of the untreated carrier [$m^2/g_{carrier}$]. To calculate the *NML* value a projection area of ibuprofen of $8.92 \cdot 10^{-19}$ m^2 [58] was assumed. Gurikov and Smirnova proclaimed that, if the number of monolayers for non-swellable carriers exceeds unity, it might be an indication of precipitation within the pores.

The results calculated by Eq.(2) are listed in Tab. 2 and show that the lowest *NML* values were obtained for MCM-41 (*NML* = 1.24) and SBA-15 (*NML* = 1.42). Due to limited space in the small mesopores the ibuprofen molecules were mainly deposited inside the pores as a monolayer. Higher *NML* values were calculated for the SASP carrier materials (SMS-1.0: *NML* = 4.09, SMS-0.8: *NML* = 9.07); thus the highest *NML* value was calculated for the ibuprofen-SMS-0.8 system. Due to the fact that these carriers have large pore diameters ibuprofen might precipitate out of the supercritical solution caused by a pressure drop and therefore the formation of crystalline structures seems to be possible.

In comparison to results published in literature significantly smaller *NML* values (0.35 - 0.42) were calculated by Gurikov and Smirnova [58] based on the data published by Hillerström et al. [59] for the impregnation of ibuprofen on MCM-41 with liquid CO_2. An *NML* value of 0.91 was obtained using the loading data from Li-Hong et al. [37] for the impregnation of MCM-41 with ibuprofen by a supercritical impregnation method. These differences can be explained by the observations that loading is dependent on the ibuprofen concentration in $scCO_2$ [36, 38].

3.4 XRD analysis of the CPD processed carrier materials

XRD analyses were performed to investigate the crystalline state of the ibuprofen molecules deposited on the carrier materials by the CPD process. The X-ray diffraction patterns of the untreated and the CPD processed carriers are plotted in Fig. 7 as a function of the angle 2Θ. Obviously, untreated ibuprofen showed XRD patterns in the range of $2\Theta = 5° - 50°$ which are characteristic for crystalline ibuprofen while the untreated carrier materials showed a broad elevation in the range of 10°– 35°. With regard to the XRD patterns of the CPD processed SASP carriers SMS-0.8 and SMS-1.0 typical peaks for crystalline ibuprofen were detected whereas these peaks were not found for CPD processed MCM-41 and SBA-15.

In accordance with DSC data published earlier [25], these observations lead to the assumption that ibuprofen, which was deposited on MCM-41 and SBA-15, is in an amorphous state whereas crystalline fractions can be found on SMS-0.8 and SMS-1.0. A possible explanation for the formation of crystalline fractions on SMS-0.8 and SMS-1.0 might be the effect of the larger pore size in comparison to the small mesopores of MCM-41 and SBA-15 (cf. Tab. 1). These observations are in good agreement with results from studies performed by Sliwinska-Bartkowiak et al. [60]. These authors reported that crystallization of nitrobenzene occurs in pores, which are 20 times larger than the guest molecule. This conclusion might be also transferable to supercritical impregnation processes. The ibuprofen peaks, which were

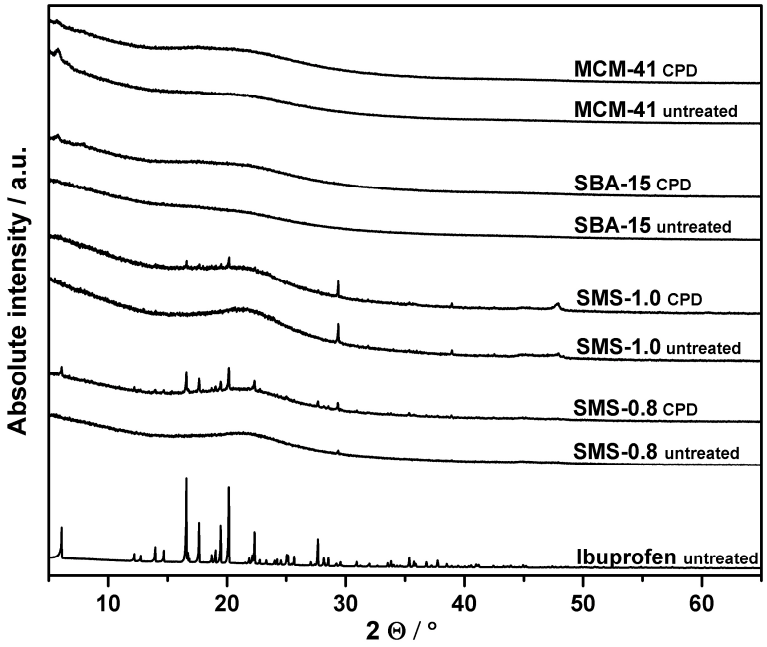

Fig. 7 XRD pattern of the untreated and CPD processed materials.

detected on SMS-0.8, seemed to have a slightly higher intensity than those of SMS-1.0, which leads to the assumption that the amount of crystalline ibuprofen on SMS-0.8 might be higher than on SMS-1.0. Thus, the XRD results confirm the assumption that the formation of crystalline structures in wider mesopores is possible. In addition to this, the formation of amorphous ibuprofen on MCM-41 and SBA-15 by different impregnation techniques has been also recognized in literature [37, 59, 61].

3.5 N_2-sorption on the CPD processed carrier materials

In section 3.2 the characterization of the untreated carrier materials by measuring N_2-sorption isotherms at $T = 77$ K was discussed. In addition to this, further experiments of the CPD processed carrier materials were carried out in order to investigate the influence of ibuprofen on the N_2-sorption behavior. Furthermore, it might be possible to detect the location of ibuprofen on the carrier materials investigated. The CPD processed samples were outgassed at $T = 393$ K for 16 h under vacuum in order to ensure the removal of entrapped water but to prevent a significant mass loss of these samples during the activation due to the evaporation of ibuprofen ($T_{melt} = 349$ K, at ambient pressure) at higher temperatures. As discussed

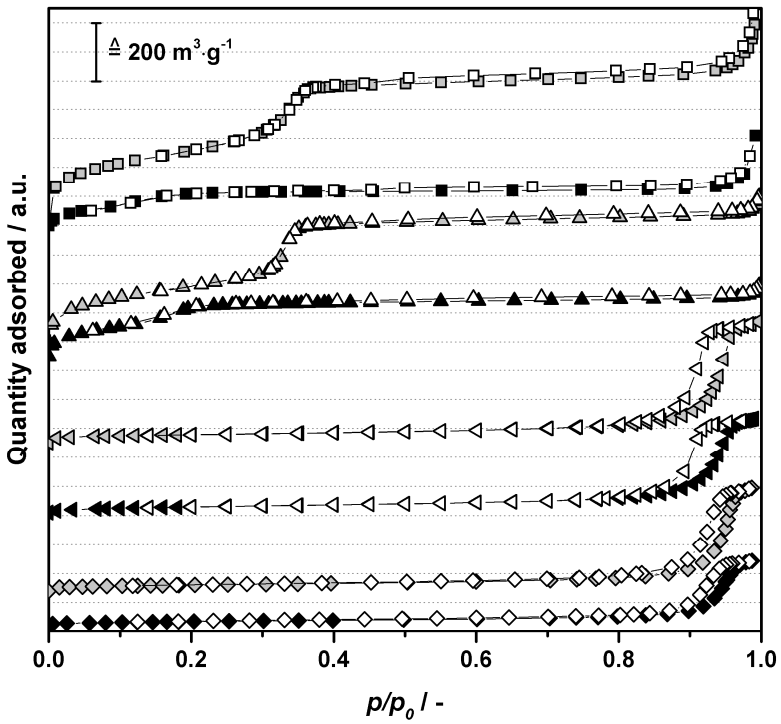

Fig. 8 N_2-sorption isotherms of untreated (light grey) and CPD processed (dark grey) carrier materials MCM-41 (square), SBA-15 (triangle), SMS-1.0 (triangle, turned left) and SMS-0.8 (diamond). The adsorption branch is represented by filled symbols while white symbols indicate the desorption branch.

in section 3.2 untreated MCM-41 and SBA-15 showed a typical capillary condensation step in the pressure range of $p/p_0 = 0.3 - 0.4$ (see Fig. 5). As shown in Fig. 8 this steep increase of the N_2-sorption isotherm was significantly smaller and shifted towards lower relative pressures ($p/p_0 = 0.1 - 0.2$) for the CPD processed MCM-41 and SBA-15 samples. The second steep increase of the isotherms was still obvious at $p/p_0 = 0.9 - 1.0$ and its intensity was nearly equally distinctive in the unprocessed and CPD processed MCM-41 and SBA-15. Furthermore, it is clarified in Tab. 3, that the quantity adsorbed (at standard temperature and pressure) of the CPD processed carriers was lower in comparison to the unprocessed materials. A possible explanation might be the fact that the weight of the sample includes also the amount of the deposited ibuprofen in the CPD processed systems. In comparison to this a distinctive shift of the capillary condensation step of CPD processed SMS-1.0 and SMS-0.8 was not detectable. This result and the fact that the second capillary condensation step at $p/p_0 = 0.95 - 1.0$ of the CPD processed MCM-41 and SBA-15 was not affected by the deposited ibuprofen leads to the assumption that in wider mesopores capillary condensation is still possible.

The specific surface area, total pore volume and average pore diameter obtained from

Tab. 3 Values of the N_2-amount adsorbed (cm^3/g) on different untreated and CPD processed carrier materials.

Amount adsorbed at	**untreated**				**CPD processed**			
	MCM-41	**SBA-15**	**SMS-1.0**	**SMS-0.8**	**MCM-41**	**SBA-15**	**SMS-1.0**	**SMS-0.8**
$\boldsymbol{p/p_0 = 0}$	0	0	0	0	0	0	0	0
$\boldsymbol{p/p_0 = 1}$	772	548	420	354	309	244	324	219

Tab. 4 Characteristic properties of untreated and CPD processed carriers. The samples were outgassed for 16 h under vacuum at $T = 573$ K (untreated) and $T = 393$ K (CPD processed).

	Specific surface area $\boldsymbol{A_{BET}}$		**Total pore volume** $\boldsymbol{V_P}$		**Av. pore diameter** $\boldsymbol{D_P}$	
	untreated m^2/g[a]	CPD processed m^2/g[b]	untreated cm^3/g[a]	CPD processed cm^3/g[b]	untreated nm	CPD processed nm
MCM-41	1030	570	1.09	0.48	4.0	3.4
SBA-15	920	418	0.84	0.38	3.6	3.1
SMS-1.0	102	79	0.63	0.49	25	25
SMS-0.8	73	50	0.55	0.38	30	30

[a] The sample mass is equivalent to the untreated carrier mass ($m_{carrier}$)
[b] The sample mass includes also the amount of deposited ibuprofen ($m_{carrier} + m_{ibuprofen}$)

the N_2-sorption isotherms of the untreated and CPD processed carriers are summarized in Tab. 4. As it can be seen that the obtained values of the specific surface area and the total pore volume for the CPD processed carrier materials were lower in comparison to the untreated carriers. Nevertheless, it has to be considered that these values as well as the quantity adsorbed were referred to a sample mass, which includes the mass of the deposited ibuprofen. The value of the calculated average pore diameter was decreased in the small mesoporous systems while it was approximately constant for SMS-1.0 and SMS-0.8 before and after CPD processing. Thus, these observations might be an additional hint for the existence of ibuprofen inside the small mesopores of MCM-41 and SBA-15.

In order to identify the reason for the shift of the capillary condensation step further N_2-sorption experiments were carried out exemplary with SBA-15 samples using different activation methods (see Fig. 9).

Among others, one possible explanation for the shift could be the different outgassing temperatures of the untreated and CPD processed samples. To exclude this assumption untreated SBA-15 was outgassed at $T = 393$ K and 573 K. The

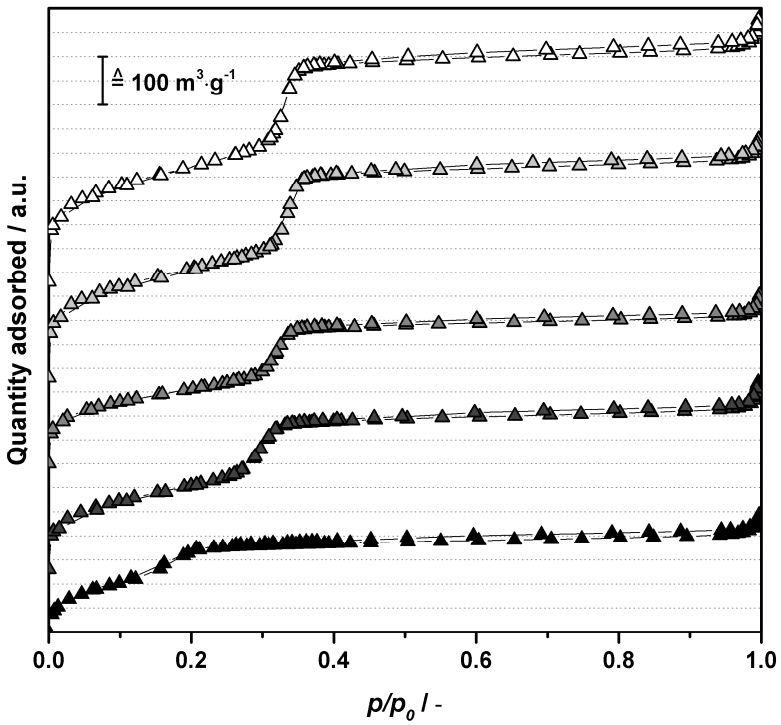

Fig. 9 N_2-sorption isotherms of SBA-15 samples outgassed under different temperature and time conditions. White triangles: SBA-$15_{\text{untreated}}$ ($T = 573$ K, $t = 16$ h); light grey triangles: SBA-$15_{\text{untreated}}$ ($T = 393$ K, $t = 16$ h); middle-grey triangles: SBA-15_{CPD} ($T = 573$ K, $t = 16$ h); dark grey triangles: SBA-15_{CPD} ($T = 573$ K, $t = 6.5$ h); black triangles: SBA-15_{CPD} ($T = 393$ K, $t = 16$ h).

resulting N_2-sorption isotherms are depicted in Fig. 9. It was observed that the quantity adsorbed was slightly lower with decreasing outgassing temperature whereas the capillary condensations step at $p/p_0 = 0.3 - 0.4$ was not affected. Therefore, it can be concluded that the lower outgassing temperature was not responsible for the shift of the capillary condensation step.

To verify the assumption that the shift was affected by ibuprofen, similar experiments were carried out with CPD processed samples. These samples were outgassed at $T = 393$ K ($t = 16$ h), $T = 573$ K ($t = 6.5$ h) and $T = 573$ K ($t = 16$ h). The resulting N_2-sorption isotherms are depicted in Fig. 9 and the values of the amount adsorbed are summarized in Tab. 5. It can be seen that with increasing temperature and time the capillary condensation step was shifted towards higher relative pressures. Furthermore, an increase of this surge and the quantity adsorbed was observed.

These results are in good agreement with TGA measurements performed with CPD processed SBA-15. An excerpt from the TGA results for the interesting temperature range up to $T = 573$ K can be seen in Fig. 10. It is obvious that the weight loss of untreated SBA-15, which is caused by the removal of entrapped water, was only 1.1 wt% at $T = 573$ K. In opposite to this, the CPD processed SBA-15 sample lost 12 wt% of its initial weight at this temperature, which is caused by evaporation of ibuprofen out of the pores.

Transferring this result to the N_2-sorption measurements depicted in Fig. 9 it can

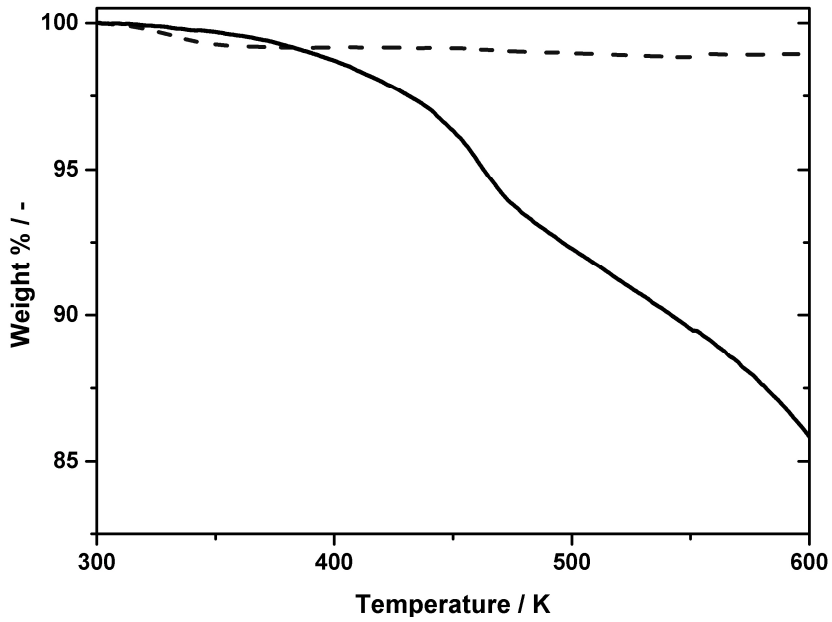

Fig. 10 TGA-analysis of untreated SBA-15 (dashed line) and CPD processed SBA-15 (solid line).

Tab. 5 Values of the N_2-amount adsorbed (cm^3/g) on unprocessed and CPD processed SBA-15 outgassed at different temperatures and time conditions before N_2-sorption experiments.

	untreated		**CPD processed**		
Amount adsorbed at	573 K 16 h	393 K 16 h	573 K 16 h	393 K 6.5 h	393 K 16 h
$p/p_0 = 0$	0	0	0	0	0
$p/p_0 = 1$	548	420	354	309	244

be concluded that with increasing outgassing temperature and time the release of ibuprofen out of the pores of the carrier materials increases. This statement could be verified by the fact that the N_2-sorption isotherm of the CPD processed SBA-15 sample outgassed at $T = 573$ K and $t = 16$ h showed a similar trend to the isotherm of the untreated SBA-15 samples. This confirms that nearly all deposited ibuprofen was evaporated out of the pores at the applied outgassing conditions.

With these results and the calculated lower pore diameter (see Tab. 4) for the CPD processed materials it could be proclaimed that the ibuprofen molecules were mainly deposited inside the small mesopores of MCM-41 and SBA-15.

3.6 Dissolution behavior

According to FDA standards the dissolution experiments were performed in a glass USP 2 apparatus (Fig. 2). The drug release profiles of the carrier materials and the dissolution of unprocessed ibuprofen at pH = 2.0 and pH = 5.5 are depicted in Fig. 11 and Fig. 12. Different models are available to describe the dissolution performance of drugs in aqueous media [62]. Nevertheless, the so-called "1st-order model" achieved the best description of the experimental results [62]. In this model the dissolution behavior *D(t)* is described by the following equation:

$$D(t) = D_{100} \cdot (1 - e^{-k \cdot t}) \tag{3}$$

In Eq.(3) k is defined as the dissolution constant and D_{100} is an adjustable parameter to model results, which are lower than complete dissolution. These parameters are listed in Tab. 6 for the different carrier materials and unprocessed ibuprofen at pH = 2.0 and pH = 5.5.

In general, it can be seen, that the dissolution rate of all investigated materials was increased with increasing pH-value. At both pH-values investigated the CPD processed carrier materials showed improved dissolution performance compared to

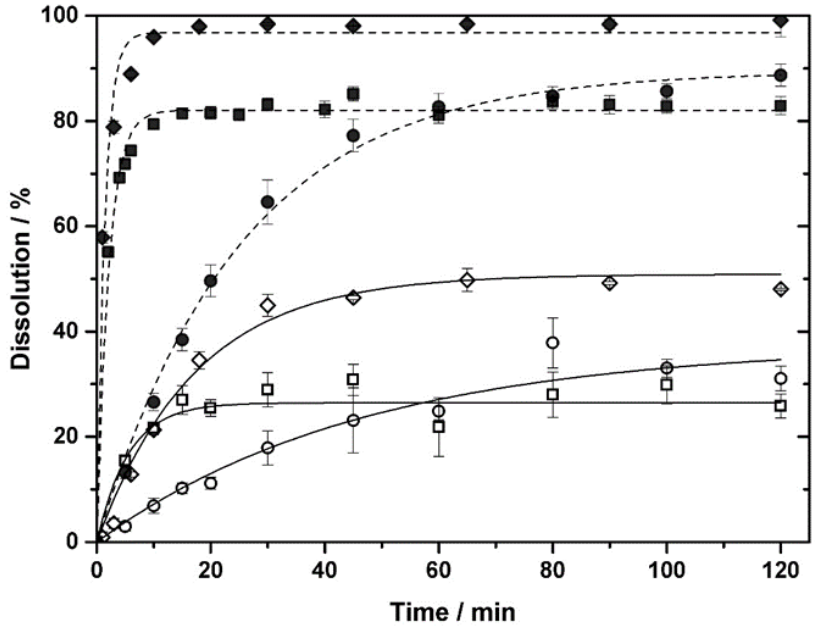

Fig. 11 Dissolution profile of untreated ibuprofen (circle), CPD processed MCM-41 (square) and SMS-0.8 (diamond) at pH = 2.0 (open symbols) and pH = 5.5 (full symbols). The lines are the kinetic fits according to the model of 1st-order; see Eq.(3).

unprocessed crystalline ibuprofen. The fast dissolution in the beginning of the experiments was completed by the formation of a plateau. This maximum dissolution depended on the pH-value and the particular drug-carrier system. At pH = 2.0 a maximum dissolution of 30 – 40 % was achieved, whereas it was increased up to almost 100 % at pH = 5.5. This might be a result of changed interactions between the drug and the silica surface at the different pH-values. It was reported by Bui and Choi [63] that the drug-carrier interactions are pH dependent and therefore adsorption might be not completely reversible in the entire pH range. At pH < 4 the net charge of the silica surface is positive while it becomes negative at pH > 4. In dissolution medias with pH < pK_a (pK_a ibuprofen = 4.4 [64]) the drug is uncharged. Due to this, attractive forces (e.g. H-bonds) between surface and the molecule might be predominating. In opposite thereto, repulsive effects become even stronger when pH > pK_a. This might explain the results that at pH = 5.5 a higher drug release from silica surfaces was obtained compared to pH = 2.0.

Furthermore, the enhancement of the dissolution rate with increasing pH-value can be explained by the fact that the ibuprofen solubility in aqueous solutions is pH dependent. At pH ≤ pK_a the solubility of ibuprofen is very low (0.06 g/l) [47] and pK_a is reached. Hence the increase of the pH-value from pH = 2.0 to pH = 5.5 leads to a higher equilibrium solubility of ibuprofen in aqueous media. This results in a higher mass transfer rate of the dissolved solid and therewith in an improved

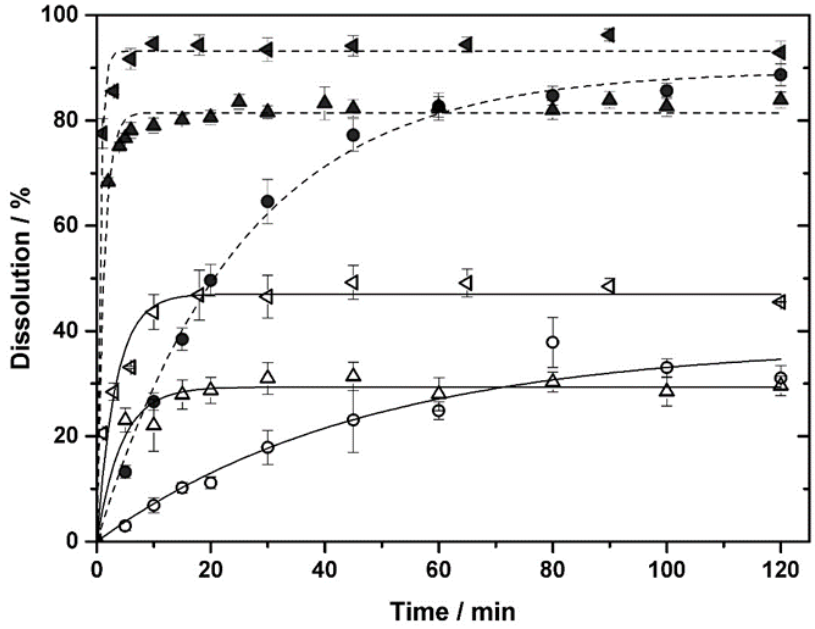

Fig. 12 Dissolution profile of untreated ibuprofen (circle), CPD processed SBA-15 (triangle) and SMS-1.0 (triangle, turned left) at pH = 2.0 (open symbols) and pH = 5.5 (full symbols). The lines are the kinetic fits according to the model of 1st-order; see Eq.(3).

dissolution behavior.

It was also obvious that at both pH-values the SASP carrier materials showed higher values for D_{100} (see Tab. 6) compared to SBA-15 and MCM-41. As discussed in section 3.3 the SASP carriers showed a higher number of monolayers and therefore a smaller amount of the deposited drug seemed to be in direct contact with the carrier surface, which might result in a faster dissolution of the drug molecules. Furthermore, the pore structure of MCM-41 and SBA-15 consists of long and small pores. Li-Hong et al. [37] proposed that during the impregnation with SCFs, molecules are able to migrate deep into pore systems. During the dissolution experiments the diffusion of ibuprofen out of the pores seems to be hindered, due to the fact that ibuprofen is hydrophobic and therefore the penetration of the long and small channels of MCM-41 and SBA-15 by the aqueous dissolution media might be hampered. Therefore, diffusion of the drug molecules out of these pores is diminished, which leads to a reduced dissolution rate compared to the SASP carriers. The water accessibility of the SASP carriers is favored due to the wide mesopores (D_P (SASP) = 10 D_P (MCM-41/SBA-15)). Similar results were observed by Horcajada et al. [65] and Jin and Liang [66].

At pH = 2.0 the maximum dissolved amount of ibuprofen was reached after 20 – 30 min for all drug-carrier systems investigated. The fastest release was obtained with SMS-1.0 (k = 0.30 1/s) followed by SBA-15 (k = 0.23 1/s). Due to similar

Tab. 6 Results of ibuprofen dissolution in aqueous media according to the 1st-order kinetic model.

	pH = 2.0			**pH = 5.5**		
	k	D_{100}	**St.dev.**	k	D_{100}	**St.dev.**
	1/s	%	%	1/s	%	%
Ibuprofen	0.02	37.5	0.73	0.04	89.5	0.40
MCM-41	0.18	26.4	0.67	0.49	82.0	0.59
SBA-15	0.23	29.3	0.39	0.83	81.5	0.69
SMS-1.0	0.30	47.0	1.23	1.75	93.2	0.63
SMS-0.8	0.06	50.9	0.77	0.73	96.8	1.72

carrier properties both SBA-15 and MCM-41 show similar dissolution profiles. Despite from its large pore size and its good accessibility for the aqueous media SMS-0.8 ($k = 0.06$ 1/s) showed the weakest dissolution performance in the beginning of the experiments compared to all other drug-carrier systems. One reason might be the crystalline amount of ibuprofen inside the pores of SMS-0.8. Since this effect vanished with increasing pH-value it can be concluded that at low pH-values the dissolution rate of ibuprofen was more affected by its crystalline state while the particle size becomes more important at higher pH-values [7, 9, 12]. Similarly, to the results obtained for pH = 2.0, the highest dissolution rate was achieved at pH = 5.5 with SMS-1.0 ($k = 1.75$ 1/s) followed by SBA-15 ($k = 0.83$ 1/s)

4. Conclusion

In this study the influence of carrier properties on drug loading and dissolution rate of ibuprofen at pH = 2.0 and pH = 5.5 was investigated. Therefore, (SASP) was used to produce porous carrier materials with defined properties. A higher salt-to-SiO_2 ratio leads to a higher specific surface area and total pore volume while the pore size of the carrier materials was decreased. The SASP carriers were loaded with ibuprofen by applying the CPD process. Their loading results and dissolution rates were compared with those of MCM-41 and SBA-15. Lower loadings were obtained for the SASP carrier materials due to their smaller specific surface area. In addition, pore size and pore volume affects the loading capacity of the carrier materials. In the wider mesopores of the SASP carrier materials a higher number of monolayers were calculated. On these carriers crystalline ibuprofen structures were detected by XRD analysis. The results of the N_2-sorption experiments performed at $T = 77$ K with the CPD processed carriers lead to the assumption that the ibuprofen was mainly

deposited inside the small mesopores of MCM-41 and SBA-15 due to the fact that the typical capillary condensation step in the pressure range of $p/p_0 = 0.3 - 0.4$ was shifted towards lower relative pressures.

In addition, dissolution experiments were carried out with the CPD processed carrier materials. It was observed that the large mesopores of the SASP carriers enhance the dissolution rate of ibuprofen in aqueous media at pH = 2.0 and pH = 5.5. In opposite to this, dissolution out of the long and small channels of MCM-41 and SBA-15 was hampered. Furthermore, it was assumed that at low pH-values the dissolution rate of ibuprofen was more affected by its crystalline state, whereas particle size became more important at higher pH-values.

Acknowledgements

This work was supported by the grants TU 93/18-1 and WE 2331/19-1 of the DFG (Deutsche Forschungsgesellschaft), which is gratefully acknowledged. Furthermore, the authors thank Prof. Dr. Claus Feldmann, Institute of Inorganic Chemistry (KIT), for providing the XRD equipment. M. Shaban and A. Weber are sincerely grateful to Dr. Jalal Postforooshan (University of Tehran) for his contribution to the SASP synthesis of mesoporous silica.

References

[1] A. Kumar, S.K. Sahoo, K. Padhee, P.P.S. Kochar, A. Satapathy, N. Pathak, Review on solubility enhancement techniques for hydrophobic drugs, Pharmacie Globale – IJCP 2(3) (2011).

[2] M. Türk, G. Upper, M. Steurenthaler, Kh. Hussein, M.A. Wahl, Complex formation of ibuprofen and β-cyclodextrin by controlled particle deposition (CPD) using sc-CO_2, J. Supercrit. Fluids 39 (2007) 435–443.

[3] H.D. Williams, N.L. Trevaskis, S.A. Charman, R.M. Shanker, W.N. Charman, C.W. Pouton, C.J. Porter, Strategies to address low drug solubility in discovery and development, Pharmacol. Rev. 65(1) (2013) 315–499.

[4] G.L. Amidon, H. Lennernäs, V.P. Shah, J.R. Crison, A theoretical basis for a biopharmaceutic drug classification: the correlation of in vitro drug product dissolution and in vivo bioavailability, Pharm. Res. 12(3) (1995) 413–420.

[5] Y. Kawabata, K. Wada, M. Nakatani, S. Yamada, S. Onoue, Formulation design for poorly water-soluble drugs based on biopharmaceutics classification system: basic approaches and practical applications, Int. J. Pharm. 420(1) (2011) 1–10.

[6] M. Türk, B. Helfgen, P. Hils, R. Lietzow, K. Schaber, Micronization of pharmaceutical substances by rapid expansion of supercritical solutions (RESS): experiments and modelling, Part. Part. Syst. Char. 19(5) (2002) 327–335.

[7] M. Türk, Manufacture of submicron drug particles with enhanced dissolution behaviour by rapid expansion processes, J. Supercrit. Fluids 47 (2009) 537–545.

[8] J. Jung, M. Perrut, Particle design using supercritical fluids: literature and patent survey, J. Supercrit. Fluids 20 (2001) 179–219.

[9] M. Türk, Particle formation with supercritical fluids - challenges and limitations, Elsevier, Amsterdam, 2014, ISBN: 978-0-444-59486-0.

[10] G.M. Schneider, Physicochemical aspects of fluid extraction, Fluid Phase Equilib. 10(2) (1983) 141–157.

[11] E. Beckman, Supercritical and near-critical CO_2 in green chemical synthesis and processing, J. Supercrit. Fluids 28 (2004) 121–191.

[12] M. Charoenchaitrakool, F. Dehghani, N.R. Foster, H.K. Chan, Micronization by rapid expansion of supercritical solutions to enhance the dissolution rates of poorly water-soluble pharmaceuticals, Ind. Eng. Chem. Res. 39(12) (2000) 4794–4802.

[13] N.R. Foster, F. Dehghani, M. Charoenchaitrakool, B. Warwick, Application of dense gas techniques for the production of fine particles, AAPS Pharm. Sci. 5 (2003) 105–111.

[14] H.J. Martin, Charakterisierung von schwerlöslichen Arzneistoff-Nanopartikeln hergestellt durch das RESS-Verfahren zur Verbesserung der Bioverfügbarkeit, PhD thesis, Eberhard-Karls-Universität Tübingen, 2003.

[15] M. Türk, Erzeugung von organischen Nanopartikeln mit überkritischen Fluiden, PhD thesis, Universität Karlsruhe (TH), 2001.

[16] M. Türk, D. Bolten, Formation of submicron poorly water-soluble drugs by rapid expansion of supercritical solution (RESS): Results for naproxen, J. Supercrit. Fluids 55 (2010) 778–785.

[17] M. Bahrami, S. Ranjbarian, Production of micro- and nano-composite particles by supercritical carbon dioxide, J. Supercrit. Fluids 40 (2007) 263–283.

[18] P.M. Gallagher, M.P. Coffey, V.J. Krukonis, N. Klasutis, Gas antisolvent recrystallization: new process to recrystallize compounds insoluble in supercritical fluids, ACS Symp. Ser. 406 (1989) 334–354.

[19] E. Reverchon, I. De Marco, E. Torino, Nanoparticles production by supercritical antisolvent precipitation: A general interpretation, J. Supercrit. Fluids 43 (2007) 126–138.

[20] E. Weidner, Z. Knez, R. Steiner, Powder generation from polyethyleneglycols with compressible fluids, in: High Pressure Chemical Engineering, Elsevier, Amsterdam, 1996.

[21] E. Weidner, High pressure micronization for food applications, J. Supercrit. Fluids 47 (2009) 556–565.

[22] M. Perrut, J. Jung, F. Leboeuf, Enhancement of dissolution rate of poorly-soluble active ingredients by supercritical fluid processes Part I: Micronization of neat particles, Int. J. Pharm. 288 (2005) 3–10.

[23] A. Diefenbacher, M. Türk, Phase equilibria of organic solid solutes and supercritical fluids with respect to the RESS process, J. Supercrit. Fluids 22 (2002) 175–184.

[24] M. Türk, T. Kraska, Experimental and theoretical investigation of the phase behavior of naproxen in supercritical CO_2, J. Chem. Eng. Data 54(5) (2009) 1592–1597.

[25] S. Reiser, M. Sun, M. Johannsen, M. Türk, Influence of chemical nature of carrier materials on the dissolution behavior of racemic ibuprofen, J. Supercrit. Fluids, 132 (2018) 91–98

[26] K. Hussein, M. Türk, M.A. Wahl, Comparative evaluation of ibuprofen/β-cyclodextrin complexes obtained by supercritical carbon dioxide and other conventional methods, Pharm. Res. 24(3) (2007) 585–592.

[27] M. Banchero, S. Ronchetti, L. Manna, Characterization of ketoprofen/methyl-β-cyclodextrin complexes prepared using supercritical carbon dioxide, J. Chem. (2013) Article ID 583952, 8 pages.

[28] M. Charoenchaitrakool, F. Dehghani, N.R. Foster, Utilization of supercritical carbon dioxide for complex formation of ibuprofen and methyl-β-cyclodextrin, Int. J. Pharm. 239 (2002) 103–112.

[29] J. He, W. Li, Preparation of borneol-methyl-β-cyclodextrin inclusion complex by supercritical carbon dioxide processing, J. Incl. Phenom. Macrocycl. Chem. 65 (2009) 249–256.

[30] Y. Tozuka, T. Fujito, K. Moribe, K. Yamamoto, Ibuprofen-cyclodextrin inclusion complex formation using supercritical carbon dioxide, J. Incl. Phenom. Macrocycl. Chem. 56 (2006) 33–37.

[31] M. Betz, C.A. García-González, R.P. Subrahmanyam, I. Smirnova, U. Kulozik, Preparation of novel whey protein-based aerogels as drug carriers for life science applications, J. Supercrit. Fluids 72 (2012) 111–119.

[32] C.A. García-González, I. Smirnova, Use of supercritical fluid technology for the production of tailor-made aerogel particles for delivery systems, J. Supercrit. Fluids 79 (2013) 152–158.

[33] I. Smirnova, M. Türk, R. Wischumerski, M.A. Wahl, Comparison of different methods to enhance the dissolution rate of poor soluble drugs: case of Griseofulvin, Eng. Life Sci. 5(3) (2005) 277–280.

[34] Y.A. Hussain, C.S. Grant, Ibuprofen impregnation into submicron polymeric films in supercritical carbon dioxide, J. Supercrit. Fluids 71 (2012) 127–135.

[35] S.G. Kazarian, G.G. Martirosyan, Spectroscopy of polymer/drug formulations processed with supercritical fluids: in situ ATR-IR and Raman study of impregnation of ibuprofen into PVP, Int. J. Pharm. 232 (2002) 81–90.

[36] R.S. Wischumerski, M. Türk, M.A. Wahl, Direct drug loading into preformed porous solid dosage units by the controlled particle deposition (CPD), a new concept for improved dissolution using SCF-technology, J. Pharm. Sci. 97(10) (2008) 4416–4424.

[37] W. Li-Hong, C. Xin, X. Hui, Z. Li-Li, H. Jing, Z. Mei-Juan, L. Jie, L. Yi, L. Jin-Wen, Z. Wei, C. Gang, A novel strategy to design sustained-release poorly water-soluble drug mesoporous silica microparticles based on supercritical fluid technique, Int. J. Pharm. 454 (2013) 135–142.

[38] M. Ni, Q.-Q. Xu, J.-Z. Yin, Preparation of controlled release nanodrug ibuprofen supported on mesoporous silica using supercritical carbon dioxide, J. Mater. Res. 27(22) (2012) 2902–2910.

[39] F. Iskandar, I.W. Lenggoro, B. Xia, K. Okuyama, Functional nanostructured silica powders derived from colloidal suspensions by sol spraying, J. Nanopart. Res. 3(4) (2001) 263–270.

[40] J. Poostforooshan, S. Rennecke, M. Gensch, S. Beuermann, G.-P. Brunotte, G. Ziegmann, A.P. Weber, Aerosol process for the in situ coating of nanoparticles with a polymer shell, Aerosol Sci. Technol. 48 (2014) 1111–1122.

[41] M. Shaban, A. Ramazani, M.M. Ahadian, Y. Tamsilian, A.P. Weber, Facile synthesis of cauliflower-like hydrophobically modified polyacrylamide nanospheres by aerosol-photopolymerization, Eur. Polym. J. 83 (2016) 323-336.

[42] M. Shaban, J. Poostforooshan, A.P. Weber, Surface-initiated polymerization on unmodified inorganic semiconductor nanoparticles via surfactant-free aerosol-based synthesis toward core-shell nanohybrids with a tunable shell thickness, J. Mater. Chem. A 5(35) (2017) 18651–18663.

[43] I. Zbicinski, A. Delag, C. Strumillo, J. Adamiec, Advanced experimental analysis of drying kinetics in spray drying, Chem. Eng. J. 86(1) (2002) 207–216.

[44] L. Zeng, A.P. Weber, Aerosol synthesis of nanoporous silica particles with controlled pore size distribution, J. Aerosol Sci. 76 (2014) 1–12.

[45] J. Poostforooshan, A. Badiei, M. Kolahdouz, A.P. Weber, Synthesis of spherical carbon nitride-based polymer composites by Continuous Aerosol-Photopolymerization with effcient light harvesting, ACS Appl. Mater. Interfaces 8 (2016) 21731–21741.

[46] E. Ruiz-Hernández, A. López-Noriega, D. Arcos, I. Izquierdo-Barba, O. Terasaki, M. Vallet-Regí, Aerosol-assisted synthesis of magnetic mesoporous silica spheres for drug targeting, Chem. Mater. 19(14) (2007) 3455–3463.

[47] L.R. Shaw, W.J. Irwin, T.J. Grattan, B.R. Conway, The effect of selected water-soluble excipients on the dissolution of paracetamol and ibuprofen, Drug Dev. Ind. Pharm. 31 (2005) 515–525.

[48] X. Bin, I.W. Lenggoro, K. Okuyama, Synthesis of CeO_2 nanoparticles by salt-assisted ultrasonic aerosol decomposition, J. Mater. Chem. 11(12) (2001) 2925–2927.

[49] C. Panatarani, I.W. Lenggoro, K. Okuyama, Synthesis of single crystalline ZnO nanoparticles by Salt-Assisted Spray Pyrolysis, J. Nanopart. Res. 5 (2003) 47–53.

[50] S.H. Kim, B.Y.H. Liu, M.R. Zachariah, Synthesis of nanoporous metal oxide particles by a new inorganic matrix spray pyrolysis method, Chem. Mater., 14 (7) (2002) 2889–2899

[51] S.G. Lee, S.M. Choi, D. Lee, The role of salt in nanoparticle generation by salt-assisted aerosol method: Microstructural changes, Thermochimica Acta, 455, 1-2 (2007) 138-147.

[52] FDA, http://www.fda.gov. FDA IV, Guidance for Industry: Waiver of in vivo bioavailability and bioequivalence studies for immediate-release solid oral dosage forms based on a biopharmaceutics classification system, 2014 (accessed October 2014).

[53] A. Friebel, Aufbau und Inbetriebnahme einer Anlage zur Untersuchung der Auflösungsgeschwindigkeit von pharmazeutischen Wirkstoffen, Master's thesis, Karlsruher Institut für Technologie, 2015.

[54] S. Klein, V.P. Shah, A standardized mini paddle apparatus as an alternative to the standard paddle, AAPS Pharm. Sci. Tech. 9(4) (2008) 1179–1184.

[55] M. Thommes, K. Kaneko, A.V. Neimark, J.P. Olivier, F. Rodriguez-Reinoso, J. Rouquerol, K.S.W. Sing, Physisorption of gases, with special reference to the evaluation of surface area and pore size distribution (IUPAC Technical Report), Pure Appl. Chem. 87(9-10) (2015) 1051–1069.

[56] S.H. Kim, B.Y.H. Liu, M.R. Zachariah, Synthesis of nanoporous metal oxide particles by a new inorganic matrix spray pyrolysis method, Chem. Mater. 14(7) (2002) 2889–2899.

[57] IUPAC Commission on Colloid and Surface Chemistry Including Catalysis. Reporting physisorption data for gas/solid systems with special reference to the determination of surface area and porosity, Pure Appl. Chem. 57(4) (1985) 603–619.

[58] P. Gurikov, I. Smirnova, Amorphization of drugs by adsorptive precipitation from supercritical solutions: A review, J. Supercrit. Fluids, 132 (2018) 105-125

[59] A. Hillerström, J. van Stam, M. Andersson, Ibuprofen loading into mesostructured silica using liquid carbon dioxide as a solvent, Green Chem. 11 (2009) 662–667.

[60] M. Sliwinska-Bartkowiak, G. Dudziak, R. Gras, R. Sikorski, R. Radhakrishnan, K.E. Gubbins, Freezing behavior in porous glasses and MCM-41, Colloids Surf. A 187-188 (2001) 523–529.

[61] S.-C. Shen, W.K. Ng, L. Chia, Y.-C. Dong, R.B.H. Tan, Stabilized amorphous state of ibuprofen by co-spray drying with mesoporous SBA-15 to enhance dissolution properties, J. Pharm. Sci. 99(4) (2010) 1997–2007.

[62] P. Costa, J.M. Sousa Lobo, Modeling and comparison of dissolution profiles, Eur. J. Pharm. Sci. 13 (2001) 123–133.

[63] T.X. Bui, H. Choi, Adsorptive removal of selected pharmaceuticals by mesoporous silica SBA-15, J. Hazard. Mater. 168(1-2) (2009) 602–608.

[64] M. Meloun, S. Bordovska, L. Galla, The thermodynamic dissociation constants of four non-steroidal anti-inflammatory drugs by the least-squares nonlinear regression of multiwavelength spectrophotometric pH-titration data, J. Pharm. Biomed. Anal. 45(4) (2007) 552–564.

[65] P. Horcajada, A. Rámila, J. Pérez-Pariente, M. Vallet-Regí, Influence of pore size of MCM-41 matrices on drug delivery rate, Microporous Mesoporous Mater. 68 (2004) 105–109.

[66] Z. Jin, H. Liang, Effects of morphology and structural characteristics of ordered SBA-15 mesoporous silica on release of ibuprofen, J. Dispers. Sci. Technol. 31 (2010) 654–659.

Sarah Reiser[1]
Dennis Bolten[1]
Reiner Staudt[2]
Michael Türk[1]

[1]Institute for Technical Thermodynamics and Refrigeration, Karlsruhe Institute of Technology (KIT), Karlsruhe, Germany.

[2]Department of Mechanical Engineering and Process Engineering, Offenburg University of Applied Sciences, Offenburg, Germany.

Adsorption of N_2 and CO_2 on Activated Carbon, AlO(OH) Nanoparticles, and AlO(OH) Hollow Spheres

Adsorption behaviors of nitrogen and CO_2 on Norit R1 Extra and AlO(OH) nanoparticles and hollow spheres were measured under different temperature and pressure conditions using a magnetic suspension balance. Independent from the substrate investigated, all isotherms increase at lower pressure, reach a maximum, and then decrease with increasing pressure. In addition, selected experimental data were correlated with different model approaches and compared with reliable literature data. In case of CO_2 on AlO(OH), capillary condensation was observed at two defined temperatures. The results suggest that the conversion of the liquid into a supercritical adsorbate phase does not take place suddenly.

Keywords: Activated carbon, AlO(OH) nanoparticles, AlO(OH) hollow spheres, Carbon dioxide adsorption, Nitrogen adsorption

Received: June 30, 2015; *revised:* September 13, 2015; *accepted:* October 06, 2015

DOI: 10.1002/ceat.201500387

Note: The paper is formatted in the style of this work. Mistakes which were not recognized during the review process were corrected. Citations and References are according to journal style.

1. Introduction

Pharmaceuticals with high specific activity are often racemic mixtures. According to Gübitz and Schmid [1] almost 50 % of the pharmaceuticals used today are chiral and in the majority of cases the pharmaceutical activity is confined to one enantiomer while the other one is ineffective or even toxic to the human body [1, 2].

Among others, adsorption processes can achieve the separation of the enantiomers. In such a process, the racemic mixture is dissolved in supercritical CO_2 ($scCO_2$) and exposed to a e.g. chemical modified porous substrate on which the pure enantiomer adsorbs.

Besides high-surface-area carriers such as silica microparticles further promising applicable substrates are AlO(OH) hollow spheres (HS) [3]. Due to their unique structure with an inner cavity that is encapsulated by a solid wall hollow spheres are

of general interest for applications in materials science [4]. Moreover, they feature a large specific surface area, low specific weight, high mechanical stability, and the possibility to use the inner cavity as a container. Their potential for applications as high-surface materials for gas storage and gas separation or as pharmaceutical agents for drug delivery has already been investigated [5, 6].

In order to design such a supercritical adsorption process, it is essential to understand the adsorption behavior of the CO_2-racemate (enantiomer)-substrate system under the particular process conditions at constant pressure and temperature. Therefore, it is imperative to measure the adsorption isotherms of the pharmaceutical of interest in scCO_2-substrate systems. From an engineering point of view, such data are essential for the accurate design and modeling of supercritical adsorption processes.

As a first step, the adsorption behavior of pure N_2 and of pure CO_2 on activated carbon AC Norit R1 Extra, on commercial AlO(OH) and on AlO(OH)-HS was investigated at $T = 298$ K, 313 K and 328 K and pressures up to $p = 23.5$ MPa using a magnetic suspension balance (MSB). In addition, selected experimental data were correlated with the different model approaches. Mainly experimental adsorption data and a few modeling results will be presented and discussed.

2. Materials and Methods

2.1 Materials

AC Norit R1 Extra is a commercial activated carbon from Norit NV (Amersfoort, Netherlands). Boehmite nanoparticles were purchased from SkySpring Nanomaterials (Houston, TX, USA). The AlO(OH) hollow spheres (HS) were produced by the group

Tab. 1 Selected properties of AlO(OH) used in this work.

		AlO(OH)		**AlO(OH)-HS**	
Primary particle size	nm	10 – 20	[23]	30 – 35	[3]
		10 – 30	[3]		
Inner diameter	nm	-		20 – 25	[3]
Wall thickness	nm	-		4 – 7	[3]
Specific surface area	m^2/g	142.8	[23]	530	[3]
		117.0	[3]		
Pore volume	cm^3/g	0.73	[23]	0.6 – 0.8	[3]

of Feldmann (Institute for Inorganic Chemistry, KIT, Karlsruhe, Germany) [3]. Some more details about the properties of AlO(OH) nanoparticles and nano hollow spheres are summarized in Tab. 1. Due to their accessible inner surface the hollow spheres offer a high specific surface area which is up to 4.5 times larger than that of the AlO(OH) used in the present investigation and about twice as high as values reported for commercial AlO(OH) particles, e.g. 264 m^2/g [7] or 264.7 m^2/g [8] in literature. Helium (He 5.0), nitrogen (N_2 5.0), and carbon dioxide (CO_2 4.5) were purchased from Air Liquide (Düsseldorf, Germany) and used without any further purification.

2.2 Methods and data handling

The adsorption measurements were carried out using a magnetic suspension balance setup, which was provided by Rubotherm (Bochum, Germany). A schematic diagram of the setup is given in Fig. 1.

The balance enables measurements up to $T_{max} = 673$ K and $p_{max} = 40$ MPa. The weighing range of the balance is 0 – 5 g with a standard deviation of $\pm\ 5{\cdot}10^{-5}$ g. The temperature inside the cell is determined with a Pt100 resistance thermometer, the pressure with a pressure transducer (± 0.05 MPa).

Before starting the adsorption measurements, the samples were regenerated by He-flushing and one-hour heating step at $p = 0.1$ MPa and $T = 353$ K. Thereafter, He was released carefully and the measuring cell was evacuated overnight ($p \approx 3{\cdot}10^{-1}$ Pa) with a vacuum pump.

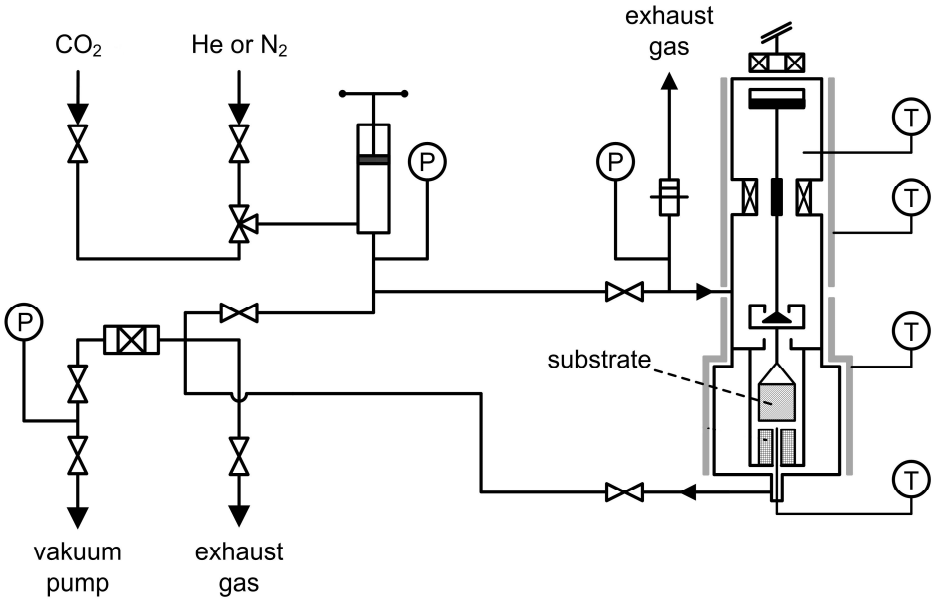

Fig. 1 Schematic diagram of the experimental setup.

The mass m_D can be described by Eq.(1) including the absolute adsorbed mass m, the mass of the interior parts m_{IP}, the mass of the sorbent m_S and the buoyancy correction described by the fluid density ϱ^f multiplied with the volume of the interior parts V_{IP} and the volume of the adsorbent/adsorbate system V^{as} [9].

$$m_D = m + m_{IP} + m_S - \rho^f \cdot V_{IP} - \rho^f \cdot V^{as} \tag{1}$$

The buoyancy of the interior floating parts (magnet, sample coupling, sample container) was determined with N_2 by taking 21 measuring points in the range $0 \leq p \leq 20$ MPa at $T = 298$ K resulting in a linear dependency with V_{IP} as gradient, m_{IP} as intercept and a coefficient of determination of $R^2 = 0.999$. The fluid density ϱ^f is calculated applying the program REFPROP [10].

Since the volume V^{as} cannot be determined directly, the reduced mass adsorbed Ω is introduced according to Keller and Staudt [9] in Eq.(2) for further calculations. V^{as} itself can be described by the sum of the sorbent volume V_S and the volume of the adsorbed fluid V^a as defined in Eq.(3).

$$\Omega = m - \rho^f \cdot V^{as} = m_D - m_{IP} - m_S + \rho^f \cdot V_{IP} \tag{2}$$

$$V^{as} = V_S + V^a \tag{3}$$

The sorbent volume V_S is determined experimentally as the so-called helium volume of the adsorbent [11, 12]. Therefore, 15 measuring points were taken before each experiment in the pressure range $0 \leq p \leq 6$ MPa which results in a linear regression with the gradient $V_{IP} + V_S$ and the intercept $m_{IP} + m_S$. From these data the true density of the sorbent material and the sample mass m_S can be determined. The excess adsorbate mass m_{GE} can be calculated by adding the buoyancy of the sorbent to Ω (Eq.(4)). Thereby, the specific surface excess amount adsorbed n^{ex}, which is applied for illustrating the adsorption isotherm, can be expressed in Eq.(5).

$$m_{GE} = \Omega + \rho^f \cdot V_S \tag{4}$$

$$n^{ex} = \frac{m_{GE}}{m_S \cdot M^f} \tag{5}$$

2.3 Calculating the relative error

The relative errors in Tab. 2 and Tab. 3 was calculated with Eq.(6).

$$\delta n^{ex} / [\%] = \frac{\delta n^{ex}}{n^{ex}} \cdot 100 \tag{6}$$

While calculating the error of the specific surface excess amount δn^{ex} (Eq.(7)), the error of the molar mass of the fluid δM^f was assumed negligible.

$$\delta n^{ex} = \left| \frac{1}{m_S \cdot M^f} \right| \delta m_{GE} + \left| \frac{m_{GE}}{{m_S}^2 \cdot M^f} \right| \delta m_S + \left| \frac{m_{GE}}{m_S \cdot M^{f^2}} \right| \delta M^f \tag{7}$$

The uncertainty of the excess adsorbate mass value δm_{GE} and the reduced mass adsorbed Ω can be calculated by Eq.(8) and Eq.(9). The errors of the interior parts (δV_{IP} and δm_{IP}) are derived from the N_2 measurements whereas δV_S and δm_S are determined from the helium measurement.

$$\delta m_{GE} = \delta\Omega + V_S \cdot \delta\rho^f + \rho^f \delta V_S \tag{8}$$

$$\delta\Omega = \delta m_D + \delta m_{IP} + \delta m_S + V_{IP} \cdot \delta\rho^f + \rho^f \delta V_{IP} \tag{9}$$

3 Results and Discussion

3.1 Adsorption of N2 and CO2 on AC Norit R1 Extra

In order to verify the reliability and accuracy of the experimental equipment, the adsorption behavior of N_2 on AC Norit R1 Extra was measured at $T = 298$ K and for pressures up to 6 MPa. The experimental results are listed in Tab. 2 and depicted in Fig. 2 together with data from literature.

The full line depicted in Fig. 2 was calculated with Eq.(10) and demonstrates that there is a good correlation between calculated values ($n_\infty = 5.29$ mmol/g; $b_L = 0.59$ 1/MPa; $R^2 = 0.999$) and the experimental data [13].

$$n = \frac{n_\infty \cdot b_L \cdot p}{1 + b_L \cdot p} \tag{10}$$

Furthermore, the experimental data are in good agreement with the reliable data from Dreisbach et al. [14] (gravimetric method), Beutekamp [15] (gravimetric method) and Bazan [16] (volumetric method). The highest deviation (~ 5 %) can be found compared to the data from Beutekamp while the deviation to Bazan is only ≤ 2 % although a volumetric method was used. It is worthy to notice that this

Tab. 2 Pressure p (MPa), excess amount n^{ex} (mmol/g) of pure N_2 and CO_2 adsorbed on AC Norit R1 Extra at T = 298 K, 313 K, 328 K and relative error (%).

N_2			**CO_2**								
T = 298 K			**T = 298 K**			**T = 313 K**			**T = 328 K**		
p	**n^{ex}**	**rel.err.**	**p**	**n^{ex}**	**rel.err**	**p**	**n^{ex}**	**rel.err**	**p**	**n^{ex}**	**rel.err.**
MPa	mmol/g	%	MPa	mmol/g	%	MPa	mmol/g	%	MPa	mmol/g	%
0.01	0.01	0.56	0.01	0.01	0.39	0.11	1.75	0.02	0.10	1.49	0.09
0.04	0.16	0.08	0.04	1.29	0.01	0.51	4.33	0.04	0.19	2.19	0.12
0.09	0.34	0.07	0.09	2.20	0.01	0.98	6.00	0.06	0.50	3.73	0.17
0.29	0.84	0.08	0.29	4.27	0.02	1.49	7.08	0.08	0.71	4.49	0.20
0.59	1.43	0.10	0.59	5.96	0.02	1.98	7.80	0.09	1.02	5.35	0.25
1.00	1.98	0.12	0.99	7.31	0.03	2.53	8.63	0.08	1.49	6.30	0.31
1.25	2.23	0.13	1.25	7.94	0.04	3.47	9.02	0.15	2.00	7.06	0.38
1.48	2.45	0.14	1.50	8.35	0.05	5.02	9.66	0.18	2.49	7.63	0.45
1.99	2.85	0.17	2.00	8.96	0.06	6.01	9.47	0.31	3.51	8.40	0.61
2.49	3.14	0.19	2.49	9.37	0.07	7.13	9.34	0.33	4.42	8.80	0.77
3.00	3.39	0.21	3.00	9.68	0.09	8.29	8.99	0.53	5.48	9.03	0.98
3.49	3.58	0.23	3.51	9.80	0.11	9.24	7.39	1.45	6.31	9.07	1.19
3.93	3.72	0.25	4.00	9.84	0.13	10.25	4.15	2.32	7.42	9.09	1.53
4.50	3.89	0.27	4.43	9.83	0.15	10.62	4.05	3.25	8.50	8.72	2.03
5.00	3.99	0.30	4.97	9.75	0.18	12.75	2.78	5.24	9.42	8.18	2.68
5.82	4.13	0.34	6.05	9.34	0.27	14.32	2.17	5.27	10.47	7.25	3.91
									11.42	6.08	5.82
									12.55	4.81	8.78
									13.30	4.19	10.88
									14.50	3.49	14.15
									16.26	2.81	19.01

deviation is lower than that found between the volumetric and gravimetric method for adsorption measurements with N_2 on activated carbon (3 %) [17].

The own experimental adsorption data for CO_2 on AC Norit R1 Extra are also listed in Tab. 2 and depicted together with experimental literature data in Fig. 3. Again, the full line was calculated with Eq.(10) while the broken line was calculated applying Eq.(11), an extended Langmuir approach. Compared to the results obtained for N_2, the former approach (n_∞ = 10.66 mmol/g; b_L = 2.35 1/MPa; R^2 = 0.991) leads to a slightly poorer description of the experimental values. In opposite thereto, the extended Langmuir-approach enables an improved description of the experimental data (n_∞ = 11.59 mmol/g; b_L = 1.93 1/MPa; c = 0.006 m^3·mmol/kg^2; R^2 = 0.996) [18].

$$n = \frac{n_\infty \cdot b_L \cdot p}{1 + b_L \cdot p} - c \cdot \rho^f \tag{11}$$

The comparison of the experimental data depicted in Fig. 3 shows that the results of the present investigation are similar to those of Dreisbach et al. [14] and Ustinov [19]. However, in the extended pressure range ($2 \le p \le 6$ MPa) the n^{ex} values of Dreisbach et al. (deviation ≤ 4 %) and Ustinov (deviation ≤ 7 %) are higher than the

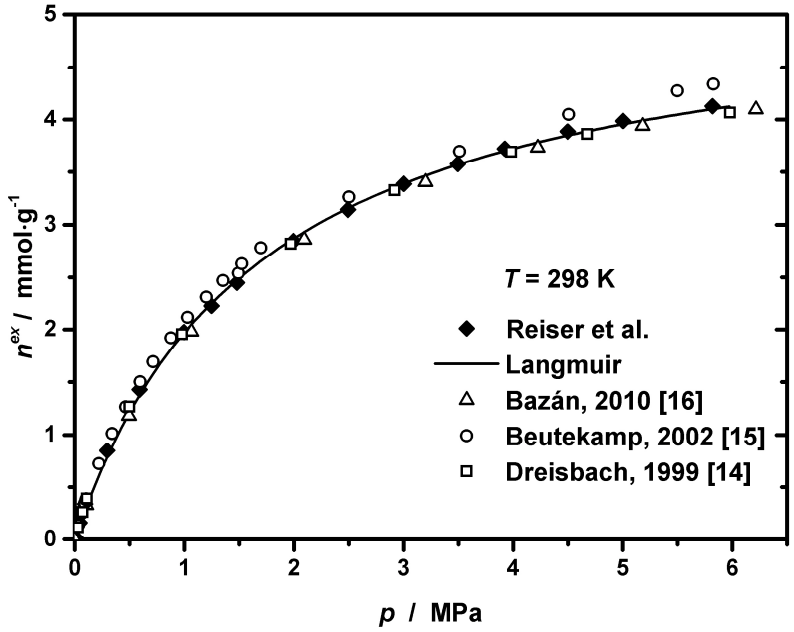

Fig. 2 Adsorption isotherm of N_2 on AC Norit R1 Extra at $T = 298$ K.

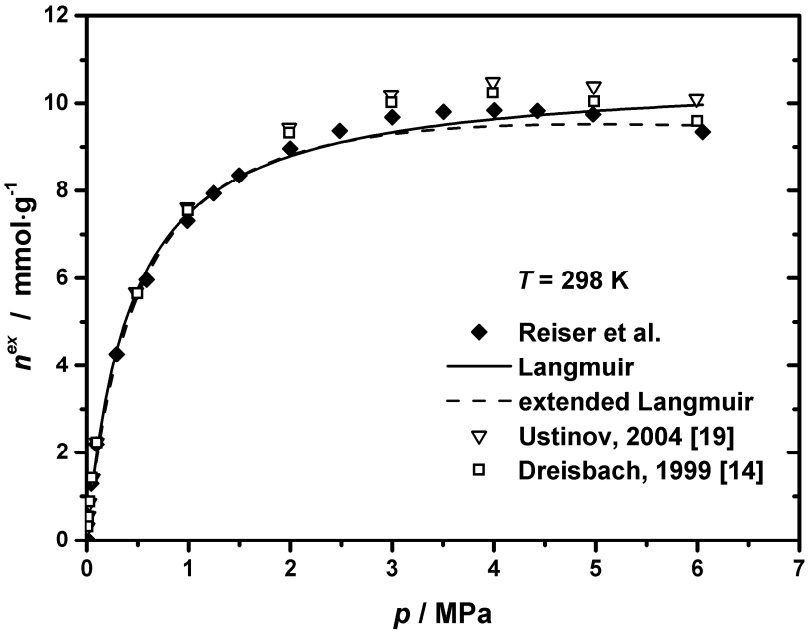

Fig. 3 Adsorption isotherm of CO_2 on AC Norit R1 Extra at $T = 298$ K.

own data. These differences might be explained by the differences in activation method, activation time and the age of the sample.

3.2 Adsorption of CO_2 on AC Norit R1 Extra at different temperatures

The experimental data for CO_2 on AC Norit R1 Extra are summarized in Tab. 2 and presented in Fig. 4.

Below the critical temperature, excess adsorption increases as the partial pressure approaches the saturation pressure, above that a discontinuity in the isotherm occurs due to the appearance of the two-phase region. For adsorption above the fluid's critical temperature, an excess adsorption isotherm increases at lower pressures, passes through a maximum and decreases at higher pressures. The maximum of the isotherms slightly shifts to higher pressures with a decrease in temperature.

In the lower pressure range ($p \leq 5$ MPa) the values of n^{ex} decrease with increasing temperatures. At constant pressure, the rise in temperature leads to a density reduction and therewith to less adsorptive molecules. Consequently, a smaller amount of molecules are able to interact with the adsorbent surface. In addition, the molecular velocity is magnified at higher temperatures, which also reduce the surface interactions between the adsorptive and adsorbent at the same density.

From the data depicted in Fig. 4 follows that the maximum of the excess isotherm shifts to higher pressures with rising temperature. This phenomenon is also a result of the enhanced kinetic energy of the single molecules at higher temperatures.

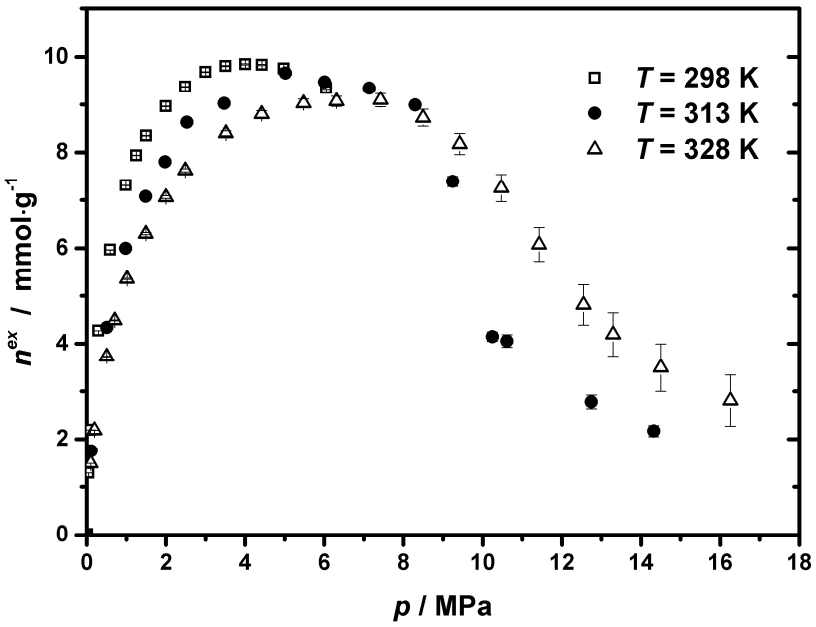

Fig. 4 Adsorption isotherm of CO_2 on AC Norit R1 Extra at $T = 298$ K, 313 K, 328 K.

Furthermore, due to the fact that attractive forces decrease with increasing temperature, desorption is more probable. Thus, higher pressures are necessary to reach maximum n^{ex} values at higher temperatures.

Above the maximum, the values of n^{ex} increase with higher temperature at constant pressure. Such a behavior can be explained by the fact that the fluid's density decreases with increasing temperature. Additionally, more molecules adsorb at the surface at lower temperatures, which leads to heavier sample masses and/or greater sample volumes. Both effects influence the buoyancy effect that dominates in this pressure range. From the results in Fig. 4 follows that beyond $p = 8$ MPa the gradient is higher at the lower temperature. This might be caused by the fact that close to the critical point of the fluid small variations in pressure lead to significant changes in density. This behavior is more pronounced at $T = 313$ K compared to $T = 328$ K and leads to smaller n^{ex} values at the lower temperature.

3.3 Adsorption of CO_2 on AlO(OH) and AlO(OH) hollow spheres at $T = 298$ K

The experimental data for the adsorption of gaseous CO_2 on AlO(OH) and on AlO(OH)-HS at $T = 298$ K are listed in Tab. 3, while the corresponding isotherms are depicted in Fig. 5.

According to Sing et al. [20] the isotherms can be assigned to type II of the IUPAC classification that indicates monolayer adsorption at low and multilayer adsorption at higher pressures [9]. This type of isotherm can be described with the model approach proposed by Brunauer et al. [21] (Eq.(12)).

$$n = n_{\infty}\left[\frac{b_{BET}\cdot\left(\frac{p}{p_s}\right)}{\left[1-\left(\frac{p}{p_s}\right)\right]\cdot\left[1+(b_{BET}+1)\cdot\left(\frac{p}{p_s}\right)\right]}\right] \tag{12}$$

The values obtained for n_∞, b_{BET} and p_S are summarized in Tab. 4. The lines depicted in Fig. 5 are calculated with Eq.(12) and demonstrate that there is a good correlation between calculated values and the experimental data. It can be seen from the R^2 value listed in Tab. 4 that Eq.(12) is able to describe the adsorption behavior of CO_2 on AlO(OH) in a satisfactory way. Assuming a totally occupied surface (monolayer) at pressures around $p \approx 1$ MPa the comparison between commercial AlO(OH) and AlO(OH)-HS shows that the adsorption capacity of the HS is about four times higher than that of the commercial material. It is worthy to notice that

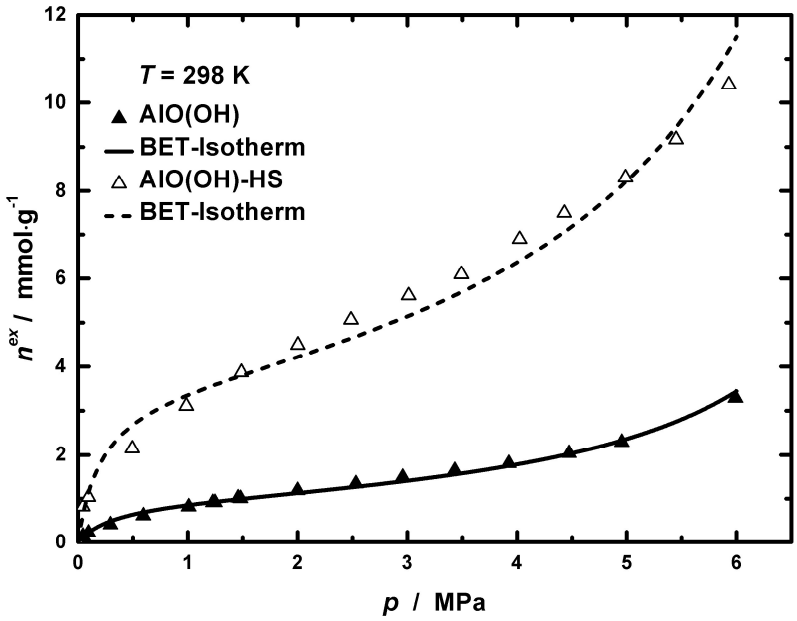

Fig. 5 Adsorption isotherm of CO_2 on AlO(OH) and on AlO(OH)-HS at $T = 298$ K.

Tab. 4 Constants of Eq.(12) for the adsorption of CO_2 on AlO(OH) and AlO(OH)-HS at $T = 298$ K.

	n_∞	b_{BET}	p_S	R^2
	mmol/g	-	MPa	-
AlO(OH)	1.04	23.72	8.271	0.998
AlO(OH)-HS	3.66	40.38	8.572	0.974

this value corresponds with the ratios of the specific surface area data (3.7 and 4.5) listed in Tab. 1.

The pore system of AlO(OH) and of AlO(OH)-HS provide specific pore volumes of $v_{PS} = 0.73$ cm^3/g and $v_{PS} = 0.6 - 0.8$ cm^3/g, respectively. In case of these materials it is not clear whether the specific pore volume data describe the pores within the single particles or additional pores formed due to agglomeration of the single particles. Assuming a total condensation of CO_2 within the pores, the pore system of AlO(OH) with a volume of $V_P = 0.719$ cm^3 (for $m_S = 0.985$ g) would be filled up to 26 % at $p = 6$ MPa ($\varrho_{CO2,liquid}' = 751.91$ kg/m^3). On the other hand the pores of AlO(OH)-HS with a volume of $V_P = 0.424 - 0.565$ cm^3 (for $m_S = 0.706$ g) would be filled in the range between 74 % and 100 % at $p = 5.9$ MPa ($\varrho_{CO2,liquid}' = 756.97$ kg/m^3).

3.4 Adsorption of CO_2 on AlO(OH) at different temperatures

The experimental data for CO_2 on AlO(OH) at $T = 298$ K, 313 K and 328 K and for pressures up to $p = 23.5$ MPa are listed in Tab. 3 and depicted in Fig. 6. Again, the single adsorption isotherm increases at low pressures, reaches a maximum and

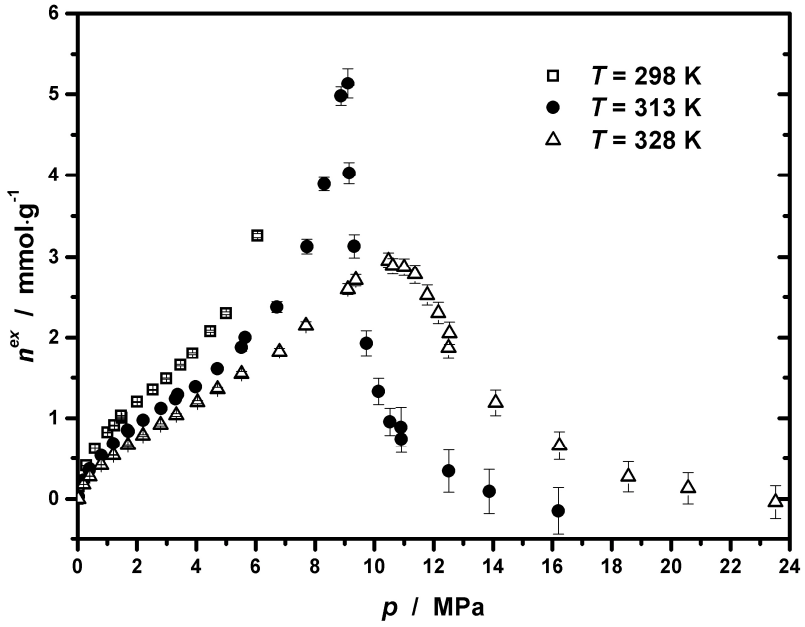

Fig. 6 Adsorption isotherm of CO_2 on AlO(OH) at $T = 298$ K, 313 K, 328 K.

decreases with increasing pressure. Reducing the temperature leads to lower maximum values and to a shift of the maximum towards higher pressure.

In the low-pressure range ($p \leq 9$ MPa) the adsorption excess n^{ex} decreases with rising temperature. Two effects can explain this behavior: The attractive forces between the adsorbate and the adsorbent surface are stronger at the lower temperature; furthermore, the kinetic energy of the molecules increases with temperature while the fluid's density decreases.

As mentioned above, below the fluids' critical temperature, excess adsorption increases as the partial pressure approaches the saturation pressure. Thus, as soon as the saturation pressure of CO_2 ($p_{vap} = 6.41$ MPa) (REFPROP [10]) is reached at $T = 298$ K, relatively high values for n^{ex} are achieved which indicate that capillary condensation takes place. Due to the strong intermolecular interactions between the individual adsorbate molecules and the weak fluid-pore interactions, the bulk fluid condenses and behaves like a liquid phase. A similar behavior can be observed in the low-pressure region at $T = 313$ K which indicates that for the confined fluid a shift for both the vapor pressure and the critical temperature must occur [22]. In contrast, the typical gas-phase adsorption behavior is observed at $T = 328$ K. The isotherm increases with higher pressure until the maximum at about 11 MPa is reached and then decreases with increasing pressure due to the prevailed buoyancy effect.

In Fig. 7 the reduced mass loss (m_D/m_{D_vac}) versus CO_2 density is illustrated. At $T = 328$ K the typical mass loss trend without capillary condensation is slightly

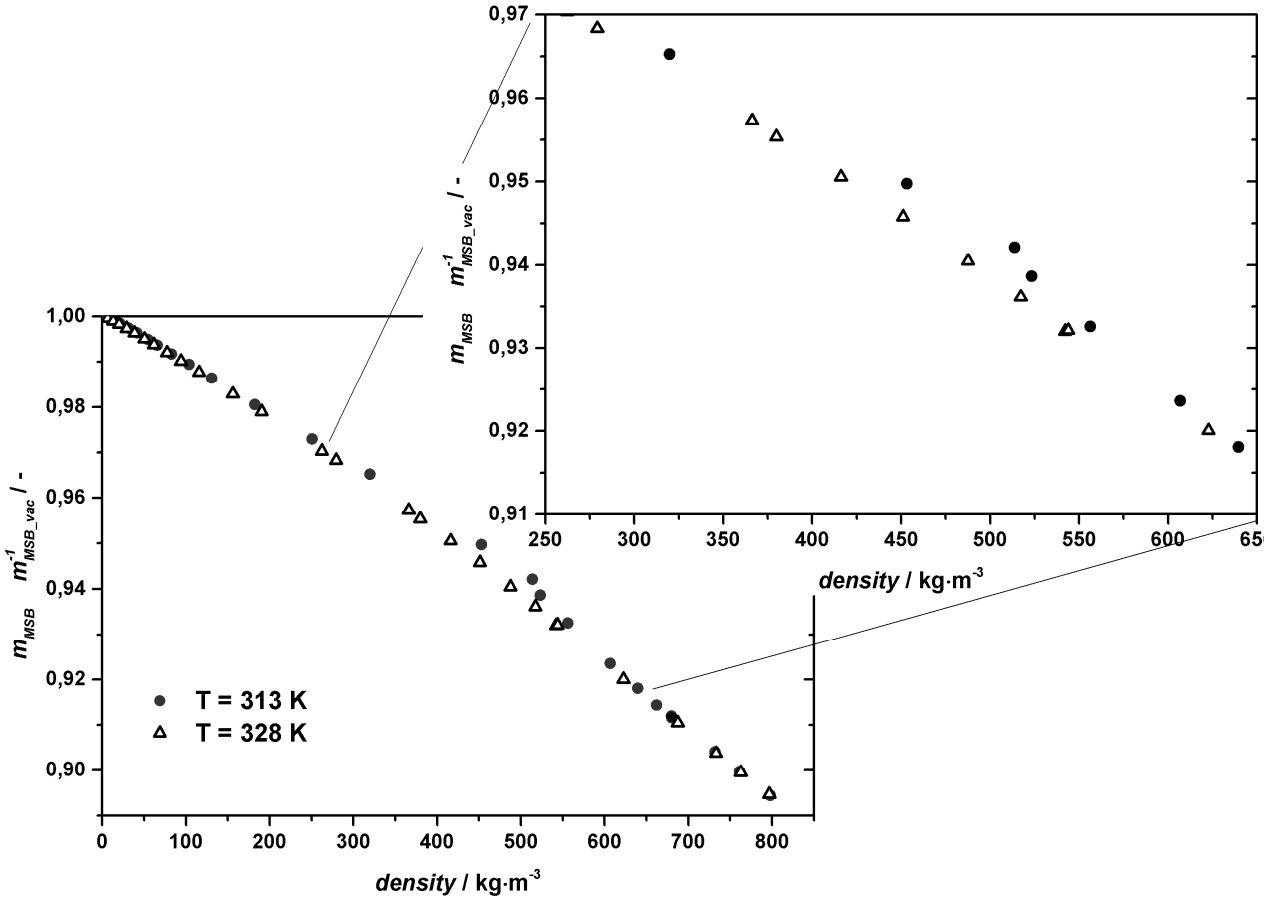

Fig. 7 Dependency of reduced mass loss versus CO_2 density at $T = 313$ K and 328 K.

concave due to the buoyancy effect. In opposite thereto, at $T = 313$ K a hump can be observed at a density of around $\varrho = \sim 450$ kg/m^3 that is close to the critical density of $\varrho = 467.6$ kg/m^3 and indicates an apparent increase in weight. One potential explanation, could be the appearance of capillary condensation inside the pores until the n^{ex} values reach a maximum at $p = 9$ MPa (Fig. 6). This assumption will be supported by the data depicted in Fig. 7 since the largest deviations from the concave curve progression occurs in the density range between $\varrho = 450$ and 525 kg/m^3.

After the near-critical isotherm ($T = 313$ K) passes through its maximum at $p = 9$ MPa the adsorption excess decreases dramatically for pressures up to $p = 13$ MPa. In general, at higher pressures the buoyancy effect prevails, but this unique behavior is mainly associated to the highly compressible state of the fluid near to the critical point. From the data in Fig. 7 follows that the transition of the liquid into a supercritical phase requires a large density increase from $\varrho = 512$ kg/m^3 which corresponds to the maximum difference between the data for $T = 313$ K and $T = 328$ K, up to $\varrho = 600$ kg/m^3 at which the difference between both curves disappears.

Tab. 3 Pressure p (MPa), excess amount n^{ex} (mmol/g) of pure CO_2 adsorbed on AlO(OH) at $T = 298$ K, 313 K and 328 K and on AlO(OH)-HS at $T = 298$ K and relative errors (%).

AlO(OH)									**AlO(OH)-HS**		
$T = 298$ K			$T = 313$ K			$T = 328$ K			$T = 298$ K		
p	n^{ex}	rel.err.	p	n^{ex}	rel.err.	p	n^{ex}	rel.err.	p	n^{ex}	rel.err.
MPa	mmol/g	%	MPa	mmol/g	%	MPa	mmol/g	%	MPa	mmol/g	%
0.01	0.01	0.56	0.19	0.23	0.53	0.20	0.18	0.47	0.04	0.82	0.02
0.04	0.15	0.07	0.40	0.35	0.70	0.41	0.28	0.61	0.09	1.04	0.03
0.09	0.22	0.10	0.41	0.37	0.52	0.80	0.42	0.80	0.49	2.14	0.08
0.29	0.41	0.16	0.80	0.53	0.94	1.21	0.54	0.96	0.99	3.11	0.11
0.59	0.62	0.22	1.20	0.68	1.12	1.70	0.67	1.12	1.49	3.87	0.13
1.00	0.83	0.28	1.68	0.85	0.98	2.20	0.79	1.25	2.00	4.49	0.16
1.23	0.91	0.32	1.71	0.84	1.33	2.80	0.92	1.39	2.49	5.06	0.18
1.24	0.91	0.32	2.21	0.98	1.52	3.33	1.04	1.50	3.01	5.61	0.20
1.48	1.01	0.35	2.81	1.12	1.74	4.03	1.20	1.64	3.49	6.09	0.22
1.46	1.03	0.34	3.29	1.24	1.90	4.72	1.36	1.75	4.03	6.90	0.24
2.00	1.20	0.41	3.37	1.29	1.43	5.52	1.55	1.89	4.43	7.49	0.26
2.53	1.35	0.48	3.97	1.39	2.14	6.80	1.83	2.16	4.987	8.31	0.27
2.99	1.49	0.53	4.71	1.61	2.31	7.69	2.15	2.24	5.45	9.17	0.29
3.46	1.65	0.58	5.52	1.88	2.49	9.37	2.71	2.61	5.93	10.41	0.32
3.87	1.80	0.62	5.64	2.00	1.84	10.47	2.96	3.13			
4.47	2.08	0.66	6.72	2.38	2.74	10.48	2.97	3.12			
5.01	2.30	0.70	7.73	3.13	2.86	10.62	2.88	3.34			
6.07	3.26	0.72	8.31	3.89	2.09	11.00	2.87	3.67			
			8.87	4.98	2.31	11.37	2.78	4.11			
			9.10	5.14	3.57	11.78	2.52	4.89			
			9.15	4.03	3.30	12.15	2.31	5.69			
			9.32	3.13	4.50	12.50	1.87	7.31			
			9.73	1.93	7.96	12.53	2.05	6.71			
			10.14	1.33	12.18	14.09	1.19	13.24			
			10.52	0.96	17.53	16.23	0.66	26.38			
			10.90	0.89	27.30	18.56	0.27	67.67			
			10.91	0.75	23.11	20.48	0.16	122.54			
			12.51	0.34	76.20	20.57	0.13	147.18			
			13.87	0.09	297.96	23.52	-0.04	517.42			
			16.20	-0.15	194.93						

4 Conclusions

A magnetic suspension balance setup was used for the investigation of the adsorption behavior of N_2 and CO_2 on activated carbon AC Norit R1 Extra at $T = 298$ K in the pressure range $0 \leq p \leq 6$ MPa. These experimental data were in good accordance to reliable experimental data published in literature. Furthermore, the adsorption behavior of CO_2 on AC Norit R1 Extra was measured at $T = 313$ K and 328 K at pressures up to $p = 16$ MPa.

On this basis, the adsorption behavior of CO_2 on AlO(OH) and on AlO(OH) hollow spheres was investigated at $T = 298$ K and pressures up to $p = 6$ MPa and the obtained data were correlated using the model approach proposed by Brunauer et al. The results show that the adsorption capacity of AlO(OH)-HS is about four times higher than that of commercial AlO(OH) which is caused by the difference in the specific surface area.

Additionally, the adsorption behavior of CO_2 on AlO(OH) was measured at $T = 313$ K and 328 K in the pressure range up to $p = 23.5$ MPa. The experimental results obtained for $T = 298$ K and 313 K indicate that capillary condensation occurs. It was also observed that the transition of the liquid into a supercritical phase requires a large density increase.

Acknowledgements

This work was supported by the Deutsche Forschungsgemeinschaft (DFG) within the priority program SPP 1570 (FE 911/5-1, JO 339/7-1, STA 428/18-1, TU 93/14-1 and TU 93/18-1) and by the Federal State of Baden-Württemberg which the authors gratefully acknowledge. They thank Sara Simonato and Claus Feldmann (KIT) as well as Johannes Kern and Monika Johannsen (Technical University Hamburg-Harburg) for a good and trustworthy cooperation within the project. In addition, the authors thank the group of Claus Feldmann (KIT) for the preparation and synthesis of the AlO(OH)-HS. Furthermore, the authors appreciate the provision of the magnetic suspension balance by Rubotherm (Bochum, Germany).

Symbols used

b_L	[1/Pa]	Langmuir-parameter
b_{BET}	[-]	BET-constant
c	[m^3·mol/g^2]	correction parameter
m	[g]	absolute adsorbed mass
m_D	[g]	mass displayed by the balance
m_{D_vac}	[g]	mass displayed by the balance at vacuum
m_{GE}	[g]	Gibbs excess adsorbate mass, corrected by the He volume
m_{IP}	[g]	mass of interior parts (magnet, sample coupling, sample container)
m_S	[g]	sorbent mass
M_f	[g/mol]	molar mass fluid
n	[mol]	adsorbed amount
n^{ex}	[mol/g]	surface excess amount adsorbed
n_∞	[mol/g]	adsorbed amount (completely covered surface)
p	[Pa]	pressure
p_S	[Pa]	saturation vapor pressure
p_{vap}	[Pa]	vapor pressure
R^2	[-]	coefficient of determination
T	[K]	temperature
V^a	[m^3]	adsorbate volume
V^{as}	[m^3]	volume of adsorbent/adsorbate system
V_{IP}	[m^3]	volume of interior parts (magnet, sample coupling, sample container)
V_P	[m^3]	pore volume
v_{PS}	[m^3/g]	specific pore volume
V_S	[m^3]	sorbent volume
v_S	[m^3/g]	specific sorbent volume

Greek symbols

Ω	[g]	reduced mass adsorbed
ϱ^f	[kg/m^3]	fluid density
ϱ'	[kg/m^3]	liquid density (boiling point)

References

[1] G. Gübitz, M.G Schmid, Mol. Biotechnol. **2006**, *32(2)*, 159-179.

[2] H.Y. Aboul-Enein, I. Ali, Chiral Separation by Liquid Chromatography and Related Technologies, Marcel Dekker, New York **2003**.

[3] S. Simonato, H. Gröger, J. Möllmer, R. Staudt, A. Puls, F. Dreisbach, C. Feldmann, Chem. Commun. **2012**, *48(6)*, 844-846.

[4] C. Feldmann, in *Produktgestaltung in der Partikeltechnologie Band 6* (Eds: U. Teipel, A. Weber), Fraunhofer IRB Verlag, Pfinztal **2013**, 9-19.

[5] H. Goesmann, C. Feldmann, Angew. Chem. Int. Edit. **2010**, *49(8)*, 1362-1395.

[6] X.W. Lou, L.A. Archer, Z. Yang, Adv. Mater. **2008**, 20(21), 3987-4019.

[7] T.C. Alex, R. Kumar, S.K. Roy, S.P. Mehrotra, Hydrometallurgy **2013**, *137*, 23-32 .

[8] G. Li, L. Guan, Y. Liu, C. Liu, J. Phys. Chem. Solids **2012**, *73(9)*, 1055-1060.

[9] U. Keller, R. Staudt, Gas adsorption equilibria – experimental methods and adsorptive isotherms, Springer, Boston **2005**.

[10] E. W. Lemmon, M. L. Huber, M. O. McLinden: *NIST standard reference database 23: Reference Fluid Thermodynamic and Transport Properties – REFPROP, Version 9.1*, National Institute of Standards and Technology, Standard Reference Data Program, Gaithersburg, MD, **2013**.

[11] D.M. Young, A.D. Crowell, *Physical adsorption of gases*, Butterworths, London **1962**.

[12] S.J. Gregg, K.S.W. Sing, Adsorption, surface area and porosity, Academic Press, London **1967**, 371.

[13] I. Langmuir, J. Am. Chem. Soc. **1918**, *40(9)*, 1361-1403.

[14] F. Dreisbach, R. Staudt, J. U. Keller,Adsorption 1999, *5(3)*, 215-227.

[15] S. Beutekamp, Adsorptionsgleichgewichte der reinen Gase CO_2, CH_4, N_2 und deren binärer Gemische an verschiedenartigen porösen Stoffen, VDI-Verlag, Düsseldorf **2002**.

[16] R. E. Bazan, *Ph.D Thesis*, Universität Leipzig **2010**.

[17] Y. Belmabkhout, M. Frère, G. De Weireld, Meas. Sci. Technol. **2004**, *15(5)*, 848-858.

[18] A. Myers, personal communication **2010**.

[19] E.A. Ustinov, R. Staudt, D.D. Do, A. Herbst, P. Harting, J. Colloid Interface Sci. **2004**, *275*, 376-385.

[20] K.S.W. Sing, D.H. Everett, R.A.W. Haul, L. Moscou, R.A. Pierotti, J. Rouquérol, T. Siemieniewska, Pure Appl. Chem. **1985**, *57(4)*, 603-619.

[21] S. Brunauer, P.H. Emmet, E. Teller, **1938**, *60(2)*, 309-319.

[22] M. Thommes, G.H. Findenegg, Langmuir **1994**, *10*, 4270-4277.

[23] SkySpring Nanomaterials, Inc., Houston, TX, Manufacturer's data. http://www.ssnano.com/inc/sdetail/boehmite_nanoparticles/192, accessed July **2013**.

Influence of temperature and high pressure on the adsorption behavior of $scCO_2$ on MCM-41 and SBA-15

Sarah Reiser[1], Michael Türk[1]*

[1]Institute for Technical Thermodynamics and Refrigeration, Karlsruhe Institute of Technology (KIT), Engler-Bunte-Ring 21, D - 76131 Karlsruhe

*Corresponding author, Email: tuerk@kit.edu, phone: +49 721 608 42330

In preparation

Abstract

The controlled particle deposition (CPD) process is a suitable way to obtain pharmaceutical drug-delivery products with controlled and improved dissolution properties which are solvent free and ready-to-use. In this high pressure process, the drug is dissolved in supercritical carbon dioxide and deposited on suitable carrier materials. For the accurate design and modeling of such a highpressure process, it is essential to understand the adsorption and desorption kinetics of the drug-carrier system as well as those of the supercritical carbon dioxide-carrier-system at the particular process conditions. It has been shown that silica (e.g. MCM-41 or SBA-15) are suitable carrier materials. Due to a lack of literature data of carbon dioxide adsorption on MCM-41 and SBA-15 at possible operating CPD process conditions six excess adsorption isotherms ($T = 298 - 353$ K, $p = 0 - 25$ MPa) which were measured by a magnetic suspension balance are presented. Furthermore, the absolute amount adsorbed as well as the isosteric heat of adsorption were calculated. In a first approach it was obvious that the adsorption of carbon dioxide was almost six times higher compared to the loading of ibuprofen on these carrier materials during the deposition step of the CPD process.

Keywords: Adsorption, supercritical carbon dioxide, silica, CPD process, ibuprofen

1. Introduction

With increasing interest scientists put lots of effort in research on nanoparticles due to their positive influence on material properties. Nanoparticles can be found e.g. in fields like advanced materials, catalysts, food, optics or pharmaceutical applications. Conventional particle size reduction processes like milling, spray-drying or crystallization cause several problems (bimodal particle size distribution, thermal or chemical degradation of the product or residues of organic compounds in the final product) [1]. To prevent these disadvantages various processes with supercritical fluids (SCF) are under investigation [2, 3]. The fact that SCFs combine liquid like densities and gaseous mass transport properties (diffusion and viscosity coefficients) [4] is exploited in that kind of processes. Particles in nanoscale range can be produced for example by the Rapid Expansion of Supercritical Solution (RESS) process [5, 6] but a further processing of the obtained products is difficult. To avoid this drawback supercritical impregnation processes like the Supercritical Fluid Reactive Deposition (SFRD) [7 - 9] or the Controlled Particle Deposition process (CPD) [3, 10] are in focus of research. In these processes substances which are soluble in a supercritical fluid can be deposited on carrier materials. The obtained nanoparticles produced by these kind of processes show improved material properties. It has been verified in various publications that e.g. catalysts prepared by SFRD exhibit an activity higher than reference samples prepared by conventional methods [11 - 13].

Another example is the improvement of the bioavailability of orally applied drugs which are poorly water soluble (class II of the Biopharmaceutical Classification System [14]). Their dissolution in the gastro intestinal tract depends amongst others on the particle size [15]. It has been shown in different studies that the dissolution of drug-carrier systems produced by the CPD process can be improved significantly compared to their unprocessed counterparts [10, 16 - 19].

Especially carbon dioxide (CO_2) is considered to be a suitable solvent for these kind of processes. Its low critical pressure and temperature ($p_c = 7.4$ MPa, $T_c = 304$ K) enables moderate processing conditions. Besides this carbon dioxide is nontoxic, inflammable and inexpensive. To characterize the process and to investigate the interactions of supercritical carbon dioxide with carrier materials adsorption data at high pressures are required. Only very few papers deal with this issue because most adsorption research is focused on developing time and cost effective CO_2 capturing and separation processes at low pressures to repeal the problem of global warming [20]. Therefore, microporous materials like zeolites, activated carbons and metal

organic frameworks (MOF) as well as mesoporous silica are under investigation [21 - 23]. Adsorbents with high specific surface areas and large pore volumes are beneficial for CO_2 storage. Because of the fact that pure silica interacts only weakly with carbon dioxide (specific adsorption sites are missing and the residual hydroxyl groups are not able to induce strong interactions) surface functionalization for instance with amines are also in focus of research [24, 25]. This functionalization might be a benefit at very low pressures ($p \leq 0.05$ MPa) but is a disadvantage at high pressures for the adsorption of carbon dioxide because of the smaller surface area compared to the un-functionalized adsorbent [25].

High pressure gas adsorption (e.g. nitrogen, methane, argon, carbon dioxide) in a wide range of pressures and temperatures on molecular sieves [26 - 28], carbon black [29, 30], activated carbon [31 - 34], MOFs [35, 36], silica gels [37] and various aerogels [38 - 40] were published. These data were typically derived by gravimetric [41] or volumetric [42] measuring techniques.

Since it has been shown that mesoporous silica [43, 44] are useful carrier materials to load pharmaceutical substances via the CPD process information about the high pressure adsorption behavior of carbon dioxide on these adsorbents is necessary. An overview of the published data is presented to the best of our knowledge in the following section. Nevertheless, supercritical adsorption data of carbon dioxide on MCM-41 and SBA-15 at the operating CPD pressure and temperature ranges ($T = 308 - 353$ K and $p = 15/25$ MPa) are rarely to find.

Strubinger et al. [45, 46] investigated the carbon dioxide adsorption on different silica, bonded/grafted silica and polymer adsorbents which are used in supercritical fluid chromatography. Adsorption isotherms at $T = 313$ K in a pressure range of $p = 0 - 14$ MPa were measured by mass spectrometric tracer pulse chromatography. The isotherms showed a maximum and multilayer adsorption close to the critical pressure. The density and dimensions of the adsorbed layer varied with pressure and temperature. A gravimetric apparatus was used by Wang and Le Van [47] to investigate carbon dioxide adsorption on grade 40 and silica at sub- and supercritical temperatures up to $p = 0.1$ MPa. Adsorption data on MCM-41 at $T = 298$ K and pressures from $p = 0 - 1$ MPa were derived by pressure-swing adsorption [48]. At the same temperature Liu et al. [49] measured the adsorption of carbon dioxide on SBA-15 at $p = 0 - 4$ MPa with a volumetric apparatus. With this technique Ozawa and Ogino [50] measured the adsorption of carbon dioxide on silica gel at supercritical temperatures ($T = 313$ K, 333 K, 353 K) up to $p = 10$ MPa. Adsorption data on

SBA-15 which were measured with a magnetic suspension balance at $T = 298$ K and 348 K in a pressure rage from $p = 0 - 5$ MPa were provided by Wang et al. [51].

Studies with regard to capillary condensation in different mesoporous silica (SBA-15 and FSM-n) were accomplished by Tadsuda et al. [52]. It was observed that the temperature up to which capillary condensation turns up is strongly pore size dependent. This temperature is decreasing with smaller pores. It was also observed that this temperature varies to the temperature at which hysteresis in capillary condensation occurs [53].

The effect that the absorption intensity of infrared light depends on the density of the media was exploited by Schneider et al. [54], to draw conclusions to the density state of the adsorbed and adsorptive phase inside silica pores.

Furthermore, the adsorption of carbon dioxide on silica was found to be heterogeneous due to surface roughness and the electrostatic interactions between carbon dioxide and the surface atoms [55]. Loganathan et al. [56] identified specific surface groups of MCM-41 which are interacting with carbon dioxide. H-bound interactions were found between isolated silanol groups and carbon dioxide whereas dispersive interactions to siloxane were found up to $p = 2.5$ MPa at supercritical temperatures.

Grand Canonical Monte Carlo simulations were performed for example by He and Seaton [57] at $T = 264$ K and 303 K and pressures up to $p = 3$ MPa. Three different surface heterogeneity models were used for the simulation. Excellent predictions of experimental data were derived if an amorphous structure surface model was used. Also long-ranged electrostatic interactions were considered.

Since there is a lack of data in the operating CPD processing conditions at high pressures ($p \leq 25$ MPa) adsorption data of carbon dioxide on MCM-41 and SBA-15 at six temperatures ($T = 298 - 353$ K) are presented. Results for the loading of the model substance ibuprofen on these carrier materials at $T = 313$ K and $p = 15$ MPa were published elsewhere [16]. With the derived data it was possible to give a first estimation of the carbon dioxide adsorption in comparison to the ibuprofen

Tab. 1 Characteristic properties of untreated carrier materials.

	Specific surface area A_{BET} m^2/g	**Total pore volume** V_P cm^3/g	**Av. pore diameter** D_P nm
MCM-41	1078	1.087	3.0 – 6.0
SBA-15	987	0.838	3.5 – 4.5

deposition on MCM-41 and SBA-15 during the CPD process.

2. Materials and Methods

2.1 Materials

In this work two commercially available mesoporous silicas (MCM-41 (Sigma-Aldrich) and SBA-15 (ACS Materials)) were investigated. To characterize these adsorbents N_2-adsorption measurements at $T = 77$ K were carried out at the INC (Institut für Nichtklassische Chemie e.V.), Leipzig [58], with a Quantachrome AutoSorb-IQ. The samples were outgassed at $T = 573$ K for 16 h under vacuum ($p = 10$ Pa). To obtain the specific surface area, pore volume and pore size (listed in Tab. 1) the measured adsorption data were evaluated by the Autosorb-Software. In Fig. 1 the calculated particle size distribution (density functional theory (DFT) method: cylinderical pore, nonlocal DFT equilibrium model) and the N_2-adsorption/desorption-isotherms are depicted.

Helium (He 5.0), nitrogen (N_2 5.0), and carbon dioxide (CO_2 4.5) were purchased from Air Liquide (Düsseldorf, Germany) and used without any further purification.

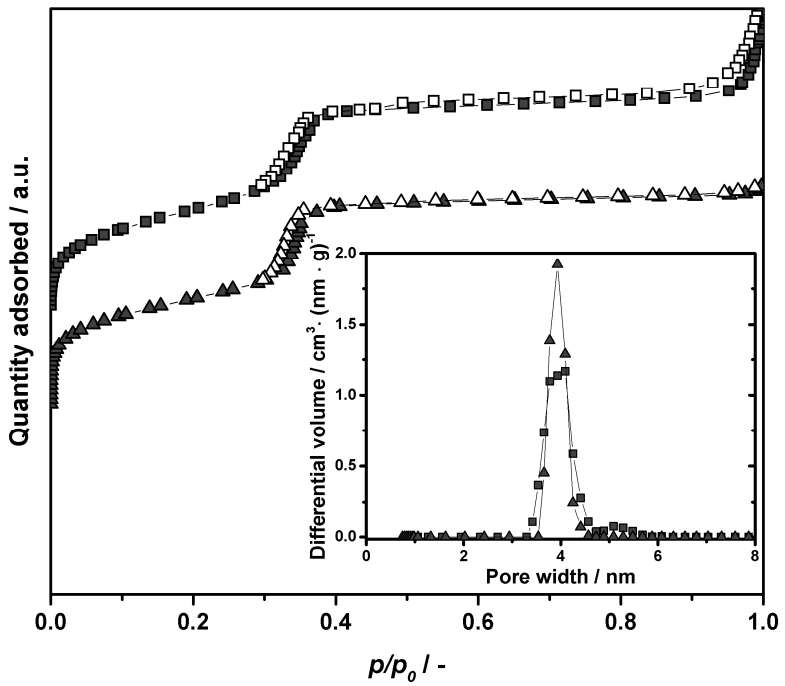

Fig. 1 N_2-sorption isotherms at $T = 77$ K and pore size distribution calculated by the DFT method for commercially available carrier materials MCM-41 (squares) and SBA-15 (triangles). Full symbols indicate the adsorption while open symbols indicate desorption data.

The carrier materials mentioned above were impregnated with ibuprofen (Knoll Pharmaceuticals, Germany) by the controlled particle deposition process [16]. A schematic diagram of the process and further process information are also published in [16].

2.2 Methods and data handling

High pressure adsorption measurements were carried out in a magnetic suspension balance (MSB) (Rubotherm, Germany) which enables measurements up to $T_{max} = 673$ K and $p_{max} = 40$ MPa. The weighing range of the balance is 0 – 5 g with a standard deviation of $\pm 5 \cdot 10^{-5}$ g. The temperature inside the cell was measured with a Pt100 resistance thermometer while the pressure was measured with a pressure transducer (± 0.05 MPa). A schematic diagram of the setup is given in Fig. 2. In a typical experiment the samples (MCM-41: ~0.3 g, SBA-15: ~0.2 g) were filled in the sample container and regenerated with He at $p = 1$ MPa and $T = 353$ K for one hour. Thereafter, He was released carefully and the measuring cell was evacuated overnight with a vacuum pump until a constant mass signal was achieved.

The signal m (see Eq.(1)) which is detected by the MSB includes the weight of the

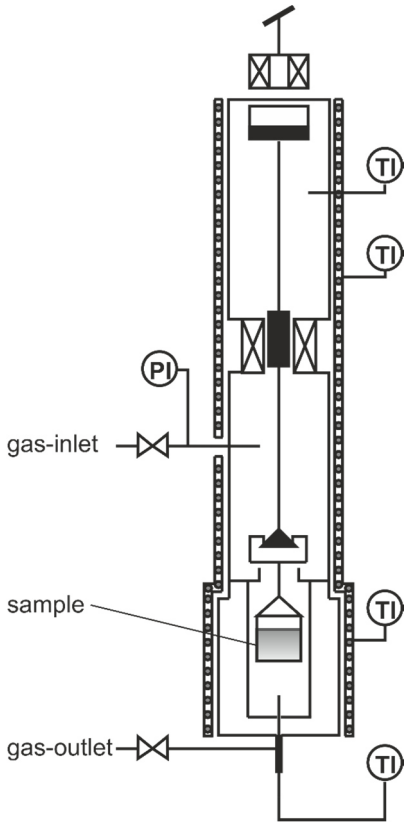

Fig. 2 Schematic setup of the magnetic suspension balance.

interior parts m_{ip} (magnet, sample coupling, sample container), the sample m_s and the amount adsorbed m_{ads}. In addition to the masses mentioned above the buoyancy effect, which is described by the fluid density ϱ_{bulk} multiplied by the volume of the interior parts V_{ip} and the volume of the adsorbent/adsorbate system ($V_s + V_{ads}$), has to be considered [59].

$$m = m_{ads} + m_s + m_{ip} - \rho_{bulk} \cdot (V_{ads} + V_s + V_{ip}) \tag{1}$$

The weight of the interior parts and their volume can be determined with nitrogen. Therefore 21 measuring points in the range of $0 \leq p \leq 25$ MPa were taken at every measured temperature. In this case the weight signal showed a linear dependency from the fluid density (calculated by the Span-Wagner-EoS [60]). The volume of the interior parts can be derived by the slope and their weight is defined by the intercept.

Since the volume V_{ads} cannot be determined directly the reduced mass adsorbed Ω is introduced for further calculations according to Keller and Staudt [59] in Eq.(2). V^{as} is equivalent to the sum of the sample volume V_s and the volume of the adsorbed fluid V_{ads} (Eq.(3)). In this equation the absolute amount adsorbed corresponds to the reduced mass Ω and a buoyancy term which includes the volume of the sample and the adsorbate V^{as}.

$$\Omega = m_{ads} - \rho_{bulk} \cdot V^{as} = m - m_s - m_{ip} + \rho_{bulk} \cdot V_{ip} \tag{2}$$

$$V^{as} = V_s + V_{ads} \tag{3}$$

The sample weight and volume can be derived by a buoyancy measurement using helium as an inert adsorptive. Therefore 10 measuring points were taken before each experiment in the pressure range $0 \leq p \leq 10$ MPa which result in a linear regression with the gradient $V_{ip} + V_s$ and the intercept $m_{ip} + m_s$. The obtained sample volume V_s is considered as the so-called helium volume of the adsorbent [61, 62], which is used to calculate the Gibbs surface excess m_{GE} (Eq.(4)).

The expression for the specific surface excess amount adsorbed n^{ex} which is applied for illustrating the adsorption isotherm is presented in Eq.(5). Therefore, m_{GE} is divided by the sample mass m_s and the molecular mass of the bulk fluid M.

$$m_{GE} = \Omega + \rho_{bulk} \cdot V_s \tag{4}$$

$$n^{ex} = \frac{m_{GE}}{m_s \cdot M} \tag{5}$$

All isotherms were measured at least in duplicate. The relative error δn^{ex} of the measured data was calculated as published elsewhere [63]. Because of the fact that the data points for the same temperature at different measurements are in good agreement with the calculated relative errors only one isotherm set for each temperature is presented.

2.3 Calculating the absolute amount adsorbed

Since it is not possible to measure the absolute amount adsorbed n_{abs} directly different calculation approaches can be found in literature. One way is to use Eq.(6) for the description of n_{abs}.

$$n_{abs} = n^{ex} + \rho_{bulk} \cdot V_{ads} \tag{6}$$

In this model there are different ways to estimate the volume of the adsorbed phase V_{ads}. Based on the assumption that all molecules inside the pores are adsorbed, V_{ads} can be related to the pore volume V_{pore}. This hypothesis is applicable especially in microporous materials when overlapping force fields of opposite pore walls enhance adsorption [34].

To assess V_{ads} in systems without enhanced adsorption ability more recommendations are given by Dubinin [64] or Menon [65]. While Dubinin proposes different calculation concepts which are temperature dependent, Menon estimates V_{ads} out of a linear regression of the experimental data. This approach is possible due to the fact that at high pressures n^{ex} shows a linear dependency from the bulk density when adsorption saturation is reached. From the resulting slope V_{ads} can be determined.

The calculation of n_{abs} by estimating the density of the adsorbed phase is proposed by Tsai et al. [66] (Eq.(7)). In this approach, the value which is used for ϱ_{ads} is temperature dependent. For subcritical adsorption conditions it seems to be suitable to use the density of the liquefied gas at its boiling point ($\varrho_{ads} = \varrho_{liq,Tboil}$) at ambient pressure or the density in the liquid triple state ($\varrho_{ads} = \varrho_{liq,\ TP}$) [59, 67]. Furthermore, it is suggested to set ϱ_{ads} as the reciprocal value of the Van der Waals constant b of the fluid [65, 68].

$$n_{abs} = \frac{n^{ex}}{(1 - \frac{\rho_{bulk}}{\rho_{ads}})} \tag{7}$$

In this paper the linear regression method of Menon was used to obtain V_{ads} to calculate the absolute amount adsorbed of all supercritical isotherms by Eq.(6). Pore filling factors (PFF) were calculated by Eq.(8).

$$PFF = \frac{V_{abs}}{V_{pore}} \tag{8}$$

3. Results and Discussion

3.1 Adsorption of carbon dioxide on MCM-41 and SBA-15 at sub- and supercritical conditions

The results of the adsorption measurements of carbon dioxide on MCM-41 and SBA-15 at sub- and supercritical conditions are listed in Tab. 2 and Tab. 3. In addition, the measured excess isotherms are illustrated in Fig. 3 and Fig. 4. To ensure a better clarity all isotherms for $T \geq 313$ K are plotted as density dependent and the error bars are only shown for n^{ex}. The typical shape of high pressure isotherms was observed at both silica. The excess amount adsorbed was increasing with rising pressure followed by a maximum and its subsequently decrease. The reason for the decrease of n^{ex} is that with rising pressure the bulk phase is more compressible compared to the adsorbed phase whereby the buoyancy effect is prevailing.

The maximum was followed by an inflection point whose location depended on the adsorbent/adsorbate interactions and the thermodynamic state of the adsorptive [67]. After the inflection point the monotonic decrease of the adsorption isotherm reflected the buoyancy of the saturated adsorbent.

At temperatures far above the critical temperature ($T/T_c \geq 1.06$) the descending branch of the isotherm was almost linear for both adsorbents, whereas “bumps” were detected around the critical density at temperatures close to T_c ($T/T_c = 1.01, 1.03$). This phenomenon was also observed for carbon dioxide adsorption on HKUST-1 [67], activated carbon [68], zeolite 13X and silica gel [69].

At constant density higher values of n^{ex} were measured at lower temperatures in both carbon dioxide-adsorbent systems. This is considered to be a result of the higher adsorption ability due to the reduced kinetic energy of carbon dioxide molecules and enhanced attractive forces at lower temperatures.

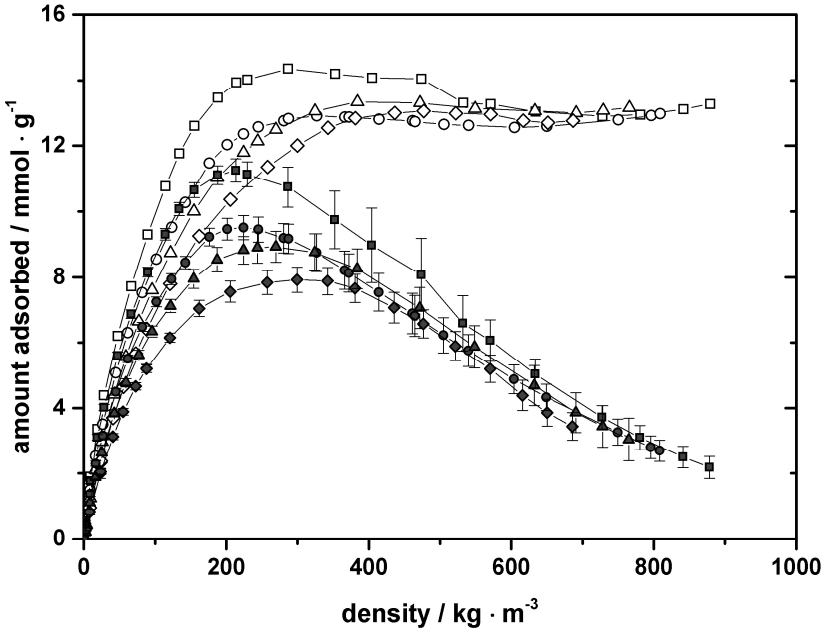

Fig. 3 Adsorption isotherms of carbon dioxide on MCM-41 at supercritical temperatures $T = 313$ K (squares), 328 K (circles), 338 K (triangles), 353 K (diamonds). Full symbols represent the measured n^{ex} data, open symbols show the absolute amount adsorbed n_{abs} (while using Eq.(6) ($T > T_c$) for calculation.

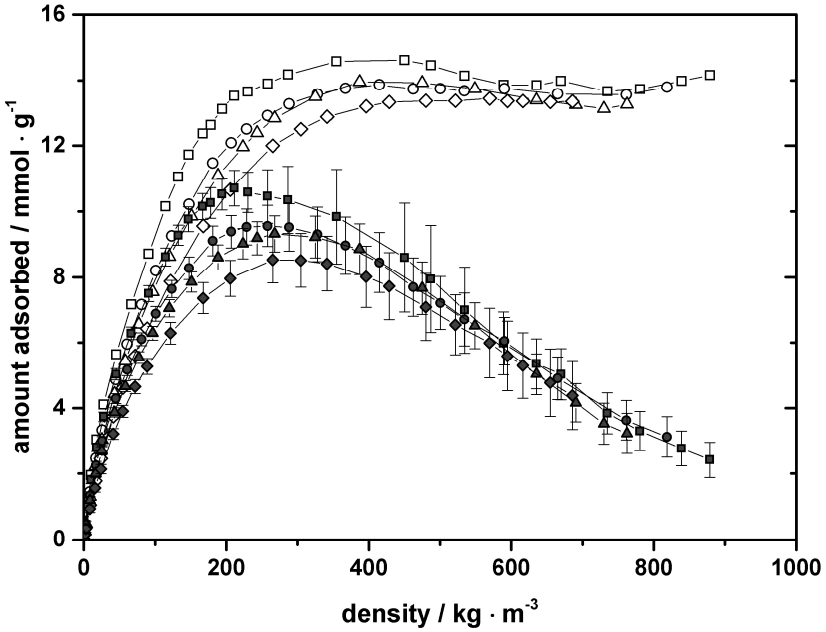

Fig. 4 Adsorption isotherms of carbon dioxide on SBA-15 at supercritical temperatures $T = 313$ K (squares), 328 K (circles), 338 K (triangles), 353 K (diamonds). Full symbols represent the measured n^{ex} data, open symbols show the absolute amount adsorbed n_{abs} (while using Eq.(6) ($T > T_c$) for calculation.

It was observed that small relative errors were obtained at low and high densities while the magnitude of the error bars became significantly high and that they were

temperature dependent in the region of $150 < \varrho < 650$ kg/m^3. Furthermore, higher relative errors were calculated at temperatures closer to T_c. Due to the fact that the density strongly influences the calculation of n^{ex} the calculation of the error bars is highly sensitive to density variations. In the density region described above, carbon dioxide shows an enormous density deviation within small variations in pressure [60]. This might be a good explanation for the higher relative errors at the isotherms close to T_c. The results of the excess amount adsorbed presented in this work are in good agreement to carbon dioxide adsorption on pore expanded MCM-41 at $T = 303$ K, 318 K, 333 K, 343 K in a pressure range of $p = 0 - 2.5$ MPa measured by Loganathan et al. [56] with a magnetic suspension balance. With the same method significant lower adsorption of carbon dioxide on Kieselgel 60 was measured by Di Giovanni et al. [70] at $T = 312 - 466$ K in a pressure range of $p = 0 - 36.6$ MPa. Due to the fact that the surface area of Kieselgel 60 ($A_{BET} = 480 - 540$ m^2/g) is significantly smaller compared to the adsorbents investigated in this work the results might be in better agreement when n^{ex} is referred to the surface area (n^{ex} / μmol/m^2). Smaller deviations in the lower pressure range were observed which might be a reason of different activation methods. In comparison to this, higher deviations were obvious in a density rage of $150 < \varrho < 550$ kg/m^3 at temperatures close to the critical temperature $T/T_c < 1.03$. These deviations are owed by the difficulty in measurement in this region. Adsorption of carbon dioxide on silica aerogels at $T = 308$ K in a pressure range of $p = 0 - 3.5$ MPa were derived by Anas et al. [40] These results are in good agreement with the results obtained in this study.

The adsorption of carbon dioxide on SBA-15 at $T = 298$ K in a pressure range of $p = 0 - 5$ MPa was published by Wang et al. [51]. In lower pressure ranges $p < 3.5$ MPa the data published by these authors were slightly higher than those presented in this work. One reason of these deviations might be the result of different activation methods. At higher pressures both data sets are comparable.

With regard to the subcritical temperature $T = 298$ K capillary condensation was not observed in both adsorptive/adsorbent systems. This is in good agreement with the results reported by Morishige et al. [53] and Tatsuda et al. [52]. These authors proclaimed that capillary condensation is only noticeable if $T \leq T_{CP}$ (critical temperature for capillary condensation). For SBA-15 ($r_P = 3.02$ nm) the critical temperature for capillary condensation was found to be $T_{CP} = 292$ K. In FSM-systems ($r_P < 2.14$ nm) capillary condensation occurred below $T_{CP} \leq 274$ K. In situ FTIR spectroscopy studies performed by Schneider et al. [54] it was proposed that monolayer adsorption at low pressures is followed by continuous pore filling with

Tab. 2 Experimental adsorption results of carbon dioxide on MCM-41.

$T = 298$ K				$T = 308$ K				$T = 313$ K			
p	ϱ	n^{ex}	$\delta\ n^{ex}$	p	ϱ	n^{ex}	$\delta\ n^{ex}$	p	ϱ	n^{ex}	$\delta\ n^{ex}$
MPa	kg/m^3	mmol/	mmol/	MPa	kg/m^3	mmol/	mmol/	MPa	kg/m^3	mmol/	mmol/
0.00	0.00	0.00	0.00	0.00	0.00	0.00	0.00	0.00	0.00	0.00	0.00
0.17	3.04	1.10	0.08	0.14	2.41	0.56	0.09	0.13	2.21	0.51	0.08
0.57	10.39	2.70	0.09	0.56	9.87	1.97	0.10	0.54	9.34	1.78	0.08
0.99	18.51	3.96	0.09	1.03	18.56	3.23	0.10	1.07	18.92	3.11	0.09
1.52	29.36	5.35	0.10	1.53	28.30	4.25	0.11	1.56	28.30	4.03	0.10
2.49	51.17	7.42	0.12	2.50	48.83	5.98	0.13	2.50	47.65	5.61	0.11
3.26	71.07	9.06	0.14	3.21	65.59	7.18	0.14	3.33	66.66	6.89	0.13
4.24	101.33	11.59	0.18	4.06	88.23	8.58	0.17	4.22	89.69	8.17	0.15
4.99	130.65	12.68	0.23	4.97	116.89	10.11	0.21	5.05	114.54	9.31	0.18
5.76	172.13	12.81	0.33	5.50	136.81	10.89	0.23	5.61	133.89	10.08	0.20
6.01	190.83	12.71	0.40	6.08	162.38	11.38	0.29	6.15	155.32	10.65	0.23
				6.62	192.28	11.56	0.37	6.83	188.02	11.10	0.29
				7.15	232.35	11.66	0.51	7.26	213.86	11.25	0.36
				7.54	277.24	11.29	0.76	7.48	229.62	11.13	0.38
				7.75	316.51	11.02	1.06	8.09	286.85	10.74	0.61
				7.92	366.58	10.77	1.95	8.51	352.74	9.75	0.87
				8.00	407.72	10.65	2.73	8.73	404.68	8.98	1.13
				8.08	464.85	10.03	2.45	8.98	473.96	8.08	1.11
				8.21	536.65	8.00	1.58	9.23	532.59	6.60	0.85
				8.44	598.46	6.05	0.87	9.46	571.23	6.07	0.63
				9.70	699.03	4.11	0.48	10.11	634.10	5.05	0.46
				12.27	771.67	3.10	0.41	12.42	727.94	3.73	0.36
				14.98	813.97	2.60	0.37	15.12	781.19	3.11	0.37
				19.77	863.25	2.10	0.38	20.29	841.84	2.51	0.33
				25.21	902.18	1.75	0.38	25.06	879.37	2.20	0.34

Tab. 2 Experimental adsorption results of carbon dioxide on MCM-41.

$T = 328$ K				$T = 338$ K				$T = 353$ K			
p	ϱ	n^{ex}	$\delta\ n^{ex}$	p	ϱ	n^{ex}	$\delta\ n^{ex}$	p	ϱ	n^{ex}	$\delta\ n^{ex}$
MPa	kg/m³	mmol/	mmol/	MPa	kg/m³	mmol/	mmol/	MPa	kg/m³	mmol/	mmol/
0.00	0.00	0.00	0.00	0.00	0.00	0.00	0.00	0.00	0.00	0.00	0.00
0.14	2.19	0.43	0.08	0.09	1.41	0.21	0.07	0.18	2.71	0.30	0.07
0.54	8.89	1.38	0.08	0.19	2.99	0.42	0.08	0.54	8.20	0.83	0.07
1.01	16.91	2.31	0.08	0.55	8.76	1.12	0.08	1.49	23.39	2.01	0.16
1.56	26.67	3.17	0.09	1.02	16.53	1.90	0.09	1.52	23.81	2.06	0.08
2.52	44.95	4.50	0.10	1.54	25.40	2.64	0.10	2.54	41.08	3.14	0.09
3.33	61.70	5.52	0.12	2.50	42.76	3.85	0.11	3.34	55.47	3.89	0.10
4.23	82.06	6.49	0.13	3.34	59.14	4.78	0.13	4.26	73.08	4.68	0.11
5.02	101.83	7.26	0.15	4.20	77.20	5.63	0.15	5.01	88.31	5.22	0.13
5.79	123.30	7.95	0.17	5.02	95.88	6.35	0.17	5.00	88.25	5.21	0.12
6.41	142.51	8.46	0.19	6.05	121.82	7.13	0.21	6.47	121.13	6.16	0.14
7.36	176.40	9.23	0.27	7.18	154.47	7.96	0.29	8.06	162.00	7.06	0.25
7.96	201.32	9.47	0.33	8.16	187.32	8.55	0.37	9.53	205.65	7.57	0.32
8.44	224.26	9.52	0.36	9.11	224.28	8.83	0.42	11.03	257.98	7.85	0.36
8.83	245.13	9.46	0.38	9.56	244.06	8.91	0.47	12.09	299.78	7.93	0.39
9.41	280.75	9.20	0.45	10.09	269.74	8.93	0.47	13.10	342.76	7.89	0.42
9.51	287.45	9.17	0.45	11.09	324.56	8.77	0.56	13.97	381.02	7.67	0.43
10.04	327.17	8.76	0.57	12.04	384.11	8.27	0.61	15.24	436.25	7.08	0.47
10.50	366.41	8.23	0.58	13.43	472.04	7.07	0.63	16.25	477.09	6.58	0.43
10.57	372.64	8.14	0.58	14.93	549.07	5.88	0.65	17.51	522.16	5.90	0.44
11.01	414.26	7.56	0.58	17.38	633.16	4.70	0.61	19.14	571.00	5.21	0.42
11.52	461.58	6.90	0.62	20.02	691.16	3.87	0.61	21.05	616.72	4.39	0.46
11.56	464.97	6.83	0.63	22.41	728.98	3.45	0.64	22.84	651.32	3.87	0.42
12.04	505.50	6.23	0.54	25.41	765.64	3.05	0.65	25.08	686.60	3.44	0.42
12.52	540.26	5.77	0.49								
13.70	604.49	4.89	0.44								
14.93	650.00	4.34	0.40								
19.75	750.24	3.27	0.40								
23.62	796.65	2.81	0.34								
24.92	809.21	2.70	0.32								

Tab. 3 Experimental adsorption results of carbon dioxide on SBA-15.

$T = 298$ K				$T = 308$ K				$T = 313$ K			
p	ϱ	n^{ex}	$\delta\ n^{ex}$	p	ϱ	n^{ex}	$\delta\ n^{ex}$	p	ϱ	n^{ex}	$\delta\ n^{ex}$
MPa	kg/m^3	mmol/	mmol/	MPa	kg/m^3	mmol/	mmol/	MPa	kg/m^3	mmol/	mmol/
0.00	0.00	0.00	0.00	0.00	0.00	0.00	0.00	0.00	0.00	0.00	0.00
0.15	2.68	0.86	0.12	0.13	2.24	0.55	0.12	0.13	2.21	0.41	0.12
0.52	9.44	2.32	0.13	0.54	9.50	1.93	0.13	0.58	10.13	1.81	0.12
1.02	19.09	3.70	0.14	1.03	18.54	3.10	0.14	1.02	18.04	2.80	0.13
1.60	31.09	4.94	0.15	1.53	28.27	4.05	0.15	1.54	27.91	3.73	0.15
2.48	50.90	6.54	0.19	2.52	49.28	5.60	0.17	2.40	45.42	5.03	0.18
3.28	71.63	8.05	0.21	3.30	67.83	6.72	0.20	3.33	66.66	6.29	0.19
4.16	98.49	10.08	0.27	4.18	91.72	8.03	0.24	4.27	90.96	7.50	0.24
4.98	129.92	11.14	0.34	5.00	117.94	9.38	0.28	5.06	114.85	8.62	0.27
5.37	148.53	11.18	0.40	5.49	136.36	10.12	0.33	5.57	132.38	9.28	0.31
5.95	184.85	10.88	0.55	6.00	158.52	10.56	0.38	5.95	146.88	9.77	0.37
				6.47	183.24	10.75	0.47	6.41	166.91	10.14	0.39
				7.08	226.63	10.91	0.64	6.64	178.03	10.26	0.46
				7.58	283.10	11.00	1.09	6.94	194.12	10.53	0.48
				7.75	315.48	11.25	1.54	7.22	211.12	10.70	0.54
				7.91	363.05	11.66	2.51	7.49	230.07	10.58	0.61
				7.98	396.60	12.24	3.35	7.82	258.01	10.45	0.81
				8.08	462.86	13.28	3.51	8.09	286.53	10.35	1.02
				8.18	521.99	11.43	2.57	8.52	354.66	9.84	1.44
				8.38	586.56	7.46	1.24	8.89	450.15	8.60	1.65
				9.50	689.55	4.55	0.65	9.03	487.09	7.94	1.63
				12.21	770.86	3.40	0.56	9.24	534.50	7.00	1.32
				14.73	810.77	2.92	0.53	9.61	589.16	5.98	0.97
				19.96	864.89	2.41	0.53	10.13	635.38	5.35	0.76
				25.95	906.47	2.09	0.54	10.73	669.77	5.03	0.79
								12.70	734.77	3.84	0.63
								15.09	780.69	3.30	0.60
								19.99	838.99	2.76	0.53
								24.98	878.74	2.41	0.53

Tab. 3 Experimental adsorption results of carbon dioxide on SBA-15.

$T = 328$ K				$T = 338$ K				$T = 353$ K			
p	ϱ	n^{ex}	$\delta\ n^{ex}$	p	ϱ	n^{ex}	$\delta\ n^{ex}$	p	ϱ	n^{ex}	$\delta\ n^{ex}$
MPa	kg/m³	mmol/	mmol/	MPa	kg/m³	mmol/	mmol/	MPa	kg/m³	mmol/	mmol/
0.00	0.00	0.00	0.00	0.00	0.00	0.00	0.00	0.00	0.00	0.00	0.00
0.10	1.62	0.28	0.11	0.09	1.41	0.24	0.11	0.07	1.12	0.15	0.09
0.53	8.70	1.32	0.12	0.18	2.83	0.46	0.11	0.18	2.71	0.34	0.11
1.02	17.09	2.24	0.13	0.54	8.60	1.19	0.11	0.56	8.52	0.93	0.11
1.51	25.80	2.98	0.14	1.03	16.69	2.00	0.12	1.04	16.06	1.56	0.12
2.51	44.80	4.27	0.15	1.53	25.23	2.69	0.13	1.53	23.91	2.13	0.14
3.29	60.83	5.14	0.18	2.52	43.17	3.87	0.14	2.56	41.43	3.21	0.16
4.20	81.34	6.08	0.20	3.30	58.32	4.67	0.16	3.31	54.92	3.90	0.18
4.99	101.05	6.85	0.23	4.20	77.22	5.54	0.18	4.20	71.90	4.65	0.21
5.80	123.62	7.61	0.26	4.98	95.08	6.22	0.74	5.03	88.72	5.27	0.25
6.57	147.78	8.23	0.34	5.05	96.58	6.29	0.21	6.51	121.97	6.29	0.34
7.48	181.15	9.05	0.45	5.98	119.97	7.06	0.26	8.27	167.67	7.37	0.47
8.08	206.93	9.32	0.49	7.08	151.36	7.86	0.31	9.52	205.52	7.97	0.55
8.52	228.44	9.45	0.54	8.19	188.45	8.61	0.38	11.22	265.27	8.53	0.70
9.05	257.81	9.48	0.62	9.09	223.48	9.02	0.46	12.21	304.77	8.52	0.81
9.52	288.09	9.42	0.72	9.54	243.40	9.19	0.50	13.07	341.57	8.42	0.83
10.05	327.83	9.19	0.82	10.05	267.73	9.32	0.55	14.32	396.46	8.02	0.94
10.51	367.51	8.84	0.87	11.09	324.87	9.22	0.63	15.06	428.51	7.73	1.02
11.02	414.81	8.31	0.91	12.09	387.17	8.86	0.77	16.33	479.92	7.10	1.03
11.53	462.55	7.55	0.89	13.48	475.02	7.67	0.80	17.49	521.50	6.55	0.92
11.97	500.22	7.05	0.82	14.92	548.91	6.52	0.70	19.09	569.65	5.99	1.07
12.43	534.13	6.53	0.81	17.47	635.32	5.04	0.62	20.07	594.55	5.59	1.06
13.40	590.34	5.85	0.73	20.00	690.77	4.16	0.59	21.04	616.49	5.30	1.00
15.44	665.05	4.69	0.65	22.49	730.11	3.52	0.62	23.06	654.95	4.77	1.03
20.57	761.42	3.37	0.61	25.12	762.54	3.22	0.61	25.03	685.81	4.38	1.04
25.95	818.47	2.84	0.62								

rising pressure at $T = 298$ K. In addition to this liquid like phase behavior in the bulk and pore phase was observed at $T > T_c$ and $\varrho > \varrho_c$.

If n^{ex} was depicted as a function of pressure it was obvious that the maximum of the adsorption isotherms shifted to higher pressures with increasing temperature. This effect vanished in a plot of n^{ex} versus density. To find the location of the maximum the n^{ex} versus p plot was fitted with a fifth-order polynom. The obtained densities and the corresponding pressures (which were calculated using the NIST REFPROP [71] software) are listed in Tab. 4. Both investigated adsorbent/adsorbate systems showed a small temperature effect in the location of the maximum. At supercritical temperatures the maximum was shifted only slightly whereas the values at the subcritical temperature $T = 298$ K were significantly lower. At $T = 298$ K the maximum occurred before the bulk phase reached its saturation pressure ($p_{sat,CO2} = 6.41$ MPa). The temperature dependency of the maximum for $T > T_c$ is in good agreement with the compressibility behavior of carbon dioxide. It was found that the inflection point of the steep increase in density with rising pressure is also temperature dependent [60]. Furthermore, it was obvious that the isotherm maxima of SBA-15 occurred at slightly higher bulk densities than those of MCM-41. A higher compressibility of the adsorbed phase in SBA-15 pores than in those of MCM-41 at the same pressure seems to be a possible explanation. One reason for this could be the existence of cross-linking channels in SBA-15. In their intersections might be more space for enhanced accumulation of the carbon dioxide molecules. The location of the maximum was also investigated in literature. Tatsuda et al. [52], who measured carbon dioxide adsorption on SBA-15 ($r_P = 3.02$ nm) at supercritical conditions, observed also a temperature dependency. The location of the excess isotherm maxima in their work varied between $0.27 - 0.30$ g/ml in the temperature range of $T = 305 - 319$ K. In comparison to this, Strubinger's et al. [46] investigation of the maximum was found to be temperature independent. These authors investigated the adsorption of carbon dioxide on silica and C18-bonded silica by mass spectrometric tracer pulse chromatography. The density values of the maxima of the excess amount adsorbed for silica ($\varrho_{max} = 0.35$ g/ml, $T = 313 - 323$ K) and C18-bonded silica ($\varrho_{max} = 0.31$ g/ml, $T = 303 - 373$ K) are higher than the values presented in this work.

It can be assumed that the location of the maximum amount adsorbed is not only dependent on the adsorptive properties. Furthermore, it can be assumed that adsorbent pore size, pore volume, pore structure and adsorbent/adsorptive interactions play an important role.

3.2 Determining the absolute amount adsorbed

The isotherms of the absolute amount adsorbed on MCM-41 and SBA-15 for temperatures $T \geq 313$ K are depicted in Fig. 3 and Fig. 4. To calculate the absolute amount adsorbed Eq.(6) was used for all supercritical temperatures. To obtain V_{ads} and ϱ_{ads} the continuously decreasing branch after the inflection point of the measured isotherms were fitted in a n^{ex} versus ϱ_{bulk} diagram by a linear regression [65, 67]. The slopes and intercepts of the fits as well as the calculated volumes and densities of the adsorbed phases are listed in Tab. 4.

From Fig. 3 and Fig. 4 it is obvious that in both investigated systems the absolute amount adsorbed increased with rising pressure and reached a saturation.

Tab. 4 Density and pressure values at maximum n^{ex} and fitting parameters to calculate the absolute amount adsorbed.

	MCM-41						SBA-15					
T K	**298**	**308**	**313**	**328**	**338**	**353**	**298**	**308**	**313**	**328**	**338**	**353**
ϱ_{bulk} [a] kg/m³	167	214	218	227	254	290	156	223	235	255	283	295
p [a] MPa	5.67	6.91	7.30	8.47	9.75	11.82	5.49	7.02	7.53	8.98	10.32	11.94
Intercept mmol/g		14.18	13.09	12.77	13.09	12.75		16.42	13.92	13.91	13.22	13.37
Slope = $-V_{ads}$ mol·cm³/g²		-0.0141	-0.0126	-0.0127	-0.0132	-0.0136		-0.0164	-0.0134	-0.0134	-0.0132	-0.0131
V_{ads} cm³/g		0.62	0.55	0.56	0.58	0.60		0.72	0.59	0.59	0.58	0.58
ϱ_{ads} [b] kg/m³		1006	1039	1006	992	938		1001	1039	1038	1002	1021
$\varrho_{ads}/\ \varrho_c$ [c] -		2.2	2.2	2.2	2.1	2.0		2.2	2.2	2.2	2.2	2.2
PFF -		0.57	0.51	0.51	0.53	0.55		0.86	0.70	0.70	0.69	0.69

[a] Bulk density at the maximum of the excess adsorption isotherm obtained by fitting the experimental data with a 5th order polynomial function; the according pressures were calculated by NIST REFPROP [71].

[b] Calculated by the intercept and slope of the linear regression at $n^{ex} = 0$ mmol/g [67].

[c] Critical density of carbon dioxide $\varrho_c = 466$ kg/m³ [71].

Furthermore, this saturation was reached at higher densities with rising temperature. It was also obvious that the saturation amount adsorbed was slightly higher for SBA-15 (~13.5 mmol/g, MCM-41: ~13 mmol/g) and was reached at higher densities in comparison to MCM-41. This might be a reason of the cross-linking channel intersections of SBA-15 since both adsorbents do not differ much in pore size.

It can be seen in Tab. 4 that the obtained values of V_{ads} are similar in both adsorbent/adsorbate systems. It is also obvious that the values for $T = 308$ K are significantly higher compared to those of other temperatures. This effect might be owed by the difficulty of measurement close to the critical temperature.

The calculated values of the adsorbate densities ϱ_{ads} are in the same range in all investigated systems ($\varrho_{ads} = 938 - 1039$ kg/m^3). The values are higher than the critical density of carbon dioxide ($\varrho_c = 466$ kg/m^3 [71]) but lower than its liquid density at the triple point ($\varrho_{liq,TP} = 1176$ kg/m^3 [71]). Similar density values might confirm the observation that adsorption saturation was reached at high pressures at the investigated temperatures. The obtained values for ϱ_{ads} are in good agreement with the theory that the density of the adsorbate is assumed to be the inverse of the Van der Waal's constant b (for carbon dioxide: $b_{VdW,CO2} = 0.0427$ l/mol [72] $\rightarrow$ $\varrho_{ads,CO2} = 1030$ kg/m^3) [65, 68]. Similar values for the density of adsorbed carbon dioxide on hydrophilic and hydrophobic silica aerogels were found by Gorle et al. [39].

The reduced density of the adsorbate ($\varrho_{ads}/\varrho_c = 2.2$) seems to be temperature independent despite from those of MCM-41 at $T = 338$ K and $T = 353$ K. A temperature independency was also observed on carbon dioxide adsorption on HKUST-1 [67].

In comparison to MCM-41 the pore filling factors (PFF) of SBA-15 are higher. This might be another hint to an enhanced accumulation of carbon dioxide in the intersections of the cross-linking channels of SBA-15. Monte-Carlo simulation studies performed by Yue and Yang [73] showed that the highest adsorbate densities can be found in these "zig-zack" intersections.

3.3 Calculating the isosteric heat of adsorption

The isosteric heat of adsorption represents the heat of adsorption at zero loading. It can be evaluated form the Henry coefficient due to the fact that it varies with temperature and that it is following the van't Hoff equation [74]. To obtain the Henry

Tab. 5 Henry coefficients to calculate the isosteric heat of adsorption at zero loading.

	Intercepts ≙ -*ln(K)*						**Slope**	**- ΔH_{iso}**
T / K	**298**	**308**	**313**	**328**	**338**	**353**	1/K	kJ/mol
MCM-41	-1.99	-1.45	-1.41	-1.15	-0.84	-0.51	-2612	-21.7
SBA-15	-1.86	-1.52	-1.36	-1.07	-0.94	-0.63	-2243	-18.6

coefficients K the experimental data were plotted in an $ln(p/n^{ex})$ versus p diagram wherein the low pressure region was fitted with a linear regression. The results for the intercepts which are similar to $ln(K)$ at different temperatures are listed in Tab. 5. In a next step the isosteric heat of adsorption was calculated from the slope of a linear fit in a $ln(K)$ versus $1/T$ plot. The obtained values for MCM-41 (- ΔH_{iso} = 21.7 kJ/mol) and SBA-15 (- ΔH_{iso} = 18.6 kJ/mol) were rather similar. Nevertheless, the interactions between carbon dioxide and the surface of SBA-15 seemed to be smaller in comparison to MCM-41. The small negative values for the isosteric heat of adsorption indicate an exothermic carbon dioxide adsorption on the investigated silicas which is governed mainly by physisorption [56]. These values are in good agreement to the calculated isosteric heat of adsorption on PE-MCM-41 (- ΔH_{iso} = 20 – 21 kJ/mol) by Loganathan et al. [56] and on silica aerogels (- ΔH_{iso} = 21.9 kJ/mol) calculated by Anas et al. [40]. An isosteric heat of - ΔH_{iso} = 24 kJ/mol was calculated out of differential thermal analysis and thermogravimetric analysis data of silica gel 40 [75]. Calorimetric studies which were performed at T = 298 K and low loadings $n < 1$ mmol/g on three different MCM-41 samples [55] and mesoporous silica [76] supplied values of - ΔH_{iso} = 20 – 25 kJ/mol. Reasons for the different values of the isosteric heat of adsorption presented in literature might be different measuring and calculation methods, but also variations in pore size of the samples [52, 55].

The course of the heat of adsorption at constant loadings (Fig. 5) can be calculated indirectly by the Clausius-Clapeyron equation [77, 78]. To obtain the corresponding pressures at specific loadings the absolute amount adsorbed for each temperature (T = 298 – 353 K) was fitted with a Padé equation [67] up to $n_{abs} \leq 10$ mmol/g. From the slope of a $ln(p)$ versus $ln(T)$ plot the heat of adsorption can be determined at constant loadings.

It can be seen in Fig. 5 that the heat of adsorption for both adsorbents decreased up to loadings of n = 7.5 mmol/g, which was also observed by Tatsuda et al. [52]. The non-constant behavior indicates that the surface of MCM-41 and SBA-15 is not energetically uniform [74]. Loganathan et al. [56] indicated specific patches of

different surface groups of MCM-41 which are interacting with carbon dioxide. H-bound interactions were found between isolated silanol groups and carbon dioxide whereas siloxane groups develop dispersive interactions.

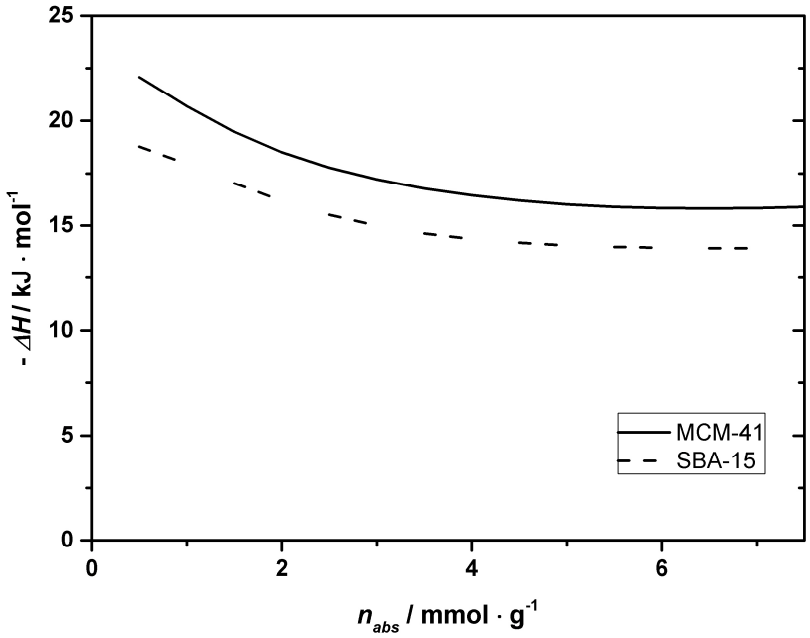

Fig. 5 Heat of adsorption as a function of loading for MCM-41 and SBA-15.

3.4 Comparison of carbon dioxide adsorption and ibuprofen loading on MCM-41 and SBA-15

Concerning an enhanced dissolution of ibuprofen in the gastro intestinal tract the investigated carrier materials MCM-41 and SBA-15 were impregnated with the drug by the Controlled Particle Deposition process [16]. The obtained loadings found by Reiser et al. [16] at $T = 313$ K and $p = 15$ MPa are listed in Tab. 6. During the deposition step of this process different interactions in the ternary system between the carrier material, $scCO_2$ and ibuprofen inside the reactor need to be considered. The loading results were used to draw first conclusions about the interactions between the surface of the carrier material and ibuprofen during the process. Furthermore, the measured adsorption isotherms of the binary system carbon dioxide-carrier material can be used to give an initial estimation of the interactions between $scCO_2$ and the carrier surface in the ternary system at the applied process conditions.

It was found that a nearly six times higher adsorption of carbon dioxide on both adsorbents were obtained in comparison to the ibuprofen loadings. This might be a

Tab. 6 Adsorption of carbon dioxide and loading of ibuprofen on MCM-41 and SBA-15 at $T = 313$ K and $p = 15$ MPa.

	$n^{ex}(CO_2)$	$n_{abs}(CO_2)$		**Loading of ibuprofen** [16]		
	mmol/g	mmol/g	μmol/m^2	wt%	mmol/g	μmol/m^2
MCM-41	3.10 ± 0.37	12.95	12.01	49.1 ± 0.5	2.38	2.22
SBA-15	3.30 ± 0.59	13.74	13.92	50.0 ± 0.5	2.43	2.46

result of the smaller molecular size of carbon dioxide compared to ibuprofen. Another possible explanation might be stronger interactions between the silica surface and carbon dioxide. The values of ibuprofen loading and carbon dioxide adsorption were only slightly different for MCM-41 and SBA-15. The major difference between these carrier materials is their pore structure while surface area, pore volume and pore size distribution are similar. This leads to the assumption that in this work the pore structure is not the most important adjusting parameter for the adsorption of ibuprofen.

Nevertheless, it must be taken into account that the amount adsorbed of carbon dioxide in the ternary system could be lower, since some binding sites might be occupied by ibuprofen molecules. To investigate, if there is a competition between carbon dioxide and ibuprofen adsorption on the surface of the carrier material, further studies have to be carried out. In addition to this, it has to be identified, if there are preferred interaction patches at the silica surface for the adsorption of ibuprofen and/or carbon dioxide.

4. Conclusion

In this study the adsorption of carbon dioxide on MCM-41 and SBA-15 at six temperatures ($T = 298 - 353$ K) in a pressure range of $0 \leq p \leq 25$ MPa was investigated by a magnetic suspension balance. The results are in good agreement to available data published in literature which were obtained at lower pressure ranges ($p \leq 3.5$ MPa). The differences in the adsorption behavior of carbon dioxide on MCM-41 and SBA-15 were small because both adsorbents show similar structural and chemical properties. Due to the fact that MCM-41 has a higher surface area the measured n^{ex} adsorption results were slightly higher. In contrast to this higher values of the absolute amount adsorbed n_{abs} were calculated for SBA-15.

The maximum of the excess isotherms shifted to higher pressures at higher temperatures. This effect vanished when the isotherms were depicted as a function

of density. Nevertheless, a small temperature dependency of the exzess isotherm maxima was observed in the investigated systems.

Furthermore, the isosteric heat of adsorption was calculated for SBA-15 and MCM-41. The obtained results are in good agreement to other already existing calculated or calorimetric measured results published in literature. It was obvious that carbon dioxide adsorption is exothermic and was governed mainly by physisorption. The heat of adsorption at different loadings did not show a constant trend which indicates an energetically heterogeneous surface of both adsorbents.

As a first approach the results of the binary system carbon dioxide–carrier material were used to draw conclusions of the interactions in the ternary system (carbon dioxide, ibuprofen and carrier material) used in the CPD process. In comparison to ibuprofen loadings on the investigated carrier materials achieved by the CPD process at $T = 313$ K and $p = 15$ MPa, it can be concluded that there is a nearly six times higher adsorption of carbon dioxide during the deposition step.

Acknowledgements

This study was supported by the Deutsche Forschungsgemeinschaft (DFG) within the priority program SPP 1570 (FE 911/5-1. JO 339/7-1. STA 428/18-1 and TU 93/14-1) and by the State of Baden-Württemberg which the authors gratefully acknowledge. Furthermore, the authors thank J. Moellmer (Institut für Nichtklassische Chemie e.V., Leipzig) for characterizing the adsorbents by measuring the nitrogen sorption and the provided data. Additionally, the authors appreciate the provision of the magnetic suspension balance by Rubotherm (Bochum, Germany).

References

[1] E. Beckman, Supercritical and near-critical CO_2 in green chemical synthesis and processing, J. Supercrit. Fluids 28 (2004) 121–191.

[2] J. Jung, M. Perrut, Particle design using supercritical fluids: literature and patent survey, J. Supercrit. Fluids 20 (2001) 179–219.

[3] M. Türk, Particle formation with supercritical fluids - challenges and limitations, Elsevier, Amsterdam, 2014, ISBN: 978-0-444-59486-0.

[4] G.M. Schneider, Physicochemical aspects of fluid extraction, Fluid Phase Equilibr. 10 (2) (1983) 141–157.

[5] H.J. Martin, Charakterisierung von schwerlöslichen Arzneistoff-Nanopartikeln hergestellt durch das RESS-Verfahren zur Verbesserung der Bioverfügbarkeit (PhD thesis), Eberhard-Karls-Universität Tübingen, 2003.

[6] M. Türk, B. Helfgen, P. Hils, R. Lietzow, K. Schaber, Micronization of pharmaceutical substances by rapid expansion of supercritical solutions (RESS): Experiments and modeling, Part. Part. Syst. Charact. 19 (5) (2002) 327–335.

[7] Y. Zhang, C. Erkey, Preparation of supported metallic nanoparticles using supercritical fluids: A review, J. Supercrit. Fluids 38 (2006) 252–267.

[8] R. Gläser, S.E. Dapurkar, M. Rajamanickam, M. Schmidt, M. Türk, G. Upper, Preparation of platinum catalysts on ordered mesoporous supports by supercritical fluid reactive deposition, Prepr. Am. *Chem.* Soc., Div. Pet. *Chem.* 51(2) (2006) 526–527.

[9] S. Wolff, M. Crone, T. Muller, M. Enders, S. Bräse, M. Türk, Preparation of supported Pt nanoparticles by supercritical fluid reactive deposition: Influence of precursor, substrate and pressure on product properties, J. Supercrit. Fluids 95 (2014) 588–596.

[10] M. Türk, G. Upper, M. Steurenthaler, Kh Hussein, M.A. Wahl, Complex formation of ibuprofen and β-Cyclodextrin by controlled particle deposition (CPD) using Sc-CO_2, J. Supercrit. Fluids 39 (2007) 435–443.

[11] M. Casapu, A. Fischer, A.M. Gaenzler, R. Popescu, M. Crone, D. Gerthsen, M. Türk, J.-D. Grunwaldt, Origin of the normal and inverse hysteresis behavior during CO oxidation over Pt/Al_2O_3, ACS Catal. 7(1) (2017) 343–355.

[12] S. Lang, M. Türk, B. Kraushaar-Czarnetzki, Novel $PtCuO/CeO_2/\alpha$-Al_2O_3 sponge catalysts for the preferential oxidation of CO (PROX) prepared by means of supercritical fluid reactive deposition (SFRD), J. Catal. 286 (2012) 78–87.

[13] G. Incera Garrido, F.C. Patcas, G. Upper, M. Türk, S. Yilmaz, B. Kraushaar-Czarnetzki, Supercritical deposition of Pt on SnO_2-coated Al_2O_3 foams: Phase behaviour and catalytic performance, Appl. Cat. A: General 338 (2008) 58–65.

[14] G.L. Amidon, H. Lennernäs, V.P. Shah, J.R. Crison, A theoretical basis for a biopharmaceutic drug classification: The correlation of in vitro drug product dissolution and in vivo bioavailability, Pharm. Res. 12 (3) (1995) 413–420.

[15] H.D. Williams, N.L. Trevaskis, S.A. Charman, R.M. Shanker, W.N. Charman, C.W. Pouton, C.J. Porter, Strategies to address low drug solubility in discovery and development, Pharmacol. Rev. 65 (1) (2013) 315–499.

[16] S. Reiser, M. Sun, M. Johannsen, M. Türk, Ibuprofen influence of chemical nature of carrier materials on the dissolution behavior of racemic ibuprofen, J. Supercrit. Fluids (2017). http://dx.doi.org/10.1016/j.supflu.2017.02.015.

[17] R.S. Wischumerski, M. Türk, M.A. Wahl, Direct drug loading into preformed porous solid dosage units by the controlled particle deposition (CPD), a new concept for improved dissolution using SCF-technology, J. Pharm. Sci. 97(10) (2008) 4416–4424.

[18] I. Smirnova, M. Türk, R. Wischumerski, M.A. Wahl, Comparison of different methods to enhance the dissolution rate of poor soluble drugs: case of Griseofulvin, Eng. Life Sci. 5(3) (2005) 277–280.

[19] M. Charoenchaitrakool, F. Dehghani, N.R. Foster, Utilization of supercritical carbon dioxide for complex formation of ibuprofen and methyl-β-cyclodextrin, Int. J. Pharm. 239 (2002) 103–112.

[20] C. Song, Global challenges and strategies for control, conversion and utilization of CO_2 for sustainable development involving energy, catalysis, adsorption and chemical processing, Catal. Today 115 (2006) 2–32.

[21] D. Bonenfant, M. Kharoune, P. Niquette, M. Mimeault, R. Hausler, Advances in principal factors influencing carbon dioxide adsorption on zeolites, Sci. Tech. Adv. Mater. 9 (1) (2008) 7pp.

[22] S. Choi, J.H. Drese, C.W. Jones, Adsorbent materials for carbon dioxide capture from large anthropogenic point sources, ChemSusChem, 32 (1) (2009) 796–854.

[23] R. Sabouni, H. Kazemian, S. Rohani, Carbon dioxide capturing technologies: a review focusing on metal organic framework materials (MOFs), Environ. Sci. Pollut. Res., 21 (8) (2014) 5427–5449.

[24] M.R. Mello, D. Phanon, G.Q. Silveira, P.L. Llewellyn, C.N. Ronconi, Amine-modified MCM-41 mesoporous silica for carbon dioxide capture, Microporous Mesoporous Mater., 143 (2011) 174-179.

[25] C. Knöfel, J. Descarpentries, A. Benzaouia, V. Zelenak, S. Mornet, P.L. Llewellyn, V. Hornebecq, Functionalised micro-/mesoporous silica for the adsorption of carbon dioxide, Microporous Mesoporous Mater., 99 (2007) 79-85.

[26] S. Ozawa, S. Kusumi, Y. Ogino, Physical adsorption of gases at high pressure. IV. An improvement of the Dubinin-Astakhov adsorption equation, J. Colloid Interface Sci. 56 (1) (1976) 83–91.

[27] M.M.K. Salem, P. Braeuer, M.v. Szombathely, M. Heuchel, P. Harting, K. Quitzsch, Thermodynamics of high-pressure adsorption of argon, nitrogen, and methane on microporous adsorbents, Langmuir, 14 (12) (1998) 3376–3389.

[28] S. Beutekamp, P. Harting, Experimental determination and analysis of high pressure adsorption data of pure gases and gas mixtures, Adsorption 8 (2002) 255-269.

[29] J. Specovius, G.H. Findenegg, Physical adsorption of gases at high pressures: argon and methane onto graphitized carbon black, Ber. Bunsen-Ges., 82 (2) (1978) 174–180.

[30] K. Murata, K. Kaneko, Nano-range interfacial layer upon high-pressure adsorption of supercritical gases, Chem. Phys. Lett. 321 (5-6) (2000) 324–348.

[31] L. Zhou, Y. Sun, Y. Zhou, An experimental study on the adsorption behavior of gases crossing the critical temperature, Chin. J. Chem. Eng. 10 (3) (2002) 259–262.

[32] F. Dreisbach, R. Staudt, J.U. Keller, High pressure adsorption data of methane, nitrogen, carbon dioxide and their binary and ternary mixtures on activated carbon, Adsorption 5 (1999) 215-227.

[33] A. Herbst, P. Harting, Thermodynamic description of excess isotherms in high-pressure adsorption of methane, argon and nitrogen, Adsorption 8 (2002) 111-123.

[34] D.D. Do, H.D. Do, Adsorption of supercritical fluids in non-porous and porous carbons: analysis of adsorbed phase volume and density, Carbon 41 (2003) 1777–1791.

[35] I. Senkovska, S. Kaskel, High pressure methane adsorption in the metal-organic frameworks $Cu_3(btc)_2$, $Zn_2(bdc)_2dabco$, and $Cr_3F(H_2O)_2O(bdc)_3$. Microporous Mesoporous Mater. 112 (1-3) (2008) 108–115.

[36] E. Poirier, A. Dailly, Thermodynamic study of the adsorbed hydrogen phase in Cu-based metal-organic frameworks at cryogenic temperatures, Energy Environ. Sci. 2 (2009) 420–425.

[37] L. Zhou, S. Bai, Y. Zhou, B. Yang, Adsorption of Nitrogen on Silica gel over a large range of temperatures, Adsorption 8 (1) (2002) 79–87.

[38] E. Bekyarova, K. Kanekoy, Adsorption of supercritical N_2 and O_2 on pore-controlled carbon aerogels, J. Colloid Interface Sci. 238 (2001) 357–361.

[39] B.S.K. Gorle, I. Smirnova, W. Arlt, Adsorptive crystallization of benzoic acid in aerogels from supercritical solutions, J. Supercrit. Fluids 52 (2010) 249–257.

[40] M. Anas, A.G. Gönel, S.E. Bozbag, C. Erkey, Thermodynamics of Adsorption of Carbon Dioxide on Various Aerogels, J. CO2 Util. 21 (2017) 82–88.

[41] R. Staudt, Habilitationsschrift, (PhD thesis) Univeristät Siegen, 2001.

[42] R. Heller, M. Zoback, Adsorption of methane and carbon dioxide on gas shale and pure mineral samples, J. Unconventional Oil and Gas Resources, 8 (2014) 14–24.

[43] W. Li-Hong, C. Xin, X. Hui, Z. Li-Li, H. Jing, Z. Mei-Juan, L. Jie, L. Yi, L. Jin-Wen, Z. Wei, C. Gang, A novel strategy to design sustained-release poorly water-soluble drug mesoporous silica microparticles based on supercritical fluid technique, Int. J. Pharm. 454 (2013) 135–142.

[44] M. Ni, Q.-Q. Xu, J.-Z. Yin, Preparation of controlled release nanodrug ibuprofen supported on mesoporous silica using supercritical carbon dioxide, J.Mater.Res. 27 (22) (2012) 2902–2910.

[45] J.F. Parcher, J.R. Strubinger, High-pressure adsorption of carbon dioxide on super-critical-fluid chromatography adsorbents, J. Chrom. 479 (2) (1989) 251–259.

[46] J.R. Strubinger, H. Song, J.F. Parcher, High-pressure phase distribution isotherms for supercritical fluid chromatographic systems. 1. Pure carbon dioxide, Anal. Chem. 63 (2) (1991) 98–103.

[47] Y. Wang, M.D. LeVan, Adsorption equilibrium of carbon dioxide and water vapor on zeolites 5A and 13X and silica gel: Pure components, J. Chem. Eng. Data 54 (19) (2009) 2839–2844.

[48] R. Nakanishi, M. Suzuki, K. Inukai, M. Maeda, CO_2 adsorption/desorption on mesoporous silica at various pressures, Transaction of the Materials Research Society of Japan 34 (4) (2009) 743–745.

[49] X, Liu, J. Li, L. Zhou, D. Huang, Y. Zhou, Adsorption of CO_2, CH_4 and N_2 on ordered mesoporous silica molecular sieve, Chem. Phys. Lett. 415 (4-6) (2005)198–201.

[50] S. Ozawa, Y. Ogino, Physical adsorption of gases at high pressures. I. Measurement of high-pressure gas adsorption with a volumetric apparatus, Nippon Kagaku Kaishi 1 (1972) 1–8.

[51] X. Wang, X. Ma, C. Song, D.R. Locke, S. Siefert, R.E. Winans, J. Möllmer, M. Lange, A. Möller, R. Gläser, Molecular basket sorbents polyethylenimine-SBA-15 for CO_2 capture from flue gas: Characterization and sorption properties, Microporous Mesoporous Mater. 169 (2013) 103–111.

[52] N. Tatsuda, Y. Goto, N. Setoyama, Y. Fukushima, Adsorption of carbon dioxide on mesoporous silicas near the critical temperature, Adsorpt. Sci. Technol. 23 (9) (2005) 763–776.

[53] K. Morishige, H. Fujii, M. Uga, D. Kinukawa, Capillary critical point of argon, nitrogen, oxygen, ethylene, and carbon dioxide in MCM-41, Langmuir 13 (1997) 3494–3498.

[54] M.S. Schneider, J.-D. Grunwaldt, A. Baiker, Near-critical CO_2 in mesoporous silica studied by in situ FTIR spectroscopy, Langmuir 20 (2004) 2890–2899.

[55] Y. He, N.A. Seaton, Heats of adsorption and adsorption heterogeneity for methane, ethane, and carbon dioxide in MCM-41, Langmuir 22 (3) (2006) 1150–1155.

[56] S. Loganathan, M. Tikmani, A.K. Ghoshal, Pore-expanded MCM-41 for CO_2 adsorption: Experimental and isotherm modeling studies, Chem. Eng. J. 280 (2015) 9–17.

[57] Y. He, N.A. Seaton, Experimental and computer simulation studies of the adsorption of ethane, carbon dioxide, and their binary mixtures in MCM-41, Langmuir 19 (2003) 10132–10138.

[58] Private communication with J. Moellmer, Institut für Nichtklassische Chemie e.V., Leipzig.

[59] U. Keller, R. Staudt, editor. Gas adsorption equilibria - Experimental methods and adsorptive isotherms. Springer, 2005.

[60] R. Span, W. Wagner, A new equation of state for carbon dioxide covering the fluid region from the triple-point temperature to 1100 K at pressures up to 800 MPa, J. Phys. Chem. Ref. Data 25 (6) (1996) 1509–1596.

[61] D.M. Young, A.D. Crowell, editor. Physical adsorption of gases, Butterworths, London, 1962.

[62] S.J. Gregg, K.S.W. Sing, Adsorption, surface area and porosity, Academic Press, London, 1967.

[63] S. Reiser, D. Bolten, R. Staudt, M. Türk, Adsorption of N_2 and CO_2 on activated carbon, AlO(OH) nanoparticles, and AlO(OH) hollow spheres, Chem. Eng. Technol. 38 (2015) 2261–2269.

[64] M.M. Dubinin, The potential theory of adsorption of gases and vapors for adsorbents with energetically nonuniform surfaces, Chem. Rev. 60 (2) (1960) 235–241.

[65] P.G. Menon, Adsorption at high pressures, Chem. Rev. 68 (3) (1968) 277–294.

[66] M.C. Tsai, W.N. Chen, P.L. Cen, R.T. Yang, Adsorption of gas mixture on activated carbon, Carbon 23 (2) (1985) 167 – 173.

[67] J. Moellmer, A. Moeller, F. Dreisbach, R. Glaeser, R. Staudt, High pressure adsorption of hydrogen, nitrogen, carbon dioxide and methane on the metal-organic framework HKUST-1, Microporous Mesoporous Mater. 138 (2011) 140–148.

[68] R. Humayun, D.L. Tomasko, High-resolution adsorption isotherms of supercritical carbon dioxide on activated carbon, AIChE J. 46 (10) (2000) 2065–2075.

[69] T. Hocker, A. Rajendran, M. Mazzotti, Measuring and modeling supercritical adsorption in porous solids. Carbon dioxide on 13X zeolite and on silica gel, Langmuir 19 (2003) 1254–1267.

[70] O. Di Giovanni, W. Doerfler, M. Mazzotti, M. Morbidelli, Adsorption of supercritical carbon dioxide on silica, Langmuir 17 (2001) 4316–4321.

[71] E. W. Lemmon, M. L. Huber, M. O. McLinden, NIST Standard reference database 23: Reference fluid thermodynamic and transport properties-REFPROP, Version 9.1, MD2013.

[72] R.C. Weast, CRC Handbook of Chemistry and Physics; 56th edition. CRC Press, Cleveland, Ohio 1976.

[73] X. Yue, X. Yang, Molecular simulation study of adsorption and diffusion on silicalite for a benzene/CO_2 mixture, Langmuir 22 (2006) 3138–3147.

[74] J. Tóth, Adsorption: theory, modeling, and analysis, Dekker, 2002.

[75] G.P. Knowles, J.V. Graham, S.W. Delaney, A.L. Chaffee, Aminopropyl-functionalized mesoporous silicas as CO_2 adsorbents, Fuel Process. Technol. 86 (2005) 1435–1448.

[76] C. Knöfel, C. Martin, V. Hornebecq, P.L. Llewellyn, Study of carbon dioxide adsorption on mesoporous aminopropylsilane-functionalized silica and titania combining microcalorimetry and in situ infrared spectroscopy, J. Phys. Chem. C 113 (2009) 21726–21734.

[77] D.D. Do, Adsorption analysis: Equilibria and kinetics, Volume 2, 1998.

[78] A.L. Myers, P.A. Monson, Adsorption in porous materials at high pressure: Theory and experiment, Langmuir 18 (2002) 10261–10273.

4. Conclusion & Outlook

The design of formulations with improved dissolution performance is an important issue in pharmaceutical research. Such formulations can be obtained e.g. by the Controlled Particle Deposition (CPD) process. CPD products can show either an enhanced or a retarded dissolution of active ingredients. According to the FDA the dissolution behavior of the obtained CPD products needs to be investigated in vitro. For the decision of suitable active ingredient-carrier systems for a targeting application a dissolution prediction method is demanded for the evaluation of new CPD products. With this method time and cost intensive in vitro dissolution studies can be prevented. The idea is to carry out this prediction just by the knowledge of the chemical nature of the active ingredient and the chemical nature and specific structural properties of the carrier material. As a consequence, the task of this work was to identify the impact of specific carrier material properties (e.g. specific surface area, pore size, pore volume and surface functionalization) on the loading and dissolution performance of the obtained CPD products. To investigate this the active ingredient R/S-ibuprofen (ibuprofen) was deposited in a systematic study on six different silica based carrier materials. These carrier materials differed in specific surface area (A_{BET} = 63 – 1030 m^2/g), pore volume (V_P = 0.55 – 1.09 cm^3/g), pore size (D_P = 3.6 – 30 nm) and surface functionalization (S-(+)-ibuprofen). In a next step, the dissolution performance of the obtained CPD products was investigated and compared to the dissolution behavior of an ibuprofen-ß-cyclodextrin inclusion complex, which was considered to be the benchmark.

The second part of this work was addressed to investigate the adsorption behavior of $scCO_2$ and ibuprofen on the carrier material during the deposition step of the CPD process. Therefore, the adsorption of CO_2 on two typical carrier materials used in this work (MCM-41 and SBA-15) was investigated with a magnetic suspension balance in a wide range of temperature ($T = 298 - 353$ K), pressure ($0 \leq p \leq 25$ MPa) and density ($\varrho_{CO2,bulk} = 0 - 900$ kg/m^3). Furthermore, this part aims to answer the question if there is a competitive adsorption between $scCO_2$ and ibuprofen on the carrier material at the operating CPD process conditions.

It was shown in this work that the CPD process is a suitable method to deposit ibuprofen on all investigated silica carrier materials without the utilization of additional substances at the chosen process conditions ($T = 313$ K, $p = 15$ MPa). The influences of specific carrier properties mentioned above on the loading and dissolution behavior of ibuprofen have been successfully identified. High loadings up to 50 wt% were achieved by the carrier materials with the highest specific surface area ($A_{BET} = 920 - 1030$ m^2/g). A linear dependency of loading ($Y = 10 - 50$ wt%) and the specific surface area ($A_{BET} = 63 - 1030$ m^2/g) could have been assumed. Nevertheless, the loading results were also influenced by pore size and pore volume. Carrier materials with the widest mesopores ($D_P \geq 25$ nm) showed higher loadings than it would be possible on the basis of their specific surface area assuming the linear dependency mentioned before. This observation could have been explained by the fact, that in wider mesopores ($D_P = 25 - 30$ nm) the formation of multilayers is possible due to the extended pore volume. This was also confirmed by the high values of the calculated "number of monolayer" ($D_P = 25$ nm: $NML = 4.09$, $D_P = 30$ nm: $NML = 9.07$). The surface functionalization (S-(+)-ibuprofen) led to lower loadings than it would have been possible by their specific surface area assuming the linear dependency mentioned above.

Investigations of the crystal structure of the deposited ibuprofen by X-ray diffraction (XRD) and differential scanning calorimetry (DSC) led to the following conclusions. The deposited ibuprofen consists primarily of amorphous fractions in long and small channels ($D_P \leq 4$ nm), whereas in wider mesopores ($D_P \geq 25$ nm) there is enough space for the formation of crystalline structures. On the functionalized carrier materials the formation of amorphous ibuprofen structures was favored.

The dissolution experiments were carried out according to the recommendations of the FDA at pH = 2.0 and 5.5 in a down-scaled device with dimensions proposed by Klein and Shah [20]. This device was designed and validated by a fluid dynamic

simulation and a systematic reproducibility study in the context of a master thesis. In this thesis it was found that the fluid dynamic profile of the mini-apparatus recommended by Klein and Shah was comparable to the profile of an FDA apparatus if the paddle stirrer speed was set to 100 rpm. In addition to this, the exact position of the paddle was identified to obtain the same fluid dynamic profile. With regard to receive reproducible results the best method was to sieve the samples before injection.

In the dissolution experiments (experimental runtime: $t = 120$ min) it was observed, that the dissolution rate of ibuprofen is generally lower at pH = 2.0 in comparison to pH = 5.5. This observation was owed by the fact that the solubility of ibuprofen is increased at higher pH-values. In addition to this, influences of the specific carrier material properties on the dissolution behavior could have been identified. One major influence of the dissolution behavior was the pore size. A higher amount of dissolved ibuprofen after 120 min was observed from wider mesopores ($D_P \geq 25$ nm) in comparison to the dissolved amount of ibuprofen out of long and small channels ($D_P \leq 4$ nm). The dissolution performance of the functionalized carrier materials was dependent on the amount and the location of the S-(+)-ibuprofen. The carrier material with a large amount of functionalization on the outer surface tended to agglomeration. Furthermore, this carrier material was poorly wettable due to the hydrophobic character of the S-(+)-ibuprofen. All this led to a diminished dissolution performance at both pH-values compared to other investigated carrier materials.

Despite from pore size and pore shape, the dissolution rate in the beginning of the experiments (t $\leq$ 20 min) was also dependent on the "degree of crystallinity" of the deposited ibuprofen. It was observed, that the dissolution rate of ibuprofen was enhanced form carrier materials with amorphous ibuprofen structures, whereas it was diminished from those with crystalline ibuprofen fractions. Furthermore, it was found that the dissolution behavior of ibuprofen was more affected by its crystalline state at pH = 2.0, whereas its particle size became more important at pH = 5.5. Hence, the "degree of crystallinity" is of crucial relevance for the prediction of dissolution results.

The ibuprofen-ß-cyclodextrin inclusion complex was considered to be the benchmark to evaluate the dissolution performance of the obtained silica CPD products. It was reported in literature that there are only one to two ibuprofen molecules inside the cavity of ß-cyclodextrin. Due to this fact and its low specific surface area ($A_{BET} = 1$ m^2/g) ß-cyclodextrin showed the lowest loading ($Y = 2.25$ wt%) of all carrier materials investigated. Nevertheless, the high solubility of ß-cyclodextrin in aqueous solutions led to the highest ibuprofen dissolution rate of all carrier materials.

At pH = 2.0 none of the other CPD products were able to keep up with the dissolution rate of the ß-cyclodextrin inclusion complex. At pH = 5.5 the carrier materials with the widest mesopores ($D_P \geq 25$ nm) showed similar dissolution rates compared to ß-cyclodextrin.

N_2-sorption experiments at $T = 77$ K were used to characterize unprocessed and CPD processed carrier materials. In the small mesopores ($D_P \leq 4$ nm) a shift of the capillary condensation step from $p/p_0 = 0.3 - 0.4$ (unprocessed carrier materials) towards lower relative pressures (CPD processed carrier materials) was observed. It was possible to definitely assign the shift of the capillary condensation step to ibuprofen which was deposited on the inner surface of the mesopores in contrast to previously performed XRD or DSC analysis.

In the second part of this work, the adsorption of CO_2 on two important carrier materials (MCM-41 and SBA-15) was investigated. In a first step the experimental set up of the MSB was successfully validated by the results obtained from the N_2 and CO_2 adsorption measurements on AC Norit R1 Extra. The adsorption of CO_2 on MCM-41 and SBA-15 was measured next at $T = 298 - 353$ K, $p = 0 - 25$ MPa and $\varrho_{CO2,bulk} = 0 - 900$ kg/m^3. Both carrier materials showed similar values of the excess amount adsorbed due to small variations in their structural and chemical properties.

The values of all excess isotherm increased with increasing density up to a certain maximum. After this maximum the excess values decreased with increasing density. At higher temperatures lower excess values were obtained and the maximum of the isotherm was shifted towards higher densities. The absolute amount adsorbed was calculated by the model of Menon. At high CO_2 densities ($\varrho_{CO2,bulk} \geq 600$ kg/m^3) the saturation amount adsorbed was reached (MCM-41: $n_{abs,sat}$ = ~13.0 mmol/g; SBA-15: $n_{abs,sat}$ = ~13.5 mmol/g). From the derived experimental data the "isosteric heat of adsorption" was calculated. Its values (MCM-41: ΔH_{iso} = -21.7 kJ/mol, SBA-15: ΔH_{iso} = -18.6 kJ/mol) led to the assumption that the adsorption of CO_2 on these carrier materials was exothermic and caused by physisorption. The non-constant curve of the "heat of adsorption" as a function of CO_2 loading implied an energetically heterogeneous surface of both adsorbents.

In a first approach conclusions on the adsorption behavior of the ternary system during the deposition step of the CPD process at $T = 313$ K and $p = 15$ MPa could have been drawn. Therefore, the adsorption results of the binary system CO_2 - carrier material (MCM-41: $n_{absolute} = 13.0$ mmol/g; SBA-15: $n_{absolute} = 13.7$ mmol/g) were

compared to the CPD loading results (MCM-41: $Y = 2.4$ mmol/g; SBA-15: $Y = 2.4$ mmol/g). It was concluded that at the operating CPD process conditions a nearly six times higher amount of CO_2 adsorbed on the carrier material MCM-41 and SBA-15 compared to ibuprofen.

In summary, it was possible in this work to identify the impact of specific carrier material properties on the loading and dissolution behavior of CPD products. With the obtained results this work supplies valuable information for the development of a method to predict the loading and dissolution behavior of new CPD products. Furthermore, it was possible by an easy to handle and cost-effective method (N_2-sorption experiments) to prove the deposition of ibuprofen inside small mesopores ($D_P \leq 4$ nm) reliably by the shift of the capillary condensation step. A solid database for a subsequently design and modelling of the ternary adsorption behavior and phase equilibria during the CPD process is also provided in this work.

Enhancing the dissolution performance of active ingredients will offer a wide and exciting field of research also for future investigations.

It was reported in this work that it is possible to predict the loading and dissolution performance of CPD products by the knowledge of the specific carrier properties and the crystal structure of the deposited ibuprofen. Nevertheless to verify these assumptions and to ensure the transferability of these results to other active ingredient-carrier systems further experiments need to be carried out.

In a first step, further investigations could be carried out with carrier materials which differ only in one of the following properties (specific surface, pore size or pore volume) but not in their chemical nature or pore structure. Thus, the influence of certain specific carrier properties on the loading and dissolution behavior can be investigated in a targeted manner.

With regard to high NML values it was obvious that multilayer formation of the deposited ibuprofen was possible in large mesopores. In addition to interactions between the carrier material surface and the first ibuprofen layer, interactions between the different ibuprofen layers needs to be taken into account. In order to examine the exact influence of these ibuprofen-ibuprofen interactions on the dissolution behavior, the already used carrier materials SMS-1.0 and SMS-0.8 could be loaded with different amounts of ibuprofen and investigate their dissolution behavior.

Furthermore, it is only possible to guess on the exact interactions between the deposited ibuprofen and the carrier material. It has not yet been proven whether the deposited ibuprofen interacts with the carrier due to physisorption or chemisorption. The identification of the exact interactions could be achieved by diffuse reflectance Fourier transform infrared spectroscopy (DRIFTS) measurements. By comparing the DRIFTS results of unloaded and loaded carrier materials, it would be possible to draw conclusions about the interactions between surface groups of the carrier material and ibuprofen through the absence or emergence of specific peaks.

Another possibility to identify the influence of certain carrier-surface groups on the loading results is to use previously heated carrier materials. It is reported in literature that different silica surface groups are released with increasing temperature [139]. If these surface groups show an effect on the loading different loading results will be achieved.

In a first estimation, the calculation of diffusion coefficients of ibuprofen in the pores of the carrier materials could be accomplished using thermogravimetric analysis (TGA) of loaded carrier materials. Due to the mass loss rate of these carrier materials during the analysis, it would be possible to draw conclusions on the diffusion of the ibuprofen within the pores.

Another issue that has not yet been sufficiently clarified is the exact influence of the process parameters such as pressure and temperature on the loading results. Above the retrograde region, the solubility of the ibuprofen in the SCF is increased with rising pressure and temperature. Due to the improved solubility, it is assumed that more ibuprofen remains molecularly dissolved in the SCF and therefore less ibuprofen is deposited on the carrier material. The same carrier materials which were used in this work could be used to verify this assumption.

Furthermore, it was reported, that amorphous structures of the deposited ibuprofen enhance its dissolution behavior especially at low pH-values. With regard to a fast acting effect of the active ingredient formulations with amorphous structures are necessary. Nevertheless, Hörter and Dressman [52] reported that the storage stability of amorphous structures is not guaranteed due to their metastable state. Therefore, it might be useful to test the long term stability of CPD products with amorphous ibuprofen structures.

The identification of carrier materials which are suitable for an enantioselective deposition can also be beneficial, as several studies have shown that S-(+)-ibuprofen has a higher potency than the racemic mixture [41, 140]. Therefore, a reduction of

the applied dosage would be realizable which reduces damages to the human body caused by the active ingredient.

Only an indirect conclusion about the ternary adsorption behavior during the deposition step of the CPD process could be made in this work by comparing the adsorption results of $scCO_2$ on the carrier materials with the ibuprofen loading results, respectively. In order to verify this conclusion and to fully clarify the question whether there is a competition between $scCO_2$ and ibuprofen on the carrier material during the deposition step of the CPD process, the ternary system should be investigated directly by means of a magnetic suspension balance.

BIBLIOGRAPHY

[1] G.L. Amidon, H. Lennernäs, V.P. Shah, J.R.A. Crison, theoretical basis for a biopharmaceutic drug classification: the correlation of in vitro drug product dissolution and in vivo bioavailability, *Pharmaceutical Research* 12(3) (1995) 413–420.

[2] H. Fazlena, A.H. Kamaruddin, M.M.D. Zulkali, Dynamic kinetic resolution: alternative approach in optimizing S-ibuprofen production, *Bioprocess and Biosystems Engineering* 28(4) (2006) 227–233.

[3] A. Kumar, S.K. Sahoo, K. Padhee, P.P.S. Kochar, A. Satapathy, N. Pathak, Review on solubility enhancement techniques for hydrophobic drugs, *Pharmacie Globale - International Journal of comprehensive pharmacy* 2(3) (2011) 1-7.

[4] H.D. Williams, N.L. Trevaskis, S.A. Charman, R.M. Shanker, W.N. Charman, C.W. Pouton, C.J. Porter, Strategies to address low drug solubility in discovery and development, *Pharmacological Reviews* 65(1) (2013) 315–499.

[5] J. Jung, M. Perrut, Particle design using supercritical fluids: literature and patent survey, *Journal of Supercritical Fluids* 20 (2011) 179–219.

[6] G.M. Schneider, Physicochemical aspects of fluid extraction, *Fluid Phase Equilibria* 10(2) (1983) 141–157.

[7] E. Beckman, Supercritical and near-critical CO_2 in green chemical synthesis and processing, *Journal of Supercritical Fluids* 28 (2004) 121–191.

[8] M. Türk, G. Upper, M. Steurenthaler, Kh. Hussein, M.A. Wahl, Complex formation of ibuprofen and β-cyclodextrin by controlled particle deposition (CPD) using sc-CO_2, *Journal of Supercritical Fluids* 39 (2007) 435–443.

[9] W. Li-Hong, C. Xin, X. Hui, Z. Li-Li, H. Jing, Z. Mei-Juan, L. Jie, L. Yi, L. Jin-Wen, Z. Wei, C. Gang, A novel strategy to design sustained-release poorly water-soluble drug mesoporous silica microparticles based on supercritical fluid technique, *International Journal of Pharmaceutics* 454 (2013) 135–142.

[10] M. Ni, Q.-Q. Xu, J.-Z. Yin, Preparation of controlled release nanodrug ibuprofen supported on mesoporous silica using supercritical carbon dioxide, *Journal of Materials Research* 27(22) (2012) 2902–2910.

[11] FDA III. Guidance for Industry: dissolution testing of immediate release solid oral dosage forms. http://www.fda.gov (October 2014).

[12] M. Betz, C.A. García-González, R.P. Subrahmanyam, I. Smirnova, U. Kulozik, Preparation of novel whey protein-based aerogels as drug carriers for life science applications, *Journal of Supercritical Fluids* 72 (2012) 111–119.

[13] C.A. García-González, I. Smirnova, Use of supercritical fluid technology for the production of tailor-made aerogel particles for delivery systems, *Journal of Supercritical Fluids* 79 (2013) 152–158.

[14] Y.A. Hussain, C.S. Grant, Ibuprofen impregnation into submicron polymeric films in supercritical carbon dioxide, *Journal of Supercritical Fluids* 71 (2012) 127–135.

[15] R.S. Wischumerski, M. Türk, M.A. Wahl, Direct drug loading into preformed porous solid dosage units by the controlled particle deposition (CPD), a new concept for improved dissolution using SCF-technology, *Journal of Pharmaceutical Sciences* 97(10) (2008) 4416–4424.

[16] S. Reiser, M. Shaban, A. Weber, M. Türk, Deposition of R/S-ibuprofen on porous particles prepared by salt assisted spray pyrolysis: influence of carrier properties on loading and dissolution behaviour, *Journal of CO_2 Utilization* 25 (2018) 216–225.

[17] S. Reiser, M. Sun, M. Johannsen, M. Türk, Influence of chemical nature of carrier materials on the dissolution behavior of racemic ibuprofen, *The Journal of Supercritical Fluids* 132 (2018) 91–98.

[18] T. Loftsson, D. Duchêne, Cyclodextrins and their pharmaceutical applications, *International Journal of Pharmaceutics* 329 (2007) 1–11.

[19] A. Friebel, Aufbau und Inbetriebnahme einer Anlage zur Untersuchung der Auflösungsgeschwindigkeit von pharmazeutischen Wirkstoffen, Master's thesis, Karlsruher Institut für Technologie (2015).

[20] S. Klein, V.P. Shah, A standardized mini paddle apparatus as an alternative to the standard paddle, *American Association of Pharmaceutical Scientists PharmSciTech* 9(4) (2008) 1179–1184.

[21] P.D. Even, Untersuchung der Auflösungsgeschwindigkeit von schwerlöslichen pharmazeutischen Wirkstoffen, Master's thesis, Karlsruher Institut für Technologie (2016).

[22] P. Gurikov, I. Smirnova, Amorphization of drugs by adsorptive precipitation from supercritical solutions: a review, *Journal of Supercritical Fluids* 132 (2018) 105–125.

[23] K.A. Levis, M.E. Lane, O.I. Corrigan, Effect of buffer media composition on the solubility and effective permeability coefficient of ibuprofen, *International Journal of Pharmaceutics* 253 (2003) 49-59.

[24] M. Gibaldi, S. Feldman, Establishment of sink conditions in dissolution rate determinations, *Journal of Pharmaceutical Sciences* 56(10) (1967) 1238–1242.

[25] P. Costa, J.M. Sousa Lobo, Modeling and comparison of dissolution profiles, *European Journal of Pharmaceutical Sciences* 13 (2001) 123–133.

[26] F. Dreisbach, R. Staudt, J.U. Keller, High pressure adsorption data of methane, nitrogen, carbon dioxide and their binary and ternary mixtures on activated carbon, *Adsorption* 5 (1999) 215-227.

[27] S. Reiser, D. Bolten, R. Staudt, M. Türk, Adsorption of N_2 and CO_2 on activated carbon, AlO(OH) nanoparticles, and AlO(OH) hollow spheres, *Chemical Engineering and Technology* 38 (2015) 2261–2269.

[28] S. Reiser, M. Türk, Influence of temperature and high pressure on the adsorption of $scCO_2$ on MCM-41 and SBA-15, in preparation.

[29] P.G. Menon, Adsorption at high pressures, *Chemical Reviews* 68(3) (1968) 277–294.

[30] M.M. Dubinin, The potential theory of adsorption of gases and vapors for adsorbents with energetically nonuniform surfaces, *Chemical Reviews* 60(2) (1960) 235–241.

[31] M.C. Tsai, W.N. Chen, P.L. Cen, R.T. Yang, Adsorption of gas mixture on activated carbon, *Carbon* 23(2) (1985) 167–173.

[32] G. Ertl, Thermodynamics of gas-surface interactions, *Pure and Applied Chemistry* 61(6) (1989) 1001–1007.

[33] J. Tóth, Adsorption: theory, modeling, and analysis, Dekker, 2002.

[34] L.Z. Benet, The role of BCS (Biopharmaceutics Classification System) and BDDCS (Biopharmaceutics Drug Disposition Classification System) in drug development, *Journal of Pharmaceutical Sciences* 102(1) (2013) 34–42.

[35] R. Ghadi, N. Dand, BCS class IV drugs: highly notorious candidates for formulation development, *Journal of Controlled Release* 248 (2017) 71–95.

[36] M.G. Papich, M.N. Martinez, Applying biopharmaceutical classification system (BCS) criteria to predict oral absorption of drugs in dogs: challenges and pitfalls, *American Association of Pharmaceutical Scientists* 17(4) (2015) 948–964.

[37] H.V. Chavda, C.N. Patel, I.S. Anand, Biopharmaceutics classification system, *Systematic Reviews in Pharmacy* 1(1) (2010) 62–69.

[38] H.D. Williams , L. Ford , S. Lim, S. Han, J. Baumann, H. Sullivan, D. Vodak, A. Igonin, H. Benameur, C.W. Pouton, P.J. Scammells, C.J.H. Porter, Transformation of biopharmaceutical classification system class I and III drugs into ionic liquids and lipophilic salts for enhanced developability using lipid formulations, *Journal of Pharmaceutical Sciences* 107 (2018) 203–216.

[39] N. Rouge, P. Buri, E. Doelker, Drug absorption sites in the gastrointestinal tract and dosage forms for site-specific delivery, *Journal of Pharmaceutics* 136(1-2) (1996) 49–59.

[40] M. Türk, D. Bolten, N. Teubner, Schutzkolloidlösungen zur Stabilisierung von in Wasser schwerlöslichen Modellwirkstoffen, *Chemie Ingenieur Technik* 84(3) (2012) 235–243.

[41] T.Y. Shen, Perspectives in nonsteroidal anti-inflammatory agents, *Angewandte Chemie (International ed. in English)* 11(6) (1972) 460–472.

[42] A.M. Evans, Comparative Pharmacology of S(+)-Ibuprofen and (RS)-Ibuprofen, *Clinical rheumatology* 20(Suppl 1) (2001) 9–14.

[43] M. Meloun, S. Bordovska, L. Galla, The thermodynamic dissociation constants of four non-steroidal anti-inflammatory drugs by the least-squares nonlinear regression of multiwavelength spectrophotometric pH-titration data, *Journal of Pharmaceutical and Biomedical Analysis* 45(4) (2007) 552–564.

[44] L.R. Shaw, W.J. Irwin, T.J. Grattan, B.R Conway, The effect of selected water-soluble excipients on the dissolution of paracetamol and ibuprofen, *Drug Development and Industrial Pharmacy* 31 (2005) 515–525.

[45] A. Avdeef, Solubility of sparingly-soluble ionizable drugs, *Advanced Drug Delivery Reviews* 59(7) (2007) 568-590.

[46] T. Azais, C. Tourné-Péteilh, F. Aussenac, N. Baccile, C. Coelho, J.M. Devoisselle, F. Babonneau, Solid-State NMR Study of Ibuprofen Confined in MCM-41 Material, *Chemistry of Materials* 18(26) (2006) 6382–6390.

[47] United States Pharmacopeia 29. <1088> In vitro and in vivo evaluation of dosage forms.
http://www.pharmacopeia.cn (October 2014).

[48] FDA IV. Guidance for Industry: waiver of in vivo bioavailability and bioequivalence studies for immediate-release solid oral dosage forms based on a biopharmaceutics classification system.
http://www.fda.gov (October 2014).

[49] International Pharmacopeia - 4. Edition.
http://apps.who.int/phint/en/p/docf/ (October 2014).

[50] United States Pharmacopeia 29. Reagents and buffer solutions.
http://www.pharmacopeia.cn (October 2014).

[51] United States Pharmacopeia 29. The dissolution procedure: development and validation.
http://www.pharmacopeia.cn (October 2014).

[52] J. Hörter, J.B. Dressman, Influence of physicochemical properties on dissolution of drugs in the gastrointestinal tract, *Advanced Drug Delivery Reviews* 46 (2001) 75–87.

[53] S.S. Jambhekar, P.J. Breen, Drug dissolution: significance of physicochemical properties and physiological conditions, *Drug Discovery Today* 18(23/24) (2013) 1173–1184.

[54] A.A. Noyes, W.R. Whitney, The rate of solution of solid substances in their own solutions, *Journal of the American Chemical Society* 19(12) (1897) 930–934.

[55] A.W. Hixson, J.H. Crowell, Dependence of reaction velocity and agitation upon surface: III experimental procedure in study of agitation, *Industrial & Engineering Chemistry* 23(10) (1931) 1160–1168.

[56] W. Weibull, A statistical distribution function of wide applicability, *Journal of Applied Mechanics* 18 (1951) 293-297.

[57] C.A. Eckert, B.L. Knutson, P.G. Debenedetti, Supercritical fluids as solvents for chemical and materials processing, *Nature* 383 (1996) 313–318.

[58] R. Noyori, Supercritical fluids: introduction, *Chemical Reviews* 99 (1999) 353–354.

[59] K. Zosel, Practical applications of material separation with supercritical gases, *Angewandte Chemie* 90 (1978) 748–755.

[60] S. Schaeffer, L.H. Zalkow, A.S. Teja, Extraction of monocrotaline from crotalaria spectabilis using supercritical carbon dioxide and carbon dioxide-ethanol mixtures, *Biotechnology and Bioengineering* 34 (1989) 1357–1365.

[61] M. Türk, B. Helfgen, P. Hils, R. Lietzow, K. Schaber, Micronization of pharmaceutical substances by rapid expansion of supercritical solutions (RESS): experiments and modelling, *Particle & Particle Systems Characterization* 19(5) (2002) 327–335.

[62] M. Türk, Manufacture of submicron drug particles with enhanced dissolution behaviour by rapid expansion processes, *Journal of Supercritical Fluids* 47 (2009) 537–545.

[63] M. Charoenchaitrakool, F. Dehghani, N.R. Foster, H.K. Chan, Micronization by rapid expansion of supercritical solutions to enhance the dissolution rates of poorly water-soluble pharmaceuticals, *Industrial & Engineering Chemistry Research* 39(12) (2000) 4794–4802.

[64] N.R. Foster, F. Dehghani, M. Charoenchaitrakool, B. Warwick, Application of dense gas techniques for the production of fine particles, *AAPS PharmSciTech* 5 (2003) 105–111.

[65] H.J. Martin, Charakterisierung von schwerlöslichen Arzneistoff-Nanopartikeln hergestellt durch das RESS-Verfahren zur Verbesserung der Bioverfügbarkeit, PhD thesis, Eberhard-Karls-Universität Tübingen, 2003.

[66] M. Türk, Erzeugung von organischen Nanopartikeln mit überkritischen Fluiden, PhD thesis, Universität Karlsruhe (TH), 2001.

[67] M. Türk, D. Bolten, Formation of submicron poorly water-soluble drugs by rapid expansion of supercritical solution (RESS): results for naproxen, *Journal of Supercritical Fluids 55* (2010) 778–785.

[68] M. Bahrami, S. Ranjbarian, Production of micro- and nano-composite particles by supercritical carbon dioxide, *Journal of Supercritical Fluids* 40 (2007) 263–283.

[69] P.M. Gallagher, M.P. Coffey, V.J. Krukonis, N. Klasutis, Gas antisolvent recrystallization: new process to recrystallize compounds insoluble in supercritical fluids, *ACS Symposium Series* 406 (1989) 334–354.

[70] E. Reverchon, I. De Marco, E. Torino, Nanoparticles production by supercritical antisolvent precipitation: a general interpretation, *Journal of Supercritical Fluids* 43 (2007) 126–138.

[71] E. Weidner, Z. Knez, R. Steiner, Powder generation from polyethyleneglycols with compressible fluids, in: High pressure chemical engineering, Elsevier, Amsterdam, 1996.

[72] E. Weidner, High pressure micronization for food applications, *Journal of Supercritical Fluids* 47 (2009) 556–565.

[73] M. Türk, Particle formation with supercritical fluids - challenges and limitations, Elsevier, Amsterdam, 2014.

[74] E. W. Lemmon, M. L. Huber, M. O. McLinden, NIST Standard reference database 23: reference fluid thermodynamic and transport properties-REFPROP, Version 9.1, MD2013.

[75] A. Michels, C. Michels, H. Wouters, Isotherms of CO_2 between 70 and 3000 atmospheres (amagat densities between 200 and 600), *Proceedings of the Royal Society A* 153 (1935) 214–224.

[76] A. Michels, C. Michels, Series evaluation of the isotherm data of CO_2 between 0 and 150 degrees C. and up to 3000 atm, *Proceedings of the Royal Society A* 160 (1937) 348–357.

[77] D. Sanli, S.E. Bozbag, C. Erkey, Synthesis of nanostructured materials using supercritical CO_2: part I. physical transformations, *Journal of Material Science* 47 (2012) 2995–3025.

[78] R.B. Gupta, J.J. Shim, Solubility in supercritical carbon dioxide, Boca Raton: Taylor & Francis, 2007.

[79] M. Ardjmand, M. Mirzajanzadeh, F. Zabihi, Measurement and correlation of solid drugs solubility in supercritical systems, *Chinese Journal of Chemical Engineering* 22(5) (2014) 549–558.

[80] J. Mendez-Santiago, A.S. Teja, The solubility of solids in supercritical fluids, *From Fluid Phase Equilibria* 159-160 (1999) 491–500.

[81] M.E. Brewster, T. Loftsson, Cyclodextrins as pharmaceutical solubilizers, *Advanced Drug Delivery Reviews* 59 (2007) 645–666.

[82] R.G. Winkler, S. Fioravanti, G. Ciccotti, C. Margheritis, M. Villa, Hydration of β-cyclodextrin: a molecular dynamics simulation study, *Journal of Computer-Aided Molecular Design* 14 (2000) 659–667.

[83] M.M. Nitalikar, D.M. Sakarkar, P.V. Jain, The cyclodextrins: a review, *Journal of Current Pharmaceutical Research* 10(1) (2013) 1–6.

[84] P.J. Salústio, G. Feio, J.L. Figueirinhas, J.F. Pinto, H.M. Cabral Marques, The influence of the preparation methods on the inclusion of model drugs in a β-cyclodextrin cavity, *European Journal of Pharmaceutics and Biopharmaceutics* 71 (2009) 377–386.

[85] L.J. Waters, S. Bedford, G.M.B. Parkes, J.C. Mitchell, Influence of lipophilicity on drug-cyclodextrin interactions: a calorimetric study, *Thermochimica Acta* 511 (2010) 102–106.

[86] M. Banchero, S. Ronchetti, L. Manna, Characterization of ketoprofen/methyl-β-cyclodextrin complexes prepared using supercritical carbon dioxide, *Journal of Chemistry* (2013) Article ID 583952, 8 pages.

[87] C.J. Núñez-Agüero, C.M. Escobar-Llanos, D. Díaz, R. Garduño-Juárez, Chiral discrimination of ibuprofen isomers in β-cyclodextrin inclusion complexes: experimental (NMR) and theoretical (MD, MM/GBSA) studies, *Tetrahedron* 62(17) (2006) 4162-4172.

[88] Ashnagar, A.; Culnane, P.T.; Easton, C.J.; Harper, J.B.; Lincoln, S.F. Complexes of Naproxen and Ibuprofen with 6-Amino-6-deoxy-β-cyclodextrin, *Australian Journal of Chemistry* 50 (1997) 447–450.

[89] M. Charoenchaitrakool, F. Dehghani, N.R. Foster, Utilization of supercritical carbon dioxide for complex formation of ibuprofen and methyl-β-cyclodextrin, *International Journal of Pharmaceutics* 239 (2002) 103–112.

[90] M.R. Eftink, M.L. Andy, K. Bystrom, H.D. Perlmutter, D.S. Kristol, Cyclodextrin inclusion complexes: studies of the variation in the size of alicyclic guests, *Journal of the American Chemical Society* 111(17) (1989) 6765–6772.

[91] A. Bounaceur, E. Rodier, J. Fages, Maturation of a ketoprofen/ β-cyclodextrin mixture with supercritical carbon dioxide, *Journal of Supercritical Fluids* 41 (2007) 429–439.

[92] CambridgeSoft Corporation a subsidiary of PerkinElmer Inc., *ChemBioDraw 14.0*.

[93] M. Cirri, C. Rangoni, F. Maestrelli, G. Corti, P. Mura, Development of fast-dissolving tablets of flurbiprofen-cyclodextrin complexes, *Drug Development and Industrial Pharmacy* 31(7) (2005) 697–707.

[94] J.R. Moyano, M.J. Arias-Blanco, J.M. Gines, F. Giordano, Solid-state characterization and dissolution characteristics of gliclazide-β-cyclodextrin inclusion complexes, *International Journal of Pharmaceutics* 148(2) (1997) 211–217.

[95] K. Hussein, M. Türk, M.A. Wahl, Comparative evaluation of ibuprofen/β-cyclodextrin complexes obtained by supercritical carbon dioxide and other conventional methods, *Pharmaceutical Research* 24(3) (2007) 585–592.

[96] C.M. Vozone, H.M. Cabral Marques, Complexation of budesonide in cyclodextrins and particle aerodynamic characterization of the complex solid form for dry powder inhalation, *Journal of Inclusion Phenomena and Macrocyclic Chemistry* 44 (2002) 111–115.

[97] F. Cao, J. Guo, Q. Ping, The physicochemical characteristics of freeze-dried scutellarin-cyclodextrin tetracomponent complexes, *Drug Development and Industrial Pharmacy* 31(8) (2005) 747–756.

[98] H.D. González, O.D. Rojo, Experimental study of silica absorption through the digestive tract as a cause of extrapulmonary silicosis, *Revista Espanola De Enfermedades Digestivas* 80(2) (1991) 95–98.

[99] C.Y. Chen, S.L. Burkett, H.X. Li, M.E. Davis, Studies on mesoporous materials II. Synthesis mechanism of MCM-41, *Microporous Materials* 2(1) (1993) 27–34.

[100] D. Zhao, J. Feng, Q. Huo, N. Melosh, G.H. Frederickson, B.F. Chmelka, G.D. Stucky, Triblock copolymer syntheses of mesoporous silica with periodic 50 to 300 angstrom pores, *Science* 279(5350) (1998) 548–552.

[101] M. do Socorro Braga Fontes, D.M. de Araújo Melo, C. de Castro Costa, R. Martins Braga; M.A. de Freitas Melo, J.A. Barros Leal Reis Alves, Comparison of kinetic study of CTMA+ removal of molecular sieve Ti-MCM-41 synthesized with natural and commercial silica, *Material Research* 18(3) (2015) 608–613.

[102] K. Schumacher, P.I. Ravikovitch, A. Du Chesne, A.V. Neimark, K.K. Unger, Characterization of MCM-48 materials, *Langmuir* 16(10) (2000) 4648-4654.

[103] M. Vallet-Regí, A. Rámila, R.P. del Real, J. Pérez-Pariente, A new property of MCM-41: drug delivery system, *Chemistry of Materials* 13 (2001) 308–311.

[104] B. Muñoz, A. Rámila, J. Pérez-Pariente, I. Díaz, M. Vallet-Regí, MCM-41 organic modification as drug delivery rate regulator, *Chemistry of Materials* 15 (2003) 500–503.

[105] D.H. Hwang, D. Lee, H. Lee, D. Choe, S.H. Lee, K. Lee, Surface functionalization of SBA-15 particles for ibuprofen delivery, *Korean Journal of Chemical Engineering* 27(4) (2010) 1087–1092.

[106] J. Kurczewska, D. Lewandowski, A. Olejnik, G. Schroeder, I. Nowak, Double barrier as an effective method for slower delivery rate of ibuprofen, *International Journal of Pharmaceutics* 472 (2014) 248–250.

[107] Y.S. Ko, J.S. Lee, J.H. Yim, J.K. Jeon, K.Y. Jung, Influence of nanopores of MCM-41 and SBA-15 confining (n-BuCp)2ZrCl2 on copolymerization of ethylene-α-olefin, *Journal of Nanoscience and Nanotechnology* 10 (2010) 180–185.

[108] S. Loganathan, M. Tikmani, A.K. Ghoshal, Pore-expanded MCM-41 for CO_2 adsorption: experimental and isotherm modeling studies, *Chemical Engineering Journal (Amsterdam, Netherlands)* 280 (2015) 9–17.

[109] D.H. Everett, Manual of symbols and terminology for physicochemical quantities and units, Appendix II: definitions, terminology and symbols in colloid and surface chemistry, *Pure and Applied Chemistry* 31(4) (1972) 577–638.

[110] R. Staudt, Habilitationsschrift, (PhD thesis) Univeristät Siegen, 2001.

[111] IUPAC commission on colloid and surface chemistry including catalysis. Reporting physisorption data for gas/solid systems with special reference to the determination of surface area and porosity, *Pure and Applied Chemistry* 57(4) (1085) 603–619.

[112] M. Thommes, K. Kaneko, A.V. Neimark, J.P. Olivier, F. Rodriguez-Reinoso, J. Rouquerol, K.S.W. Sing, Physisorption of gases, with special reference to the evaluation of surface area and pore size distribution (IUPAC Technical Report), *Pure and Applied Chemistry* 87(9-10) (2015) 1051–1069.

[113] Quantachrome Instruments. Nova operation manual - high speed gassorption analyzer, Version: 11.02, 2009.

[114] S. Brunauer, P.H. Emmett, E. Teller, Adsorption of gases in multimolecular layers, *Journal of the American Chemical Society* 60(2) (1938) 309–319.

[115] J. Rouquerol, F. Rouquerol, K.S.W. Sing, P. Llewellyn, G. Maurin, Adsorption by powders and porous solids: principles, methodology and applications, Academic Press, 2014.

[116] S. Lowell, J. Shields, M.A. Thomas, M. Thommes, Characterization of porous solids and powders: surface area, porosity and density, Springer, 2004.

[117] E.P. Barrett, L.G. Joyner, P.P. Halenda, The determination of pore volume and area distributions in porous substances. I computations from nitrogen isotherms, *Journal of the American Chemical Society* 73(1) (1951) 373–380.

[118] G. Lindau, Über Adsorption und Kapillarkondensation, *Kolloid Zeitschrift* Band LX(3) (1932) 253–263.

[119] R. Heller, M. Zoback, Adsorption of methane and carbon dioxide on gas shale and pure mineral samples, *Journal of Unconventional Oil and Gas Resources* 8 (2014) 14–24.

[120] H. Yi, B. Huang, X. Tang, K. Li, Q. Yuan, R. Lai, P. Wang, Simultaneous adsorption of SO_2, NO, and CO_2 by K_2CO_3-modified γ-Alumina, *Chemical Engineering & Technology* 37(6) (2014) 1049–1054.

[121] R. Staudt, G. Sailer, M. Tomalla, J.U. Keller, A Note on gravimetric measurements of gas adsorption equilibria, *Berichte der Bunsengesellschaft/Physical Chemistry Chemical Physics* 97 (1993) 98–105.

[122] D.D. Do, H.D. Do, Adsorption of supercritical fluids in non-porous and porous carbons: analysis of adsorbed phase volume and density, *Carbon* 41 (2003) 1777–1791.

[123] J. Möllmer, A. Möller, F. Dreisbach, R. Glaeser, R. Staudt, High pressure adsorption of hydrogen, nitrogen, carbon dioxide and methane on the metal-organic framework HKUST-1, *Microporous and Mesoporous Materials* 138 (2011) 140–148.

[124] M. Polanyi, Adsorption from the point of view of the third law of thermodynamics, *Verhandlungen der Deutschen Physikalischen Gesellschaft* 16 (1914) 1012–1016.

[125] I. Langmuir, The adsorption of gases on plane surfaces of glass, mica and platinum, *Journal of the American Chemical Society* 40(9) (1918) 1361–1403.

[126] J.U. Keller, R. Staudt, Gas adsorption equilibria - experimental methods and adsorptive isotherms, Springer, 2005.

[127] W. Rudzinski, D.H. Everett, Adsorption of gases on heterogeneous surfaces, Elsevier Ltd., 1991.

[128] D.D. Do, Adsorption analysis: equilibria and kinetics, Volume 2, Imperial College Press, 1998.

[129] H. Freundlich, Of the adsorption of gases. Section II. Kinetics and energetics of gas adsorption. Introductory paper to section II, *Transactions of the Faraday Society* 28 (1932) 195–201.

[130] R. Sips, On the structure of a catalyst surface, *The Journal of Chemical Physics* 16 (1948) 490–495.

[131] D.D. Frey, A.E. Rodrigues, Explicit calculation of multicomponent equilibria for ideal adsorbed solutions, *American Institute of Chemical Engineers Journal* 40(1) (1994) 182–186.

[132] J. Fischer, J. Specovius, G.H. Findenegg, Quantitative Beschreibung der Adsorption von Gasen bei erhöhten Drücken, *Chemie Ingenieur Technik* 50(1) (1078) 41–42.

[133] S. Sircar, R. Mohr, C. Ristic, M.B. Rao, Isosteric heat of adsorption: theory and experiment, *Journal of Physical Chemistry B* 103 (1999) 6539–6546.

[134] G.P. Knowles, J.V. Graham, S.W. Delaney, A.L. Chaffee, Aminopropyl-functionalized mesoporous silicas as CO_2 adsorbents, *Fuel Processing Technology* 86 (2005) 1435–1448.

[135] A.L. Myers, P.A. Monson, Adsorption in porous materials at high pressure: theory and experiment, *Langmuir* 18 (2002) 10261–10273.

[136] S. Beutekamp, P. Harting, Experimental determination and analysis of high pressure adsorption data of pure gases and gas mixtures, *Adsorption* 8 (2002) 255–269.

[137] N. Tatsuda, Y. Goto, N. Setoyama, Y. Fukushima, Adsorption of carbon dioxide on mesoporous silicas near the critical temperature, *Adsorption Science & Technology* 23(9) (2005) 763–776.

[138] Y. He, N.A. Seaton, Heats of adsorption and adsorption heterogeneity for methane, ethane, and carbon dioxide in MCM-41, *Langmuir* 22(3) (2006) 1150–1155.

[139] J.P. Gallas, J.M. Goupil, A. Vimont, J.C. Lavalley, B. Gil, J.P. Gilson, O. Miserque, Quantification of water and silanol species on various silicas by coupling IR spectroscopy and in-situ thermogravimetry *Langmuir* 25(10) (2009) 5825–5834.

[140] S.S. Adams, P. Bresloff, C.G. Mason, Pharmacological differences between the optical isomers of ibuprofen: evidence for metabolic inversion of the (-)-isomer, *Journal of Pharmacy and Pharmacology* 28(3) (1976) 256–257.

Appendix

Additional figures and results

Dimensions of the dissolution apparatus

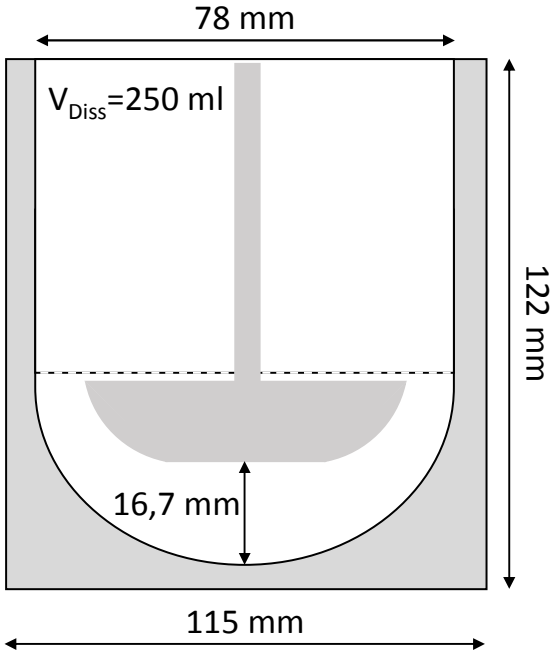

Fig. A.1 Dimensions of the mini-apparatus recommended by Klein and Shah: Dissolution vessel [20]. Design by [19].

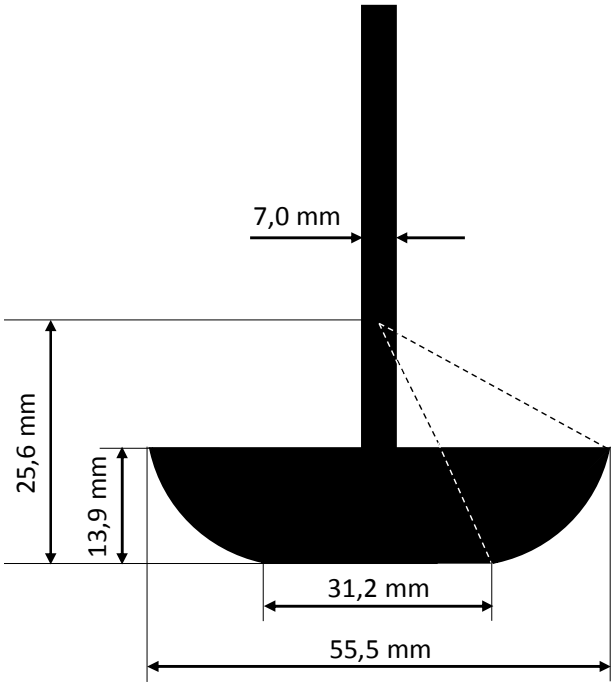

Fig. A.2 Dimensions of the mini-apparatus recommended by Klein and Shah: Paddle [20]. Design by [19].

Results of the Fluid Dynamic Simulation by Ansys Fluent

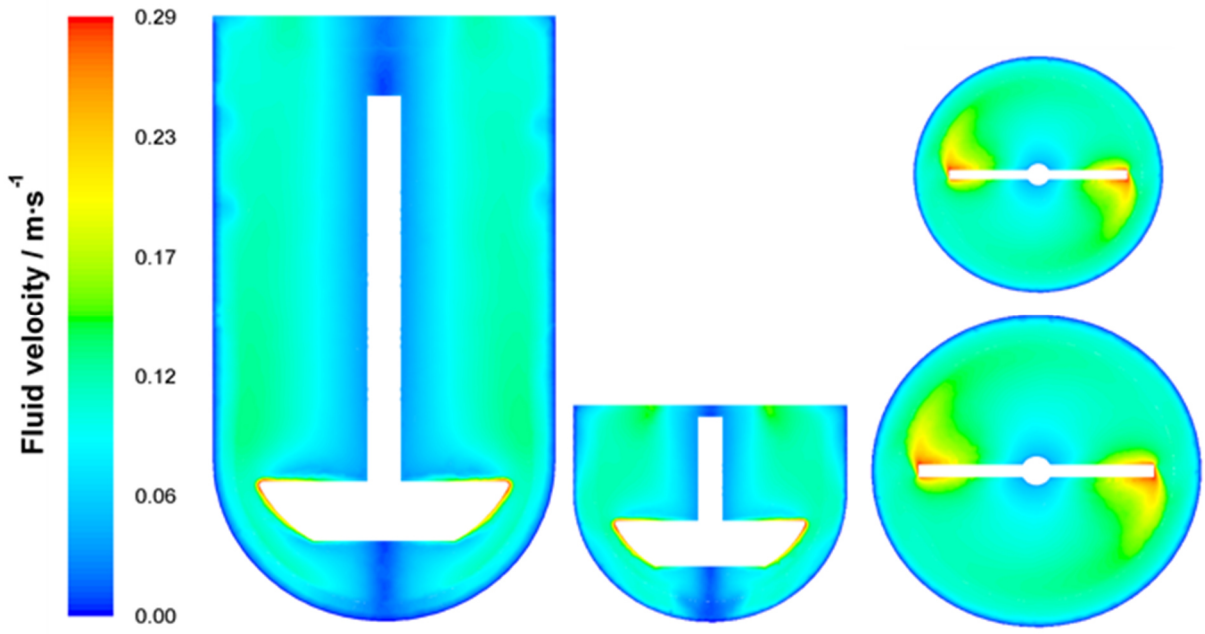

Fig. A.3 Fluid dynamic profile of an USP-2 apparatus with dimensions recommended by the FDA (left and right bottom) and with the dimensions recommended by Klein and Shah [20] (middle and right top) [19].

Selected results of the reproducibility study

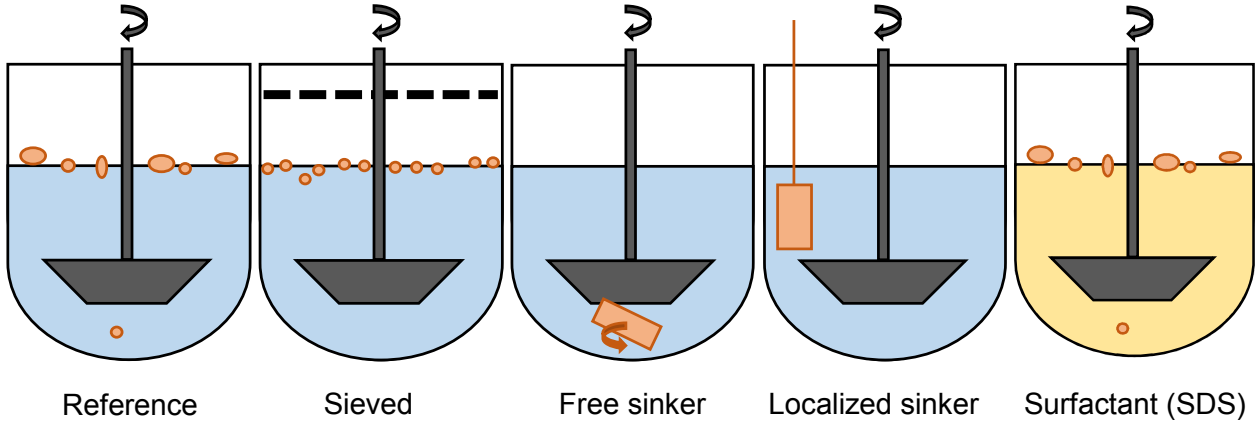

Fig. A.4 Different sample injection methods investigated in the reproducibility study [19]. Design by [19].

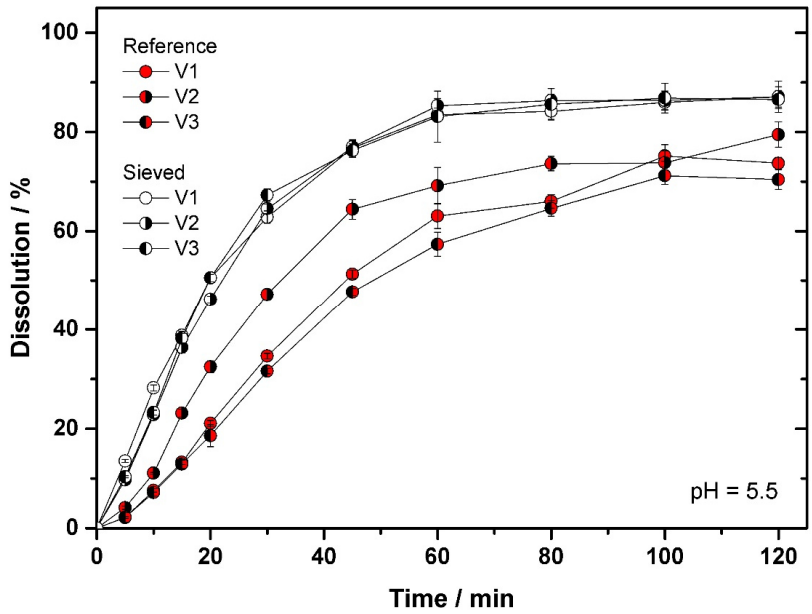

Fig. A.5 Results of the reproducibility study: Dissolution as a function of time at pH = 5.5 for different sample injection methods. Red symbols: reference, white symbols: sieved [19].